

Atomistic mechanisms of hydrogen embrittlement

THÈSE N° 8227 (2017)

PRÉSENTÉE LE 18 DÉCEMBRE 2017
À LA FACULTÉ DES SCIENCES ET TECHNIQUES DE L'INGÉNIEUR
LABORATOIRE DE MODÉLISATION MÉCANIQUE MULTI-ÉCHELLE
PROGRAMME DOCTORAL EN MÉCANIQUE

ÉCOLE POLYTECHNIQUE FÉDÉRALE DE LAUSANNE

POUR L'OBTENTION DU GRADE DE DOCTEUR ÈS SCIENCES

PAR

Ali TEHRANCHI

acceptée sur proposition du jury:

Prof. F. Gallaire, président du jury
Prof. W. Curtin, directeur de thèse
Dr J. Song, rapporteur
Prof. D. Kochmann, rapporteur
Dr P. Derlet, rapporteur



ÉCOLE POLYTECHNIQUE
FÉDÉRALE DE LAUSANNE

Suisse
2017

Acknowledgements

First of all, I express my deepest and sincerest thanks to my thesis advisor Professor Bill Curtin, who gave me the opportunity to join and work in his prestigious Laboratory for Multi-scale Mechanics Modeling (LAMMM) at EPFL. He constantly gave me courage, taught me how to research, and initiated very interesting and deep discussions to keep me on the right track.

Moreover, because of Bill's universally acknowledged excellence in the field of mechanics of materials, LAMMM hosts many good researchers who I really enjoyed to collaborate with. Specifically, I should mention our post-docs and scientists in the lab. Aitor Luque, Fabio Pavia, Céline Varvenne, Kris Baker, Philip Moseley, Mike Francis, Zhaoxuan Wu, Varun Rajan, Francesco Maresca, Till Junge, Binglun Yin, Satish Rao, and Nikolas Bouklas. I had also the opportunity to make friend and collaborate with, Ben Szajewsky, Seyed Mostafa Khosrownejad, Wolfram Nöhring, Max Hodapp, Predrag Andric, Vladimir Dorodnitsyn, Shankha Nag, Rasool Ahmad, Yi Hu, and Eleanor Mak as the other graduate students in the lab. We share a lot of good memories and had fruitful discussions. Also, many thanks go to LAMMM's secretary Ms. Géraldine Palaj who dedicatedly helps all members of LAMMM to focus only on their research.

I also should acknowledge the fact that I have very good friends including Ehsan Kazemi who was my coach in body transformation, Nakisa Mosavi, Farzan Jazayeri, Seyedeh Golzar Mesbah, Azadeh Yazdan-Yar, Mahsa Silatani, Mokhtar Bozorg, Samira Kouchali, and Farzaneh Jahanbakhshi in Lausanne with whom I share a lot of good memories and moments.

I also thank my friends all around the world who I always was remotely consulting with. Specifically, I should thank Hamed Haftbaradaran, Hanif Ostadhossein, Farzaneh Ojaghnezhad, Alireza Khorshidi, Amin Nozari, Kamyar Davoudi, Fatemeh Ahmadpoor, S. Mohadeseh Taheri Mousavi, Shaghayegh and Pouya Rezazadeh, and Shahriar Houshmand. Last but definitely the best; I express my warmest respects and gratitude to my parents Mahmoud and Sima, and my brother Arash who were always unconditionally supportive, patient and encouraging. I don't think that this thesis could be written without their emotional support and patience.

Lausanne, 28 Nov 2017

ACI T.

Abstract

The detrimental effects of H on the mechanical properties of metals are known for more than a century. One of the most important degradation mechanisms is H embrittlement (HE). In this thesis, we examine a few famous proposed mechanisms in the field by performing careful atomistic simulations. Moreover, novel mechanisms which can be responsible for the HE process in metals are demonstrated in this work.

First, we used atomistic simulations to investigate the effects of segregated H on the behavior of cracks along various symmetric tilt grain boundaries in fcc Nickel. Mode I fracture behavior is then studied, examining the influence of H in altering the competition between dislocation emission (“ductile” behavior) and cleavage fracture (“brittle” behavior) for intergranular cracks. Simulations revealed that the embrittling effects of H atoms are limited. We examined the effect of H atoms on the nucleation of intergranular cracks in Ni. The theoretical strength is ~ 25 GPa and the yield strength is ~ 10 GPa, so that (i) the theoretical strength is always well above the yield strength, with or without H, and (ii) both strengths are far above the bulk plastic flow stress, σ_y^B , of Ni and Ni alloys. So H does not significantly facilitate nucleation of intergranular cracks.

We performed simulations of the interactions between dislocations, H atoms, and vacancies to assess the viability of a recently-proposed mechanism for the formation of nanoscale voids in Fe-based steels in the presence of H. The effectiveness of annihilation/reduction processes is not reduced by the presence of H in the vacancy clusters because typical V-H cluster binding energies are much lower than the vacancy formation energy, except at very high H content in the cluster. Experimental observations of nanovoids on the fracture surfaces of steels must be due to as-yet undetermined processes.

The possible strengthening effects of H atoms in metals at low temperature is examined via the solute strengthening (SS) theory. The results of the SS theory can explain recent experimental observations of strengthening of H-charged polycrystalline nickel at low temperature. Moreover, the possible softening/hardening effects of H atoms due to their interaction with pre-existing solutes are demonstrated and, for the first time, a softening process in nickel alloys is shown.

The effect of the H atoms in increasing the precipitate hardening in α -Iron is also shown in this thesis. The direct molecular dynamics simulations of the bow out of an edge dislocation in H-free and H-charged samples reveals that the presence of H atoms decreases the magnitude of the bow out of the dislocation. The hardening effect of H on the interaction of dislocations and grain boundaries in nickel is also investigated in this

Abstract

thesis. To this end, we simulated the interaction of mixed and screw dislocations with the grain boundaries that have access to the slip planes in nickel. The presence of H atoms along the grain boundaries induces stress in the neighborhood of the grain boundary. These stress fields can repel/attract mixed dislocations while the screw dislocations are not interacting with them. The simulation of the interaction of the mixed dislocations with the H-free and H-charged GBs shows hardening due to the presence of H atoms. The simulations of the screw dislocations do not show significant hardening due to the presence of this stress field.

Key words: Hydrogen embrittlement, ductile to brittle transition, polycrystalline metals, solute strengthening, Grain boundary, dislocation, fracture mechanics

Zusammenfassung

Der schädliche Einfluss von Wasserstoff auf die mechanischen Eigenschaften der Metalle ist seit mehr als einem Jahrhundert bekannt. Einer der wichtigsten Schädigungsmechanismen ist die Wasserstoffversprödung. In dieser Arbeit untersuchen wir einige der in diesem Gebiet vorgeschlagenen Mechanismen mittels sorgfältig durchgeführter atomistischer Simulationen. Zudem werden neue Mechanismen aufgezeigt, die für die Wasserstoffversprödung verantwortlich sein könnten. Zunächst wurde der Einfluss von segregiertem Wasserstoff auf das Verhalten von Rissen entlang verschiedener symmetrischer Kippkorn Grenzen in kfz-Nickel mit atomistischen Simulationen untersucht. Danach wird das Rissverhalten im Modus I betrachtet. Es wird untersucht, wie der Wasserstoff bei intergranularen Rissen den Widerstreit zwischen Versetzungsemission („duktiler“ Verhalten) und Spaltbruch („sprödes“ Verhalten) beeinflusst. Simulationen zeigten, dass der versprödende Effekt des Wasserstoffs begrenzt ist. Wir haben den Einfluss des Wasserstoffs auf die Nukleation intergranularer Risse in Ni untersucht. Die theoretische Festigkeit beträgt ~ 25 GPa und die Streckgrenze ~ 10 GPa, sodass (i) die theoretische Festigkeit immer über der Streckgrenze liegt, mit oder ohne H, und (ii) beide Festigkeitswerte weit über der mittleren Fließspannung σ_y^B von Ni und Ni-Legierungen liegen. Daher erleichtert H die Nukleation von intergranularen Rissen nicht wesentlich.

Die Wechselwirkung zwischen Versetzungen, Wasserstoffatomen und Leerstellen wurde simuliert, um zu prüfen, ob ein jüngst vorgeschlagener Mechanismus für die Bildung von nanoskaligen Poren in Stählen die Wasserstoff ausgesetzt sind plausibel ist. Die Effektivität von Bildungs-/Annihilationsprozessen wird durch die Präsenz von H-Atomen in den Leerstellen-Clustern nicht gemindert, weil typische Bindungsenergien für Leerstellen-Wasserstoff-Cluster viel größer als die Leerstellenbildungsenergie sind, außer bei sehr hohem Wasserstoffanteil im Cluster. Für die in Experimenten beobachteten nanoskaligen Poren an Bruchflächen von Stählen müssen daher bislang noch unbestimmte Prozesse verantwortlich sein. Ein möglicher festigkeitssteigernder Effekt von H-Atomen in Metallen bei niedriger Temperatur wird mit der Theorie der Mischkristallhärtung untersucht. Die Ergebnisse der Theorie können experimentelle Beobachtungen einer erhöhten Festigkeit von wasserstoffgesättigtem, polykristallinem Nickel bei niedrigen Temperaturen erklären. Zudem werden mögliche festigkeitsmindernde/-steigernde Effekt von H-Atomen demonstriert, die sich aus ihrer Wechselwirkung mit bereits vorhandenen Lösungsatomen ergeben. Zum ersten Mal wird ein festigkeitsmindernder Prozess in Nickel-Legierungen gezeigt.

Abstract

Auch eine Steigerung der Ausscheidungshärtung in α -Eisen durch H-Atome wird in dieser Arbeit nachgewiesen. Direkte Molekulardynamik-Simulationen einer gekrümmten Stufenversetzung in wasserstofffreien und -gesättigten Proben zeigen, dass die Präsenz von H-Atomen die Krümmung vermindert. Ferner wird in dieser Arbeit der festigkeitssteigernde Einfluss von H-Atomen auf die Interaktion von Versetzungen und Korngrenzen in Nickel untersucht. Zu diesem Zweck wurde für Nickel die Wechselwirkung von gemischten Versetzungen und Schraubenversetzungen mit jenen Korngrenzen die Zugang zu den Gleitebenen haben untersucht. H-Atome entlang der Korngrenzen verursachen Spannungen in der Umgebung der Korngrenze. Diese Spannungsfelder können gemischte Versetzungen abstoßen oder anziehen, wohingegen Schraubenversetzungen nicht mit ihnen wechselwirken. Simulationen der Wechselwirkungen von gemischten Versetzungen mit wasserstofffreien und mit Wasserstoff angereicherten Korngrenzen weisen auf eine Festigkeitssteigerung bei Anwesenheit von H-Atomen hin. In Simulationen mit Schraubenversetzungen zeigt sich keine ausgeprägte Festigkeitssteigerung durch dieses Spannungsfeld.

Schlüsselwörter: Wasserstoffversprödung, duktiler bis spröder Übergang, polykristalline Metalle, solute Verstärkung

Contents

Acknowledgements	i
Abstract (English/Français/Deutsch)	iii
List of figures	xi
List of tables	xix
1 Motivation and background	1
1.1 Introduction	1
1.2 Background of the hydrogen embrittlement studies	2
1.2.1 Experimental studies	2
1.2.2 Theoretical approaches	7
1.2.3 Simulations	10
1.3 Atomistic studies of hydrogen embrittlement in metals	13
1.4 Outline of the thesis	16
2 Atomistic study of Hydrogen embrittlement of grain boundaries in Nickel	17
2.1 Introduction	17
2.2 Energetics of Hydrogen in Ni grain boundaries and fracture surfaces	18
2.2.1 Validated Ni–H interatomic potential	18
2.2.2 Energies of H in grain boundaries and fracture surfaces	19
2.3 Simulation of the tensile strength and yield strength of grain boundaries	22
2.3.1 Results	25
2.3.2 Discussion	40
2.4 Fracture simulations	42
2.4.1 Theoretical framework	42
2.4.2 Simulation details	45
2.4.3 Results	47
2.4.4 Discussion of the fracture simulations	49
2.5 Summary	56

Contents

3	Softening and hardening of yield stress by hydrogen interstitials	57
3.1	Introduction	57
3.2	General theory of solute strengthening	58
3.2.1	Input of the model	63
3.2.2	Pressure field of the dislocation	64
3.2.3	Calibration of the model	64
3.3	The strengthening effects of H atoms on nickel	65
3.4	Hardening/softening effects of H atoms in nickel alloys	67
3.4.1	Solute strengthening of straight dislocations	67
3.4.2	Atomistic Simulation Methodology	70
3.4.3	Results and discussion	72
3.4.4	Interaction of Carbon and Sulfur solutes with Hydrogen in Nickel	76
3.5	Summary	80
4	Hydrogen–vacancy–dislocation interactions in α-Fe	83
4.1	Introduction	83
4.2	Simulation Details	84
4.3	Vacancy/Hydrogen/Dislocation interaction energies in Fe	85
4.4	Reactions of dislocations with Vacancy-Hydrogen clusters	88
4.5	Discussion	92
4.6	Summary	94
5	Effect of hydrogen atoms on precipitate hardening in α-Iron	95
5.1	Theoretical framework	95
5.1.1	Bow out of the dislocation with a fixed remote concentration c_0 .	97
5.1.2	Bow out of the dislocation with fixed number of absorbed hydrogen atoms	97
5.2	Validation of the assumptions of the model	98
5.2.1	Interaction of the H atoms and dislocations with different character angles	98
5.2.2	Barriers for diffusion of H atoms along and across the dislocation	100
5.3	Input of the model	101
5.4	Simulation of the bow out of the dislocation	102
5.5	Summary	104
6	Effect of segregated hydrogen atoms on the dislocation–grain boundary interactions	107
6.1	Stress fields induced by the segregated hydrogen atoms at the grain boundaries	107
6.2	Interaction of straight dislocations and the grain boundaries	108
6.2.1	Screw dislocations	111
6.2.2	Mixed dislocations	117
6.3	Summary	123

Contents

7 Conclusion	125
Bibliography	140
Curriculum Vitae	141

List of Figures

1.1	The effect of the presence of H_2 gas on (a) fracture toughness (b) reduction of the area of the tensile specimen made of carbon steels. The data is extracted from the technical reference for hydrogen compatibility of materials [7].	1
1.2	The separation distance of dislocations in steel in the presence and absence of H_2 gas. In Fig. (a) the composite image of the pile-up of the dislocations in vacuum (black lines) superimposed by the figure of the same pile up at same stress in the presence of 95 torr of hydrogen gas in the environment. (b) Shows the separation distances for various hydrogen gas pressure. The images are taken from Ferreira et al.[23].	4
1.3	Side surfaces of the tensile specimens (a) $c_H = 0$ (b) $c_H = 1800appm$ and (c) $c_H = 24000appm$. The pictures are taken from the work of Abraham et al.[21].	4
1.4	Micrographs of the nickel specimen held in (a) vacuum and (b) $p(H_2) = 10^4Pa$. The pictures are taken from the work of Matsumoto et al.[25]. . .	5
1.5	The load-displacement curves for the nanoindentation experiments of nickel samples (a) with H (b) without H. The figures are taken from the work of Barnoush and Vehoff [26].	5
1.6	(a) The crack opening displacement of the intergranular crack observed in the H-charged polycrystalline nickel. (b) The fracture surface of the intergranular crack. The pictures are taken from the work of Lassila and Birnbaum[30].	6
1.7	(a) and (b) show the conjugate fracture surfaces of cracks in H-charged X65 steel. (c) and (d) show the conjugate fracture surfaces of cracks in H-charged X80 steel. The examples of the clusters with same features are circled for the aid of eye. The pictures are taken from the work of Neeraj et al.[31].	7
2.1	Structure and Hydrogen binding sites in various symmetric tilt boundaries and free surfaces. Atoms colored by Common Neighbor Analysis (Green: fcc Ni; Red: hcp Ni; White: Ni with less than 12 neighbors; Purple: Hydrogen sites)	21
2.2	Schematic diagram of the rigid grain boundary separation process.	24

List of Figures

2.3	Normal stress versus normal displacement during rigid-block separation across the minimum strength cleavage plane, with and without H, and for a range of grain boundary structures.	27
2.4	Atomic configurations of Ni Σ 9(221) \langle 110 \rangle . The relaxed and unrelaxed configuration of the separated grains through three different cutting planes are given. In all figures the atoms colored by Common Neighbor Analysis (Green: fcc Ni; Red: hcp Ni; White: Ni with less than 12 neighbors; Purple: H) of the connected grain boundary.	28
2.5	Atomic configurations of Ni Σ 19(331) \langle 110 \rangle . The relaxed and unrelaxed configuration of the separated grains through three different cutting planes are given. In all figures the atoms colored by Common Neighbor Analysis (Green: fcc Ni; Red: hcp Ni; White: Ni with less than 12 neighbors; Purple: H) of the connected grain boundary.	29
2.6	Atomic configurations of Ni Σ 27(115) \langle 110 \rangle . The relaxed and unrelaxed configuration of the separated grains through three different cutting planes are given. In all figures the atoms colored by Common Neighbor Analysis (Green: fcc Ni; Red: hcp Ni; White: Ni with less than 12 neighbors; Purple: H) of the connected grain boundary.	30
2.7	Atomic configurations of Ni Σ 33a(441) \langle 110 \rangle . The relaxed and unrelaxed configuration of the separated grains through three different cutting planes are given. In all figures the atoms colored by Common Neighbor Analysis (Green: fcc Ni; Red: hcp Ni; White: Ni with less than 12 neighbors; Purple: H) of the connected grain boundary.	31
2.8	Atomic configurations of Ni Σ 33b(554) \langle 110 \rangle . The relaxed and unrelaxed configuration of the separated grains through three different cutting planes are given. In all figures the atoms colored by Common Neighbor Analysis (Green: fcc Ni; Red: hcp Ni; White: Ni with less than 12 neighbors; Purple: H) of the connected grain boundary.	32
2.9	Atomic configurations of Ni Σ 41(443) \langle 110 \rangle . The relaxed and unrelaxed configuration of the separated grains through three different cutting planes are given. In all figures the atoms colored by Common Neighbor Analysis (Green: fcc Ni; Red: hcp Ni; White: Ni with less than 12 neighbors; Purple: H) of the connected grain boundary.	33
2.10	Atomic configurations of Ni Σ 99(557) \langle 110 \rangle . The relaxed and unrelaxed configuration of the separated grains through three different cutting planes are given. In all figures the atoms colored by Common Neighbor Analysis (Green: fcc Ni; Red: hcp Ni; White: Ni with less than 12 neighbors; Purple: H) of the connected grain boundary.	34

2.11	Atomic configurations of Ni Σ 5(120) \langle 100 \rangle . The relaxed and unrelaxed configuration of the separated grains through three different cutting planes are given. In all figures the atoms colored by Common Neighbor Analysis (Green: fcc Ni; Red: hcp Ni; White: Ni with less than 12 neighbors; Purple: H) of the connected grain boundary.	35
2.12	Key atomic configurations of (a) H-free and (b) H-charged Ni Σ 9(221) \langle 110 \rangle at room temperature, at the onset of the first plastic activity. (c) Configuration of the H-charged specimen subjected to tensile stress of $\sigma_{22} = 15GPa$. Atoms colored by Common Neighbor Analysis (Green: fcc Ni; Red: hcp Ni; White: Ni with less than 12 neighbors; Purple: H)	36
2.13	Key atomic configurations of (a) H-free and (b) H-charged Ni Σ 19(331) \langle 110 \rangle at room temperature, at the onset of the first plastic activity. (c) Configuration of the H-charged specimen subjected to tensile stress of $\sigma_{22} = 15GPa$. Atoms colored by Common Neighbor Analysis (Green: fcc Ni; Red: hcp Ni; White: Ni with less than 12 neighbors; Purple: H)	37
2.14	Key atomic configurations of (a) H-free and (b) H-charged Ni Σ 27(115) \langle 110 \rangle at room temperature, at the onset of the first plastic activity. (c) Configuration of the H-charged specimen subjected to tensile stress of $\sigma_{22} = 20GPa$. Atoms colored by Common Neighbor Analysis (Green: fcc Ni; Red: hcp Ni; White: Ni with less than 12 neighbors; Purple: H)	37
2.15	Key atomic configurations of (a) H-free and (b) H-charged Ni Σ 33(441) \langle 110 \rangle at room temperature, at the onset of the first plastic activity. (c) Configuration of the H-charged specimen subjected to tensile stress of $\sigma_{22} = 15GPa$. Atoms colored by Common Neighbor Analysis (Green: fcc Ni; Red: hcp Ni; White: Ni with less than 12 neighbors; Purple: H)	37
2.16	Key atomic configurations of (a) H-free and (b) H-charged Ni Σ 33b(554) \langle 110 \rangle at room temperature, at the onset of the first plastic activity. (c) Configuration of the H-charged specimen subjected to tensile stress of $\sigma_{22} = 15GPa$. Atoms colored by Common Neighbor Analysis (Green: fcc Ni; Red: hcp Ni; White: Ni with less than 12 neighbors; Purple: H)	38
2.17	Key atomic configurations of (a) H-free and (b) H-charged Ni Σ 41(443) \langle 110 \rangle at room temperature, at the onset of the first plastic activity. (c) Configuration of the H-charged specimen subjected to tensile stress of $\sigma_{22} = 15GPa$. Atoms colored by Common Neighbor Analysis (Green: fcc Ni; Red: hcp Ni; White: Ni with less than 12 neighbors; Purple: H)	38
2.18	Key atomic configurations of (a) H-free and (b) H-charged Ni Σ 99(557) \langle 110 \rangle at room temperature, at the onset of the first plastic activity. (c) Configuration of the H-charged specimen subjected to tensile stress of $\sigma_{22} = 17.5GPa$. Atoms colored by Common Neighbor Analysis (Green: fcc Ni; Red: hcp Ni; White: Ni with less than 12 neighbors; Purple: H)	38

List of Figures

2.19 (a) H-free and (b) H-charged specimenes containing $\text{Ni}\Sigma_{33\text{b}}(554)\langle 110 \rangle$ at room temperature, subjected to $\sigma_{22} = 15\text{GPa}$. (c) H-free and (d) H-charged specimens containing $\text{Ni}\Sigma_9(221)\langle 110 \rangle$ at temperature and tensile load. Atoms colored by Common Neighbor Analysis (Green: fcc Ni; Red: hcp Ni; White: Ni with less than 12 neighbors; Purple: H) 39

2.20 Schematic diagram of a crack along a symmetric tilt boundary, showing the differences in slip plane orientation at the two crack tips. 43

2.21 Sharp crack tip atomic structure at load levels where various events occur in the simulations of $\text{Ni}\Sigma_3(111)\langle 110 \rangle$ along $[11\bar{2}]$ direction. Atoms colored by Common Neighbor Analysis (Green: fcc Ni; Red: hcp Ni; White: Ni with less than 12 neighbors; Purple: H) 50

2.22 Crack tip atomic structure at load levels where various events occur in the simulations of $\text{Ni}\Sigma_3(111)\langle 110 \rangle$ along $[\bar{1}\bar{1}2]$ direction. Atoms colored by Common Neighbor Analysis (Green: fcc Ni; Red: hcp Ni; White: Ni with less than 12 neighbors; Purple: H) 50

2.23 Crack tip atomic structure at load levels where various events occur in the simulations of $\text{Ni}\Sigma_9(221)\langle 110 \rangle$ along the theoretically cleavage favorable direction. Atoms colored by Common Neighbor Analysis (Green: fcc Ni; Red: hcp Ni; White: Ni with less than 12 neighbors; Purple: H) 51

2.24 Crack tip atomic structure at load levels where various events occur in the simulations of $\text{Ni}\Sigma_9(221)\langle 110 \rangle$ along the theoretically emission favorable direction. Atoms colored by Common Neighbor Analysis (Green: fcc Ni; Red: hcp Ni; White: Ni with less than 12 neighbors; Purple: H) 51

2.25 Process of an intergranular crack propagation in $\text{Ni}\Sigma_{99}(557)\langle 110 \rangle$ along the theoretically cleavage favorable direction. Atoms colored by Common Neighbor Analysis (Green: fcc Ni; Red: hcp Ni; White: Ni with less than 12 neighbors; Purple: H) 52

2.26 Process of an intergranular crack propagation in $\text{Ni}\Sigma_{99}(557)\langle 110 \rangle$ along the theoretically emission favorable direction. Atoms colored by Common Neighbor Analysis (Green: fcc Ni; Red: hcp Ni; White: Ni with less than 12 neighbors; Purple: H) 52

2.27 Process of an intergranular crack propagation in $\text{Ni}\Sigma_5(120)\langle 100 \rangle$ along $[2\bar{1}0]$ direction. Atoms colored by Common Neighbor Analysis (Green: fcc Ni; Red: hcp Ni; White: Ni with less than 12 neighbors; Purple: H) . . . 53

2.28 Process of an intergranular crack propagation in $\text{Ni}\Sigma_5(100)\langle 100 \rangle$ along $[\bar{2}10]$ direction. Atoms colored by Common Neighbor Analysis (Green: fcc Ni; Red: hcp Ni; White: Ni with less than 12 neighbors; Purple: H) . . . 53

3.1	Schematic diagram of roughening of an originally straight edge dislocation lying on the z axis surrounded by the multiple solutes of different types. The red and blue circles refer to types -1 and -2 solute atoms, respectively. The length of the straight segment is ζ_c and the amplitude of roughening is w_c	60
3.2	Distribution of the total energy versus the roughening amplitude for $c_0 = 3000\text{appm}$ and $c_0 = 4000\text{appm}$ in nickel. The line tension of the edge dislocation is assumed to be $0.48\text{eV}/\text{\AA}$	61
3.3	Variation of the increase in yield strength of nickel due to the presence of bulk H interstitials versus temperature for $c_0 = 0.004$	66
3.4	An edge dislocation originally lying on the x_3 axis surrounded by the multiple solutes of different types. The red and blue circles refer to two types of solute atoms. The principal misfit strain coordinate system of the solutes are $\{x_i^{(m)}\}$. The dislocation glides a distance w along the x_1 axis.	68
3.5	Schematic diagram of the simulation cell containing the straight dislocation and vacancies subjected to the applied shear traction. The color coding for the atomistic picture uses common neighbor analysis (green: fcc; red: hcp indicating the stacking fault; white: atoms having fewer than 12 neighbors and thus surrounding a vacancy "solute".	71
3.6	Normalized volumetric and deviatoric parts of the interaction energy as a function of polar angle around a Volterra edge dislocation, for different orientations of the VH solute complexes studied here.	73
3.7	Applied shear stress τ^{app} versus dislocation glide distance d , for several concentrations of solutes V (solid lines) and VH (dashed lines) solutes in fcc Nickel. Same-color solid and dashed lines show results for the same spatial distribution of solutes.	74
3.8	Shear yield stress τ_{y0} as a function of the solute concentration.	75
3.9	Supercells containing (a) a substitutional S solute and (b) an interstitial C solute at the octahedral site. Gray, dark blue, and orange spheres denote the Ni, C, and S atoms, respectively.	77
3.10	Supercell pressure versus concentration for different solute complexes. Solid and dashed lines denote the cases without and with H atoms, respectively.	78
3.11	Stable position of hydrogen interstitial in the vicinity of (a) a substitutional Sulfur atom and (b) an interstitial Carbon atom. Gray, dark blue, and orange spheres denote the Ni, C, and S atoms, respectively.	80
4.1	Schematic of the simulation cell used to study edge dislocation/vacancy/hydrogen interactions. Color coding uses due to Common Neighbor Analysis with green indicating a bcc environment and purple indicating non-bcc environments.	85

List of Figures

4.2	The atomistic structure of an edge dislocation core in Fe as computed by molecular statics simulations using (a) the Fe-H EAM potential and (b) the QM/MM method. Blue symbols denote atoms in a local bcc environment and red symbols indicate all other atom environments. With a vacancy located on the first plane on the compressive side of the glide plane, and in the middle of the core, the computed structures are computed with (c) the QM/MM method and (d) the Fe-H EAM potential [134].	87
4.3	Interaction of an edge dislocation with (a) V_2 (b) V_2H_2 (c) V_2H_{10} clusters.	90
4.4	Interaction of an edge dislocation with a V_{49} cluster. (a) Prior to dislocation intersection; (b) during dislocation bow out under increasing stress; (c) after the dislocation is unpinned, showing the formation of a double jog. .	92
5.1	Schematic diagram of an initially straight edge dislocation (dashed line) which is bowed out under application of shear. The light blue and purple spheres denote the Fe and H atoms, respectively. The initial length of the dislocation segment between two obstacles is L	96
5.2	Binding sites of the H atoms to different dislocations in α -Iron. The blue, white and yellow spheres denote the bcc Fe, dislocated Fe and H atoms, respectively.	99
5.3	(a) Normalized maximum bow out of the hydrogen charged dislocation subjected to different shear stresses. Dashed lines are the results of unconstrained theory and the solid lines are the results of constrained theory. (b) The relative decrease in the number of attached hydrogen atoms during bow out for various initial number of H atoms.	103
5.4	Configuration of the bowed dislocation in the H-free specimen under different applied shear.	104
5.5	Configuration of the bowed dislocation in the specimen charged with $N_H = 300$ under different applied shear strengths.	105
6.1	Distribution of the resolved shear stress along the GBs of interest in both H-free and H-charged cases for two different slip planes. The hydrogen atoms are not shown for the sake of better illustration. c_0 is the remote concentration of the H atoms in the bulk of the material. $\tau(S_i)$ denotes the resolved shear along slip plane S_i	109
6.2	The schematic diagram of the interaction of typical regions along the grain boundaries and the edge dislocations were driven to the GB by the external (a) shear and (b) tensile loading. The average net Burgers vector is shown in both H-free and H-charged cases. The blue and red regions illustrate the repulsive and attractive regions, respectively. WOH and WH stands for the H-free and H-charged cases, respectively. \mathbf{b}_{net} is the average Burgers vector in the grain boundary.	110

-
- 6.3 Key atomistic configurations of the interaction of a screw dislocation with a $\Sigma 19(331)\langle 110 \rangle$ grain boundary. The purple spheres are the H atoms and the other spheres are the non-fcc nickel atoms which are colored due to their energy. (a)–(c), (d)–(f), (g)–(i), and (j)–(l) configurations denote the initial, intermediate and final configuration of first dislocation in H-free, second dislocation in H-free, first dislocation in H-charged, and the second dislocation in H-charged samples, respectively. 112
- 6.4 Key atomistic configurations of the interaction of a screw dislocation with a $\Sigma 33a(441)\langle 110 \rangle$ grain boundary. The purple spheres are the H atoms and the other spheres are the non-fcc nickel atoms which are colored due to their energy. (a)–(c), (d)–(f), (g)–(i), and (j)–(l) configurations denote the initial, intermediate and final configuration of first dislocation in H-free, second dislocation in H-free, first dislocation in H-charged, and the second dislocation in H-charged samples, respectively. 113
- 6.5 Key atomistic configurations of the interaction of a screw dislocation with a $\Sigma 33b(554)\langle 110 \rangle$ grain boundary. The purple spheres are the H atoms and the other spheres are the non-fcc nickel atoms which are colored due to their energy. (a)–(c), (d)–(f), (g)–(i), and (j)–(l) configurations denote the initial, intermediate and final configuration of first dislocation in H-free, second dislocation in H-free, first dislocation in H-charged, and the second dislocation in H-charged samples, respectively. 114
- 6.6 Key atomistic configurations of the interaction of a screw dislocation with a $\Sigma 41(443)\langle 110 \rangle$ grain boundary. The purple spheres are the H atoms and the other spheres are the non-fcc nickel atoms which are colored due to their energy. (a)–(c), (d)–(f), (g)–(i), and (j)–(l) configurations denote the initial, intermediate and final configuration of first dislocation in H-free, second dislocation in H-free, first dislocation in H-charged, and the second dislocation in H-charged samples, respectively. 115
- 6.7 Key atomistic configurations of the interaction of a mixed dislocation with a $\Sigma 19(331)\langle 110 \rangle$ grain boundary. The purple spheres are the H atoms and the other spheres are the non-fcc nickel atoms which are colored due to their energy. (a)–(c), (d)–(f), (g)–(i), and (j)–(l) configurations denote the initial, intermediate and final configuration of first dislocation in H-free, second dislocation in H-free, first dislocation in H-charged, and the second dislocation in H-charged samples, respectively. 118
- 6.8 Key atomistic configurations of the interaction of a mixed dislocation with a $\Sigma 33a(441)\langle 110 \rangle$ grain boundary. The purple spheres are the H atoms and the other spheres are the non-fcc nickel atoms which are colored due to their energy. (a)–(c), (d)–(f), (g)–(i), and (j)–(l) configurations denote the initial, intermediate and final configuration of first dislocation in H-free, second dislocation in H-free, first dislocation in H-charged, and the second dislocation in H-charged samples, respectively. 119

List of Figures

- 6.9 Key atomistic configurations of the interaction of a mixed dislocation with a $\Sigma 33b(554)\langle 110 \rangle$ grain boundary. The purple spheres are the H atoms and the other spheres are the non-fcc nickel atoms which are colored due to their energy. (a)–(c), (d)–(f), (g)–(i), and (j)–(l) configurations denote the initial, intermediate and final configuration of first dislocation in H-free, second dislocation in H-free, first dislocation in H-charged, and the second dislocation in H-charged samples, respectively. 120
- 6.10 Key atomistic configurations of the interaction of a mixed dislocation with a $\Sigma 41(443)\langle 110 \rangle$ grain boundary. The purple spheres are the H atoms and the other spheres are the non-fcc nickel atoms which are colored due to their energy. (a)–(c), (d)–(f), (g)–(i), and (j)–(l) configurations denote the initial, intermediate and final configuration of first dislocation in H-free, second dislocation in H-free, first dislocation in H-charged, and the second dislocation in H-charged samples, respectively. 121

List of Tables

2.1	Interaction energies for Hydrogen atoms in Ni(120) Σ 5 \langle 100 \rangle at various sites indicated in Fig. 2.1a. Results are shown for computations using DFT Alvaro et al. [59], Di Stefano et al. [60], using the original Ni–H EAM potential [48], and using the modified Ni–H EAM potential developed in this thesis.	19
2.2	Original and modified parameters for the Ni–H EAM potential based on the formulation of [90,91]. Also shown are relevant properties of bulk Ni, as predicted by the potential.	20
2.3	Interaction energies for Hydrogen atoms at various sites in different grain boundaries and surfaces as predicted by the modified EAM potential. . .	22
2.4	Interaction energies for hydrogen atoms at various sites in different grain boundaries as predicted by the modified EAM potential.	22
2.5	Theoretical cohesive strengths and yield strengths of the grain boundaries of interest. The percentages are calculated with reference to the hydrogen free cases. P_i are the cleavage planes.	26
2.6	Theoretical cohesive strength of single crystal Ni separated across different crystallographic planes corresponding to planes parallel to the various grain boundaries studied here, in pure Ni and Ni-H (100% occupation of octahedral sites in Ni).	26
2.7	Unrelaxed and fully relaxed fracture energies (mJ/m^2) for the separation of GBs along different possible fracture planes. The minimum separation energy for each GB is highlighted in bold.	36
2.8	Unrelaxed and fully relaxed fracture energies (mJ/m^2) for the separation of GBs along different possible fracture planes. The minimum separation energy for each GB is highlighted.	46
2.9	Geometrical parameters describing slip orientations in grains adjacent to each grain boundary.	46
2.10	Theoretical cleavage and emission stress intensities for all grain boundaries studied here. The predicted behavior (cleavage or emission) is indicated, as dictated by the lower of the two predicted stress intensities as highlighted in bold. The simulation results are tabulated as well.	47

List of Tables

3.1	Increase in the the tensile yield strength of polycrystalline nickel due to the presence of hydrogen at 300K and 77K. The H concentration in bulk is $c_0 = 0.004$	66
3.2	Parameters describing the misfit strain tensor of each type of solutes. . .	72
3.3	Misfit strain tensor parameters for S and C atoms, and SH and CH complexes, in Ni.	79
4.1	Hydrogen-Vacancy-Dislocation interaction energies and barriers as calculated via DFT, QM/MM, and EAM interatomic potentials. E_V^f , E_{VH}^b , E_{VV}^b , E_{d-V}^{int} , E_{d-H}^b , E_{V-d}^m , E_{V-H}^b , E_{d-VH}^m , are the formation energy of a single vacancy, vacancy–H binding energy, vacancy–vacancy binding energy, dislocation–vacancy interaction energy, dislocation–H binding energy, migration barrier of a vacancy in the dislocation core, binding energy of a VH cluster in the dislocation core, and migration barrier of VH in the core of the dislocation, respectively.	86
4.2	Reactions of an edge dislocation with various planar vacancy clusters, with and without hydrogen atoms. JD and D denote jogged and unjogged dislocations, respectively.	91
5.1	The dimensions and orientation of the simulation boxes containing dislocations with different character angles in α -Iron.	99
5.2	Binding energies (eV) of H atoms to different energy favorable sites in different dislocations in α -Iron.	100
5.3	Maximum migration barriers (eV) of H atoms for diffusion between different energy favorable sites in different dislocations in α -Iron.	101
6.1	Reactions of the screw dislocations and grain boundaries of interest in different nickel bicrystals. The critical resolved shear stresses $\tau_c(MPa)$, at which the reactions happened are given. The following abbreviations are used. A: Dislocation Absorbed, D: Dislocation dissociated, T: Slip transmitted, P: partial dislocation emitted from the GB , J: the dislocation formed a junction with the stacking faults in GB.	111
6.2	Reactions of the screw dislocations and grain boundaries of interest in different nickel bicrystals. The critical resolved shear stresses $\tau_c(MPa)$, at which the reactions happened are given. The following abbreviations are used. A: Dislocation Absorbed, D: Dislocation dissociated, T: Slip transmitted, P: partial dislocation emitted from the GB , J: the dislocation formed a junction with the stacking faults in GB.	122

1 Motivation and background

1.1 Introduction

The detrimental effects of hydrogen atoms on the mechanical properties of metals have been known for over a century [1]. One of the most important effects of hydrogen in Iron and Nickel based alloys is embrittlement [2, 3, 4, 5, 6], i.e. premature fracture or reduced ductility. High strength steels, nickel, aluminum, and copper alloys are among the metals that are susceptible to hydrogen embrittlement (HE) which reduces their applicability in industry. Fig. 1.1 shows the decrease in both fracture toughness and reduction of the area of the tensile specimen made of carbon steels in the presence of H_2 environment [7].

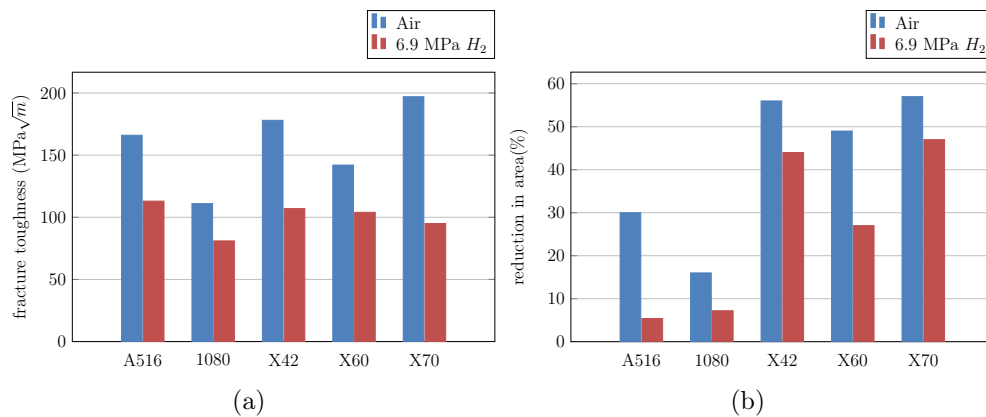


Figure 1.1 – The effect of the presence of H_2 gas on (a) fracture toughness (b) reduction of the area of the tensile specimen made of carbon steels. The data is extracted from the technical reference for hydrogen compatibility of materials [7].

Hydrogen can enter metals from various sources such as, aqueous solutions, the hydrocarbons that are flowing through the pipelines, humidity, and other aggressive environments. This ingress leads to catastrophic degradation of the mechanical properties of metals.

Hydrogen atoms can occupy interstitial sites in bulk of the metals, on the other hand, there are traps in the metals that can absorb H atoms. These traps that can play role in HE are, the core of the dislocation, free surfaces, grain boundaries, precipitate/matrix interfaces, vacancies and vacancy clusters, microcracks, and nanovoids. Hydrogen can also diffuse in metals, this diffusion between traps of different strengths induces rate and temperature effects on the response of the H charged metals. Given these multifarious H sources and traps in metals, and the kinetic effect of H diffusion a comprehensive description of the HE process that could be valid for all metals is hard to achieve.

1.2 Background of the hydrogen embrittlement studies

1.2.1 Experimental studies

Since hydrogen embrittlement is an important source of the metal degradations, a huge number of experimental studies are devoted to investigating this phenomenon in different metals. These extensive experimental studies have indirectly revealed phenomena associated with, or affected by, the presence of hydrogen, at macroscopic, mesoscopic, or atomistic scales. However, the big picture of the hydrogen embrittlement process is yet to understand via these studies. Here we introduce and discuss some very important experimental studies in the field. These experiments provide a basis for the theories of hydrogen embrittlement.

Macro-scale experiments

One natural way for examining the effect of hydrogen embrittlement is to do mechanical testing on metals in the presence and absence of hydrogen and measure the changes induced by hydrogen [8, 9, 10, 11, 12, 13, 14, 15, 16, 2, 6, 17, 18]. For example, Gangloff and his coworkers [16, 2, 6, 17, 18] studied the process of the crack growth in different steels in the presence of both internal and environmental hydrogen. The crack growth has three stages: In stage I, after reaching a threshold stress intensity factor (K_{TH}) less than the fracture toughness of the metal the crack growth velocity sharply increases. The stage II at which the crack growth rate become independent of stress intensity factor. And finally stage III at which the crack growth rate increases by increasing stress intensity factor to values near the fracture toughness. The studies show that the presence of hydrogen promotes the stage I cracking and reduces the fracture toughness in metals. They also stated that the fundamental understanding of the H induced cracking needs nano-scale investigations [16].

The ultimate tensile strength of the specimens can also be determined in the presence and absence of hydrogen [7] and the ultimate strength is decreased by introduction of the hydrogen atoms [7, 19]. Again, the explanation of the exact process of observed HE

1.2. Background of the hydrogen embrittlement studies

needs more detailed investigation.

The effect of hydrogen solutes on strengthening/softening the global behavior of metals is also important and is investigated by several researchers [8, 10, 12, 13, 15]. In these experiments both softening and hardening effects induced by hydrogen atoms are observed. There are recent experiments showing that the presence of H atoms with concentration of $c_H \sim 3000 \text{ appm}$ can strengthen metals [20, 19]. The study by Lawrence et al. shows that the stress-strain curves corresponding to polycrystalline nickel with different grain sizes demonstrate strengthening in the presence of H atoms in low and room temperature [20]. The experiment by Harris et al. [19] shows similar trend. These experiments use thermal desorption spectroscopy (TDS) and positron annihilation spectroscopy (PAS) to determine the content of hydrogen and free volume evolution in polycrystalline nickel. On the other hand, some experiments in steels show softening [8, 10, 12] or no change [21] in the strain-stress curves by the introduction of hydrogen atoms.

Micro/nano-scale experimental observations

Micro/nano-scale studies are performed to investigate the interaction between hydrogen and the microstructure of metals such as dislocation, grain boundaries, voids, and precipitates. These investigations are crucial for the fundamental understanding of the hydrogen embrittlement process. Here we discuss some the most important experimental observations in the field.

The effect of hydrogen atoms on the behavior of dislocations that are main surrogates of plastic flow is an important feature to investigate. To this end, researchers did a number of transmission electron microscopy (TEM) observations. For example, the observations were done by Birnbaum, Robertson, and Sofronis and their coworkers showing that the separation distance between dislocations in pile-ups in steels and aluminum is significantly different in the presence and the absence of hydrogen [22, 23]. Fig. 1.2 shows the separation distance between dislocations in S310 steels in the presence and absence of hydrogen atoms. It can be seen that the distance between the dislocation is decreased by increasing the pressure of H_2 gas. These experiments imply that the presence of hydrogen can give rise to more compact pile-ups and weaken the dislocation–dislocation interaction and thus localize the plastic deformation. There are also experimental studies performed on hydrogen charged S310 stainless steels that reveal pre-yield microstrains while the H-free samples did not show this behavior. Scanning electron microscopy (SEM) experiments of the specimens show extensive *plastic-like* strain localization and slip bands at the vicinity of the crack tips in the presence of H atoms. Performing TEM experiment on same samples showed microtwinning and austenite faulting in hydrogen charged specimens tested at room temperature [21, 24]. For example, Fig. 1.3 shows the side surfaces of S310 specimen under tensile loading at room temperature and different amount of H charging. It can that by increasing the amount of H in the metal the slip

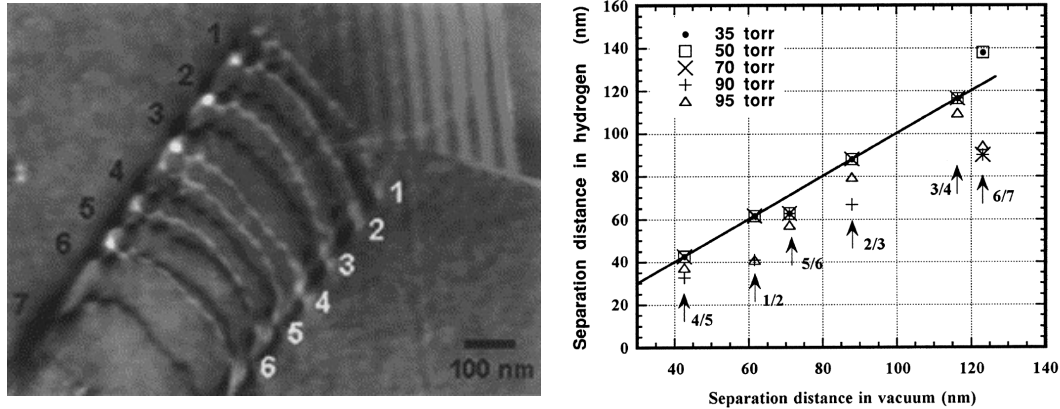


Figure 1.2 – The separation distance of dislocations in steel in the presence and absence of H_2 gas. In Fig. (a) the composite image of the pile-up of the dislocations in vacuum (black lines) superimposed by the figure of the same pile up at same stress in the presence of 95 torr of hydrogen gas in the environment. (b) Shows the separation distances for various hydrogen gas pressure. The images are taken from Ferreira et al.[23].

bands get coarser and slip is localized. This is another example of the localized plasticity in the presence of hydrogen atoms. However, this experiment shows no significant change in the stress-strain curve in the presence of 1800 appm hydrogen. This observation implies that even if localized softening is happening in the crack-tip regions, it does not have any macroscopic trace.

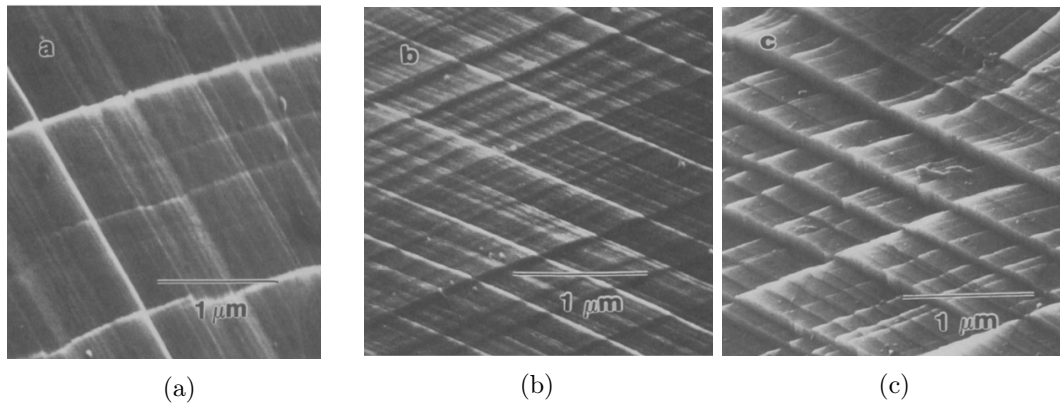


Figure 1.3 – Side surfaces of the tensile specimens (a) $c_H = 0$ (b) $c_H = 1800\text{appm}$ and (c) $c_H = 24000\text{appm}$. The pictures are taken from the work of Abraham et al.[21].

Moreover, the SEM micrographs of the fracture surfaces in the hydrogen-charged specimens usually show an extensive amount of plastic deformation beneath the fracture surfaces. For example Fig. 1.4 shows this activities in nickel [25].

The aforementioned observations motivate the hydrogen enhanced localized plasticity

1.2. Background of the hydrogen embrittlement studies

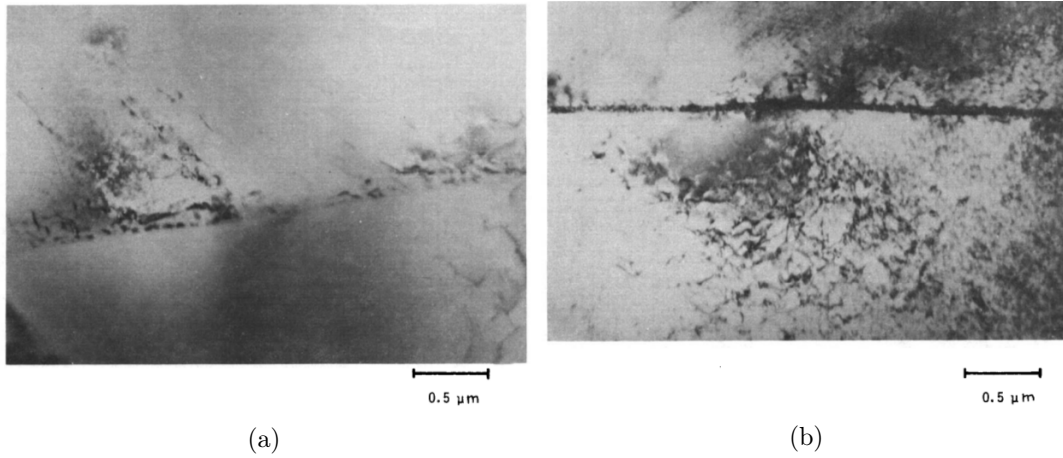


Figure 1.4 – Micrographs of the nickel specimen held in (a) vacuum and (b) $p(H_2) = 10^4 Pa$. The pictures are taken from the work of Matsumoto et al.[25].

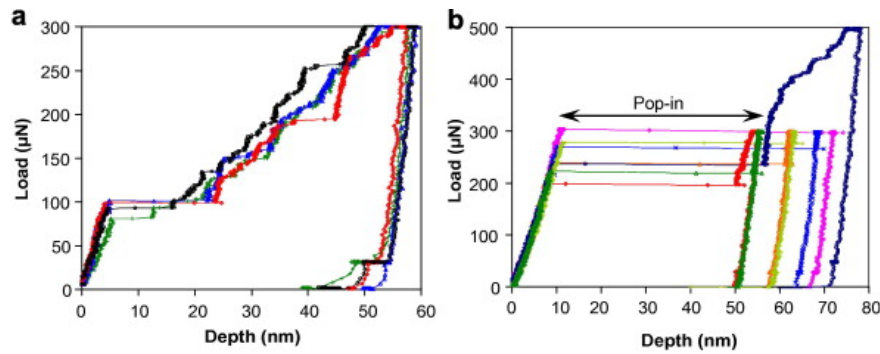


Figure 1.5 – The load-displacement curves for the nanoindentation experiments of nickel samples (a) with H (b) without H. The figures are taken from the work of Barnoush and Vehoff [26].

theory which will be discussed in the following section.

Another question is the effect of H atoms in facilitating/inhibiting the nucleation of dislocations or other defects. To investigate this issue, a series of nanoindentation experiments on nickel and different ferritic alloys were performed by Barnoush and his coworkers [26, 27]. These experiments show that the pop-in load denoting the load at which a sudden and significant increase in displacement of the tip of the indenter occurs is reduced by the introduction of cathodically charged hydrogen [26, 27]. Fig. 1.5 shows the load–depth curves of nickel samples under both cathodic and anodic potentials. The conclusion was that the presence of H atoms in the metal can facilitate the nucleation and formation of the dislocation loops which are surrogates for the plastic deformation.

One of the most typical ways of thinking about the hydrogen embrittlement process is thinking about the competition between ductile transgranular and brittle intergranular

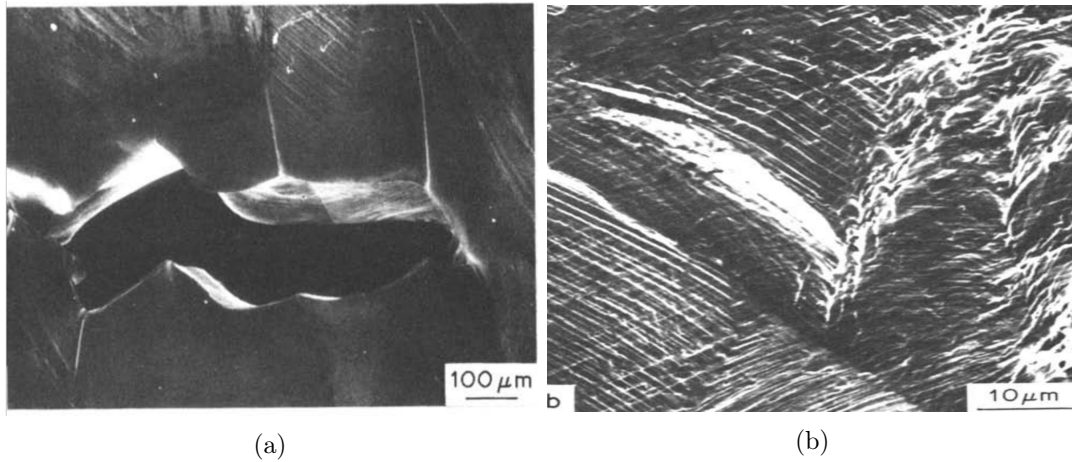


Figure 1.6 – (a) The crack opening displacement of the intergranular crack observed in the H-charged polycrystalline nickel. (b) The fracture surface of the intergranular crack. The pictures are taken from the work of Lassila and Birnbaum[30].

fracture in polycrystalline metals. Experiments show that the presence of hydrogen causes a change in failure mode from ductile fracture to brittle intergranular fracture in polycrystalline nickel [4, 28, 29]. Particularly the co-segregation of H atoms and other solutes like Sulfur to the grain boundaries in nickel can change the transgranular fracture to an intergranular one [30]. Fig. 1.6 shows a typical picture of the intergranular fracture in nickel in the presence of H environment. However, the exact mechanism(s) which is responsible for this ductile-to-brittle transition is not understood yet. Again here we can see the slip traces at the intergranular fracture surfaces. This observation means that even in the quasi-brittle intergranular fracture, the presence of H atoms is associated with locally intense plastic activities.

More recently, experiments in Fe-based steels have revealed the presence of nanoscale voids on the grain boundary cleavage planes in the presence of hydrogen [31]. Fig. 1.7 shows the conjugate fracture surfaces of the crack have same nano dimple features. This means that nano-voids are formed ahead of the crack tip and once the crack opens, it passes through the void and forms dimples on the fracture surfaces. This observation means that the nanovoids form ahead of the crack tip in the presence of hydrogen. However, the mechanism that is responsible for this phenomenon is not fully discovered.

In summary, different experimental studies are carried on for enhancing the knowledge about hydrogen embrittlement process. However, a comprehensive picture of the HE process is still missing. Thus, theoretical approaches exist in the field to capture different aspects of HE process.

1.2. Background of the hydrogen embrittlement studies

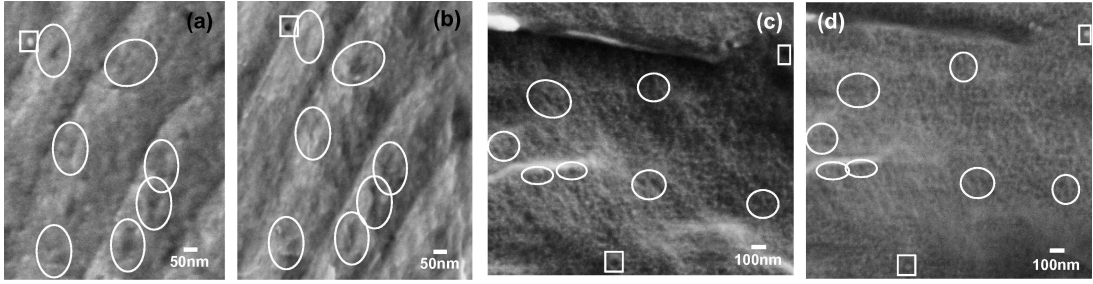


Figure 1.7 – (a) and (b) show the conjugate fracture surfaces of cracks in H-charged X65 steel. (c) and (d) show the conjugate fracture surfaces of cracks in H-charged X80 steel. The examples of the clusters with same features are circled for the aid of eye. The pictures are taken from the work of Neeraj et al.[31].

1.2.2 Theoretical approaches

Although intense scientific effort has been devoted to understanding different aspects of hydrogen embrittlement (HE), there is still no consensus on the mechanisms causing the behavior, nor any general theory that can describe the many effects of H on metal flow and fracture. We know that hydrogen can interact with (i) dislocations to change the overall plastic flow behavior, (ii) crack tips to change the local deformation (enhancing or suppressing cleavage relative to dislocation emission), (iii) grain boundaries to enhance intergranular failure, (iv) interfaces to enhance interfacial decohesion, and/or (v) other defects such as precipitates, vacancies, and solutes. Any combination of these phenomena may occur in a given material, but how these process(es) actually lead to embrittlement (premature failure relative to a hydrogen-free material) is unclear. The experimental studies not only provide some insight into the problem of the hydrogen embrittlement but also give motivations and evidence for new theories explaining them.

Hereby, we discuss a few theories that can partially capture some features of HE.

Hydrogen enhanced decohesion

Hydrogen enhanced decohesion (HEDE) postulates that H atoms reduce the surface energy and strength of cleavage surfaces, reducing the applied stress intensity required for cleavage fracture [32, 33, 34, 35, 36, 37]. This reduction in the surface energy makes the cleavage of the crack surfaces easier. This theory can roughly explain the macroscopic observations of ductile-to-brittle transition. The HEDE theory mainly stems from the macroscopic experiments in which the growth of the cracks in the metals enhances by the presence of the hydrogen environment.

However, there are some issues that need to be addressed in this theory. HEDE is a pure continuum theory that does not consider the atomistic features of HE as well as the kinetic properties of H diffusion in metals. We know that significant decrease

Chapter 1. Motivation and background

in the fracture energy of the interfaces needs high concentrations of hydrogen. These concentrations are orders of magnitude higher than the bulk concentration of hydrogen in metals. Thus, diffusion processes are crucial for achieving these concentration levels at the crack tip regions. Moreover, the ductile/brittle behavior of the cracks in the material strongly depends on the metal atomistic features, such as the surface energy, stacking fault energy, slip plane direction, the dislocation density and etc. All of these properties are also a function of the hydrogen-metal interactions and these interactions are absent in this theory. Atomistic simulations also show that this theory cannot fully predict the ductile/brittle behavior of the cracks in materials [38]. Thus, HEDE is not a predictive theory in the sense that with a known number of parameters can determine the failure mode of the metal.

Hydrogen enhanced localized plasticity

An entirely different concept is Hydrogen-Enhanced Localized Plasticity (HELP) [39, 40, 41], for which several mechanisms have been postulated based on experiments in Ni and Al which we introduced in the previous section. The HELP theory is mainly motivated by the nanoscale experimental pieces of evidence that show the traces of the local and intense plastic activity near crack tips in the presence of H atoms. The general idea in HELP is that dislocation motion or nucleation is facilitated by H, leading to either more dislocations, more localized pile-ups, or more extensive plastic straining around a crack tip. The connection to embrittlement is not direct, but some macroscopic experiments show that H can lead to plastic softening and to higher dislocation activity near crack tips or fracture surfaces in some metals and alloys. However, there exist other experiments that show the opposite macroscopic behavior. For example adding hydrogen to steels induced little change in the stress-strain curves [21]. In other experiments in nickel, the strengthening effect of hydrogen solute is observed at room temperature and 77K [20]. Moreover, in the experiment done by Teter et al. [42] the embrittlement of β -titanium was not associated with the extensive plastic activities in the crack tip region.

It is also noteworthy that the evidence supporting this theory is limited to TEM observations in which the specimen geometry and size of them have certain limitations. For example, thin foils that are used for these experiments induces the plane stress state which is not representative of the bulk behavior. Moreover, the connection of the localized plasticity to the embrittlement process is not clear yet. Thus, this theory cannot provide a full explanation for all features of hydrogen charged metals and it is not predictive.

Defactant theory

One of the other theories that exist in the field is the defactant theory. In this theory which was proposed by Kirchheim [43], H atoms are considered as solutes namely "defactant"s which reduce the defect formation energies. Thus, their presence in metals makes the

1.2. Background of the hydrogen embrittlement studies

nucleation of defects easier. For example, Kirchheim claimed that the presence of H can reduce the dislocation line tension [44]. Thus, it can be envisioned that if the H concentration in metal becomes more than a certain critical value, the dislocation nucleation becomes spontaneous and subsequently material fails. In this sense, this theory can be considered as a HELP-like theory. The defectants can also reduce the surface/interface energy in metals in a way that cleavage becomes spontaneous [45]. In this sense, this theory can be considered as a HEDE like theory. However, the H_2 gas pressure at which this phenomenon happens is calculated to be in the order of 1GPa which is far larger than the experimental values at which embrittlement is observed. This theory can provide an explanation for the observed lowering effect of H atoms on the pop-in load during nanoindentation experiments [46] in which the nucleation of the dislocation loops become easier due to the presence of H.

It should be noted that equilibrium thermodynamics which is the main pillar of this theory can hardly be achieved in the real situations. For example saturating all the surfaces, dislocations and grain boundaries with the equilibrium concentration of hydrogen atoms needs diffusion and happens at time scales larger than the time scales at which hydrogen embrittlement is observed. Also, the concentration of hydrogen atoms needed for achieving that coverage is far larger than the concentrations at which HE is observed. Thus, this theory that basically predicts failure of metals in the presence of enough hydrogen after a very long time cannot explain the experimental observations.

Hydrogen enhanced nano-void nucleation and growth

The experimental observations of [31] in which the evidence of formation of nano-voids ahead of the crack tip is revealed motivates proposition of the hydrogen enhanced nano-void nucleation and growth theory. This theory says that the presence of the H atoms can stabilize the vacancies formed during plastic activity. Then these vacancies can form nano-voids and these nano voids can growth. To support this idea, atomistic simulations based on Fe–H embedded atom method (EAM) potential were used to show that a single vacancy in bcc Fe can be transported by a single dislocation and then released when the vacancy encounters a hydrogen atom. A second vacancy swept into the same location was shown to lead to the formation of a two-vacancy/one-hydrogen cluster. From these two studies, and the knowledge that vacancy-hydrogen interactions in Fe (and many other metals) are attractive, such that the general reaction $nV + mH \rightarrow V_nH_m$ is energetically favorable, it was speculated that the observed nanovoid growth in steels is due to sequential vacancy sweeping by dislocations, trapping by hydrogen, and subsequent diffusion and coalescence of vacancies and voids [47]. However, more broad simulations show that hydrogen atoms cannot significantly stabilize the vacancies from annihilation by the jog formation processes in the metal. The details of these simulations are given in Chapter 4.

Nano-hydride formation theory

One recent theory is that the transport and aggregation of H atoms to a crack tip inhibits dislocation emission, which prevents crack blunting, leaving cleavage as the only mechanism of reducing energy around the crack. Such a local “*ductile-to-brittle*” transition is driven by the prevention of ductile blunting processes rather than the decrease in cohesion energies [48, 49]. This theory incorporates the kinetics of hydrogen diffusion in the metal to explain the temperature and rate dependency of the ductile/brittle behavior of cracks in nickel and iron. This theory has found quantitative success in prediction of the ductile/brittle behavior of different steels such as X42, X52, A516 Gr70, AERMET 100, and 10XX at room temperature in which the hydrogen atoms are mobile [49]. Although this theory cannot explain all observed features of embrittlement, it is a predictive theory. By having loading rate, diffusion coefficient, and the bulk concentration of H atoms as an input, this theory can determine the failure mode of the metal at room temperature. However, the reason for the observed embrittlement at low temperatures needs to be investigated.

1.2.3 Simulations

In tandem with experiments, numerical simulations are a valuable tool for probing specific mechanisms that occur at the atomic scale, which encompasses most of the above phenomena. Both continuum and atomistic scale simulations can shed light on the behavior of the hydrogen in metals. The emphasis of this thesis is on the atomistic simulations which can address the interaction of hydrogen atoms with defects at the atomistic level.

Continuum scale simulations

The effect of hydrogen atoms on the macroscopic behavior of the metals can be investigated by continuum scale simulations. In these simulations, following the work of Sofronis and McMeeking [50] the coupled problem of the diffusion of H interstitials to the crack tip region in linear elastoplastic materials is investigated [51, 52, 53, 54, 55]. Different features are added to these models, for example, the transport of the hydrogen atoms by means of the dislocations to the crack tip region is modeled in [56].

In fact, the outcome of all these continuum scale simulations is a concentration map of H atoms at the crack tip region with a resolution of $\sim 1\mu m$. Thus, in order to link the results of these simulations to the real HE cases observed in experiments one should know the mechanism of HE in that particular metal and the critical H concentration at which that process happens. Both of these pieces of information need further theoretical and experimental efforts and cannot be found by continuum scale simulations. One strategy is to compare the results of the simulations and the macroscopic experiments to find a

1.2. Background of the hydrogen embrittlement studies

correlation between the hydrogen concentration calculated in the simulations with the damaged zones in the experiment. In any case these simulations cannot determine the exact mechanism of HE.

Atomistic simulations

Atomistic simulations are valuable tools for studying the hydrogen embrittlement process, validating the proposed mechanisms and theories. Ab initio simulations such as density functional theory (DFT) simulations can be used for finding the effect of the presence of H atoms on the key parameters controlling the HE process such as surface energy, grain boundary energy, stacking faults energies, and theoretical strength.

For example, the segregation of H atoms to $\Sigma 5$ symmetric tilt and twin grain boundaries in nickel was investigated recently using density functional theory (DFT) calculations [59, 60, 61, 62]. Alvaro et al. [59] calculated the change in the ideal fracture energy in the presence of hydrogen atoms at the same boundaries in nickel for an assumed fracture plane. They observed that the presence of H atoms significantly reduces the ideal fracture energy of $\Sigma 5$ GB. Recently, Zhou et al. [63, 64] showed the correlation between the volume distortion of structural units of the grain boundaries in various materials including nickel and the binding energies via DFT calculations.

However, due to the huge computational costs of DFT calculations, simulation of the plastic behavior of the metals which needs the simulation of dislocations which are long-range defects is impossible in this scheme. Although, newly developed quantum mechanics/molecular mechanics (QM/MM) [65, 66, 67] simulations can help in finding the dislocation–H interaction energies but the simulation of more complicated phenomena like glide of dislocations is still impossible.

To overcome this issue, atomistic simulations based on empirical interatomic potentials can be used. The literature of these types of simulations is rich. For example, see [68, 69, 70, 71, 72, 73, 74, 75, 76, 77, 78, 79, 80, 81] in which the molecular dynamics (MD) and Monte Carlo (MC) simulations are used to capture the different aspects of the HE.

However, it should be noted that the results of the atomistic simulations are strongly dependent on the interatomic potentials and the simulation conditions. One should make sure that the interatomic potential is validated to give physical predictions of the parameters which are crucial in the simulations. Moreover, the loading rates, the size of the simulation sample and time scales of the simulations and all other properties of the simulations must be as relevant as possible to the real situations.

For example, in one of the most recent simulations done by Xiong et al. [76], the effect of hydrogen atoms on the interfacial damage in Ni-based single crystal superalloys is investigated by conventional MD method. They found that hydrogen atoms enhanced

damage in the interphase by stabilizing the vacancies. However, the hydrogen diffusion in nickel cannot be captured in the MD time-scales and there is no experimental evidence for nano-void formation in hydrogen charged nickel alloys. Thus, the connection of the results of this simulation to the physical situation needs more clarifications.

As another instance one can refer to work of Matsumoto et al. [81] in which a psuedo-hydrogen effect is included in the embedded atom method (EAM) potential. To this end, they modified the potential and produce the defect formation energies which are in thermodynamic equilibrium. With this potential they performed fracture and nanoin-indentation simulations. However, given the absence of the kinetics of hydrogen diffusion and misfit volume of the hydrogen interstitials, the H–H interactions in these simulations, the connection of the results with physics is not clear. In general, the interpretation of atomistic simulation results needs particular attention.

Our general approach in this thesis is to modify the interatomic potentials to close the gap between their particular predictions about the key parameters relevant to the mechanism of interest to those of more reliable calculations such as DFT. Then we will use the modified potentials in the simulations.

The results of atomistic simulations can (i) validate/invalidate the proposed theories in the literature (ii) provide input data for the continuum scale simulations that can directly be compared with the experiments (iii) propose new mechanisms responsible for hydrogen embrittlement.

Key role of atomistic simulations in validating the theories

There are many studies in the literature where the operation of a specific mechanism is studied, and some comparisons made between the responses with and without hydrogen [68, 69, 70, 71, 72, 73, 74, 48, 49, 38, 82, 83, 84]. The general approach which is also followed in this thesis is to establish simulations that suitably reflect the basic concept (e.g. H reduces the tensile strength, and enables cleavage), and make quantitative measurements. If a concept is not supported by simulations, then it may still occur but for reasons beyond the basic rationale upon which the concept is usually based. Insight from such studies may point to those mechanisms that are most important for embrittlement, as opposed to mechanisms that operate but are tangential or secondary to the failure process.

Here some examples of using atomistic simulations in examining the validity of proposed theories are given. Song et al. [38] examined the prediction of continuum theories for cleavage and dislocation emission in presence of Hydrogen atoms in Ni, and compared them with direct atomistic simulations. The results of their study showed that the continuum predictions are accurate at low H concentrations which are associated with the dislocation emission dominant regime. At higher H concentrations above the embrittlement point, the continuum predictions of cleavage deviate from the atomistic results and cleavage has

1.3. Atomistic studies of hydrogen embrittlement in metals

not been observed whenever emission was possible. These results indicate the HE in Ni is more complicated than what can be fully addressed with a simple HEDE theory.

Moreover, Song and Curtin [85] analyzed the effect of the accumulation of H atoms at the core of dislocations in α -Fe, in which H diffusion is fast enough to be captured in MD time scales. Interestingly, they observed that H reduces the dislocation mobility and put it in the drag regime. Also, the structure of the dislocation pile-ups remains unaltered by H. Thus, in accordance with elegant continuum calculations done by Sofronis and his coworkers [86], H induces no shielding in dislocation/dislocation interaction. It seems that understanding HELP processes requires study of more complicated dislocation/H interactions.

1.3 Atomistic studies of hydrogen embrittlement in metals

In this thesis, we use atomistic simulations to examine the validity of the few existing theories of HE in metals. The main motivation of this study is to examine the present theories of HE and determine the domain of validity of each of them. With that we can clarify the multifaceted problem of hydrogen embrittlement and find the key parameters that need to be studied to complete attain a comprehensive theory of HE in metals. Hereby we introduce the key problems that are studied in this thesis and discuss their importance.

First, we start with the simulation of the intergranular fracture in nickel. These simulations will give us insights about the validity of simple HEDE theory, in which the presence of segregated hydrogen atoms at the interface can give rise to ductile-to-brittle transitions. One feature of hydrogen embrittlement is often cleavage-like failure, frequently along grain boundaries in polycrystalline metals such as Ni. We thus believe the understanding of embrittlement is likely to be achieved by understanding the behavior of cracks, and at the nanoscale. Cleavage-like failure implies that sharp cracks can propagate without blunting, and this points toward studying crack-tip specific phenomena associated with hydrogen. As it is mentioned in the introduction there exist experimental studies showing the role of the hydrogen atoms in changing the ductile fracture into brittle intergranular fracture along grain boundaries in polycrystalline nickel [30, 4, 28, 29].

There are two coupled phenomena involved in possible embrittlement at a grain boundary: crack nucleation and crack growth. These processes could occur quasi-statically or dynamically, introducing a possible time dependence into the phenomena. An additional time dependence occurs if H can diffuse into grain boundaries or toward grain boundary crack tips within the time scale of the mechanical loading [48, 49]. In the present work, we do not consider explicit long-range H diffusion during mechanical testing, and only consider H pre-segregated to the grain boundaries. Several material properties then control the crack nucleation and growth phenomena. The first property of interest is

the grain boundary tensile strength under cleavage-like separation. Complicating the concept of tensile strength of a grain boundary is the fact that a grain boundary can emit dislocations under tensile load, which dissipates energy and precludes purely cleavage-like separation. The second property of interest is the brittle cleavage fracture energy, which is the difference between the intact grain boundary and the fractured system wherein two free surfaces near/along the grain boundary are present. The third property of interest is the propensity for crack-tip dislocation emission, which is a mechanism of crack blunting and, thus, prevention of cleavage. In polycrystalline metals, segregation of H to grain boundaries during the H charging process provides the possibility of embrittlement without active diffusion. That is if the segregation of H to a grain boundary can prevent blunting of grain boundary cracks, and permit cleavage along the grain boundary (which is also expected to be easier due to the H segregation), then the embrittlement may proceed without diffusion. The question is whether or not H segregation decreases the work of fracture, and by how much, without consideration of the competing crack tip mode of dislocation emission and blunting. Thus, the aim of the present work is to investigate the effects of H on modifying the crack tip behavior of cracks along grain boundaries in fcc Ni. In this thesis, we answer these questions by performing careful atomistic simulations by incorporating accurate interatomic potentials.

Another set of theoretical development and simulations in this thesis is devoted to investigating the interaction of the hydrogen atoms with solute atoms in the alloys. Many advanced engineering metals contain solutes, either for direct solute strengthening or as a residual of precipitate strengthening. In both cases, there is a contribution to the flow stress from the solutes in the matrix due to dislocation interactions with the field of solute atoms. A recent predictive model for the finite-temperature, finite-strain rate, solute strengthening by Leyson et al. [87, 88, 89] is a parameter-free theory whose only inputs are the specific dislocation/solute interaction energies and assumed random fluctuations of the solute distribution. This theory thus provides the specific guidance needed to connect Solute-Hydrogen-Solute (S-H) interactions to the solute strengthening of the host metal. Specifically, if pre-existing solutes can bind hydrogen atoms to form S-H complexes, the difference in misfit distortion between the Solute and the S-H complex will change the interactions with the dislocations, and raise or lower the flow stress. This idea was considered by Birnbaum and Sofronis [40], who performed a finite element analysis to estimate the effect of the H atoms on the interaction energy between interstitial carbon atoms and edge dislocations in Nb and found a decrease of 0.5 eV in the maximum interaction. While no direct connection to lower flow stresses was made, a reduction would be expected. The purpose of the present work is to clearly demonstrate this mechanism, in the case of softening in an fcc metal, using direct atomistic simulations as guided by solute strengthening theory. For simplicity in dealing with "chemical" interactions among multiple atom types, we do not use realistic solutes but instead, use vacancies (S=Vacancy V) as the "solutes" in Ni. The use of a vacancy "solute" enables the use of a well-established Ni-H binary potential for the study of the Ni-H-V system. We show that

1.3. Atomistic studies of hydrogen embrittlement in metals

H modifies the misfit strain tensor of the solute and that an individual dislocation moves through a field of S–H complexes at lower stresses than through a field of solutes in exactly the same random configuration. The scaling of the effects with solute concentration follows the predictions of the theory, verifying the origins of the strengthening of the solutes and of the softening due to the introduction of H bound to the solutes. Our study here is in no way representative of real vacancy-Hydrogen effects; we reiterate that the vacancy is used as a surrogate for a realistic solute. As a preliminary step toward realistic situations, we then use first-principles calculations based on density functional theory to study the interaction of H atoms with the pre-existing Sulfur and Carbon solutes in Ni. These cases show H–Solute repulsion and increases in misfit strain tensor, thus indicating no softening, but serve to demonstrate the approach for general H–Solute–Matrix studies. The overall results and analysis here provide a path for understanding softening and hardening due to H in metal alloys.

We also investigate the viability of the nano-void formation and growth theory with simulations. Recent experiments reveal that the nano-voids are formed and coalesce ahead of the crack tips in steel [31]. However, the role of the hydrogen atoms on facilitating the growth of the voids and the precise role of the voids in facilitating crack growth is unclear. Nonetheless, mechanisms can be envisioned so that the mechanism(s) of nanovoid creation merits study. A potential concept that is believed to be responsible for facilitated void growth in steels can be described as follows. It is true that hydrogen atoms tend to bind to the vacancies and form VH complexes, namely "Hycancies". These hycancies are believed to be more stable against the usual vacancy annihilating processes which occur during plastic deformation. And coalescence of this hycancies with the other hycancies and/or vacancies can lead to formation and growth of nanovoids in hydrogen-rich regions around the crack tip. In this work, we examine the key assumptions of this theory.

Defactant theory is investigated by direct simulation of the problem of the dislocation bow-out in the presence of H atoms. Due to their positive misfit volume, the hydrogen atoms tend to bind to the tensile side of the dislocations. Thus, a Cottrell cloud forms around the dislocation. This phenomenon is believed to reduce the line tension of the dislocations and make dislocation more easy to generate. Along with this way of thought Kirchheim used the concept of "defactant" for the segregated hydrogen atoms and concluded that the presence of H atoms can significantly reduce the line tension of the dislocation in a way that the generation of the dislocation becomes spontaneous. This concept can be believed as a HELP like the process of HE. In this work, we examined the effect of the hydrogen atoms on the problem of bowing out of an edge dislocation in α -Iron to answer the question of whether the presence of hydrogen hardens or softens the response of the dislocation during bowing out.

Although the nano-hydride formation mechanism has good predictions about the embrittlement of steels in room temperature. However, in the low-temperature situations in which the hydrogen is mainly immobile and thus incapable to accumulate at the crack

tip region, we still witness intergranular fracture in the experiments. One of the possible explanations for this phenomenon is the effect of hydrogen on the mode of the interaction of the grain boundaries. The dislocations can react with the grain boundaries and (i) dissociate into grain boundary dislocations, (ii) transmit to the next grain, (iii) absorb to the boundary and form residual slip at the GB, (iv) form pile ups near the grain boundaries. The presence of the hydrogen atoms along can change the scenario that happens in an intact GB via three main processes. In the low-temperature regime, the immobile hydrogen atoms can act as solutes with considerable misfit volume. This may lead to solute strengthening and increase the yield stress of the metal. Furthermore, the presence of the hydrogen atoms along the grain boundaries leads to the development of the stressed regions along the grain boundary. These stress fields can repel/attract the dislocations along the boundary and change the net Burgers vector along the boundary. This phenomenon can facilitate the rupture the GB. Moreover, the dissociation of the dislocation into grain boundary dislocation which is a mechanism for addressing the slip is hindered by the presence of immobile H atoms that need to diffuse due to the GB migration. In this work, we examine a few aspects of this problem.

1.4 Outline of the thesis

This thesis is organized as follows. In chapter 2, the effect of segregated hydrogen atoms in HE of polycrystalline nickel is clarified by direct simulations. An interesting softening/hardening of yield stress by hydrogen–solute interactions in nickel is demonstrated in chapter 3. Chapter 4, examines a newly proposed mechanism for H assisted void growth in Iron. The effect of the H atoms on the precipitate hardening in bcc Iron is investigated in chapter 5. Chapter 6 is devoted to investigating the effect of H atoms on the dislocation–GB interactions in polycrystalline nickel. The conclusions of this thesis are given in chapter 8.

2 Atomistic study of Hydrogen embrittlement of grain boundaries in Nickel

This chapter is extracted from the following publications:

- (1) Atomistic study of hydrogen embrittlement of grain boundaries in nickel: I. Fracture, A. Tehrani, and W. A. Curtin, *Journal of the mechanics and physics of solids*, Volume 101, 2017, Pages 150–165
- (2) Atomistic study of hydrogen embrittlement of grain boundaries in nickel: II. Decohesion, A. Tehrani, and W. A. Curtin, *Modeling and simulations in material science and engineering*, Volume 25, 2017, 075013

2.1 Introduction

The aim of this chapter is to investigate the role of the segregated hydrogen atoms on the embrittlement of polycrystalline nickel as a representative fcc metal. To this end, first we examine the tensile failure behavior of representative GBs in Ni, with and without segregated H, to draw conclusions about crack nucleation. Then we turn our attention to the growth of the cracks and investigate the effects of H on modifying the crack tip behavior of cracks along GBs in fcc Ni. We consider GBs containing equilibrium segregation of H under conditions typical of embrittlement in Ni, and study several different GBs of increasing complexity. To guide understanding, we correlate the results of direct MD simulations to predictions based on the Griffith and Rice theories for cleavage and emission, respectively, and assess whether these theories are useful for predicting or understanding H embrittlement at GBs.

2.2 Energetics of Hydrogen in Ni grain boundaries and fracture surfaces

In bulk fcc Ni, H atoms occupy octahedral interstitial sites. The binding sites in and around any particular grain boundary must be determined, and depend strongly on the local atomic structure [63]. For a possible H site i , we define the interaction energy of an H atom relative to the energy of H in a bulk octahedral site as

$$E_{\text{int},i} = E_i^{\text{GB+H}} - E_{\text{bulk}}^{\text{GB+H}} \quad (2.1)$$

where $E_i^{\text{GB+H}}$ is the energy of a fully-relaxed material containing a grain boundary with an H atom at site $\#i$ and where $E_{\text{bulk}}^{\text{GB+H}}$ the energy of the same fully-relaxed material with an H atom in a bulk interstitial site far from the GB.

2.2.1 Validated Ni–H interatomic potential

For the complex crack studies here, atomistic simulations must use semi-empirical interatomic potentials; direct first principles computations are prohibitively expensive. It is thus essential that the interatomic potential function be validated against higher-fidelity calculations. Here, we adapt the embedded atom method (EAM) potential for Ni–H introduced by Angelo et al. [90, 91], and previously modified by Song and Curtin [48], to obtain good agreement with recent results obtained using density functional theory (DFT) (Alvaro et al. [59], Di Stefano et al. [60]) for the case of H in Ni Σ 5(120)(100). Fig. 2.1a shows the positions of the binding sites found in the two different sets of DFT calculations; the corresponding H/GB interaction energies are shown in Table 2.1. Alvaro et al. [59] show that H binds to octahedral-like sites at the boundary, with site $\#5$ in a very open region of the GB being unstable. This result is slightly counter-intuitive because H atoms have large misfit volume and so generally prefer to occupy sites with more open structure, and surfaces are also quite favorable relative to the bulk. Di Stefano et al. [60] show this site to be stable and with a large interaction energy of -0.22 eV. In spite of the discrepancy at site $\#5$, the results are comparable for H at binding sites $\#1$ and $\#2$. The EAM potential finds all the octahedral-like sites $\#1$ – $\#4$ and the site $\#5$ to be stable and binding. For the existing Ni–H EAM potential, however, the interaction energies at all sites are 0.1eV higher (stronger binding) than the DFT calculations. This discrepancy would lead to large overestimation of the probability of occupation of such sites in the Ni Σ 5(120)(100) as well as errors in the GB and surface energies in the presence of H. The existing Ni–H EAM potential is thus inadequate.

We have modified the existing EAM potential by changing some of the parameters that describe the Ni–H interactions but while maintaining good overall properties. Table 2.2 shows the original and revised values for the modified parameters in the potential as well as the relevant bulk properties of Ni that are used in the analyses provided in this work.

2.2. Energetics of Hydrogen in Ni grain boundaries and fracture surfaces

Table 2.1 – Interaction energies for Hydrogen atoms in Ni(120) Σ 5 \langle 100 \rangle at various sites indicated in Fig. 2.1a. Results are shown for computations using DFT Alvaro et al. [59], Di Stefano et al. [60], using the original Ni–H EAM potential [48], and using the modified Ni–H EAM potential developed in this thesis.

# site	$E_{\text{int}}(\text{eV})$			
	DFT [59]	DFT [60]	EAM [48]	Modified EAM (this work)
1	-0.23	-0.23	-0.37	-0.25
2	-0.14	-0.17	-0.26	-0.13
3	-0.09	not studied	-0.24	-0.16
4	+0.04	not studied	-0.09	-0.05
5	not stable	-0.22	-0.28	-0.14
6	not stable	-0.09	+0.05	+0.07

With the new potential, the positions of the energetically favorable sites for H remain unchanged but the binding energies are closer to the DFT calculations, as shown in Table 2.1. The surface energy of Ni(111) with H has also been computed as [92]

$$\gamma_s = \frac{1}{2A} (E_s(N^{\text{Ni}}, N^{\text{H}}) - N^{\text{Ni}} E_{\text{coh}}^{\text{Ni}} - N^{\text{H}} E_{\text{bulk}}^{\text{H}}) \quad (2.2)$$

in which A , N^{Ni} , N^{H} , $E_s(N, c)$, $E_{\text{coh}}^{\text{Ni}}$, and $E_{\text{bulk}}^{\text{H}}$ are the surface area, number of the Ni and H atoms in the specimen, total energy of the specimen with two free surfaces, the cohesive energy of the Ni atoms in the bulk, and the solution energy of one H atom in the bulk Ni, respectively. The surface energy of Ni(111) is a linear function of H concentration c (i.e. $\gamma_s(c) = a + bc$). The original potential has $a = 2.044 \text{ J/m}^2$, $b = -1.599 \text{ J/m}^2$ while the revised potential has the same a for pure Ni and $b = -1.465 \text{ J/m}^2$, which is not a significant change. Since other properties of the pure Ni remain unchanged, the new Ni–H potential provides a significant improvement for the study of the grain boundary problems of interest here.

2.2.2 Energies of H in grain boundaries and fracture surfaces

We used the new Ni–H potential to find binding sites for H and their associated energies in and around the Ni Σ 3(111) \langle 110 \rangle , Ni Σ 9(221) \langle 110 \rangle , Ni Σ 99(557) \langle 110 \rangle , Ni Σ 19(331) \langle 110 \rangle , Ni Σ 27(115) \langle 110 \rangle , Ni Σ 33a(441) \langle 110 \rangle , Ni Σ 33b(554) \langle 110 \rangle , and Ni Σ 41(443) \langle 110 \rangle grain boundaries. Fig. 2.1 show the position of the binding sites for H in each GB. The corresponding interaction energies are shown in Tables 2.3 and 2.4. It should be noted that the molecular statics simulations are performed using the Large-scale Atomic/Molecular Massively Parallel Simulator (LAMMPS) [93] and atomic configurations are visualized using the Open Visualization Tool (OVITO) [94]. For Ni Σ 3(111) \langle 110 \rangle , the twin boundary, there is only one site for H and it has a very small interaction energy. For Ni Σ 9(221) \langle 110 \rangle

Chapter 2. Atomistic study of Hydrogen embrittlement of grain boundaries in Nickel

Table 2.2 – Original and modified parameters for the Ni–H EAM potential based on the formulation of [90,91]. Also shown are relevant properties of bulk Ni, as predicted by the potential.

parameter	original [90, 91]	modified
$c_{10}^H(eV)$	13.26	13.85
$c_6(eV)$	0.53419208	0.52
c_9	1.1292331	1.092
$r_c^H(\text{\AA})$	2.8	2.7
$C_{11}(GPa)$	251.7	251.7
$C_{12}(GPa)$	147.3	147.3
$C_{44}(GPa)$	130.6	130.6
$\gamma_{\text{usf}}(mJ/m^2)$	276	276

and Ni Σ 99(557) \langle 110 \rangle , the binding sites are concentrated in the areas with more open structure. We have evaluated the H–H interactions for H atoms in two types of sites; in all cases, the H–H interactions are repulsive but fairly small (all less than 0.02 eV). We thus neglect the H–H interactions and consider the interaction energy of each site as independent of the H occupation of any other sites. We followed the same procedure to find the binding sites and energies on and around the free surfaces that are related to surfaces created by advancement of the intergranular crack along the grain boundary. The position of the binding sites for Ni(111), Ni(120), Ni(221), and Ni(557) are illustrated in Fig. 2.1 and the interaction energies are displaced in Table 2.3. The interaction energies of H atoms with the free surfaces are necessary for calculation of the equilibrium concentration of the H atoms on the initial crack faces, but do not enter in any other calculations here. It also should be mentioned that the repulsive H–H interaction of the adjacent sites at these surfaces is also negligible.

Apart from the chemical interaction between the host metal and H atoms, the main parameter that controls the binding energy of a site in the grain boundary is the volume distortion of the grain boundary due to the presence of H atoms. Recently, Zhou et al. [63, 64] investigated the effect of volume distortion of structural units of the GBs in various materials including nickel and gave a predictive formulation for calculation of the binding energies. This is a manifestation of the dependency of the interaction energy of the stable binding sites to the structure of the grain boundary.

We have further verified that H–H interactions in nearby binding sites are negligible. Therefore, we compute the probability of occupation c_i of sites of type i , which we refer to as the concentration at site i , using a simple solution model as

$$c_i = \frac{c_0 \exp(-E_{\text{int},i}/k_B T)}{1 + c_0 \exp(-E_{\text{int},i}/k_B T)}. \quad (2.3)$$

2.2. Energetics of Hydrogen in Ni grain boundaries and fracture surfaces

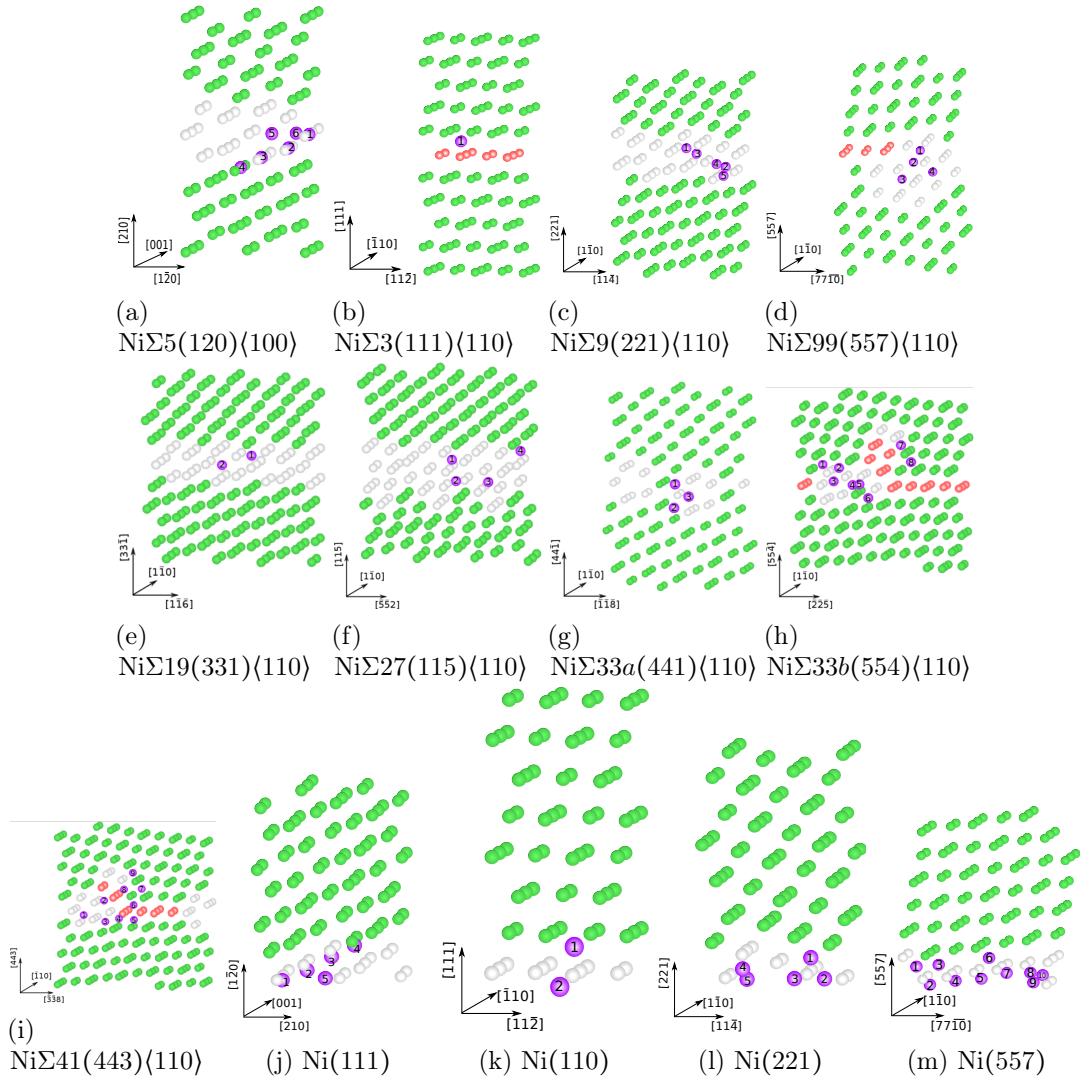


Figure 2.1 – Structure and Hydrogen binding sites in various symmetric tilt boundaries and free surfaces. Atoms colored by Common Neighbor Analysis (Green: fcc Ni; Red: hcp Ni; White: Ni with less than 12 neighbors; Purple: Hydrogen sites)

Chapter 2. Atomistic study of Hydrogen embrittlement of grain boundaries in Nickel

Table 2.3 – Interaction energies for Hydrogen atoms at various sites in different grain boundaries and surfaces as predicted by the modified EAM potential.

# site	$E_{\text{int}}(\text{eV})$						
	Ni Σ 3(111) \langle 110 \rangle	Ni Σ 9(221) \langle 110 \rangle	Ni Σ 99(557) \langle 110 \rangle	Ni(111)	Ni(120)	Ni(221)	Ni(557)
1	-0.04	-0.20	-0.15	-0.19	-0.55	-0.22	-0.16
2	-	-0.16	-0.20	-0.47	-0.55	-0.51	-0.56
3	-	-0.16	-0.26	-	-0.24	-0.46	-0.23
4	-	-0.20	-0.21	-	-0.07	-0.46	-0.48
5	-	-0.16	-	-	-0.43	-0.48	-0.48
6	-	-	-	-	-	-	-0.21
7	-	-	-	-	-	-	-0.48
8	-	-	-	-	-	-	-0.43
9	-	-	-	-	-	-	-0.48
10	-	-	-	-	-	-	-0.61

Here, T is the temperature and k_B is Boltzmann's constant, while c_0 is the bulk concentration of H atoms which corresponds to some imposed H chemical potential for the entire specimen. These concentrations c_i are used for preparing the simulation specimens as described in the next section.

Table 2.4 – Interaction energies for hydrogen atoms at various sites in different grain boundaries as predicted by the modified EAM potential.

# site	$E_{\text{int}}(\text{eV})$				
	Ni Σ 19(331) \langle 110 \rangle	Ni Σ 27(115) \langle 110 \rangle	Ni Σ 33a(441) \langle 110 \rangle	Ni Σ 33b(554) \langle 110 \rangle	Ni Σ 41(443) \langle 110 \rangle
1	-0.15	-0.11	-0.25	-0.11	-0.18
2	-0.22	-0.19	-0.25	-0.14	-0.27
3	-	-0.20	-0.25	-0.19	-0.25
4	-	-0.10	-	-0.18	-0.22
5	-	-	-	-0.15	-0.18
6	-	-	-	-0.20	-0.25
7	-	-	-	-0.19	-0.25
8	-	-	-	-0.14	-0.14
9	-	-	-	-	-0.22

2.3 Simulation of the tensile strength and yield strength of grain boundaries

In this section, the details of the simulations pertinent to the calculation of the theoretical cohesive strength $\hat{\sigma}$, the fracture energies γ_{fr} , and the grain boundary yield strength σ_y of the various grain boundaries are presented.

We examine the effect of the hydrogen atoms on the theoretical strength of various grain boundaries as follows. We construct simulation cells of size $l_1 \in [200\text{\AA}, 260\text{\AA}]$, $l_2 \in [209\text{\AA}, 211\text{\AA}]$ and $l_3 = 12.4\text{\AA}$ containing a GB (Ni Σ 9(221) \langle 110 \rangle , Ni Σ 19(331) \langle 110 \rangle , Ni Σ 27(115) \langle 110 \rangle , Ni Σ 33a(441) \langle 110 \rangle , Ni Σ 33b(554) \langle 110 \rangle , Ni Σ 41(443) \langle 110 \rangle or Ni Σ 99(557) \langle 110 \rangle

2.3. Simulation of the tensile strength and yield strength of grain boundaries

along the central plane $x_2 = 0$. The simulation cells are periodic in x_1 and x_3 directions and have free boundaries in the x_2 direction. We note that grain boundaries have an intrinsic stress. Therefore, in a finite size sample that is fully relaxed to zero net stress in all directions, this intrinsic GB stress is balanced by a compensating stress in the two grains on either side of the boundary. This compensating stress decreases with increasing height l_2 of the sample and would vanish in a large-grain sample. To avoid spurious effects of this compensating stress in finite-size MD samples, we fix the l_1 width of the sample at the size corresponding to the bulk Ni lattice constant, and the Ni grains are under zero stress while the GB stress is equal to the stress of the same GB embedded in an infinitely extended bulk.

After proper relaxation of the specimen, we saturate the binding sites of the grain boundaries with hydrogen atoms due to the concentrations c_i calculated via by inserting interaction energies calculated in the previous section into Eq. (2.7). The bulk concentration of hydrogen is set to $c_0 = 0.001$, typical of embrittlement conditions in Ni at $T=300K$ [3]. For each GB we prepare H-charged samples at both $T = 300K$ and $T = 50K$. The latter low temperature gives rise to $c_i > 0.994$ for all binding sites that are not also nearly fully occupied at $T = 300K$. Thus, in the low-T sample, the H concentrations in the GB are nearly fully-saturated, and independent of c_0 , thus representing a highly-charged system. After insertion of the H atoms in the binding sites, we relax the system again to mechanical equilibrium at $T = 0K$ (maintaining the fixed l_1 sample length, however). Since the barrier for the diffusion of hydrogen atoms in fcc nickel is $\sim 0.5eV$, H diffusion cannot be captured in molecular dynamics (MD) timescales at $T = 300K$. Moreover, we are not concerned with any thermally activated process here. Therefore, we execute all simulations at $T=0K$.

Starting from the relaxed boundary, we rigidly separate the two grains across a specified plane parallel to the grain boundary as schematically shown in Fig. 2.2. We measure the interfacial stress σ_{22} as a function of the planar separation distance δ , up to $\delta = 10\text{\AA}$ at which point the stress is always zero (beyond the range of the EAM potential).

The unrelaxed fracture energy γ_{fr}^u is the difference between the initial and final system energies, with no relaxation during the rigid separation process, divided by the GB area. The γ_{fr}^u is exactly equal to the work done in the separation process, which corresponds to the area under the measured stress-opening ($\sigma_{22}-\delta$) curve. We then allow full relaxation of the separated surfaces to obtain the relaxed fracture energy γ_{fr}^r ; this is the relevant energy in the equilibrium Griffith criterion for cleavage crack growth along the selected plane of separation with no H diffusion. Several possible separation planes are chosen for each GB so as to find the *minimum* cohesive strength and *minimum* fracture energy surfaces for each GB. For each GB, three different cutting planes P_i ($i = 1, 2, 3$) are chosen shown in Figures 2.4–2.10. It is possible that local diffusion processes (one or a few atomic hops) could transport H atoms from just above/below the fracture surface to the fracture surface sufficiently fast so as to affect the fracture process through a lowering

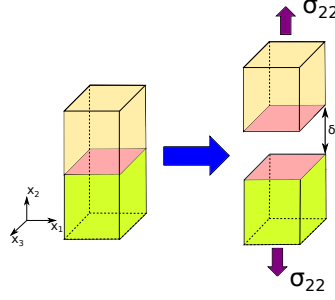


Figure 2.2 – Schematic diagram of the rigid grain boundary separation process.

of the fracture energy. Direct modeling of such diffusion is not possible on MD time scales, and so we create worst-case (full diffusion) scenarios and examine their energies. Specifically, we move all sub-surface H atoms onto the final fracture surface, placing these H in favorable binding sites on the surface. We calculate the surface energy of this configuration and the corresponding $\gamma_{\text{fr}}^{\text{f}}$.

To measure the yield strength of the GB, we use the same initial specimens those used for the cohesive strength and fracture energy studies above. All GBs studied here have slip planes with normal vectors in the x_1, x_2 plane, and so are able to emit straight dislocations consistent with the periodic boundary conditions imposed in x_3 which is coincident with the tilt axes of the grain boundaries of interest. The specimen is subjected to an increasing strain tensor corresponding to an increasing uniaxial stress, in increments of $\Delta\epsilon = \mathbf{C}^{-1}\Delta\sigma$ where \mathbf{C} is the elastic stiffness tensor calculated with respect to x_i coordinate system and

$$\Delta\sigma = \begin{pmatrix} \sigma_{11} & \sigma_{12} & \sigma_{13} \\ \sigma_{21} & \sigma_{22} & \sigma_{23} \\ \sigma_{31} & \sigma_{32} & \sigma_{33} \end{pmatrix} = \begin{pmatrix} 0 & 0 & 0 \\ 0 & 200 & 0 \\ 0 & 0 & 0 \end{pmatrix} \text{MPa.} \quad (2.4)$$

Since we are simulating $\langle 110 \rangle$ symmetric tilt boundaries in fcc, the stress field is symmetric with respect to the GB plane ($x_2 = 0$). We thus do not need to solve the general anisotropic elasticity problem for tension of a bi-material to find $\Delta\epsilon$. Thus it is sufficient to only use the Hook's law to find the incremental strain tensor. After each load increment, the specimen is relaxed via the conjugate gradient method [95]. We measure the GB yield stress as that uniaxial stress at which dislocation(s) are first emitted from the grain boundary.

Furthermore, we examine the possible effects of H atoms on the plastic activity of the GB at loads higher than the initial GB yield stresses. However, previously emitted dislocations cannot be pinned at the sample boundaries and, thus, exert improper backstresses on the GB. Therefore, in these simulations, the system is loaded by application of forces on the x_2 surfaces corresponding to desired tensile stress. Application of the forces at the free top and bottom enables the emitted dislocations exit from these free surfaces and

2.3. Simulation of the tensile strength and yield strength of grain boundaries

thus exert no spurious forces that might affect subsequent emission from the GB. MD simulations are then performed using the velocity–Verlet algorithm [96] with integration time step of 1 fs. A Langevin thermostat [97] is used for fixing the temperature of the system $10^{-3}K$, so that MD is very nearly equivalent to a steepest-descent minimization. After application of the total desired load, MD is executed for $t = 50$ ps.

2.3.1 Results

Fig. 2.3 shows the computed σ_{22} – δ curves for all the grain boundaries, for pure Ni, and with H at bulk concentration of $c_0 = 0.001$ at both $T = 300K$, and $T = 50K$. In each case, these curves are those for the cutting plane having the minimum theoretical cohesive strength. Table 6.1 shows the computed cohesive strength of each boundary. The cohesive strengths of the boundaries are not significantly altered by the presence of H atoms, with a maximum reduction of ≈ 4 percent. In addition, the strengths are all very high, on the order of 25 GPa, which is expected from simple estimates ($25 \text{ GPa} \sim E/5$ where E is the Young’s modulus for polycrystalline Ni). There is thus no significant effect of H on the cohesive strength of any of these GBs.

As stated before, for further investigation of the maximal role of H atoms on the theoretical strength, we prepared samples in which all the binding sites of the grain boundary were filled with hydrogen, i.e. $c_i = 1$ by setting $T = 50$ in Eq. (2.7). These samples are not in the thermodynamical equilibrium at room temperature but they may represent situations in which, due to local transport phenomena, the concentration of H might become high in the GB. For example dislocations carrying Cottrell clouds of hydrogen may come to the GB and provide additional H that is redistributed locally (out of global equilibrium). Even in these extreme cases, there are no significant decrease in the theoretical cohesive strength, with a maximum reduction of only 5.4%, found for the $\text{Ni}\Sigma 27(115)\langle 110 \rangle$ case.

For completeness, the theoretical cohesive strength of a single Ni grain that is separated across a plane parallel to each GB has also been examined for both $c_0 = 0$ and $c_0 = 1$ (complete filling of all octahedral sites in the entire specimen), as shown in Table 2.6. In all of these “single crystal” orientations, the pure Ni specimens have theoretical cohesive strengths around 28 GPa, roughly 12% higher than the corresponding bicrystal specimens. The reductions in theoretical cohesive strength due to the presence of the hydrogen atoms remain small, less than 3.5%, except for $\text{Ni}(115)$ where the reduction is 19%.

The unrelaxed and relaxed fracture energies calculated for each grain boundary and each plane of separation are shown in Table 2.8. Relaxation reduces the minimum fracture energy by 21% and 23% in the H-free and H-charged cases, respectively. Moreover, the presence of H atoms does not significantly reduce the unrelaxed nor relaxed minimum fracture energy of any grain boundary. The maximum reduction due to H is 10%, obtained for $\text{Ni}\Sigma 41(443)\langle 110 \rangle$. Interestingly, the relaxed fracture energy is slightly increased due to

Chapter 2. Atomistic study of Hydrogen embrittlement of grain boundaries in Nickel

Table 2.5 – Theoretical cohesive strengths and yield strengths of the grain boundaries of interest. The percentages are calculated with reference to the hydrogen free cases. P_i are the cleavage planes.

	Yield stress (GPa)					Theoretical strength (GPa)					
	$c_0 = 0$	$c_0 = 0.001$				$c_0 = 0$	$c_0 = 0.001$				
		300K	(%)	50K	(%)		300K	(%)	50K	(%)	
NiΣ9	6.1	6.7	9.8	7.0	14.7	P_1	26.6	26.3	-1.1	26.2	-1.5
						P_2	26.4	26.4	0.0	26.6	0.8
						P_3	26.6	27.1	1.9	26.3	-1.1
NiΣ19	8.66	7.94	-8.3	10	15.5	P_1	25.4	24.4	-3.9	26.6	4.7
						P_2	25.4	24.4	-3.9	26.9	5.9
						P_3	27.9	27.1	-2.9	26.5	-5.0
NiΣ27	7.6	16.7	119.7	17.4	128.9	P_1	27.0	27.3	1.1	27.1	0.4
						P_2	27.0	27.3	1.1	27.1	0.4
						P_3	26.1	25.1	-3.8	24.7	-5.4
NiΣ33a	4.9	6.7	36.7	6.9	40.8	P_1	26.4	26.5	0.37	26.6	0.8
						P_2	26.9	26.7	-0.7	26.7	-0.7
						P_3	27.0	26.6	-1.5	26.5	-1.9
NiΣ33b	2.7	3.4	25.9	3.6	33.4	P_1	26.2	26.8	2.3	26.1	-0.4
						P_2	27.0	26.4	-2.2	26.0	-3.7
						P_3	26.5	26.5	0	27.0	1.9
NiΣ41	2.4	3.0	25	3.7	54.2	P_1	26.7	27.1	1.5	27.5	3.0
						P_2	27.5	27.1	-1.5	27.1	-1.5
						P_3	27.1	26.9	-0.7	27.0	-0.4
NiΣ99	11.2	13.6	21.4	13.8	23.2	P_1	26.6	27.0	1.5	26.2	-1.5
						P_2	26.3	26.4	0.4	26.6	1.1
						P_3	27.2	26.4	-2.9	26.3	-3.3

Table 2.6 – Theoretical cohesive strength of single crystal Ni separated across different crystallographic planes corresponding to planes parallel to the various grain boundaries studied here, in pure Ni and Ni-H (100% occupation of octahedral sites in Ni).

	Theoretical strength (GPa)		
	$c_0 = 0$	$c_0 = 1$	change (%)
Ni(221)	28.6	28.0	-2.1
Ni(331)	27.5	27.6	0.3
Ni(115)	28.4	23.0	-19.0
Ni(441)	27.1	27.2	0.37
Ni(554)	28.6	27.7	-3.1
Ni(443)	28.5	27.7	-2.8
Ni(557)	28.6	28.0	-2.1

2.3. Simulation of the tensile strength and yield strength of grain boundaries

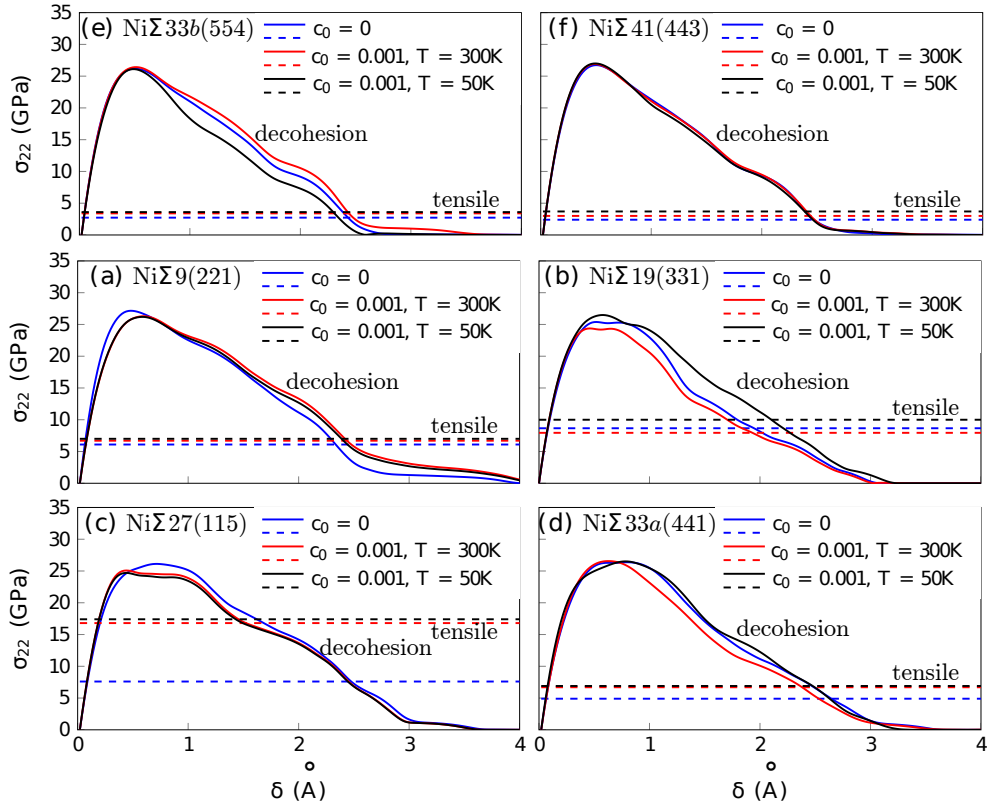
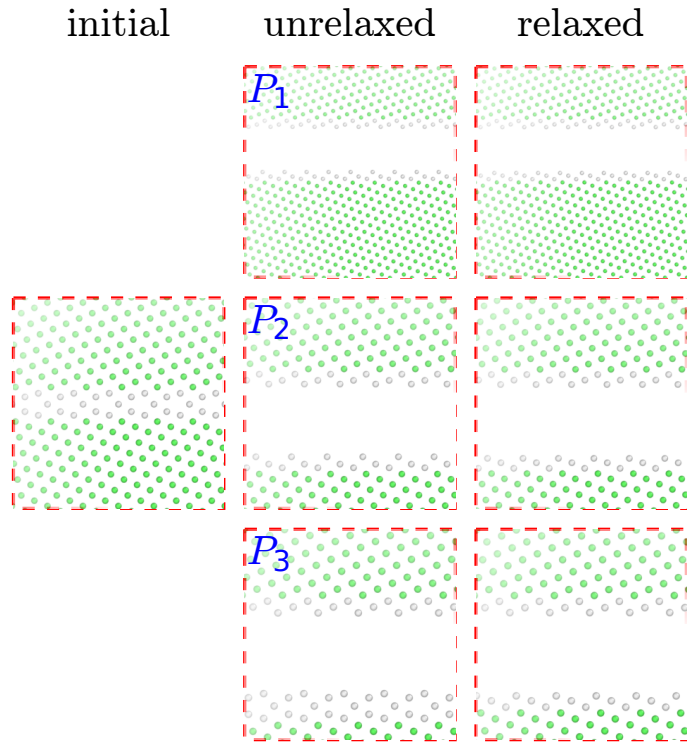


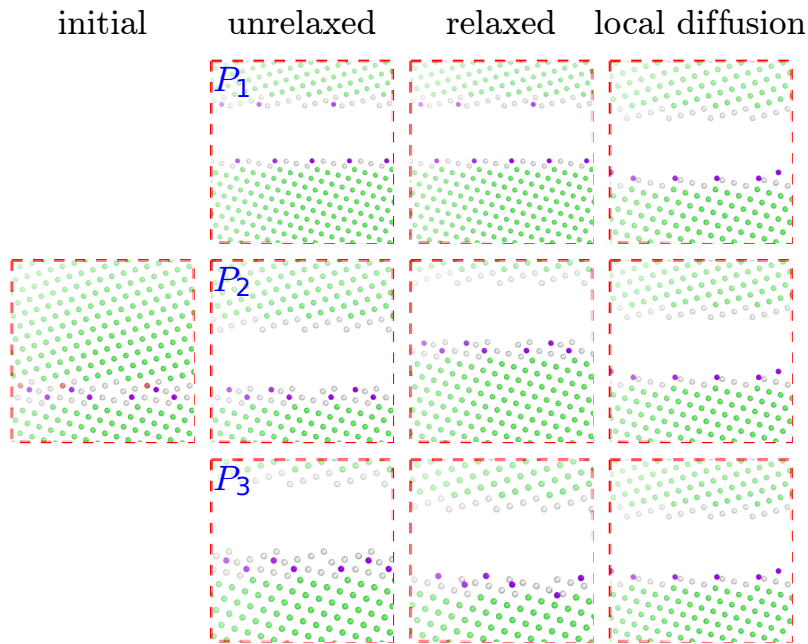
Figure 2.3 – Normal stress versus normal displacement during rigid-block separation across the minimum strength cleavage plane, with and without H, and for a range of grain boundary structures.

the presence of H atoms in $\text{Ni}\Sigma 27(115)\langle 110 \rangle$ and $\text{Ni}\Sigma 33a(441)\langle 110 \rangle$ because the H atoms are not on the separated surfaces. In general, when H atoms are not on the “fracture surface”, we can envision rapid nanoscale diffusion, due to both a reduction in energy and a short diffusion distance, that transports H to the fracture surfaces. We have thus manually moved all subsurface H atoms to the separated surfaces and calculated the relaxed fracture energy; the computed configurations are shown in Figs. 2.4–2.11. This nanoscale diffusion does decrease in γ_{fr}^r but the reductions in fracture energy due to segregated H remain less than 25%. Table 2.8 summarizes all of these results. By of these simulations, we conclude that the presence of hydrogen, even in conjunction with local diffusion processes bringing nearby H to the fracture surfaces, does not significantly change the fracture energies of any of the grain boundaries studied here.

We now turn to results for the GB “yield strength” under uniaxial tensile load. We consider grain boundaries with no H, with segregated H at $c_0 = 0.001$ and $T = 300\text{K}$, and with saturated H wherein all binding sites are filled independent of any thermodynamic considerations at room temperature. All grain boundaries show dislocation emission at some tensile stress that is well below the theoretical cohesive strength, as shown by the



(a) $c_0 = 0.0$



(b) $c_0 = 0.001$

Figure 2.4 – Atomic configurations of $\text{Ni}\Sigma 9(221)(110)$. The relaxed and unrelaxed configuration of the separated grains through three different cutting planes are given. In all figures the atoms colored by Common Neighbor Analysis (Green: fcc Ni; Red: hcp Ni; White: Ni with less than 12 neighbors; Purple: H) of the connected grain boundary.

2.3. Simulation of the tensile strength and yield strength of grain boundaries

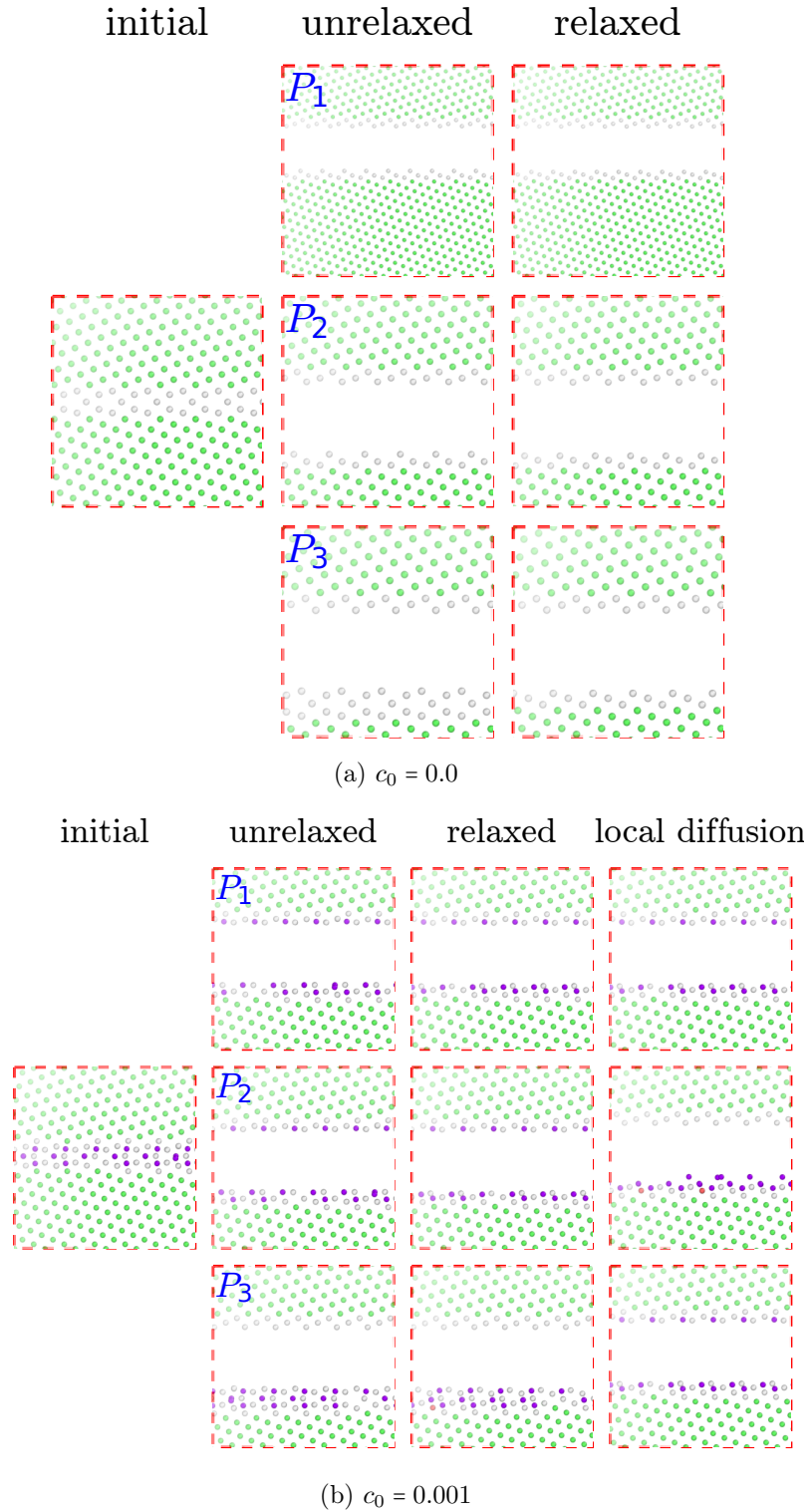
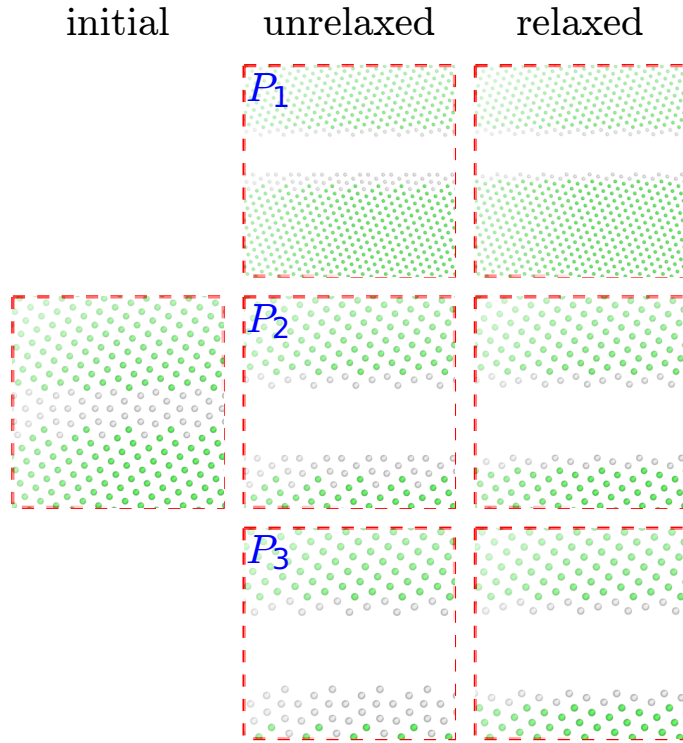
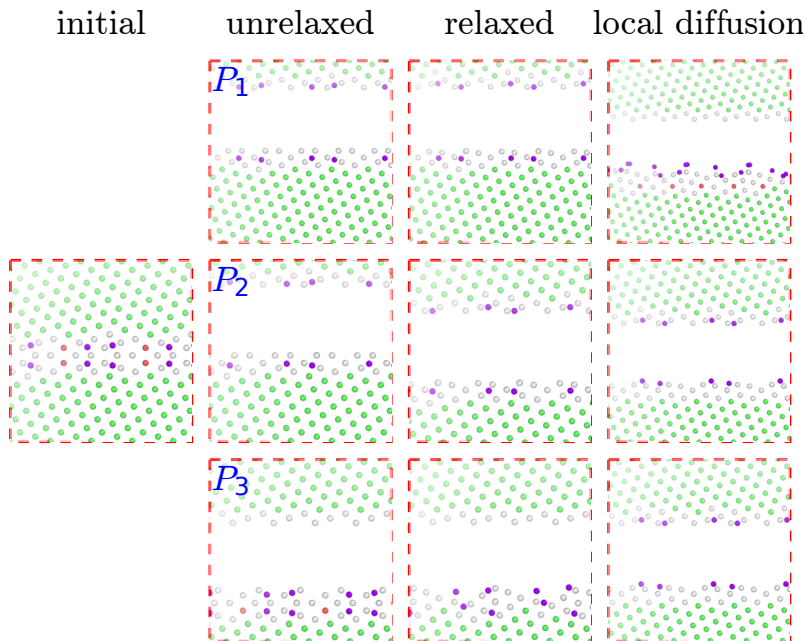


Figure 2.5 – Atomic configurations of $\text{Ni}\Sigma_{19}(331)\langle 110 \rangle$. The relaxed and unrelaxed configuration of the separated grains through three different cutting planes are given. In all figures the atoms colored by Common Neighbor Analysis (Green: fcc Ni; Red: hcp Ni; White: Ni with less than 12 neighbors; Purple: H) of the connected grain boundary.



(a) $c_0 = 0.0$



(b) $c_0 = 0.001$

Figure 2.6 – Atomic configurations of Ni Σ 27(115){110}. The relaxed and unrelaxed configuration of the separated grains through three different cutting planes are given. In all figures the atoms colored by Common Neighbor Analysis (Green: fcc Ni; Red: hcp Ni; White: Ni with less than 12 neighbors; Purple: H) of the connected grain boundary.

2.3. Simulation of the tensile strength and yield strength of grain boundaries

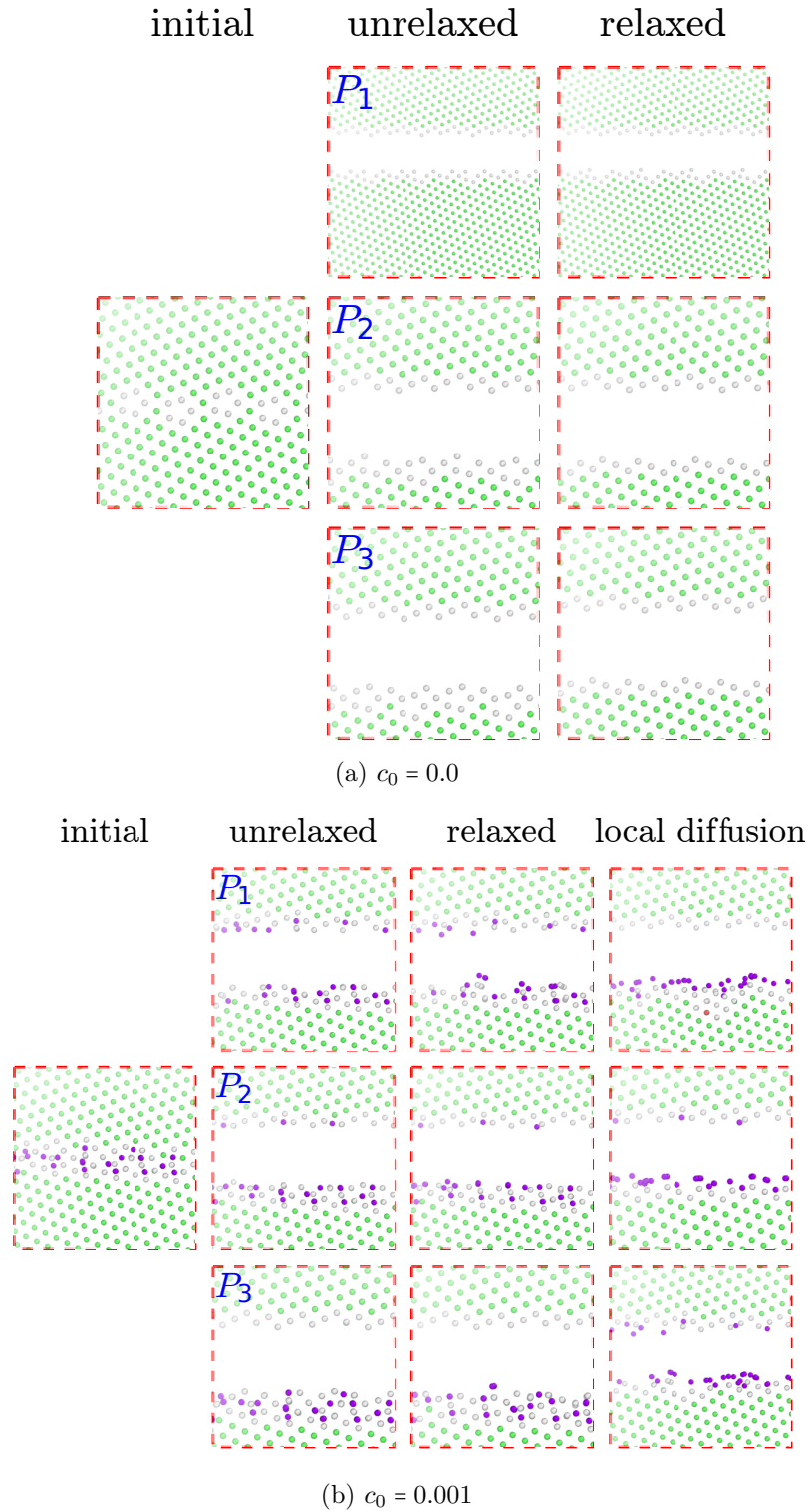
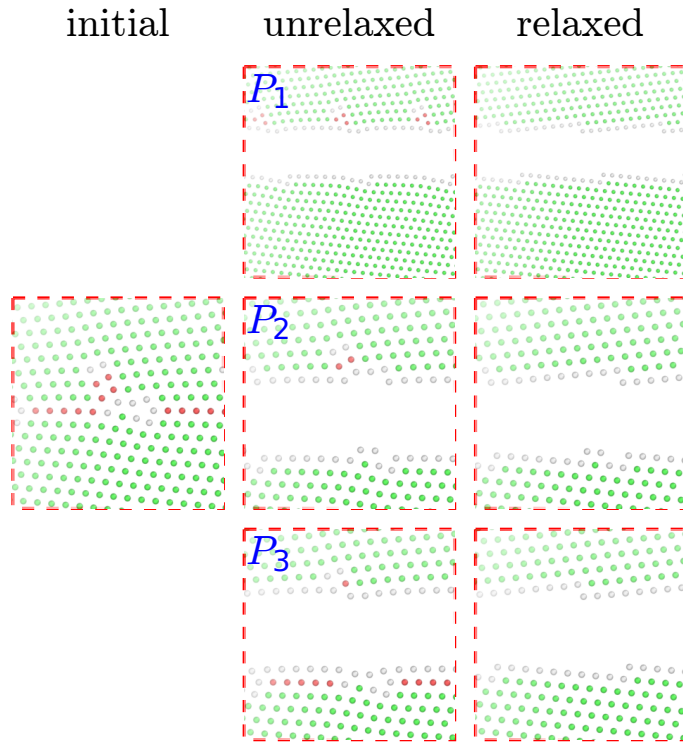
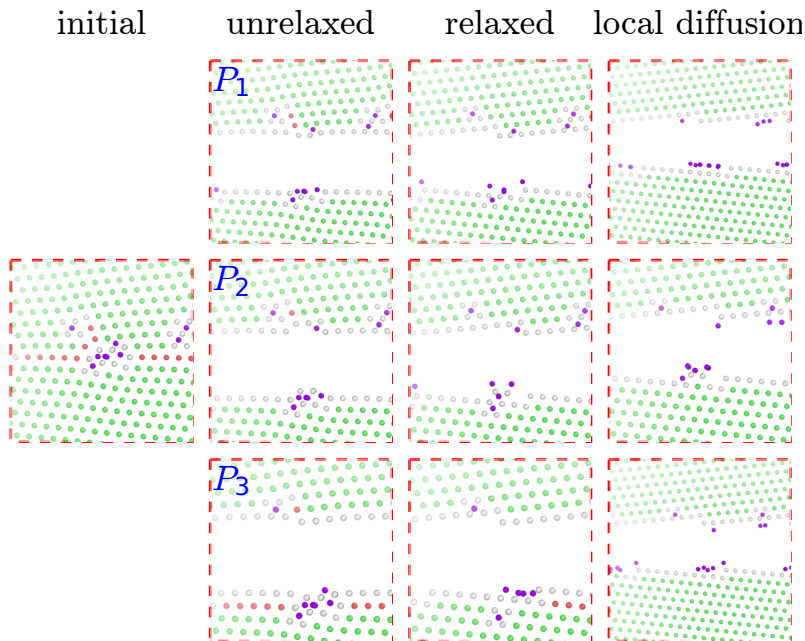


Figure 2.7 – Atomic configurations of $\text{Ni}\Sigma 33\text{a}(441)\langle 110 \rangle$. The relaxed and unrelaxed configuration of the separated grains through three different cutting planes are given. In all figures the atoms colored by Common Neighbor Analysis (Green: fcc Ni; Red: hcp Ni; White: Ni with less than 12 neighbors; Purple: H) of the connected grain boundary.



(a) $c_0 = 0.0$



(b) $c_0 = 0.001$

Figure 2.8 – Atomic configurations of $\text{Ni}\Sigma_{33}\text{b}(554)\langle 110 \rangle$. The relaxed and unrelaxed configuration of the separated grains through three different cutting planes are given. In all figures the atoms colored by Common Neighbor Analysis (Green: fcc Ni; Red: hcp Ni; White: Ni with less than 12 neighbors; Purple: H) of the connected grain boundary.

2.3. Simulation of the tensile strength and yield strength of grain boundaries

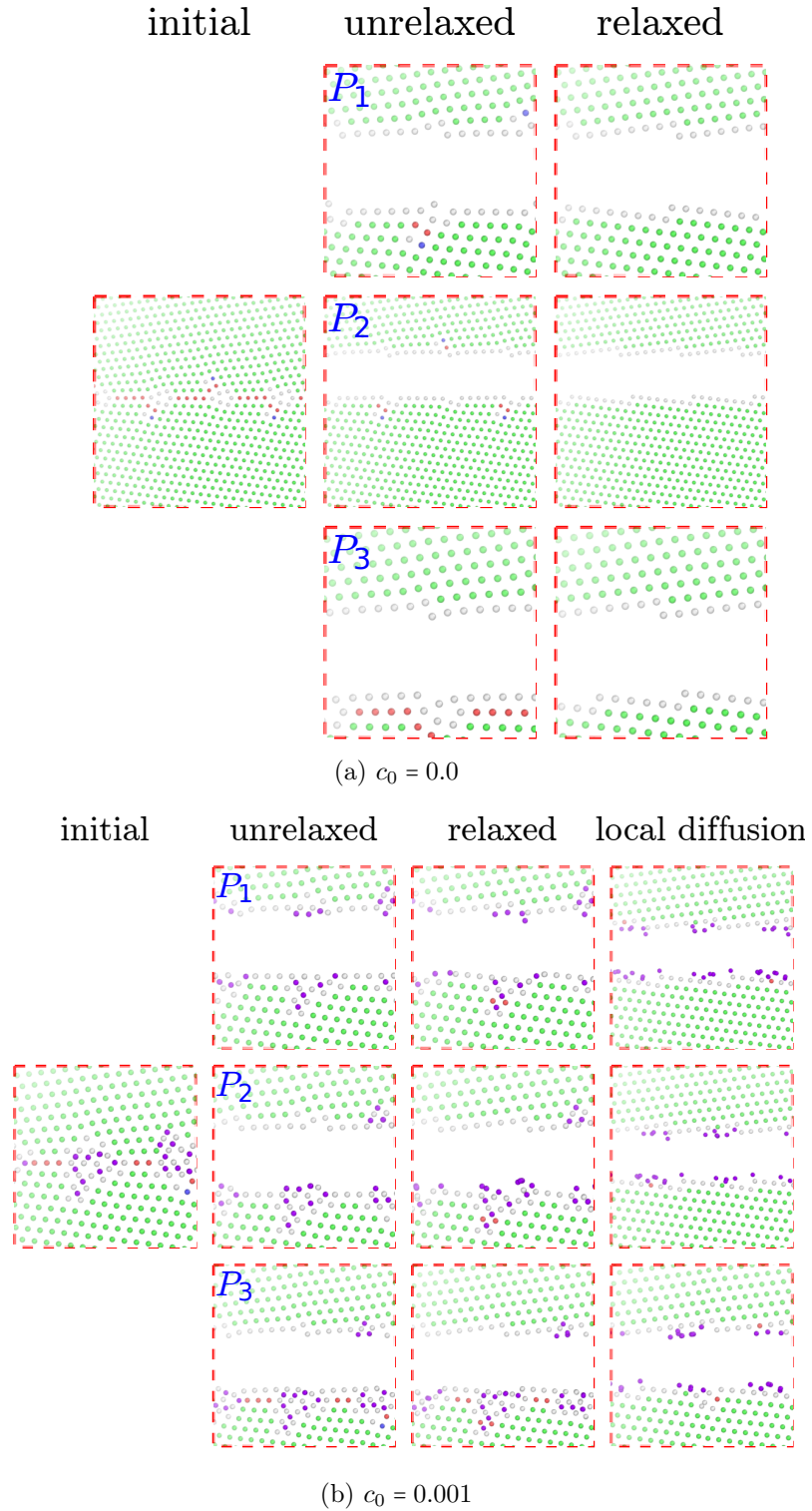
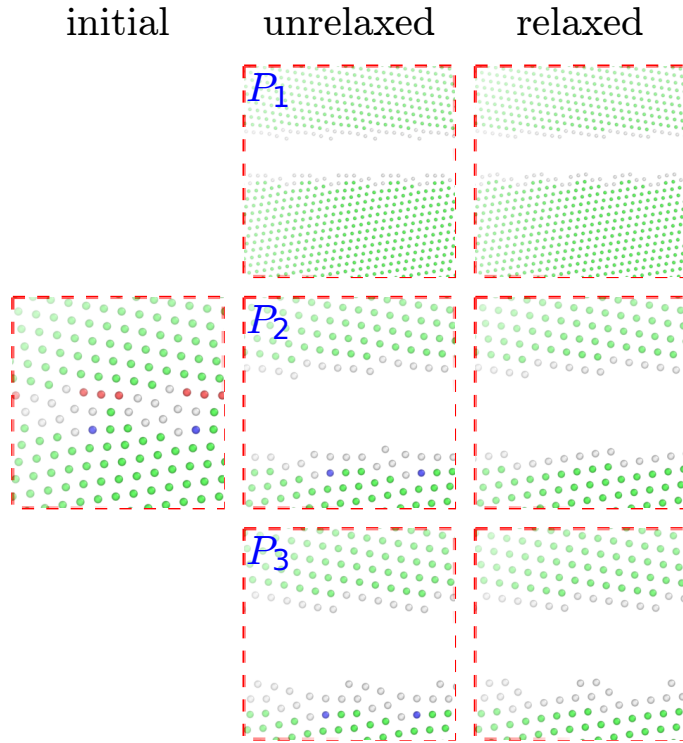
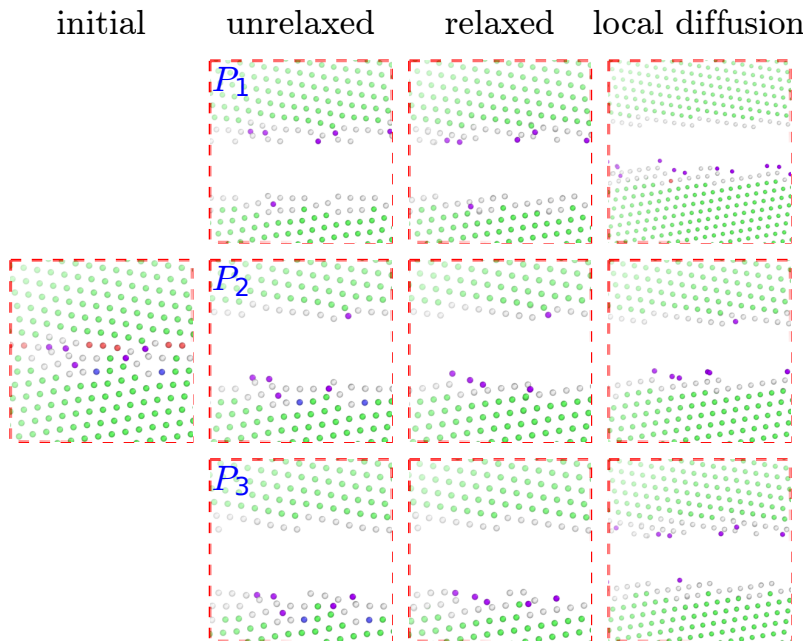


Figure 2.9 – Atomic configurations of $\text{Ni}\Sigma_{41}(443)\langle 110 \rangle$. The relaxed and unrelaxed configuration of the separated grains through three different cutting planes are given. In all figures the atoms colored by Common Neighbor Analysis (Green: fcc Ni; Red: hcp Ni; White: Ni with less than 12 neighbors; Purple: H) of the connected grain boundary.



(a) $c_0 = 0.0$



(b) $c_0 = 0.001$

Figure 2.10 – Atomic configurations of $\text{Ni}\Sigma_{99}(557)\langle 110 \rangle$. The relaxed and unrelaxed configuration of the separated grains through three different cutting planes are given. In all figures the atoms colored by Common Neighbor Analysis (Green: fcc Ni; Red: hcp Ni; White: Ni with less than 12 neighbors; Purple: H) of the connected grain boundary.

2.3. Simulation of the tensile strength and yield strength of grain boundaries

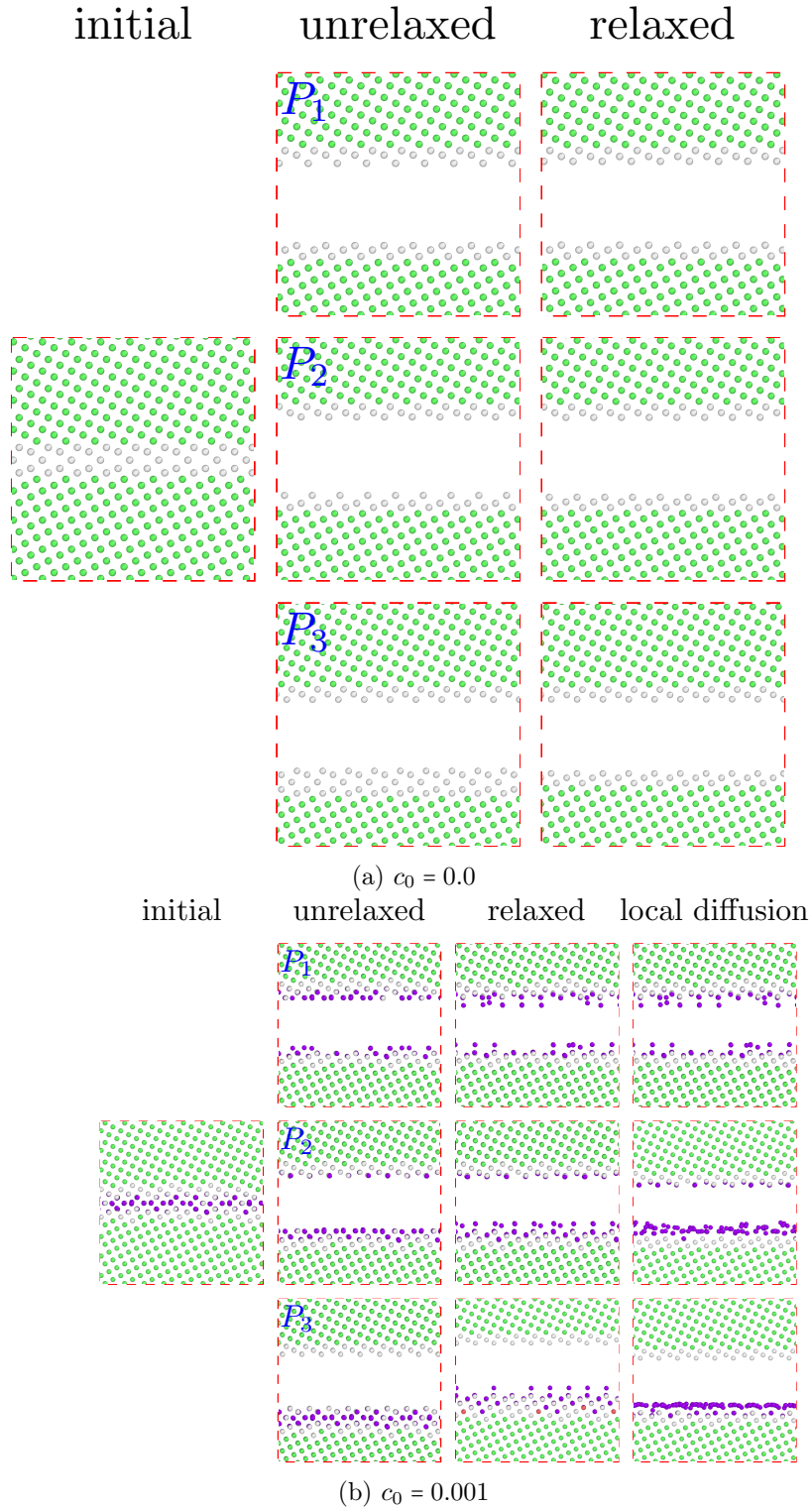


Figure 2.11 – Atomic configurations of $\text{Ni}\Sigma 5(120)\{100\}$. The relaxed and unrelaxed configuration of the separated grains through three different cutting planes are given. In all figures the atoms colored by Common Neighbor Analysis (Green: fcc Ni; Red: hcp Ni; White: Ni with less than 12 neighbors; Purple: H) of the connected grain boundary.

Chapter 2. Atomistic study of Hydrogen embrittlement of grain boundaries in Nickel

Table 2.7 – Unrelaxed and fully relaxed fracture energies (mJ/m^2) for the separation of GBs along different possible fracture planes. The minimum separation energy for each GB is highlighted in bold.

		$c_0 = 0$			$c_0 = 0.001$			$c_0 = 0.001(\text{local diffusion})$	
		γ_{fr}^u	γ_{fr}^r	(%)	γ_{fr}^u	γ_{fr}^r	(%)	γ_{fr}^r	(%)
Ni Σ 9	P_1	3625	3438	-5	3562	3377	-4.9	3377	-1.8
	P_2	4482	3437	-23	4462	3384	-24.1	3384	-1.5
	P_3	4753	3427	-27	4745	3437	-27	3370	-1.7
Ni Σ 19	P_1	3940	3589	-8.9	3674	3254	-11.5	3254	-9.3
	P_2	3940	3589	-8.9	3677	3254	-11.6	3254	-9.3
	P_3	4886	3589	-26.5	4732	3547	-25	3135	-12.6
Ni Σ 27	P_1	4305	3464	-19.5	4131	3649	-11.7	3483	0.5
	P_2	4312	3462	-19.7	4131	3649	-11.7	3483	0.6
	P_3	4823	3479	-28	4665	3862	-17.2	3582	3.0
Ni Σ 33a	P_1	4252	3426	-19.4	4576	4073	-11	3273	-4.5
	P_2	4376	3396	-22.4	4800	3724	-22.4	3019	-11.1
	P_3	4823	3479	-28	4665	3862	-22.8	3028	-13.0
Ni Σ 33b	P_1	3857	3314	-14.1	3655	3104	-15.1	3055	-7.8
	P_2	4236	3476	-18	4175	3358	-19	3274	-5.8
	P_3	4059	3306	-18.5	3979	3257	-18	2935	-11.2
Ni Σ 41	P_1	3942	3238	-17.8	3667	2932	-20	2482	-23.3
	P_2	4159	3238	-22.5	3922	3008	-23	2482	-23.3
	P_3	4121	3310	-19.7	3980	3557	-10.6	2482	-25.0
Ni Σ 99	P_1	4378	3718	-15.1	4853	3801	-21	3787	-1.9
	P_2	4162	3273	-21.3	4170	3191	-23	3162	-3.4
	P_3	4475	3756	-16	4484	3541	-21	3515	-6.4

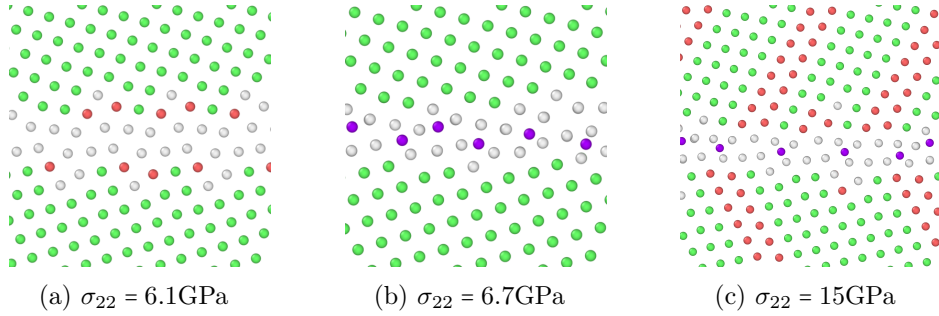


Figure 2.12 – Key atomic configurations of (a) H-free and (b) H-charged Ni Σ 9(221)(110) at room temperature, at the onset of the first plastic activity. (c) Configuration of the H-charged specimen subjected to tensile stress of $\sigma_{22} = 15\text{GPa}$. Atoms colored by Common Neighbor Analysis (Green: fcc Ni; Red: hcp Ni; White: Ni with less than 12 neighbors; Purple: H)

2.3. Simulation of the tensile strength and yield strength of grain boundaries

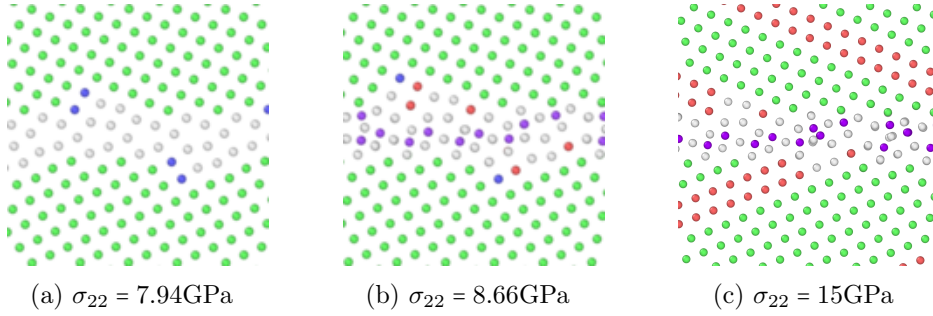


Figure 2.13 – Key atomic configurations of (a) H-free and (b) H-charged Ni Σ 19(331)(110) at room temperature, at the onset of the first plastic activity. (c) Configuration of the H-charged specimen subjected to tensile stress of $\sigma_{22} = 15\text{GPa}$. Atoms colored by Common Neighbor Analysis (Green: fcc Ni; Red: hcp Ni; White: Ni with less than 12 neighbors; Purple: H)

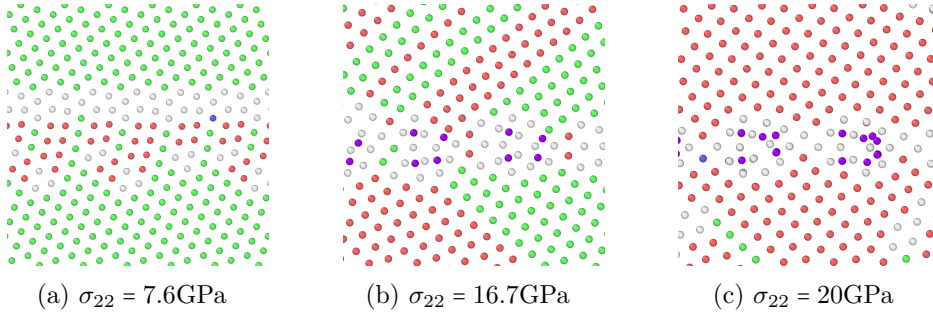


Figure 2.14 – Key atomic configurations of (a) H-free and (b) H-charged Ni Σ 27(115)(110) at room temperature, at the onset of the first plastic activity. (c) Configuration of the H-charged specimen subjected to tensile stress of $\sigma_{22} = 20\text{GPa}$. Atoms colored by Common Neighbor Analysis (Green: fcc Ni; Red: hcp Ni; White: Ni with less than 12 neighbors; Purple: H)

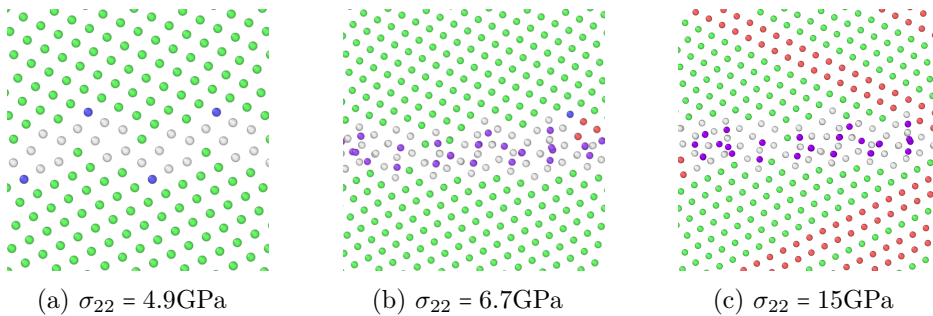


Figure 2.15 – Key atomic configurations of (a) H-free and (b) H-charged Ni Σ 33(441)(110) at room temperature, at the onset of the first plastic activity. (c) Configuration of the H-charged specimen subjected to tensile stress of $\sigma_{22} = 15\text{GPa}$. Atoms colored by Common Neighbor Analysis (Green: fcc Ni; Red: hcp Ni; White: Ni with less than 12 neighbors; Purple: H)

Chapter 2. Atomistic study of Hydrogen embrittlement of grain boundaries in Nickel

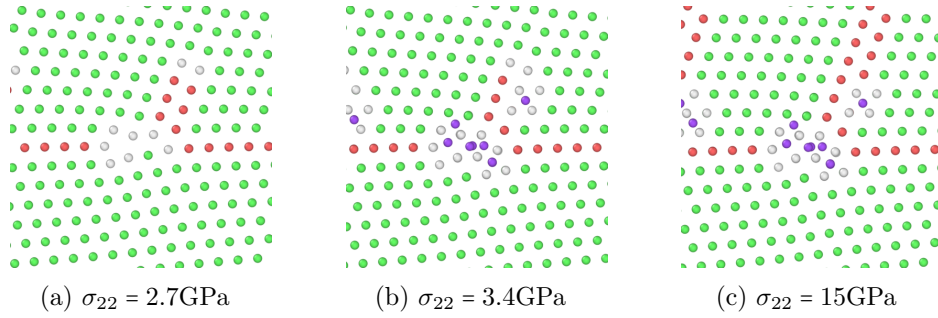


Figure 2.16 – Key atomic configurations of (a) H-free and (b) H-charged $\text{Ni}\Sigma_{33b}(554)\langle 110 \rangle$ at room temperature, at the onset of the first plastic activity. (c) Configuration of the H-charged specimen subjected to tensile stress of $\sigma_{22} = 15\text{GPa}$. Atoms colored by Common Neighbor Analysis (Green: fcc Ni; Red: hcp Ni; White: Ni with less than 12 neighbors; Purple: H)

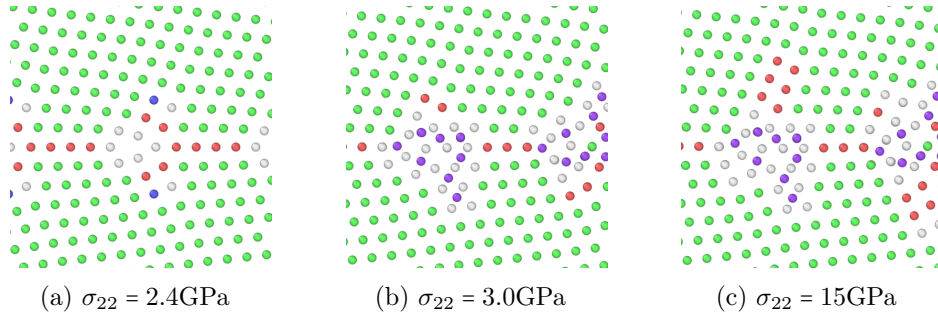


Figure 2.17 – Key atomic configurations of (a) H-free and (b) H-charged $\text{Ni}\Sigma_{41}(443)\langle 110 \rangle$ at room temperature, at the onset of the first plastic activity. (c) Configuration of the H-charged specimen subjected to tensile stress of $\sigma_{22} = 15\text{GPa}$. Atoms colored by Common Neighbor Analysis (Green: fcc Ni; Red: hcp Ni; White: Ni with less than 12 neighbors; Purple: H)

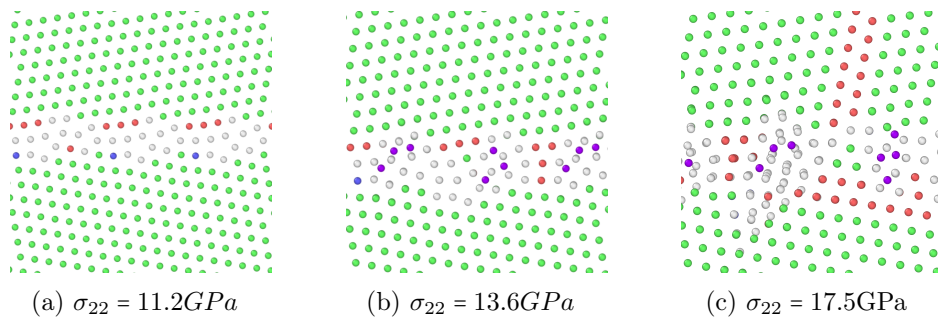


Figure 2.18 – Key atomic configurations of (a) H-free and (b) H-charged $\text{Ni}\Sigma_{99}(557)\langle 110 \rangle$ at room temperature, at the onset of the first plastic activity. (c) Configuration of the H-charged specimen subjected to tensile stress of $\sigma_{22} = 17.5\text{GPa}$. Atoms colored by Common Neighbor Analysis (Green: fcc Ni; Red: hcp Ni; White: Ni with less than 12 neighbors; Purple: H)

2.3. Simulation of the tensile strength and yield strength of grain boundaries

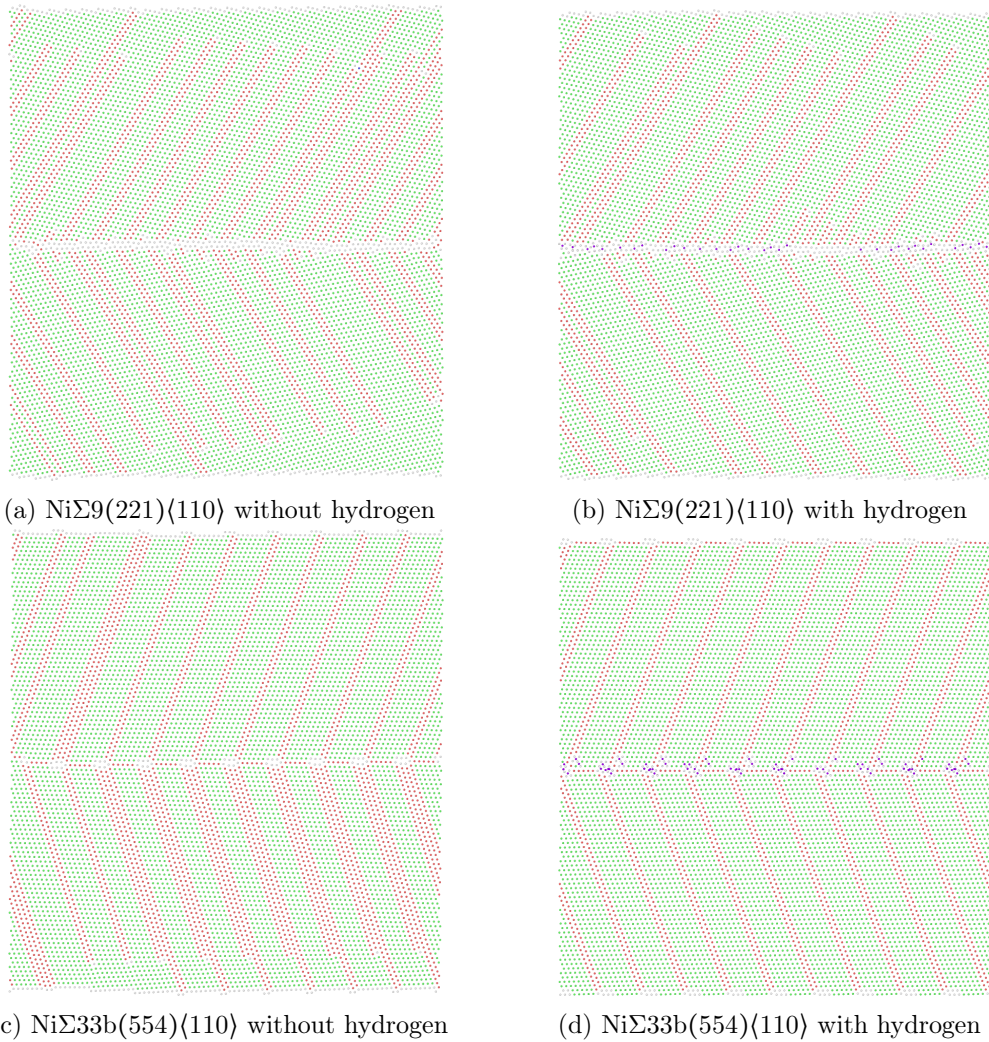


Figure 2.19 – (a) H-free and (b) H-charged specimenes containing $\text{Ni}\Sigma 33b(554)\langle 110 \rangle$ at room temperature, subjected to $\sigma_{22} = 15\text{GPa}$. (c) H-free and (d) H-charged specimens containing $\text{Ni}\Sigma 9(221)\langle 110 \rangle$ at temperature and tensile load. Atoms colored by Common Neighbor Analysis (Green: fcc Ni; Red: hcp Ni; White: Ni with less than 12 neighbors; Purple: H)

Chapter 2. Atomistic study of Hydrogen embrittlement of grain boundaries in Nickel

dashed lines in Fig. 2.3. In no cases do we find any crack nucleation or evidence of decohesion prior to dislocation emission. Furthermore, the presence of H has very little effect on the stress at which dislocation emission occurs, except in one case Ni Σ 27(115) \langle 110 \rangle where dislocation emission is significantly suppressed but still occurring well below the theoretical cohesive strength. The details of the dislocation emission vary from GB to GB, but the emphasis here is on when dislocation emission occurs and whether the emission is affected by segregated H. Figs. 2.12–2.18, show the atomic GB structures at the first points of GB reorganization, both with and without H. These results show that dislocation emission is the preferred response of each GB under tensile load, which is expected since intergranular fracture is not observed in pure Ni, and that H has no significant influence on the stress levels at which emission occurs.

Furthermore, all the grain boundaries with and without hydrogen continue emitting dislocation as the loading levels increase above the initial yield stress. Figs. 2.12(c)–2.18(c) show the structure around the GBs with segregated hydrogen atoms under tensile stresses higher than the yield stress. For Ni Σ 27(115) \langle 110 \rangle , and Ni Σ 99(557) \langle 110 \rangle boundaries, the applied tensile stresses in the Figure are $\sigma_{22} = 20\text{GPa}$ and $\sigma_{22} = 17.5\text{GPa}$, respectively, while for all other boundaries the stress in the Figure is $\sigma_{22} = 15\text{GPa}$. Fig. 2.19 show structure of the entire specimen, for the Ni Σ 9(221) \langle 110 \rangle and Ni Σ 33b(554) \langle 110 \rangle under $\sigma_{22} = 15\text{GPa}$ at $t = 50\text{ps}$, respectively. The emitted dislocations exit the top and bottom surfaces, which are thus roughened. Extensive twinning can be seen, which is not necessarily physical but the point is that there is no crack nucleation.

2.3.2 Discussion

In all simulations reported here, the fracture energies and theoretical cohesive strengths of the boundaries are not significantly reduced by the presence of the hydrogen atoms. Furthermore, in all cases, the emission of dislocations occurs well before decohesion. And, aside from the case of Ni Σ 27(115) \langle 110 \rangle , no significant change in σ_y is observed in the H-charged specimens. Thus we find little or no evidence that segregated hydrogen atoms can facilitate the nucleation of the cracks along GBs in Ni under conditions where embrittlement is typically observed in experiments. Below we discuss different features and implications of this conclusion.

The main material parameter controlling nucleation of a crack is the theoretical cohesive strength $\hat{\sigma}$. If the tensile stress somewhere along the GB can reach $\hat{\sigma}$, a crack can nucleate. After nucleation, if the local stress field remains high, the energy release rate may be well above both the fracture energy for cleavage and the unstable stacking fault energy (γ_{usf}) for dislocation emission. Although recent simulation studies suggest otherwise [98], a crack could then grow dynamically under such high-stress conditions rather than blunt out and stop. As the crack grows longer, the applied stress intensity can increase even when the overall applied stresses are decreasing as the crack tips move away from the original

2.3. Simulation of the tensile strength and yield strength of grain boundaries

high-stress nucleation point, and this could allow crack growth to continue. At present, however, our nanoscale assessment of fracture behavior is mainly limited to quasistatic situations, with cleavage and blunting governed by the Griffith (fracture energy) and Rice [99] (unstable stacking fault energy) criteria, respectively. And, as alluded to above, recent simulations show that when a dynamic cleavage crack enters a material that is quasistatically ductile (emits dislocations under quasistatic loading) then the dynamic crack emits dislocations and stops growing. Thus, based on quasistatic considerations, our analysis here and in our earlier work shows that the presence of H along symmetric tilt grain boundaries in Ni does not significantly change either the cohesive strength, fracture energy, or induce a change from emission to cleavage at a crack front. Thus, the nanoscale mechanisms of crack nucleation and growth at GBs are similar in Ni and Ni-H. Ni itself does not show intergranular fracture, and hence results here do not point to the creation of intergranular fracture due to pre-segregated H to GBs in Ni. These analyses are at the nanoscale. One might put aside nanoscale details in favor of a larger-scale analysis of fracture, as discussed next.

The role of H could be to inhibit or change mechanisms of ductile failure, e.g. H could change the plastic flow behavior of the bulk matrix so as to inhibit void nucleation, growth, and/or coalescence. Recent experiments in steels suggest that, in the presence of H, nanovoids are formed along GBs and that coalescence of these nanovoids could lead to embrittlement fracture along grain boundaries [31]. Mechanisms for this behavior remain to be uncovered, however [47, 83].

Another large-scale perspective assumes some effective crack tip cohesive behavior, which represents all of the complex nano/micro scale phenomena that exists along with the bulk plasticity of the surrounding metal. Numerical simulations of such cohesive cracks growing through power-law-plasticity metals show that the steady-state toughness enhancement due to plasticity, $\Gamma/\gamma_{\text{fr}}$, depends sensitively on the ratio $\hat{\sigma}/\sigma_y^{\text{B}}$ [100, 101] and on the power-law hardening rate N . If the introduction of H could decrease $\hat{\sigma}$ and/or γ_{fr} or increase σ_y^{B} , then the macroscopic toughness Γ could decrease substantially if the ratio $\hat{\sigma}/\sigma_y^{\text{B}}$ decreases below $\sim 3 - 5$. The nanoscale material parameters here suggest $\hat{\sigma}/\sigma_y^{\text{B}} \sim 15 - 40$, both with and without H along the GBs, so that cohesive cracks in a power-law plastic matrix should not be embrittled. However, the increase in plastic flow stress in small volumes and/or under high strain or stress gradients around crack tips leads to much higher flow stresses at the micron-scale, which facilitates fracture [101, 102, 103, 104]. In specific numerical studies, crack propagation becomes possible for larger ratios of $\hat{\sigma}/\sigma_y^{\text{B}}$. For instance, Discrete Dislocation Dynamics simulations show crack growth for $\hat{\sigma}/\sigma_y^{\text{B}} \sim 10 - 12$. However, the toughness varies much more smoothly with $\hat{\sigma}/\sigma_y^{\text{B}}$ than in standard size-independent plasticity models so that no abrupt embrittlement would be anticipated for modest changes in material properties. Plastic flow is also rate-dependent, with increasing plastic flow stress σ_y^{B} with increasing strain rate, and this could affect fracture [105, 106, 107]. Rate-dependent flow could thus reduce $\hat{\sigma}/\sigma_y^{\text{B}}$ further, corresponding to lower predicted fracture toughness. However, both rate- and size-effects

Chapter 2. Atomistic study of Hydrogen embrittlement of grain boundaries in Nickel

should operate for H-free materials (e.g. pure Ni or Ni alloys), and such materials are not low-toughness. The modest effects of H segregated to GBs (modest decreases in cohesive strength and fracture energy) that are caused here by H segregation to grain boundaries do not suggest significant embrittlement effects even when larger-scale phenomena are considered.

It may be useful to combine all of the effects noted above (rate- and size-dependent plasticity; reductions in cohesive strength and fracture energy due to H) into appropriate computational models so as to quantitatively assess the total effects of segregated H on toughening. This would be especially useful if the presence of H could lead to crack nucleation that creates a dynamic situation that would not prevail in the absence of H. Such computations neglect, however, the blunting of cracks by dislocation emission that should inhibit embrittlement, and the origin of easier crack nucleation in the presence of H is not indicated by the present results.

2.4 Fracture simulations

2.4.1 Theoretical framework

In this section, a brief overview of the Griffith and Rice criteria for cleavage and dislocation emission, respectively, and some subtleties in their application to GB problems are discussed. The influence of interstitial hydrogen atoms on the key parameters in each criterion is then also presented.

We consider a symmetric tilt grain boundary with the tilt angle of ψ containing an intergranular crack, as illustrated in Fig. 2.20. The stiffness tensor of the material in the coordinate system $\{x_i\}$ ($i = 1, 2, 3$) is \mathbf{C} . The deformation mode at the crack tip is determined by the competition between cleavage and dislocation emission mechanisms. According to Griffith theory, cleavage occurs when the energy release rate at the crack tip $G = \alpha K_{Ic}^2$ reaches the critical value, $G_c = \gamma_i = \gamma_{s_1} + \gamma_{s_2} - \gamma_{GB}$, where γ_{s_i} ($i = 1, 2$), and γ_{GB} are the energies of the surfaces made after cleavage and grain boundary energy, respectively. The critical stress intensity factor for cleavage can be determined as

$$K_{Ic} = \sqrt{\frac{\gamma_i}{\alpha}} \quad (2.5)$$

The calculation of $\alpha(\mathbf{C}, \psi)$ within anisotropic linear elasticity is well-established, and recently presented in Ref. [108]. The surface and interface energies are functions of the crystallographic orientation of the GB and the Hydrogen concentration in the GB.

An important subtlety in using Eq. (2.5) is that the value for γ_i is required but the proper fracture surface for many intergranular crack problems is not well defined. The lowest-energy surface may be kinked (non-flat), which changes the local crack tip stress

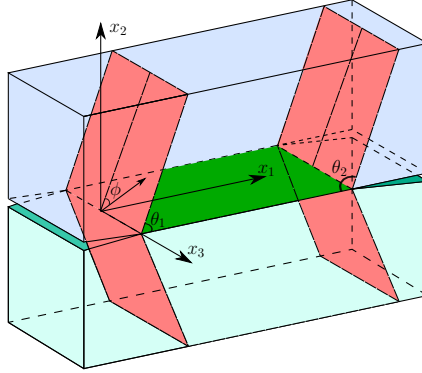


Figure 2.20 – Schematic diagram of a crack along a symmetric tilt boundary, showing the differences in slip plane orientation at the two crack tips.

intensity. The grain boundary structure can also have a long periodic repeat distance, so that the crack could be “trapped” in some local region of the GB where the local energy to extend the crack exceeds the average surface energy. Thus, the critical K_{Ic} computed by the Griffith theory may not be accurate, and could be lower or higher than an assessment based on an assumed fracture surface. The presence of hydrogen makes this problem even more complicated. Hydrogen generally decreases both the surfaces energy and the GB energy, and it is thus not guaranteed that $\gamma_i = \gamma_{s_1} + \gamma_{s_2} - \gamma_{GB}$ decreases in all cases. We will consider these subtleties below.

The emission of a dislocation can occur at the crack tip when the stress intensity K_I reaches the critical value K_{Ie} required for a dislocation to be nucleated on a slip system available at the crack tip [99]. For cases where a slip system exists that contains the crack front line, emission of a straight dislocation along the length of the crack can occur, and this is generally the easiest (lowest K_{Ie}) or most-ductile situation. In this case, the critical K_{Ie} is

$$K_{Ie} = \sqrt{\beta(\theta, \phi, \mathbf{C}, \psi)\gamma_{\text{usf}}} \quad (2.6)$$

where θ , ϕ , and γ_{usf} are the angle between the slip and crack planes, the complementary angle of the crack front and the slip direction, and the unstable stacking fault, respectively. Details for calculating β within anisotropic elasticity are also given in [108]. The same formulation can be used for the case of the symmetric tilt GBs in cubic metals, which is the case studied here. The unstable stacking fault energy is a function of hydrogen concentration (see, for instance, [38]). However, the slip planes of interest are usually inclined with respect to the grain boundary plane so that H may exist only very locally at the crack tip along the grain boundary, and it is unclear whether the H will influence the unstable stacking fault energy that controls the emission. However, in any case, emission is into one of the two grains, and hence the unstable stacking fault energy of the bulk

Chapter 2. Atomistic study of Hydrogen embrittlement of grain boundaries in Nickel

material is probably the relevant quantity. In this work, we use the value of γ_{usf} for pure Ni in all cases, which should provide a lower bound on emission since H increases the unstable stacking fault energy for the Ni–H system [38].

An important feature of intergranular fracture is the directional anisotropy of a crack which is observed in experiments [109, 110] and simulations [111, 112, 113]. This feature can be explained by means of Rice theory [99]. Since K_{Ie} depends on θ and ϕ , a finite crack with two cracks tips along the same GB has two different values for θ and ϕ . One crack tip may show ductile behavior, $K_{Ie} < K_{Ic}$, while the opposite crack tip may show brittle fracture, $K_{Ic} < K_{Ie}$. Here, we define “emission” to refer to cases where emission is theoretically predicted to be favored over cleavage. Likewise, we define “cleavage” to refer to cases where cleavage is theoretically predicted to be favored over emission. Since Ni, and most other fcc metals, do not show intergranular failure in the absence of H, we can safely assume that brittle crack growth in a “cleavage” cases alone is not sufficient for embrittlement. We thus focus mainly on the behavior of the “emission” cases, searching for a ductile-to-brittle transition.

Based on the computed binding energies and small magnitudes of H–H interactions, we can construct GB structures with equilibrium segregation of H. We use a simple solution model to compute the concentration c_i of H segregated to sites of type i with binding energy $E_{\text{int},i}$ as

$$c_i = \frac{c_0 \exp(-E_{\text{int},i}/k_B T)}{1 + c_0 \exp(-E_{\text{int},i}/k_B T)} \quad (2.7)$$

where T is the temperature, c_0 is the bulk concentration of H atoms, corresponding to some imposed H chemical potential during charging, and k_B is Boltzmann’s constant. The simple solution model neglects specific entropy contributions beyond the entropy of mixing. Given a desired concentration c_i , specific atomic sites of type i are occupied with H by selecting a random number in the domain $R \in [0, 1]$ and occupying the specific site if $R < c_i$.

For cleavage fracture, we require the initial grain boundary energy γ_{GB} and the final energies of the two new fracture surfaces γ_{s1}, γ_{s2} that are created by the cleavage. These quantities combine to yield $\gamma_i = \gamma_{s1} + \gamma_{s2} - \gamma_{GB}$ that enters the Griffith theory for cleavage. The GB energies without H are easily computed. In the presence of H, we can also compute the total energy knowing the H/GB interaction energies $E_{\text{int},i}$ and the equilibrium concentrations c_i for all site types i per unit of GB area. The final surface energies γ_{s1}, γ_{s2} depend, however, on the precise fracture surface, which is not defined a priori. Imagining fracture to occur by the separation across a specified planar surface, we can consider several possible planar surfaces and compute the energy $\gamma_{s1} + \gamma_{s2}$ for each planar surface. We compute the energy for both rigid separation and following atomistic relaxation of the separated surfaces to examine the effects of such relaxations. We then select the lowest energy among all of these choices as the final surface energy

used in the theory. For each GB, the three different choices of planar surface are shown in Figs. 2.4–2.6 and the resulting final surface energies are shown in Table 2.8, for cases with and without H. Table 2.8 shows that the variations in γ_i versus choice of separation plane are generally not large for the fully relaxed surfaces. The largest differences upon relaxation occur for those surfaces with high unrelaxed energies. More interestingly, the presence of H does not lead to significant changes in the fracture energy γ_i , except for the case of the Ni(120) Σ 5(100) GB, which is expected to be brittle even without H.

The above calculations ignore the possibility of H diffusion near the crack tip during the (possible) crack opening. These results are thus the “fast” limit considered by Rice [114], in contrast to the “slow” limit where the final fracture surfaces are considered to have full equilibrium H concentrations of the surfaces. The “slow” limit is achieved by H diffusion, and at very low bulk H concentrations would require diffusion over significant distances continuously during crack growth. Here, we consider another more realistic limit wherein all H that is near the fracture surface, due to having been segregated to the GB prior to fracture, can diffuse via a few atomic hops to some lower-energy position on the fracture surface. Such diffusion could be envisioned to occur right at the crack tip during the opening process. To examine this “local diffusion” case, we have started from the relaxed separated fracture surfaces and then moved all subsurface H atoms to nearby low-energy sites on the fracture surface. These atomic configurations are shown in Fig. 2.4–2.6. The entire system is then relaxed to obtain new energies γ_{s1}, γ_{s2} and hence new fracture energies γ_i , as shown in Table 2.8. We find very limited changes in the fracture energy due to this local diffusion, especially for the lowest fracture-energy cases that control the fracture behavior.

Figs. 2.4–2.6 shows the structure of the grain boundaries of interest in the presence and absence of H atoms. The relaxed and unrelaxed states of the separated grain boundaries for different cutting planes are given in these Figures as well. It should be noted that since the interaction energy of the H atoms with the twin boundary is extremely low, the amount of H atoms along the boundary is low such that the separation energy in the H-charged cases is identical to that of the H-free case. Thus, local diffusion effects are also insignificant.

2.4.2 Simulation details

With the above baseline of GB and fracture energies with and without H, we now examine the explicit simulation of crack-tip processes in molecular statics. We construct simulation cells of size $l_1 \in [420\text{\AA}, 490\text{\AA}]$, $l_2 \in [400\text{\AA}, 500\text{\AA}]$ and $l_3 \in [17\text{\AA}, 20\text{\AA}]$ containing a GB (Ni Σ 9(221) \langle 110 \rangle , Ni Σ 99(557) \langle 110 \rangle , Ni Σ 5(120) \langle 100 \rangle or Ni Σ 3(111) \langle 110 \rangle) along the central plane $x_2 = 0$. For all grain boundaries except the twin boundary, we insert a crack in the x_1x_3 plane of the grain boundary with crack front along $[1\bar{1}0]$ by removing three atomic layers. For the twin, using a blunted crack leads to unphysical results and so a sharp

Chapter 2. Atomistic study of Hydrogen embrittlement of grain boundaries in Nickel

Table 2.8 – Unrelaxed and fully relaxed fracture energies (mJ/m^2) for the separation of GBs along different possible fracture planes. The minimum separation energy for each GB is highlighted.

		$c_0 = 0$			$c_0 = 0.001$			$c_0 = 0.001(\text{local diffusion})$	
		unrelaxed	relaxed	(%)	unrelaxed	relaxed	(%)	relaxed	(%)
Ni Σ 9	P_1	3625	3438	5	3562	3377	4.9	3377	0
	P_2	4482	3437	23	4462	3384	24.1	3384	0
	P_3	4753	3427	27	4745	3437	27	3370	1.9
Ni Σ 99	P_1	4378	3718	15.1	4853	3801	21	3787	0.5
	P_2	4162	3273	21.3	4170	3191	23	3162	0.9
	P_3	4475	3756	16	4484	3541	21	3515	0.7
Ni Σ 5	P_1	4145	3716	10.3	3020	2135	29.3	2135	0.0
	P_2	4145	3716	10.3	3122	2145	31.3	2257	-5.2
	P_3	5176	3732	27.9	4638	2909	37.3	2208	24.9

Table 2.9 – Geometrical parameters describing slip orientations in grains adjacent to each grain boundary.

GB	case	$\phi(^{\circ})$	$\theta(^{\circ})$
Ni Σ 3(111)(110)	cleavage	60	109.5
	emission	0	70.5
Ni Σ 9(221)(110)	cleavage	60	125
	emission	0	55
Ni Σ 99(557)(110)	cleavage	60	103
	emission	0	77
Ni Σ 5(120)(100)	cleavage	45	N.A.
	emission	45	N.A.

crack is inserted by artificially eliminating atomic interactions across the crack faces. For this crack geometry, all cases except Ni Σ 5(120)(100) have a slip plane that allows for the emission of straight dislocations from the crack tip. We chose these grain boundaries to examine the possible role of segregated hydrogen atoms for inducing ductile-to-brittle transition by suppressing the *easy* slips. For the cases with H atoms, we saturate the binding sites of the crack faces at the equilibrium concentrations c_i according to Eq. (2.7). To study the directional anisotropy of the intergranular cracks, we consider crack growth in both emission and cleavage directions, and both directions for the Ni Σ 5(120)(100) GB. The simulation cell is then subjected to incremental K -field loading by displacing all atoms within 10Å of the outer cell boundary according to the asymptotic continuum solution for a semi-infinite crack in an anisotropic linear elastic symmetric bicrystal. After each increment of loading, the boundary of the specimen is held fixed and the remaining atoms in the simulation cell are relaxed to the minimum total energy of the system using the conjugated gradient method [95]. The relevant geometric parameters describing the slip in the grains are tabulated in Table 2.9.

2.4. Fracture simulations

Table 2.10 – Theoretical cleavage and emission stress intensities for all grain boundaries studied here. The predicted behavior (cleavage or emission) is indicated, as dictated by the lower of the two predicted stress intensities as highlighted in bold. The simulation results are tabulated as well.

	c_0	Rice theory (MPa $\sqrt{\text{m}}$)	Griffith theory (MPa $\sqrt{\text{m}}$)	simulation results (MPa $\sqrt{\text{m}}$)
Ni Σ 3(111)(110)	0.0	1.01	1.03	1.20 cleavage
Ni Σ 3(111)(110)	0.001	1.01	1.03	1.20 cleavage
	0.0	0.38	1.03	0.62 emission
	0.001	0.38	1.03	0.58 emission
	0.0	1.500	0.98	1.49 rearrangement
Ni Σ 9(221)(110)	0.001	1.50	0.97	1.39 cleavage
	0.0	0.64	0.98	0.72 emission
	0.001	0.64	0.97	0.93 emission of two partials
	0.0	1.41	1.00	1.52 rearrangement
Ni Σ 99(557)(110)	0.001	1.41	0.92	1.07 cleavage
	0.0	0.62	1.00	0.63 emission
	0.001	0.62	0.92	0.58 emission
	0.0	N.A.	0.92	0.91 cleavage
Ni Σ 5(120)(100)	0.001	N.A.	0.75	0.65 cleavage
	0.0	N.A.	0.92	1.38 cleavage
	0.001	N.A.	0.75	1.20 cleavage

Note that we use H segregation computed at finite temperature but execute the simulations at zero T. This ensures that there is no diffusion during the simulation, nor any other thermally activated behavior, so that the simulation probes the energetics of fracture with no time dependence. Performing finite-T molecular dynamics would introduce a time scale into the problem, and all results would then depend on the simulation time and/or loading rate. Since MD loading rates are unrealistically high, as compared to experiments, the finite-T/finite-time results would provide little or no additional insights beyond the T=0K simulations. It is then clear that, for comparison with theory, the relevant interface energy in the Griffith theory is the minimum value of γ_i without local diffusion as shown in Table 2.8.

2.4.3 Results

Table 2.10 summarizes the results of the theoretical predictions of the Griffith and Rice theories as well as the simulation results. The values for the theoretical cleavage loads are obtained by inserting the corresponding information in Table 2.8 into Eq. (2.5) while the theoretical emission loads are calculated by incorporating the information in Tables 2.2 and 2.9 into Eq. (2.6).

Figs. 2.21 and 2.22 show key atomistic configurations for the sharp intergranular crack along $[11\bar{2}]$, and $[\bar{1}\bar{1}2]$ directions of twin boundary, respectively. The theoretical cleavage load both with and without hydrogen is 1.03 MPa $\sqrt{\text{m}}$ since H binds weakly to this

Chapter 2. Atomistic study of Hydrogen embrittlement of grain boundaries in Nickel

twin. For the case in which the crack is along $[11\bar{2}]$ direction, the theoretical emission load is $1.01\text{MPa}\sqrt{\text{m}}$, quite close but less than the theoretical cleavage load. In the H-free specimen, the crack starts to propagate at $1.20\text{MPa}\sqrt{\text{m}}$, slightly higher than the emission/cleavage predictions. For the H-charged case, with hydrogen atoms covering the crack faces, an initial $K=0.80\text{MPa}\sqrt{\text{m}}$ is applied to avoid closure of the crack. In this case, cleavage occurs at $1.20\text{MPa}\sqrt{\text{m}}$, equal to the critical cleavage load for the H-free case. This result is expected because the twin boundary does not absorb any H atom. In the case in which the crack is along the theoretically ductile direction $[\bar{1}\bar{1}2]$, the predicted emission load is $0.38\text{MPa}\sqrt{\text{m}}$, whereas the simulations without H show emission at $0.624\text{MPa}\sqrt{\text{m}}$. With H, the emission load decreases slightly to $0.58\text{MPa}\sqrt{\text{m}}$. Both with and without H, the crack tip emits several partial dislocations. H thus does not change the ductile/brittle nature of the twin boundary, with most effects here associated with H absorbed on the pre-existing crack faces rather than with H segregated to the twin boundary itself.

Figs. 2.23 and 2.24 show key atomistic configurations for the intergranular crack along the $\text{Ni}\Sigma 9(221)\langle 110 \rangle$ boundary for the two directions of cracking, respectively. For the theoretical cleavage case, the predicted cleavage load decreases from $0.98\text{MPa}\sqrt{\text{m}}$ in pure Ni to $0.97\text{MPa}\sqrt{\text{m}}$ in the presence of H, both less than the emission load of $1.50\text{MPa}\sqrt{\text{m}}$. Thus, cleavage is predicted with and without H. The simulations show that crack behavior is more complicated than a simple cleavage process. In pure Ni, a tiny partial cleavage starts at $0.496\text{MPa}\sqrt{\text{m}}$ but atoms at the crack tip rearrange and suppress continued cleavage. At a much higher load of $1.49\text{MPa}\sqrt{\text{m}}$, dislocations are emitted ahead of the crack tip, thus cleavage does not occur in this case - this theoretical cleavage case is in fact ductile. With H, a tiny partial cleavage starts at $0.544\text{MPa}\sqrt{\text{m}}$ followed by emission of dislocations at $1.10\text{MPa}\sqrt{\text{m}}$ but eventually the crack faces cleave at $1.39\text{MPa}\sqrt{\text{m}}$. This ductile-to-brittle transition for a case expected to be brittle without H may be explained if H reduces lattice trapping at the crack tip (see Discussion). For the theoretical emission case, the predicted emission load is $0.64\text{MPa}\sqrt{\text{m}}$ and pure Ni shows emission at $0.72\text{MPa}\sqrt{\text{m}}$, within the typical accuracy of the emission model. With H, leading and twinning partials are emitted at the same time at a much higher load of $0.928\text{MPa}\sqrt{\text{m}}$. H thus delays emission, but the emission load remains below the predicted cleavage load of $0.97\text{MPa}\sqrt{\text{m}}$. The difference is small, however, indicating that H could push this boundary close to a transition from ductile-to-brittle, but no actual transition is observed in these simulations. The origin of the increase in the emission load is also not understood within the context of the emission theory, which does not account for any H-induced phenomena occurring right at the crack tip.

Figs. 2.25 and 2.26 show key atomistic configurations for the intergranular crack along the $\text{Ni}\Sigma 99(557)\langle 110 \rangle$ GB for the two directions of cracking, respectively. For the predicted cleavage case, the cleavage load decreases from $1.00\text{MPa}\sqrt{\text{m}}$ in pure Ni to $0.92\text{MPa}\sqrt{\text{m}}$ in the presence of H. Simulations in pure Ni show partial cleavage at $0.912\text{MPa}\sqrt{\text{m}}$, followed by some atomic rearrangements at the crack tip, with cleavage finally occurring

at $1.52 \text{ MPa}\sqrt{\text{m}}$. In the presence of H, the final cleavage load is reduced to $1.072 \text{ MPa}\sqrt{\text{m}}$, approaching the predicted values, with the H atoms preventing the local rearrangement at the crack tip. For the predicted emission case, simulations for pure Ni show emission at $0.624 \text{ MPa}\sqrt{\text{m}}$ which is quite close to the predicted value of $0.62 \text{ MPa}\sqrt{\text{m}}$. With H, the emission load is reduced to $0.576 \text{ MPa}\sqrt{\text{m}}$, slightly lower than the predicted value. As noted, distortions and energy of H near the crack tip are not included in the emission theory, and hence some deviations between simulation and emission theory can be expected. In any case, however, no ductile-to-brittle transition is observed due to the introduction of H into this GB.

Figs. 2.27 and 2.28 show key atomistic configurations for the intergranular crack along the $\text{Ni}\Sigma 5(120)(100)$ for the two crack directions, respectively. Recall that for this boundary there are no slip planes containing the crack front so that any emission is on oblique planes, which requires higher loads and which is also outside the scope of the emission theory used here. Such three-dimensional behavior is beyond the scope of this work and so our simulations use short crack front lengths and are quasi-2d so as to suppress the oblique emission. Both crack directions are thus expected to be "cleavage" cases. The predicted cleavage load is $0.92 \text{ MPa}\sqrt{\text{m}}$ in pure Ni and decreases to $0.75 \text{ MPa}\sqrt{\text{m}}$ in the presence of H. Simulations along $[2\bar{1}0]$ show partial cleavage at $0.75 \text{ MPa}\sqrt{\text{m}}$ in pure Ni followed by rearrangement of the crack tip atoms around $0.87 \text{ MPa}\sqrt{\text{m}}$. This rearrangement is a result of the tendency of the crack tip to emit oblique dislocation loops. Cleavage then proceeds at $0.91 \text{ MPa}\sqrt{\text{m}}$, close to the predicted value. With H, partial cleavage starts at $0.32 \text{ MPa}\sqrt{\text{m}}$ followed by cleavage at $0.51 \text{ MPa}\sqrt{\text{m}}$. This reduction in the cleavage load is strong evidence of the suppression of oblique dislocation emission by H atoms. For the crack along the opposite direction, partial cleavage occurs at $0.99 \text{ MPa}\sqrt{\text{m}}$ in pure Ni, followed by atomic rearranged at $1.04 \text{ MPa}\sqrt{\text{m}}$ and cleavage at $1.2 \text{ MPa}\sqrt{\text{m}}$. With H, rearrangements occur at $0.90 \text{ MPa}\sqrt{\text{m}}$ followed by cleavage at $1.14 \text{ MPa}\sqrt{\text{m}}$, which is slightly lower than that of the pure Ni but larger than the predicted value. No ductile-to-brittle transition is observed due to the introduction of H into this GB, and H generally facilitates cleavage, consistent with the trend of the theory.

2.4.4 Discussion of the fracture simulations

The simulations show that no ductile-to-brittle transition is observed for the predicted ductile cracks in the presence of segregated hydrogen atoms along any of the GBs studied here. However, hydrogen does make cleavage easier for crack growth in the intrinsically brittle directions. In the particular case of $\text{Ni}\Sigma 9(221)(110)$, the theoretically-brittle case is actually ductile, and the presence of H leads to the expected cleavage/brittle behavior. In the case of the twin boundary, which has no absorbed H, the cleavage load remains unaltered. These observations indicate that hydrogen has limited embrittling effects due to a change in the crack tip behavior, but can help intergranular fracture to be more favorable in theoretically brittle cases. These results, except the case of $\text{Ni}\Sigma 9(221)(110)$,

Chapter 2. Atomistic study of Hydrogen embrittlement of grain boundaries in Nickel

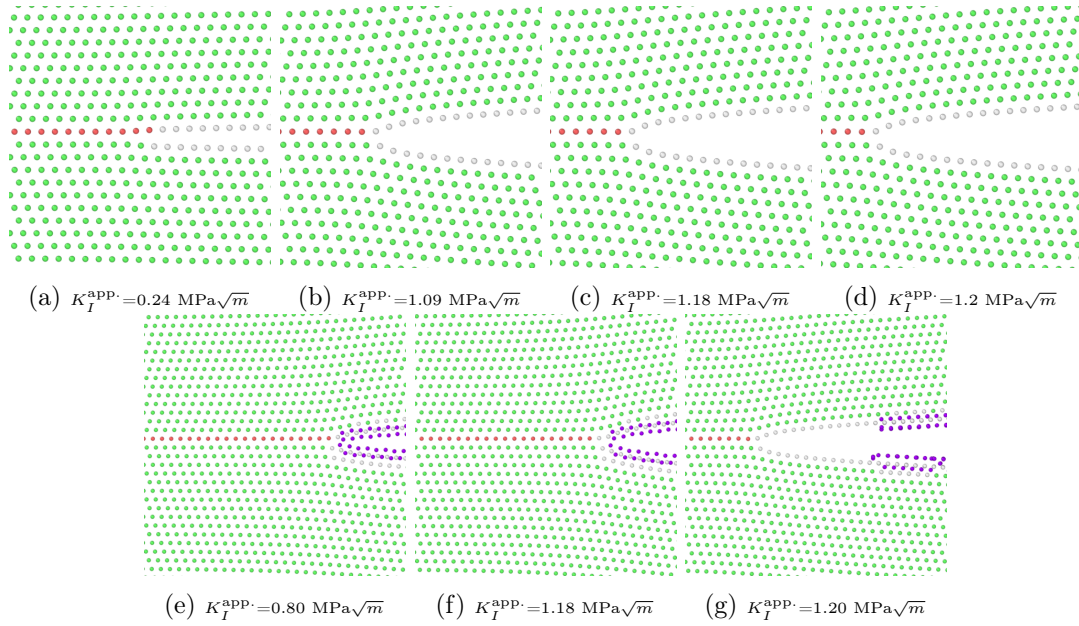


Figure 2.21 – Sharp crack tip atomic structure at load levels where various events occur in the simulations of $\text{Ni}\Sigma 3(111)\langle 110 \rangle$ along $[11\bar{2}]$ direction. Atoms colored by Common Neighbor Analysis (Green: fcc Ni; Red: hcp Ni; White: Ni with less than 12 neighbors; Purple: H)

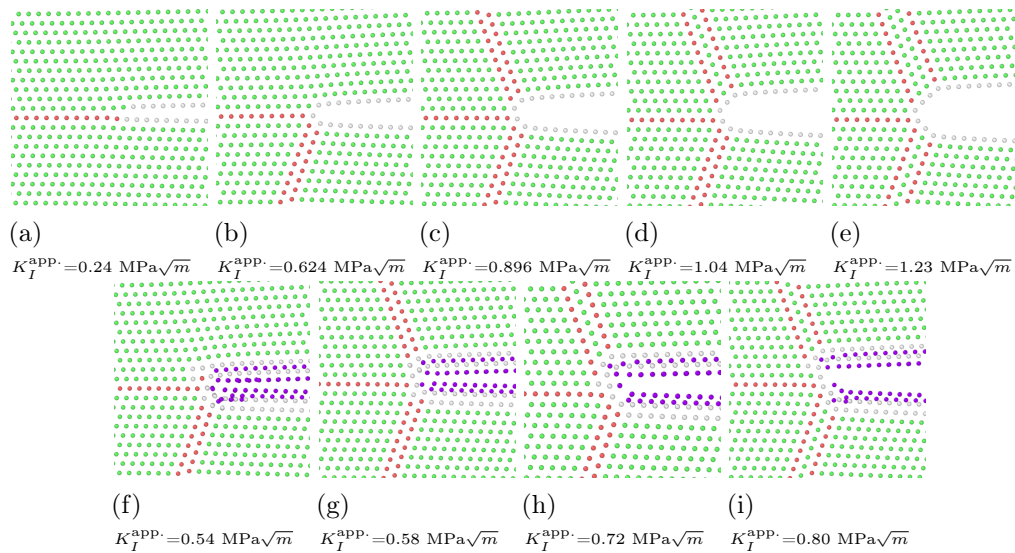


Figure 2.22 – Crack tip atomic structure at load levels where various events occur in the simulations of $\text{Ni}\Sigma 3(111)\langle 110 \rangle$ along $[\bar{1}\bar{1}2]$ direction. Atoms colored by Common Neighbor Analysis (Green: fcc Ni; Red: hcp Ni; White: Ni with less than 12 neighbors; Purple: H)

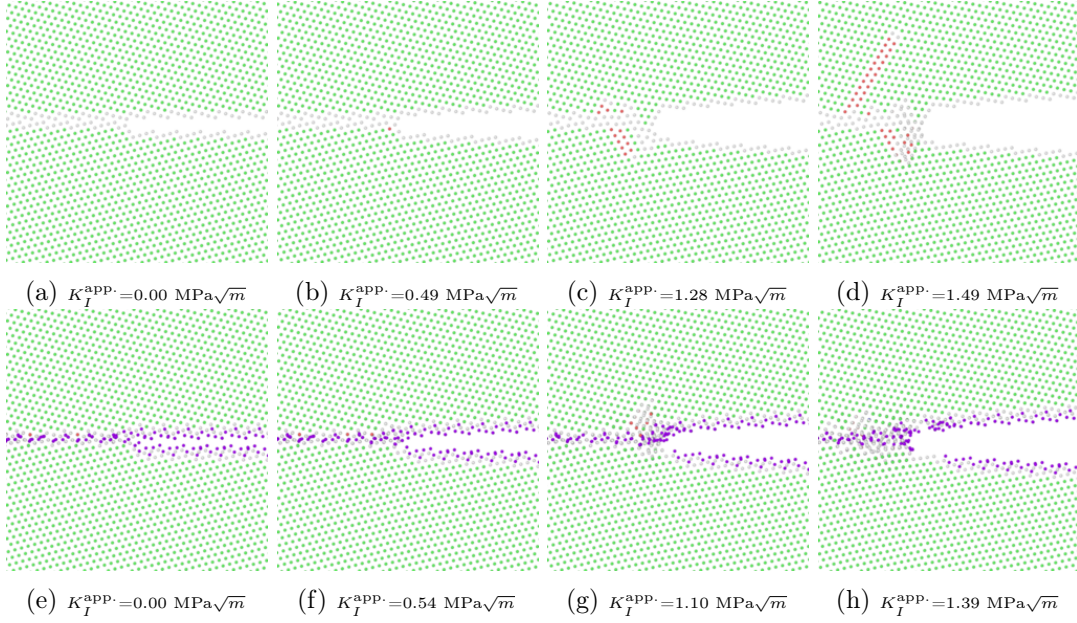


Figure 2.23 – Crack tip atomic structure at load levels where various events occur in the simulations of $\text{Ni}\Sigma 9(221)\langle 110 \rangle$ along the theoretically cleavage favorable direction. Atoms colored by Common Neighbor Analysis (Green: fcc Ni; Red: hcp Ni; White: Ni with less than 12 neighbors; Purple: H)

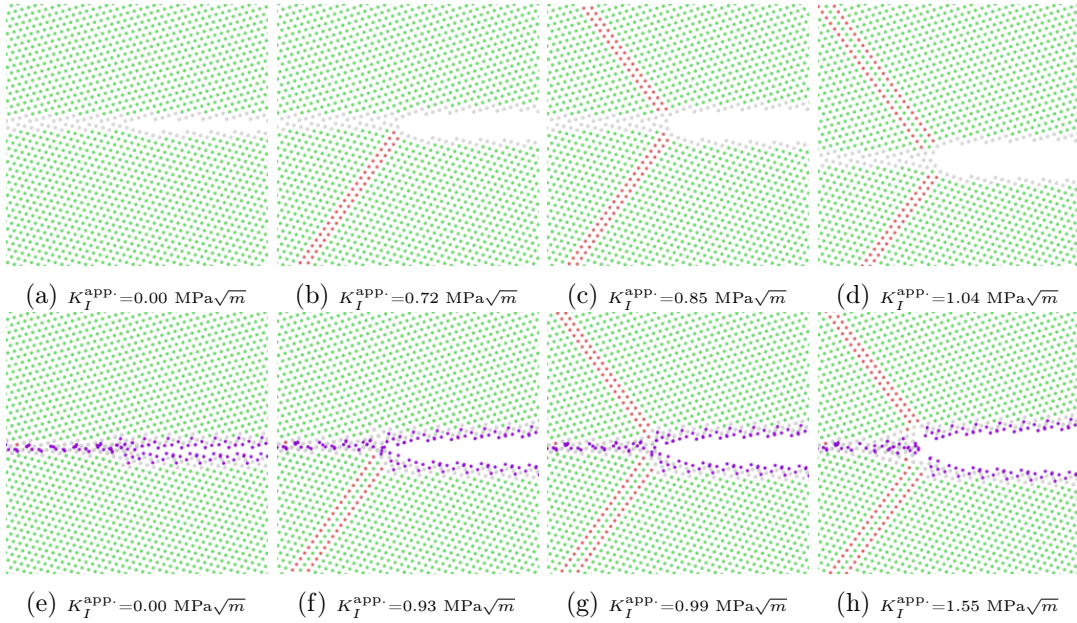


Figure 2.24 – Crack tip atomic structure at load levels where various events occur in the simulations of $\text{Ni}\Sigma 9(221)\langle 110 \rangle$ along the theoretically emission favorable direction. Atoms colored by Common Neighbor Analysis (Green: fcc Ni; Red: hcp Ni; White: Ni with less than 12 neighbors; Purple: H)

Chapter 2. Atomistic study of Hydrogen embrittlement of grain boundaries in Nickel

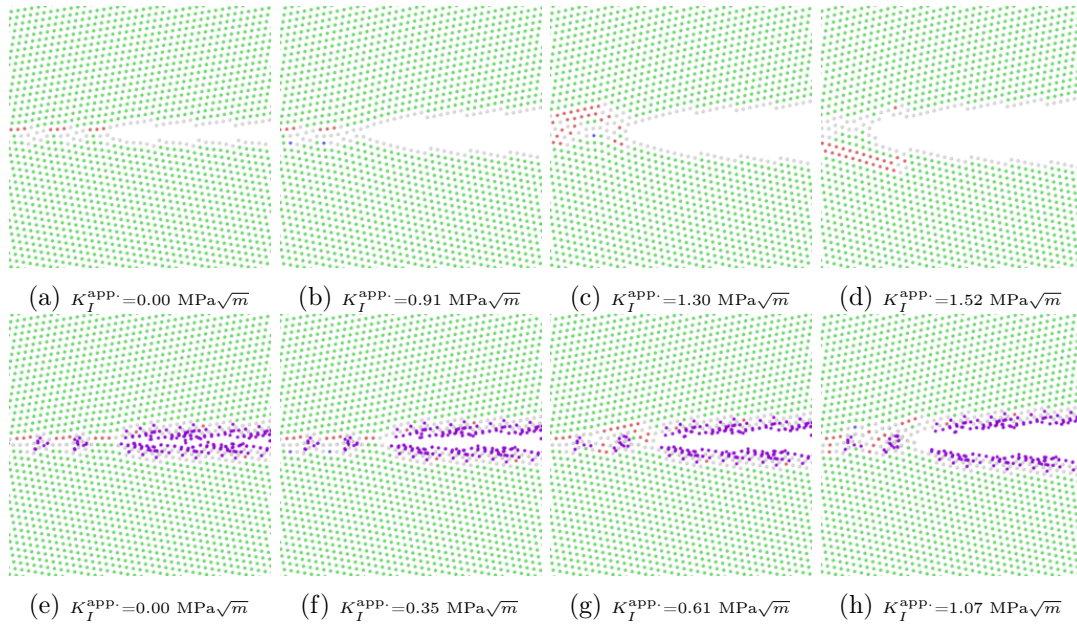


Figure 2.25 – Process of an intergranular crack propagation in NiΣ99(557)⟨110⟩ along the theoretically cleavage favorable direction. Atoms colored by Common Neighbor Analysis (Green: fcc Ni; Red: hcp Ni; White: Ni with less than 12 neighbors; Purple: H)

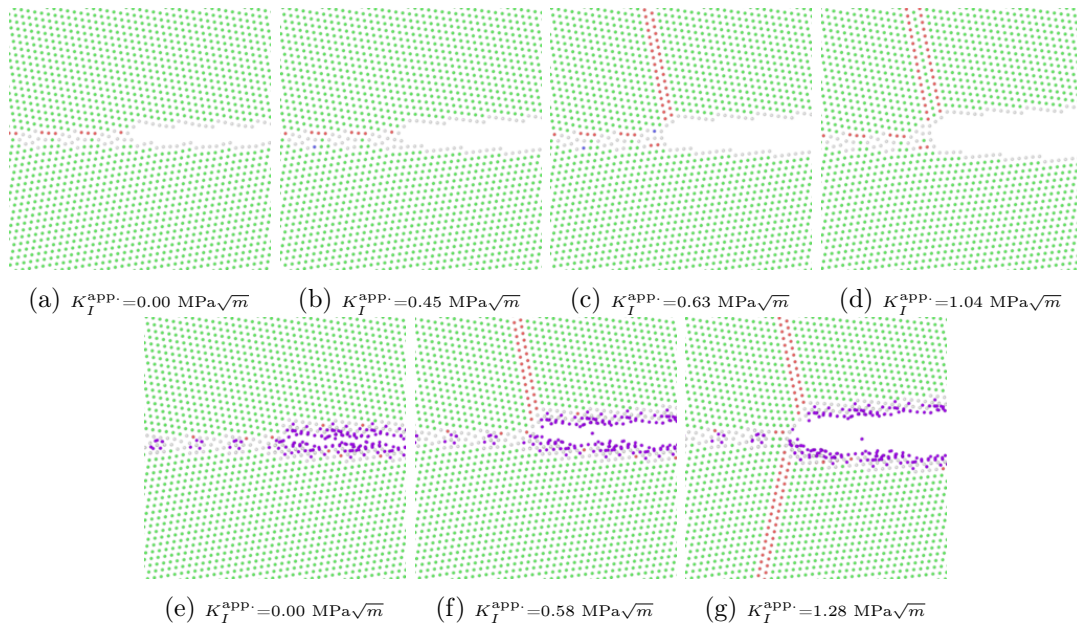


Figure 2.26 – Process of an intergranular crack propagation in NiΣ99(557)⟨110⟩ along the theoretically emission favorable direction. Atoms colored by Common Neighbor Analysis (Green: fcc Ni; Red: hcp Ni; White: Ni with less than 12 neighbors; Purple: H)

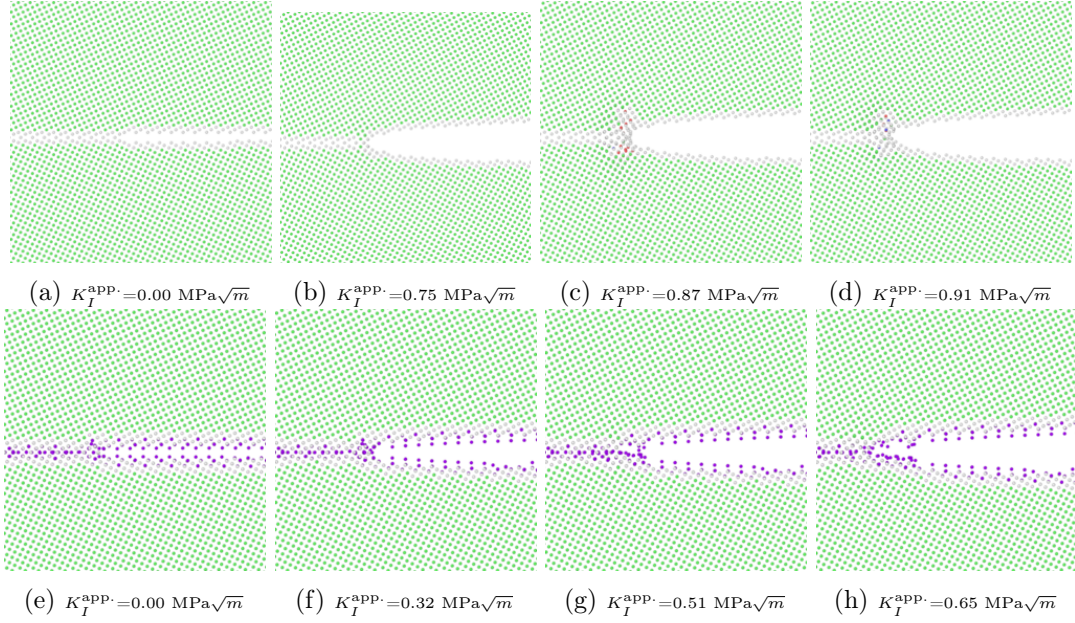


Figure 2.27 – Process of an intergranular crack propagation in $\text{Ni}\Sigma 5(120)\langle 100 \rangle$ along $[2\bar{1}0]$ direction. Atoms colored by Common Neighbor Analysis (Green: fcc Ni; Red: hcp Ni; White: Ni with less than 12 neighbors; Purple: H)

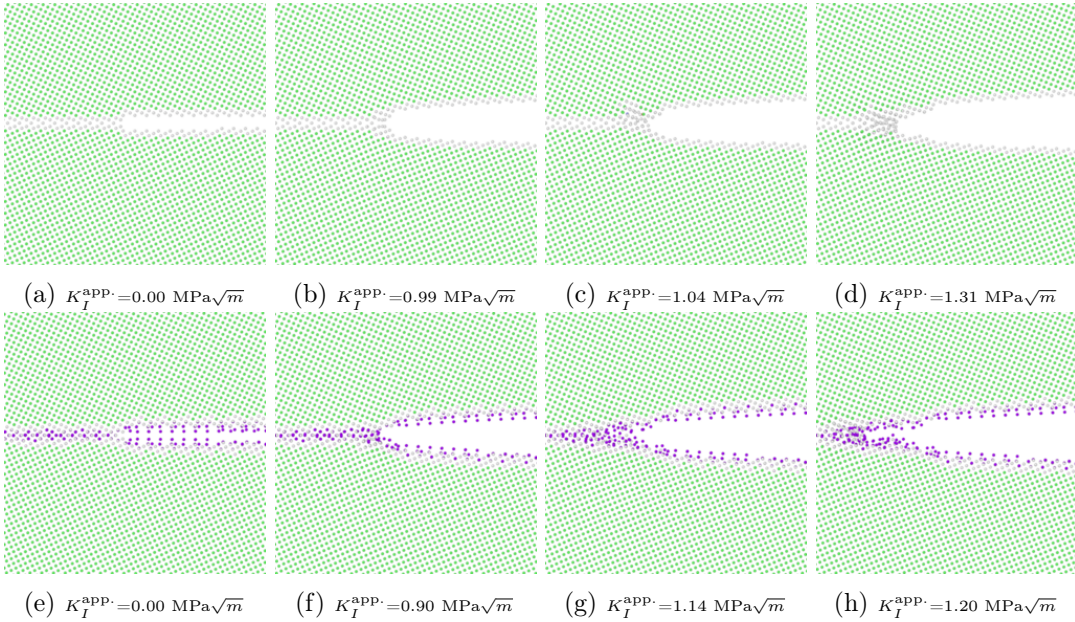


Figure 2.28 – Process of an intergranular crack propagation in $\text{Ni}\Sigma 5(100)\langle 100 \rangle$ along $[2\bar{1}0]$ direction. Atoms colored by Common Neighbor Analysis (Green: fcc Ni; Red: hcp Ni; White: Ni with less than 12 neighbors; Purple: H)

Chapter 2. Atomistic study of Hydrogen embrittlement of grain boundaries in Nickel

are in qualitative agreement with the theoretical Rice and Griffith criteria. However in all cases, the exact values of the K -loads at which critical events occur are different between theory and simulation, and the nature of the different atomic scale mechanisms of crack growth vary. Below, we thus discuss the origins of these differences and further elucidate the effects of segregated hydrogen on these intergranular fracture processes.

One major effect that hinders easy cleavage of the crack faces, and that raises the fracture K above the Griffith prediction, is crack trapping within the GB structure. Since the grain boundary has a complicated discrete structure at the atomistic level, the crack tip can be arrested within the higher-toughness regions of the GB. The crack may first extend through lower-toughness regions but ultimately encounters the locally-tougher regions. Griffith theory considers only the surface energy, which is an average over the various structural units in the GB. With trapping, a higher K^+ is required for crack growth. If K^+ is higher than the critical emission load, local plastic events can occur prior to, or in place of, cleavage. In pure Ni Σ 9(221) \langle 110 \rangle , the final event in the predicted cleavage direction is actually emission ahead of the crack tip and thus no cleavage is observed. In this case, this final event occurs at a K slightly higher than the theoretical Rice criterion and is a manifestation of trapping with $K^+ > K_{Ie}$. Further evidence of strong trapping is seen for cracking in the $[\bar{2}10]$ direction of the Ni Σ 5(120) \langle 100 \rangle where, after a partial cleavage at a K slightly higher than the theoretical cleavage K , the final cleavage occurs only after a further 50% increase in load. Finite temperatures allow thermal activation over trapping energy barriers, and so can alleviate trapping and facilitate cleavage at K values lower than the value measured at T=0K.

The presence of H atoms could also help the crack tip overcome trapping. Specifically, the presence of H along the grain boundary occurs mainly in the open spaces of the boundary, presumably making the energy along the surface more uniform, and thus reducing trapping. In the predicted cleavage case for the Ni Σ 9(221) \langle 110 \rangle , in which the crack tip in pure Ni actually emits dislocations, adding H makes cleavage favorable by preventing local atomic rearrangements. This is the only case in which we observe any ductile-to-brittle transition. Per the discussion above, the embrittlement in this case presumably arises from reduction of trapping effects rather than reduction in the fracture energy. As stated earlier, temperature can reduce the trapping effect, thus even in this case we expect that embrittlement may not occur at finite-T. A similar effect reduces the critical K -load for cleavage in the predicted cleavage direction of Ni Σ 99(557) \langle 110 \rangle . The cleavage load remains higher than the Griffith prediction, but less than the theoretical emission load. For the crack along $[\bar{2}10]$ of the Ni Σ 5(120) \langle 100 \rangle , H atoms reduce the cleavage load by 8%.

Another issue in relating simulations to theory is the occurrence of local distortions at the crack tip. These distortions could be an artifact of the interatomic potential or a consequence of complicated "plastic" activity at the crack tip. For an intergranular crack along $[\bar{2}\bar{1}0]$ of the Ni Σ 5(120) \langle 100 \rangle , such plastic activity is the start of emission of oblique

dislocation loops that, due to the short crack front length, interact and prevent larger-scale expansion of the dislocation loops. This activity hinders the crack from propagating until the load has been increased by an additional 15% . Careful simulation geometries in which emission of oblique dislocation loops can occur requires three dimensional simulations that are beyond the scope of this work.

Aside from the case of the twin boundary, in all the other simulations the cracks are inserted by removing three atomic layers. This removal slightly blunts the tip of the intergranular crack. However, independent simulations of the sharp cracks (achieved by eliminating atomic interactions across the crack faces) and blunted cracks in single crystalline nickel show that the critical load for emission of the first partial dislocations from the crack tip in pure nickel does not change due to blunting. Introducing sharp cracks by eliminating some atomic interactions in the present GB simulations with and without H leads to distorted crack tip geometries that we do not believe are realistic, and so we confined analysis to blunted crack geometries. Moreover, this blunting exists in both H-free and H-charged specimens. Thus the limited effects of blunting are not expected to change the conclusions drawn about the embrittling/nonembrittling effects of segregated H atoms.

H atoms could also have both increasing and decreasing effects on the emission load. A high H concentration along the inclined slip planes in the grains will increase γ_{usf} and hence increase the emission load [38]; this is not present in our simulations because H is only present in the grain boundaries. Emission in mode I loading is accompanied by creation of a surface step, and the energy cost for creation of this surface step is proportional to the surface energy of the metal; this effect is not included in the Rice theory. Since H atoms saturate the crack faces in most cases, the surface energy could be reduced and the critical K for emission also reduced, but this depends on H rearrangements as the step is being created. Here, for the predicted emission directions of $\text{Ni}\Sigma 3(111)\langle 110\rangle$ and $\text{Ni}\Sigma 99(557)\langle 110\rangle$, the presence of H atoms along the GB and on the crack faces indeed reduces the critical K for emission. In the case of the $\text{Ni}\Sigma 3(111)\langle 110\rangle$ GB, where H atoms are present only on the crack faces, the reduction in the emission load is due to this effect. In the case of the $\text{Ni}\Sigma 9(221)\langle 110\rangle$ GB, adding H atoms does not decrease the emission load. However, the crack tip emitted both leading and twinning partials at the same K . Hydrogen-enhanced emission of dislocations from crack tips is reported in the literature, for example see [115].

All simulations and theoretical calculations presented in this work are done for $T=0K$, and finite-T thermal activation might be envisioned to alter the results. However, we believe the $T=0K$ results are reasonable for understanding most finite-T conditions. The Griffith theory is a thermodynamic criterion and so the effects of temperature are due only to temperature-dependent changes in surface/interface energies and elastic moduli. These quantities both typically decrease with increasing temperature. Thus, the K for cleavage should reduce with increasing temperature. The Rice criterion is an instability

Chapter 2. Atomistic study of Hydrogen embrittlement of grain boundaries in Nickel

condition, and so there is an energy barrier that can be overcome at lower loads at finite T . However, the energy barriers are typically large [116, 117] and so the decrease in applied K is relatively small at moderate temperatures ($T=300\text{K}$). The main effects of temperature on the Rice condition are thus due to changes in γ_{usf} and elastic moduli. The decrease in K for emission is thus expected to change similarly to the K for cleavage. Thus, the temperature-dependent competition between cleavage and emission will not change dramatically and predictions at $T=0\text{K}$ are thus expected to be representative of results at finite T , in general. The only exception to this discussion involves lattice trapping, where we noted earlier that finite temperatures will reduce trapping and allow cleavage to occur closer to the thermodynamic Griffith limit.

2.5 Summary

In summary, the present results, on the effects of H segregation to grain boundaries in Ni show no noticeable propensity for H to induce significant embrittlement in Ni. These results are time-independent, and thus do not consider H transport. A recent model by one of the present authors [48, 49] suggests that H transport to the region around an existing crack tip can suppress dislocation emission and consequent blunting, thereby preserving a sharp crack and enabling cleavage failure. Estimates of embrittlement in Ni using this model are consistent with experimental trends, including reduced embrittlement in materials engineered to contain more twin boundaries, but are not yet quantitative. Experiments are also mixed regarding time dependence, with some embrittlement being explicitly time-dependent and other reports of embrittlement at low temperatures (e.g. 77K) where H transport should be very slow. Thus, the mechanisms of H embrittlement, even in a relatively simple metal like fcc Ni where experimental evidence is abundant, remain open for discovery.

3 Softening and hardening of yield stress by hydrogen interstitials

This chapter is in part extracted from the following publication:

- (1) Tehranchi, A., Yin, B. and Curtin, W.A., 2017, Softening and hardening of yield stress by hydrogen–Solute interactions, *Philosophical Magazine*, Volume 97, issue 6, Pages. 400–418

3.1 Introduction

The hydrogen atoms can be considered as interstitial solute atoms with positive misfit volume. Thus, the interaction of them with the dislocations can induce strengthening in H-charged metals. Particularly, at the low temperature domain where the H atoms are immobile, this effect is more dominant. Moreover, these atoms can bind to the pre-existing solutes in the alloys and form solute–H complexes. Changing the misfit strain tensors of the pre-existing solutes, the presence of H can have hardening/softening effects in alloys.

The aim of this chapter is to examine these effects. To this end the general theory of solute strengthening is introduced and discussed in section 3.2. The input of the solute strengthening model is discussed in Section 3.2.1. The results of the theory is compared with the recent experimental results in Section 3.3. Then, in Section 3.4.1, a specific version of the solute strengthening theory which is relevant to the glide of the straight dislocations is derived and adapted to the problem of interstitial solutes with tetragonal misfit distortions. In Section 3.4.2, the details of atomistic simulations of dislocation motion through a field of solutes (vacancies) and solutes (vacancies) with bound H, with the same spatial distribution of solutes, are presented. Section 3.4.3 presents the results of the simulations and discussion of the softening effect of H. Section 3.4.4 presents a density functional theory (DFT) study of the interaction Carbon and Sulfur solute atoms with H, including computation of the misfit strain tensors. A summary of our findings is

given in Section 3.5.

3.2 General theory of solute strengthening

Consider a straight edge dislocation with Burgers vector $\mathbf{b} = b\mathbf{e}_1$ lying along the z -axis in an isotropic medium with shear modulus μ and Poisson's ratio ν containing M different types of solutes with concentrations c_m ($m = 1, 2, \dots, M$) as shown in Fig. 3.4. For taking the advantage of the spatial concentration fluctuations of the solutes, the dislocation roughens and forms a sinusoidal shape as shown in Fig. 3.4. Values for the parameters ζ_c and w_c which are respectively the characteristic length of the straight segment of the dislocation and the amplitude of its roughening can be found by using the minimization of the total energy of the system [87, 88, 89]. The details of this calculation are given below. The decrease in the total energy of the system due to the roughening of the dislocation can be decomposed in two separate parts

$$\Delta E_{\text{tot}} = \Delta E_{\text{p}} + \Delta E_{\text{el}} \quad (3.1)$$

where ΔE_{p} and ΔE_{el} are the change in the total energy due to the interaction of the roughened dislocation with the solutes, and changing the length of it, respectively. Using isotropic line tension model one can obtain ΔE_{el} in terms of the line tension Γ , and the parameters describing the geometry of the roughened dislocation w and ζ as

$$\Delta E_{\text{el}} = \Gamma \left[(\zeta^2 + w^2)^{\frac{1}{2}} - \zeta \right] \cdot \left(\frac{L}{2\zeta} \right) \approx \Gamma \left(\frac{w^2}{2\zeta} \right) \left(\frac{L}{2\zeta} \right) \quad (3.2)$$

the latter result is valid under $w \ll \zeta$ condition. Obtaining the contribution of the solutes in the energy decrease is more subtle. The interaction energy between a dislocation segment of length ζ and the solutes is approximated by considering the elastic interaction due to the misfit strain of the solute and its interaction with the stacking fault. Thus, one can write the following expression for the total potential energy of the segment:

$$U_{\text{tot}}(\zeta) = \sum_{ijk} \sum_m s_{ijk}^m U_{ij}^m \quad (3.3)$$

with $s_{ijk}^m = 1$ if a type- m solute exists at position (x_i, y_j, z_k) and 0 otherwise (e.g. in the case depicted in Fig. 3.4, $s_{ijk}^2 = s_{lmn}^1 = 1$ while $s_{lmk}^1 = s_{lmk}^2 = s_{ijn}^1 = s_{ijn}^2 = 0$). U_{ij}^m is the interaction energy of a type m solute located at (x_i, y_j, z_k) with the dislocation. If the dislocation glides a distance w along the glide direction \mathbf{e}_1 , the change in the interaction energy becomes

3.2. General theory of solute strengthening

$$\begin{aligned}\Delta U_{\text{tot}}(\zeta, w) &= \sum_{ijk} \sum_m s_{ijk}^m \{U_{ij}^m(x_i - w, y_j) - U_{ij}^m(x_i, y_j)\} \\ &= \sum_{ijk} \sum_m s_{ijk}^m \Delta U_{ij}^m(x_i, y_j; w)\end{aligned}\quad (3.4)$$

The key quantity in solute strengthening model is the standard deviation of the total interaction energy change

$$\sigma_{\Delta U_{\text{tot}}}^2(\zeta, w) = \langle \Delta U_{\text{tot}}(\zeta, w)^2 \rangle - \langle \Delta U_{\text{tot}}(\zeta, w) \rangle^2. \quad (3.5)$$

After some manipulations which are given and discussed in [118], we get the following expression for the standard deviation

$$\begin{aligned}\sigma_{\Delta U_{\text{tot}}}^2(\zeta, w) &= \sum_{ij} \sum_m \Delta U_{ij}^m(x_i, y_j; w)^2 \left(\langle \mathbf{n}_{ij}^{(m)2} \rangle - \langle \mathbf{n}_{ij}^m \rangle^2 \right) \\ &\quad + \sum_{ij} \sum_{m, l \neq m} \Delta U_{ij}^m(x_i, y_j; w) \Delta U_{ij}^l(x_i, y_j; w) \left(\langle \mathbf{n}_{ij}^m \mathbf{n}_{ij}^l \rangle - \langle \mathbf{n}_{ij}^m \rangle \langle \mathbf{n}_{ij}^l \rangle \right)\end{aligned}\quad (3.6)$$

where

$$\begin{aligned}\langle \mathbf{n}_{ij}^m \rangle &= c_m N_s \\ \langle \mathbf{n}_{ij}^m \mathbf{n}_{ij}^l \rangle &= c_m c_l N_s (N_s - 1) \\ \langle \mathbf{n}_{ij}^{m2} \rangle &= c_m N_s + c_m^2 N_s (N_s - 1)\end{aligned}$$

and $N_s = \frac{\zeta}{\sqrt{3}b}$ is the total number of the sites that can be potentially occupied by solutes available on the atomic row of length ζ which is along $\langle 110 \rangle$ direction in an fcc lattice. Thus, for the dilute cases which are relevant to the concentrations at which we observe H embrittlement (i.e. $c_m \ll 1$, $m = 1, 2, \dots, M$), we have

$$\sigma_{\Delta U_{\text{tot}}}^2(\zeta, w) = \frac{\zeta c}{\sqrt{3}b} \Delta \tilde{E}_p^2 = \frac{\zeta c}{\sqrt{3}b} \sum_{ij} \sum_m \Delta U_{ij}^m(x_i, y_j; w)^2 \bar{c}_m. \quad (3.7)$$

in which $c = \sum c_m$ and $\bar{c}_m = c_m/c$. $\Delta \tilde{E}_p$ function contains the characteristics of the solute–dislocation interactions.

After the roughening process, some regions give rise to $\Delta E_p > 0$ while the other region give rise to negative values. The magnitude of the characteristic energy change in both cases is $\sigma_{\Delta U_{\text{tot}}}$. Thus, the change in the potential energy of the dislocation due to the

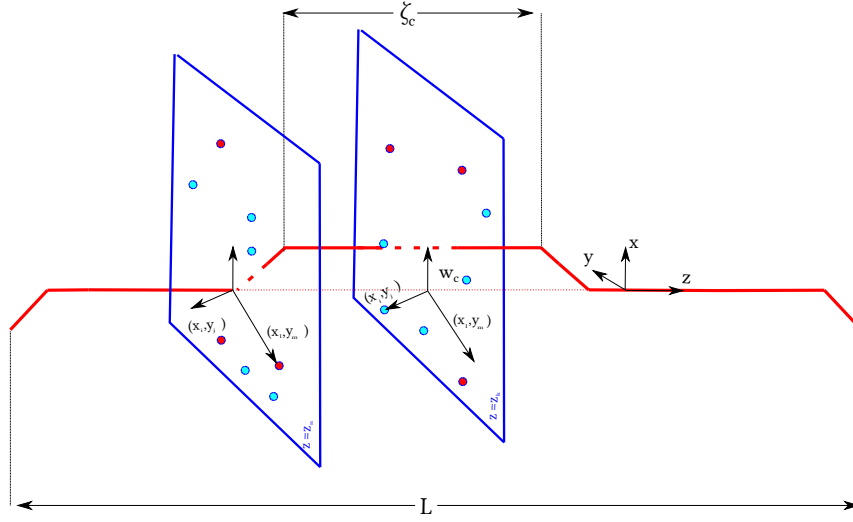


Figure 3.1 – Schematic diagram of roughening of an originally straight edge dislocation lying on the z axis surrounded by the multiple solutes of different types. The red and blue circles refer to types -1 and -2 solute atoms, respectively. The length of the straight segment is ζ_c and the amplitude of roughening is w_c .

roughening can be written as

$$\Delta E_p = -\sigma \Delta U_{\text{tot}} \frac{L}{2\zeta}. \quad (3.8)$$

In view of Eqs. (3.1), (3.2), (3.7), and (3.8) the change in the total energy can be written as

$$\Delta E_{\text{tot}} = \left[\Gamma \left(\frac{w^2}{2\zeta} \right) - \left(\frac{c\zeta}{\sqrt{3}b} \right)^{\frac{1}{2}} \Delta \tilde{E}_p(w) \right] \cdot \left(\frac{L}{2\zeta} \right) \quad (3.9)$$

Now the characteristic critical value for ζ can be found by minimization of the in the total energy as

$$\bar{\zeta}_c(w) = \frac{c^{\frac{1}{3}}}{\Gamma^{\frac{2}{3}}} \zeta_c = \left(4\sqrt{3} \frac{w^4 b}{\Delta \tilde{E}_p^2(w)} \right)^{\frac{1}{3}} \quad (3.10)$$

Interestingly, $\bar{\zeta}_c$ is independent of the total concentration of the solutes and the line tension and only depends on $\Delta \tilde{E}_p$ which contains the solute–dislocation interaction information. Incorporating the Eq. (3.10) into Eq. (3.9) we get the following expression for total

3.2. General theory of solute strengthening

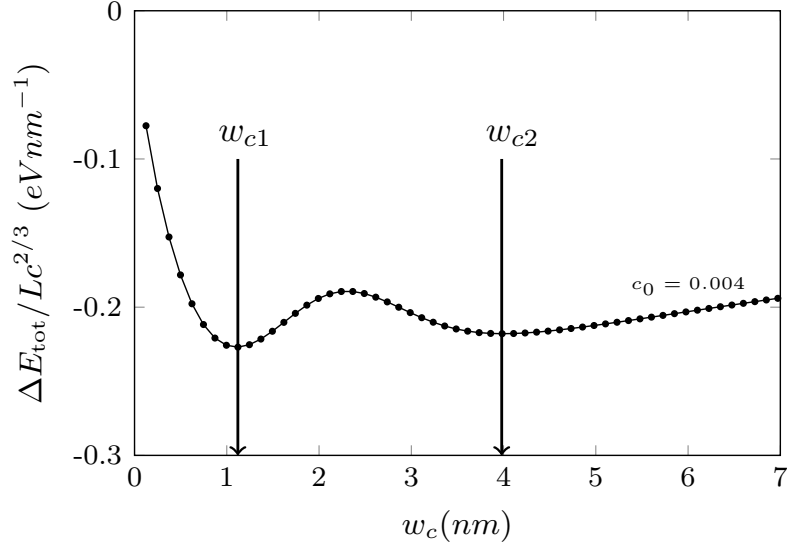


Figure 3.2 – Distribution of the total energy versus the roughening amplitude for $c_0 = 3000\text{appm}$ and $c_0 = 4000\text{appm}$ in nickel. The line tension of the edge dislocation is assumed to be $0.48\text{eV}/$.

energy

$$\Delta E_{\text{tot}}(\zeta_c(w), w) = -\frac{3^{2/3}}{8.2^{1/3}} \left(\frac{\Delta \tilde{E}_p^4}{b^2 w^2 \Gamma} \right)^{1/3} L \quad (3.11)$$

The critical amplitude, w_c , can be found by minimization of $E_{\text{tot}}(\zeta_c(w), w)$ with respect to w which leads to the following equation.

$$\frac{\partial \Delta \tilde{E}_p}{\partial w} - \frac{\Delta \tilde{E}_p}{2w} = 0. \quad (3.12)$$

Numerical methods are used to perform this minimization. To this end the function $\Delta E_{\text{tot}}(\zeta_c(w), w)$ is sketched versus w and the minima can be found. Fig. 3.2 shows an example of this procedure for two different concentration of H atoms in nickel.

After finding the critical values w_c , the characteristic energy of the dislocation segment then becomes

$$\Delta E_c = \Delta E_{\text{tot}}(w_c, \zeta_c) \frac{2\zeta_c}{L} = -\frac{3^{5/6}}{2^{2/3}} \left(\frac{c w_c^2 \Gamma \Delta \tilde{E}_p^2(w_c)}{b} \right)^{1/3} \quad (3.13)$$

The potential energy length landscape associated with the segment ζ_c of the dislocation

Chapter 3. Softening and hardening of yield stress by hydrogen interstitials

in the glide direction can be approximated by the following sinusoidal function

$$E(\zeta_c, x) = \frac{\Delta E'_b(\zeta_c, w_c)}{2} \left[1 - \cos\left(\frac{\pi x}{w_c}\right) \right] \quad (3.14)$$

where $\Delta E'_b$ is the height of the barrier. $\Delta E'_b$ can be found by considering the fact that the proposed energy landscape must reproduce the standard deviation pertinent to the solute–dislocation interaction, thus

$$\sigma_{\Delta U}(\zeta, w_c) = \left[\int_0^{2w_c} (E(\zeta, x - w_c) - E(\zeta, x))^2 dx \right]^{\frac{1}{2}} = \frac{1}{\sqrt{2}} \Delta E'_b(\zeta, w_c). \quad (3.15)$$

We know that the elastic energy that is stored in the roughened dislocation helps it to overcome the barrier $\Delta E'_b$ thus the effective barrier that enters in the kinetic calculations is

$$\Delta E_b = \Delta E'_b - \Delta E_{el} = \left(\frac{4\sqrt{2} - 1}{3} \frac{3^{\frac{5}{6}}}{2^{\frac{5}{3}}} \right) \left(\frac{cw_c^3 \Gamma \Delta \tilde{E}_p^2(w_c)}{b} \right)^{\frac{1}{3}} \quad (3.16)$$

The characteristic energy barrier which is independent of the total concentration of the solutes and the line tension of the dislocation is defined as

$$\Delta \bar{E}_b = \frac{\Delta E_b}{c^{\frac{1}{3}} \Gamma^{\frac{1}{3}}} \quad (3.17)$$

When the medium is subjected to shear stress the energy landscape is modified as follows

$$E(\tau, x) = \frac{\Delta E_b(\zeta_c, w_c)}{2} \left[1 - \cos\left(\frac{\pi x}{w_c}\right) \right] - \tau \zeta b x \quad (3.18)$$

where τ is the applied shear stress. The yield shearing stress at which the landscape has not any barrier to the dislocation movement simply computed as

$$\tau_{y0} = \frac{\pi}{2} \frac{\Delta E_b}{bw_c \zeta_c} = 1.01 \left(\frac{c^2 \Delta \tilde{E}_p^4(w_c)}{\Gamma b^5 w_c^5} \right)^{\frac{1}{3}} \quad (3.19)$$

The characteristic zero temperature yield stress is given by

$$\bar{\tau}_0 = \frac{\Gamma^{\frac{1}{3}} \tau_0}{c^{\frac{2}{3}}}.$$

3.2. General theory of solute strengthening

The temperature dependent yield strength can be calculated by the following formulation

$$\tau_y(T) = \begin{cases} \tau_{0y} \left[1 - \left(\frac{k_B T}{\Delta E_b} \ln \frac{\dot{\epsilon}_0}{\dot{\epsilon}} \right)^{\frac{2}{3}} \right] & \tau_y/\tau_{y0} > 0.5 \\ \tau_{0y} \exp \left(-\frac{1}{C_l} \frac{k_B T}{\Delta E_b} \ln \frac{\dot{\epsilon}_0}{\dot{\epsilon}} \right) & 0.2 < \tau_y/\tau_{y0} < 0.5 \\ \tau_{0y} \left(\frac{1}{C_p} \frac{k_B T}{\Delta E_b} \ln \frac{\dot{\epsilon}_0}{\dot{\epsilon}} \right)^{-\frac{1}{\varphi}} & \tau_y/\tau_{y0} < 0.03 \end{cases} \quad (3.20)$$

in which k_B , T , $\dot{\epsilon}$ are $\dot{\epsilon}_0$ are the Boltzmann constant, temperature, the actual and reference strain rates. $C_l = 0.55$, $C_p = 0.52$, and $\varphi = 0.54$ are parameters of the multiscale bow-out theory. The details of derivation of Eq. (3.20) in which the multi-scale bowing out of the dislocation is taken into account is given in [119].

3.2.1 Input of the model

Using the theory described in the previous section, we can find the finite temperature yield stress of given solid solutions by plugging the interaction energies, line tension and strain rate into the theory. We discuss the input of the theory.

As it is stated in the previous subsection, the low energy configuration of the dislocation and its corresponding energy barrier and yield strength largely depend on the function $\Delta \tilde{E}_p$ which itself is a function of the solute–dislocation interactions. Thus, having a correct description of the interaction energy of the solutes in alloy and the dislocation is crucial for the accuracy of the results. In this work we approximate the interaction of hydrogen atoms and dislocation by only the elastic interaction of them:

$$U_{ij}^m = V_0 \boldsymbol{\sigma}(x_i, y_j) : \boldsymbol{\varepsilon}^m \quad (3.21)$$

where V_0 , $\boldsymbol{\sigma}$, and $\boldsymbol{\varepsilon}^m$ are the volume of matrix atoms, stress field induced by the dislocation, and the misfit strain tensor of the m^{th} type of solutes, respectively. For the cases in which the misfit strain of the solutes are purely volumetric, we can simplify the Eq. (3.21) as

$$U_{ij}^m = p(x_i, y_j) \Delta V^m \quad (3.22)$$

in which, p and ΔV^m are the pressure field of the dislocation and the misfit volume of the m^{th} type of the solutes. If we plug Eq. (3.22) into Eq. (3.7) we get the following

Chapter 3. Softening and hardening of yield stress by hydrogen interstitials

relation for $\Delta\tilde{E}_p^2$

$$\Delta\tilde{E}_p^2 = \sum_{ij} \sum_m p^2(x_i, y_j) \Delta V^{m2} \quad (3.23)$$

It is evident that the sign of the misfit volume does not play any role in the results of the theory.

3.2.2 Pressure field of the dislocation

We know that the edge dislocation in an fcc lattice dissociates into two partial dislocations. Thus, the slip is spread along the dissociated dislocation. To have a good approximation of the distribution of the Burgers vector along the dislocation width, we use the following Gaussian function describing the intensity of Burgers vector along the slip plane.

$$\frac{db}{dx} = \exp\left(-\left(\frac{x-d/2}{\sigma\sqrt{2}}\right)^2\right) + \exp\left(-\left(\frac{x+d/2}{\sigma\sqrt{2}}\right)^2\right) \quad (3.24)$$

This model contains two parameters σ and d which are respectively characterizing the width and distance between the partial dislocations. These two parameters should be found by fitting the results of the theory with DFT calculations. Using this function the following relation can be written for the pressure field of the dissociated dislocation

$$p(x, y) = K \int_{-\infty}^{+\infty} \frac{y dx'}{[x' - (b/2)]^2 + y^2} \left(\exp\left(-\left(\frac{x' - d/2}{\sigma\sqrt{2}}\right)^2\right) + \exp\left(-\left(\frac{x' + d/2}{\sigma\sqrt{2}}\right)^2\right) \right) \quad (3.25)$$

$$K = \frac{-\mu(\nu + 1)b}{3\pi(1 - \nu)}$$

The magnitude of the Burgers vector for basal dislocation is $b = 2.48\text{\AA}$. Thus, the contribution of the misfit volume of the solutes in the energy landscape of the dislocation can be found by multiplying the pressure field at each spatial point (x_i, y_j, z_k) by the misfit volume of the solute.

3.2.3 Calibration of the model

Given the theoretical framework in conjunction with the approximate description of the solute–dislocation interaction energy, we need to choose proper values for σ and d by which the dislocation solute interactions can be reproduced by incorporating the dislocation pressure field and stacking fault interaction of solutes. To this end, using the values given in Varvenne et al. paper for nickel [118]. We used $\mu = 79$ GPa and $\nu = 0.29$ for calculating the interaction energies in the theoretical model. After testing various

3.3. The strengthening effects of H atoms on nickel

choices for (σ, d) pairs, the best results obtained by choosing $\sigma = 1.74b$ and $d = 9.36b$. The misfit volume of H in nickel is 3.27\AA^3 . The value of the line tension is calculated by the following relation

$$\Gamma = \alpha\mu b^2 \quad (3.26)$$

in which $\alpha = 0.123$ [118].

3.3 The strengthening effects of H atoms on nickel

Hydrogen interstitials can be sources of solute strengthening. This phenomenon must be more important when the temperature is low such that the H atoms can not diffuse in the bulk of the metal and find the traps. A recent experiment [19] shows the increase in the yield strength of fine grain polycrystalline nickel with average grain size of $35 \times 10^{-6}m$ at 77K and 300K [19] due to the presence of H atoms. In the experiment, the H atoms are injected into the specimen via thermal charging. The specimens are kept at 573K and charging pressure of 96.5 MPa for 120 hours. Then the specimens are kept in the freezer at 223K. Theoretical calculations which are given in [3] show that this method can increase the bulk concentration of the H atoms to 4000 appm. The actual measured the concentration of H atoms in the charge specimens are found to be 4660 appm. This 15% increase is due to the release of the trapped H atoms in defects such as grain boundaries, dislocations, and vacancies.

Since the concentration of the solutes is one of the key parameters of the solute strengthening theory, here we use a simple estimation of the change in the concentration of H atoms in bulk due to the presence of grain boundaries. To this end, we consider a cubic grain; the volume of the grain boundary and bulk regions can be estimated by $V_{GB} = 6L^2d$, and $V_{bulk} = l^3$, respectively. Here, L and d are the grain dimension and the thickness of the GB. In fcc metals there exist one octahedral site per each lattice site. If we assume that the same ratio is true for the grain boundary region then the number of binding sites can be estimated by the volume of GB and bulk. It should be noted that this assumption magnifies the number of the H atoms at the grain boundary.

$$\frac{N_H^{GB}}{N_H^{bulk}} = \frac{6dc_{GB}}{Lc_0} = \frac{6 \times 10^{-9}}{35 \times 10^{-6}} \frac{c_{GB}}{c_0} \approx 1.7 \times 10^{-4} \frac{c_{GB}}{c_0} \quad (3.27)$$

If we consider full coverage of the GB sites (i.e $c_{GB} = 1$), then we have:

$$\frac{N_H^{GB}}{N_H^{bulk}} \approx 1.7 \times 10^{-4} \frac{1}{0.004} \approx 0.042 \quad (3.28)$$

Thus, an increase about 5% in the average measured concentration is anticipated due to the presence of H atoms. The remainder of the increase is due to the trapping of H in

Chapter 3. Softening and hardening of yield stress by hydrogen interstitials

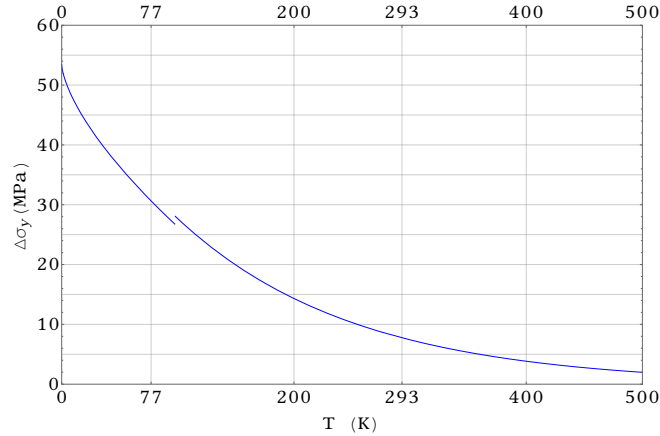


Figure 3.3 – Variation of the increase in yield strength of nickel due to the presence of bulk H interstitials versus temperature for $c_0 = 0.004$.

Table 3.1 – Increase in the the tensile yield strength of polycrystalline nickel due to the presence of hydrogen at 300K and 77K. The H concentration in bulk is $c_0 = 0.004$

T(K)	$\Delta\sigma_y$ (MPa)	
	theory	experimental
77	31	30.6
300	13	7.5

other defects.

Another possibility that should be addressed is the fact that at charging temperature, 573K, the coverage of the H atoms at the binding sites of the GB can be far less than $c_{GB} = 1$. Thus, it can be envisioned that some bulk H atoms migrate to GBs at very low temperature in which the full coverage can be achieved. However, based on the results of Eq. (3.28) this effect can only reduce the bulk concentration by at most 5%. Thus, it is safe to use the bulk concentration in the solute strengthening theory.

Table 3.1 contains the experimental yield strengths in the experiment. To examine the effect of H atoms on the strengthening of polycrystalline nickel we use a solute strengthening model as described in the previous section. Thus, the distribution of the for critical resolved shear versus the temperature for concentration $c = 4000\text{appm}$ is given in Fig. 3.3.

It can be seen that the results of the solute strengthening theory in 77 K are in good agreement with the experimental results. However, for the room temperature experiments show a higher increase in the strength of the H-charged samples. This can be due to the fact that at room temperature the H atoms are mobile within the bulk and thus the solute drag can play a role in the strengthening of the polycrystalline samples. This speculation can be validated by using the atomistically informed solute drag theory which

is given in [120].

3.4 Hardening/softening effects of H atoms in nickel alloys

In this section, we demonstrate the possible softening/hardening effects of the formation solute–H complexes in nickel alloys. To this end, we first introduce a specific version of solute strengthening theory which can be verified by the direct atomistic simulations. The results of the direct simulations demonstrate the hardening/softening effects of H contamination.

3.4.1 Solute strengthening of straight dislocations

In this section, we introduce the key features and results of the theory, without a complete derivation and generalize the theory to include tetragonal misfit distortions.

For the present atomistic study, we are interested only in the motion of a single straight dislocation of some length $\zeta < \zeta_c$, which should remain straight since the energy cost to bow out is too high. The straight dislocation is pinned in regions where the energy is $-\sigma_{\Delta E_{\text{int}}}$ and must be thermally activated over regions where the energy is $+\sigma_{\Delta E_{\text{int}}}$, with these maxima and minimum being separated by w_c . That is, the single segment is envisioned as moving through an energy landscape that is locally sinusoidal.

$$E(\zeta, x_1) = \frac{\Delta E'_b}{2} \left[1 - \cos\left(\frac{\pi x_1}{w_c}\right) \right] \quad (3.29)$$

where $\Delta E'_b = \sqrt{2}\sigma_{\Delta E_{\text{int}}}$ is the energy barrier. Under an applied resolved shear stress τ that drives the dislocation and further lowers the energy as a function of glide distance x_1 , the energy landscape becomes

$$E(\zeta, x_1) = \frac{\Delta E'_b(\zeta, w_c)}{2} \left[1 - \cos\left(\frac{\pi x_1}{w_c}\right) \right] - \tau \zeta b x_1 \quad (3.30)$$

The zero-temperature flow stress τ_{y0} is the stress at which the barrier in the total energy landscape becomes zero. This is obtained analytically from Eq. (3.30) and is given by

$$\tau_{y0} = \frac{\pi}{2} \frac{\Delta E'_b}{b w_c \zeta} = -\frac{\pi}{w_c \sqrt{2}} \left(\frac{V}{\zeta \sqrt{3} b^3} \right)^{\frac{1}{2}} \sqrt{\sum_{ij} \sum_m \left(\Delta \sigma \left(x_1^{(i)}, x_2^{(j)}; w_c \right) : \boldsymbol{\varepsilon}^{(m)} \right)^2 c_m} \quad (3.31)$$

where we have substituted the expression for $\sigma_{\Delta E_{\text{int}}}$ and V is the atomic volume of the matrix. Eq. (3.31) is the theoretical result *relevant to the simulations discussed below*, providing the relationship between the underlying solute/dislocation interaction energies, here assumed to be only elastic, and the typical stress required to move a dislocation through a field of such solutes. The original theory does not rely on the

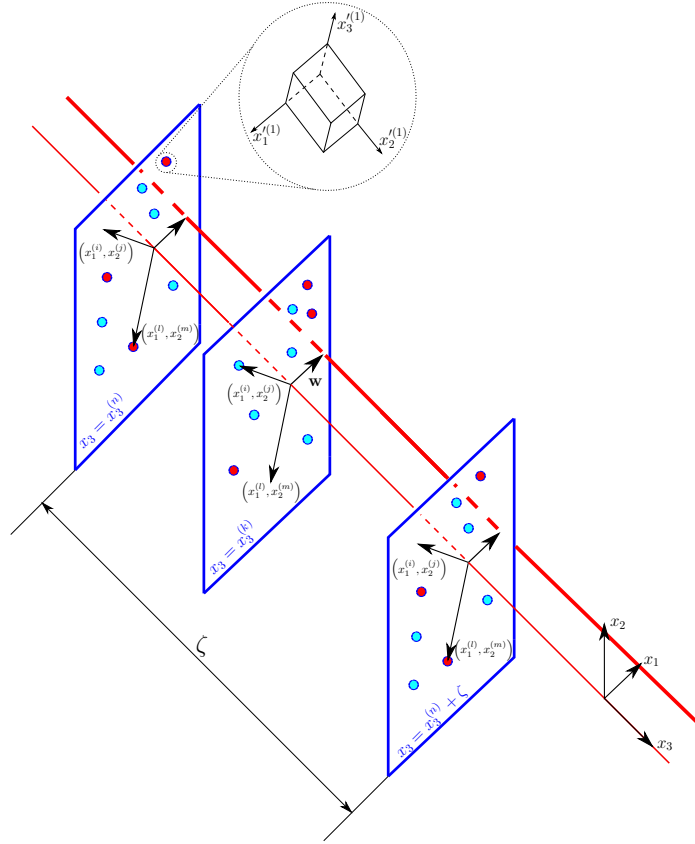


Figure 3.4 – An edge dislocation originally lying on the x_3 axis surrounded by the multiple solutes of different types. The red and blue circles refer to two types of solute atoms. The principal misfit strain coordinate system of the solutes are $\{x_i^{(m)}\}$. The dislocation glides a distance w along the x_1 axis.

elasticity assumption and uses full DFT-computed solute/dislocation interaction energies, but that is beyond the scope of the present work.

The misfit strain tensor of a solute or solute complex can, in general, be separated into volumetric and deviatoric components. Written in its principal coordinate $\{x_i^{(m)}\}$ ($i = 1, 2, 3$), the misfit strain tensor is

$$\boldsymbol{\varepsilon}^{I(m)} = \boldsymbol{\varepsilon}_d^{I(m)} + \boldsymbol{\varepsilon}_v^{(m)} \quad (3.32)$$

where

$$\boldsymbol{\varepsilon}'_d^{(m)} = \frac{\Delta V^{(m)}}{3V} \begin{pmatrix} \frac{2-\xi-\eta}{1+\xi+\eta} & 0 & 0 \\ 0 & \frac{2\xi-1-\eta}{1+\xi+\eta} & 0 \\ 0 & 0 & \frac{2\eta-\xi-1}{1+\xi+\eta} \end{pmatrix}$$

and

$$\boldsymbol{\varepsilon}_v^{(m)} = \frac{\Delta V^{(m)}}{3V} \begin{pmatrix} 1 & 0 & 0 \\ 0 & 1 & 0 \\ 0 & 0 & 1 \end{pmatrix}$$

with $\Delta V^{(m)}/V$, the misfit volumetric strain, and ξ and η the ratios of the second and third principal strains to the first principal strain, respectively. The stress field induced by the dislocations can also be expressed in terms of volumetric and deviatoric contributions as

$$\boldsymbol{\sigma}(x_1, x_2) = \boldsymbol{\sigma}'(x_1, x_2) + \boldsymbol{p}(x_1, x_2)$$

Inserting these decompositions into Eq. (3.31), we obtain

$$\tau_0 = - \left(\frac{\pi^2 V}{2w_c^2 \zeta \sqrt{3} b^3} \right)^{\frac{1}{2}} \times \sqrt{\sum_{ij} \sum_m \left((\Delta \boldsymbol{\sigma}'(x_1^{(i)}, x_2^{(j)}; w_c) : \boldsymbol{\varepsilon}_d^{(m)})^2 + \Delta p^2(x_1^{(i)}, x_2^{(j)}; w_c) \left(\frac{\Delta V^{(m)}}{V} \right)^2 \right) c_m} \quad (3.33)$$

There are thus two contributions to the strengthening, a volumetric piece due to the misfit volumes of the solutes and a deviatoric piece due to tetragonal strains. For substitutional solutes, the deviatoric part is zero by symmetry, and was not previously considered. We note also that the stress field entering the strengthening is the *difference* in stress field between the dislocation at w_c and at the origin.

Specific results emerge by using the true stress field of the dislocation. In fcc matrices, the edge dislocation dissociates into two partials separated by a stacking fault, and so the classical Volterra solution for the singular dislocation is inappropriate. Furthermore, the value for w_c is not specified here and emerges from detailed computations. Here, we focus not on specific predictions but on the major trends predicted by the model. Specifically, the model shows that the strengthening is controlled by contributions from both volumetric and deviatoric strains and that the solute concentrations enter within a sum that is within an overall square-root. If all solutes have the same concentration c ,

the strengthening of a straight dislocation moving through the random field of solutes scales as $c^{1/2}$; this scaling is *different* from that for the long roughened dislocation where the strength scales as $c^{2/3}$ due to the difference in geometry. The present model, with $c^{1/2}$ scaling, is only appropriate for the case of short segments $\zeta < \zeta_c$ considered in the simulations here.

3.4.2 Atomistic Simulation Methodology

We use a simulation cell comprised of a rectangular fcc Ni lattice oriented as $\hat{\mathbf{e}}_1 = \frac{1}{\sqrt{2}}[10\bar{1}]$, $\hat{\mathbf{e}}_2 = \frac{1}{\sqrt{3}}[111]$, $\hat{\mathbf{e}}_3 = \frac{6}{\sqrt{3}}[1\bar{2}1]$. The dimensions of the simulation cell are $L_1 = 503\text{\AA}$, $L_2 = 306\text{\AA}$ and $L_3 = 155\text{\AA}$. The simulation cell is periodic in the x_1 and x_2 directions and has free boundaries in the x_3 direction. Loading is then accomplished by applying a shear traction $\tau_{12}^{\text{app}} = \tau^{\text{app}}$ to top and bottom (normal vectors $+/-x_3$) of the specimen.

As noted earlier, we use vacancies as the ‘‘solutes’’ in this problem. To insert these solutes (vacancies) with desired concentrations, we randomly delete $N_v = cN$ of the N Ni atoms in the simulation cell. However, we do not insert any vacancies along the two atomic planes above and two atomic planes below the dislocation (111) glide plane. This is a special restriction for the vacancies because, unlike real solutes, vacancies can have unusual interactions with the dislocation core. In particular, randomly occurring vacancy clusters can lead to the formation of dislocation jogs, which are strengthening obstacles. This special exclusion of vacancies from several atomic rows has *no* consequences for the form of the theory in Eq. (3.33) since the summation is restricted to sites where the solutes exist. In fact, eliminating solute/core and solute/stacking fault interactions also makes the elastic interactions dominant. After deleting the Ni atoms, we relax the specimen with standard conjugate gradient method [95] For every specimen containing a particular spatial distribution of solutes (vacancies). We create a second specimen in which we insert one hydrogen atom at each solute site and then relax the system again. During relaxation, the hydrogen moves to one of the symmetry-related low-energy positions associated with the vacancy. Thus, we have two samples with identical spatial distributions of either solutes or solute-hydrogen (S-H) complexes.

After initial relaxation, we insert an edge dislocation of Burgers vector $\frac{a}{2}[10\bar{1}]$, where $a = 3.52\text{\AA}$ is the lattice constant, and line direction $[1\bar{2}1]$ along the x_3 -axis at the center of the specimen $x_1 = X_0$. We use the standard procedure [121] of removing the atoms with coordinates $-\frac{b}{2} < x_1 - X_0 < b/2$, $x_3 < L_2/2$ from the perfect crystal followed by relaxation of the system with the conjugate gradient method. During relaxation, a dislocation is formed and it dissociates into two partial dislocations with Burgers vectors $\frac{a}{6}[\bar{1}\bar{1}2]$ and $\frac{a}{6}[2\bar{1}\bar{1}]$. The geometric details of the simulation cell are shown in Fig. 3.5.

3.4. Hardening/softening effects of H atoms in nickel alloys

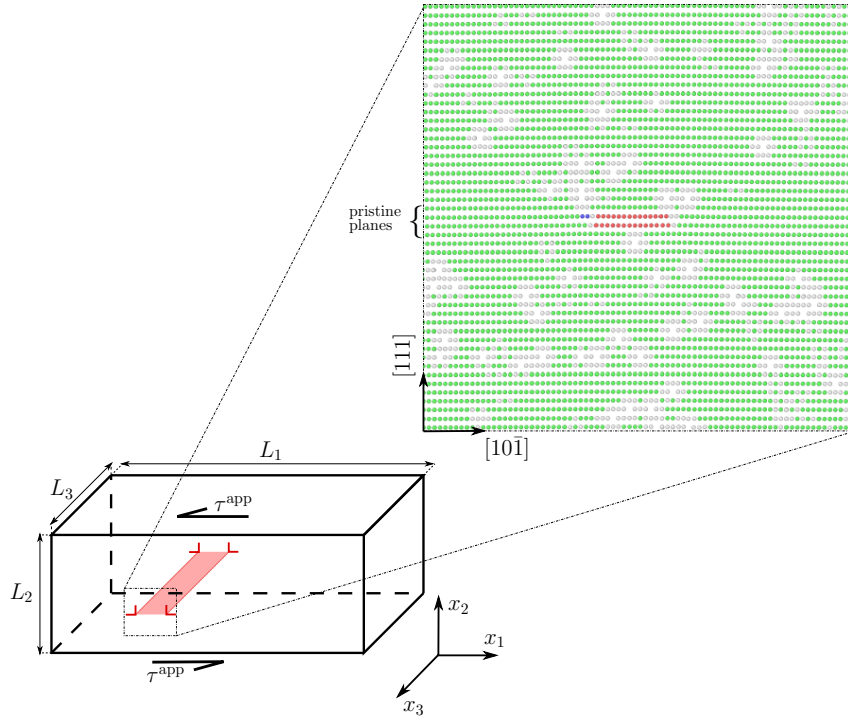


Figure 3.5 – Schematic diagram of the simulation cell containing the straight dislocation and vacancies subjected to the applied shear traction. The color coding for the atomistic picture uses common neighbor analysis (green: fcc; red: hcp indicating the stacking fault; white: atoms having fewer than 12 neighbors and thus surrounding a vacancy “solute”).

The MD simulations are performed in the NVT ensemble using a Langevin thermostat [97] and the velocity–Verlet algorithm [96] with integration time step of 1 fs. The temperature of the system is fixed to be $10^{-3}K$ since we are not probing thermally-activated flow here. The interatomic interactions among atoms are described using the Ni-H embedded atom method (EAM) potential introduced by Angelo et al. [90] and modified by Song and Curtin [48]. The shear stress is increased from $\tau_{12}^{\text{app}} = 0$ in increments of $\Delta\tau = 1\text{MPa}$. After each loading step, MD is executed for $\Delta t = 30\text{ps}$ and then the x_1 -coordinate of the dislocation core, defined as the centerline of the stacking fault between two partials, is compared to that of the previous step. If the incremental displacement of the dislocation core is larger than $\Delta d = 1.1\text{\AA}$, then the MD simulation is executed for another period of Δt . Otherwise, the load is increased by $\Delta\tau$. During the simulation, we determine the dislocation position along the glide plane versus the applied stress τ^{app} . We perform loading steps until the dislocation has passed through the entire periodic length L_x of the glide plane in the simulation cell. The applied stress τ^{app} at this point of the simulation is taken as a measure of the flow stress.

3.4.3 Results and discussion

We have measured the values for the misfit strain tensor quantities (misfit volume, ξ , η) and their principal directions for an isolated solute and isolated S-H complex. Results for the vacancy “solute”, denoted V now, and for an isolated VH complex for the Ni-H EAM potential used here are shown in Table 3.2. Note that the maximum principal strain associated with VH can be oriented along one of three distinct crystallographic directions. We consider these differently-oriented VHs as different types of solutes, since they interact differently with the dislocation; we denote the three types of complexes as $\text{VH}^{(m)}$, ($m = 1, 2, 3$) with equal concentrations $c_m = c/3$ ($m = 1, 2, 3$) where c is the V concentration. For the V, the misfit strain is purely volumetric and so the interaction energy only involves the dislocation pressure field. For the VH complexes, the volumetric term is nearly zero but the deviatoric strains are not negligible, so that the interaction energy is dominated by the deviatoric field of the dislocation. Thus, there is a fundamental change in the nature of the dislocation/vacancy interactions upon the introduction of H to form the VH complex. Fig. 3.6 illustrates the angular variation of the normalized deviatoric and volumetric components of the interaction energy density for a V and each $\text{VH}^{(m)}$ complex as computed by Eqs. (10) for a singular Volterra dislocation. Clearly, the angular dependence of the interaction energy of VH is different from that of V. Most importantly, the maximum interaction energy is *reduced* by 44% by the addition of H. Thus, the theory predicts that Hydrogen should have a significant *softening* effect (lower stress to move a dislocation) when interacting with suitable solutes. Considering that (i) a realistic dislocation is dissociated into two partials, (ii) the largest interaction energies occur close to the core, and (iii) the theory depends on the *difference* in dislocation stress field at w_c and at the origin (with w_c typically emerging as comparable to the dissociation distance), the angular dependence shown in Fig. 3.6 does not translate directly into a precise prediction for the change in flow stress upon addition of H. But a softening effect is expected due to the overall reduction in interaction energies. We next show this explicitly in the atomistic simulations.

Table 3.2 – Parameters describing the misfit strain tensor of each type of solutes.

solute	ξ	η	$\frac{\Delta V}{V}$	\mathbf{e}'_1	\mathbf{e}'_2	\mathbf{e}'_3
$\text{VH}^{(1)}$	1.0	-1.7857	0.00836	[100]	[010]	[001]
$\text{VH}^{(2)}$	1.0	-1.7857	0.00836	[010]	[001]	[100]
$\text{VH}^{(3)}$	1.0	-1.7857	0.00836	[001]	[100]	[010]
V	1.0	1.0	-0.16168	-	-	-

To demonstrate the expected softening effect of hydrogen, we study specimens with a range of solute (V) or VH complex concentrations from 0.5% to 3.5%. These are realistic concentrations for real solutes in metal alloys, and are not relevant for real vacancies; recall that the vacancies here are *surrogates* for solutes. The corresponding concentration

3.4. Hardening/softening effects of H atoms in nickel alloys

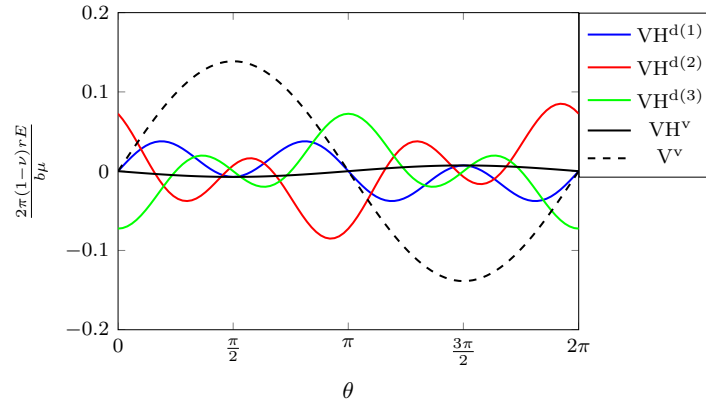


Figure 3.6 – Normalized volumetric and deviatoric parts of the interaction energy as a function of polar angle around a Volterra edge dislocation, for different orientations of the VH solute complexes studied here.

of VH complexes implies that the H concentration is 0.5% to 3.5%, which is much higher than nominal concentrations at which H embrittlement is observed. However, elevated H concentrations could be anticipated around crack tips. Dislocations themselves can transport H via “solute drag”, and so the dislocation plasticity around a crack may itself serve as a means to provide the H that can bind to solutes and reduce the flow stress around the crack. Thus, our studies here, while meant to be illustrative of the phenomenon, are within the scope of realistic material systems given mechanisms of local enhancement of the H concentration.

Fig. 3.7 shows the dislocation position versus applied shear stress as obtained from the MD simulations for specimens with different concentrations of V and VH complexes. Multiple random solute arrangements are shown for each average concentration. For each random solute arrangement, two curves are shown corresponding to the cases without (solid lines) and with (dashed lines) H. In every specimen, the stress at any given dislocation position is always lower in the presence of H. That is, in every specimen, H softens/reduces the flow stress of that specific specimen. This is the main result of this chapter.

The general occurrence of softening is independent of the glide distance. However, the step-wise nature of the stress vs. glide distance found in all specimens requires some remarks. The nominally straight dislocation segment encounters different random solute environments as it glides. It will, therefore, get pinned at statistically stronger binding regions as it glides. An increasing stress is thus required to overcome each successive barrier. However, since the distribution of barriers is expected to be Gaussian with standard deviation $\sigma_{\Delta E_{\text{int}}}$, stronger binding regions become increasingly unlikely. Thus, at a certain stress level, the dislocation becomes unpinned and does not encounter any

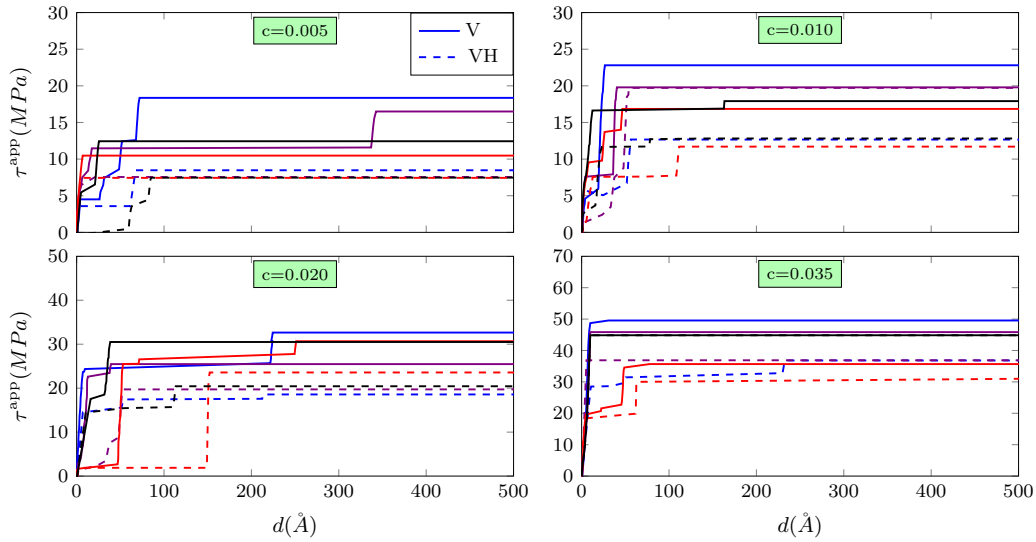


Figure 3.7 – Applied shear stress τ^{app} versus dislocation glide distance d , for several concentrations of solutes V (solid lines) and VH (dashed lines) solutes in fcc Nickel. Same-color solid and dashed lines show results for the same spatial distribution of solutes.

stronger-binding region in the remainder of the sample. The statistical distribution of binding regions thus gives rise to the stochastic pinning and depinning, culminating in a final stage of unabated glide. In addition, variations in the location of the pinning points between the otherwise identical V and VH specimens arises because of the differences in spatial variations of the interaction energy, as shown for the Volterra dislocation in Fig. (3.6). Specifically, the specific fluctuations in spatial V distribution that give rise to the pinning in the presence of vacancies only are not necessarily the same as the fluctuations in spatial VH distribution that give rise to pinning in the presence of H.

Turning to a more quantitative assessment of the results, for comparison purposes, we consider the maximum shear stress (the stress at which the dislocation undergoes glide through the remainder of the specimen) as a nominal “strength” that should scale with the predicted τ_{y0} . Based on arguments above, we expect this strength to be larger than the true strength of a long dislocation undergoing roughening because it corresponds to a pinning strength that scales with, but is larger than, $\sigma_{\Delta E_{\text{int}}}$. As guided by the theory, Fig. 3.8 shows the strength as a function of the square root of solute concentration, with a linear fit at small concentrations as a guide to the eye. At low concentrations, the measured strength scales directly with $c^{1/2}$ and the samples with H are clearly statistically weaker than those without H. Thus, there is a distinct softening effect that scales according to the general solute strengthening theory. The deviation from $c^{1/2}$ at the highest concentration could be due to the increasing occurrence of divacancies or

3.4. Hardening/softening effects of H atoms in nickel alloys

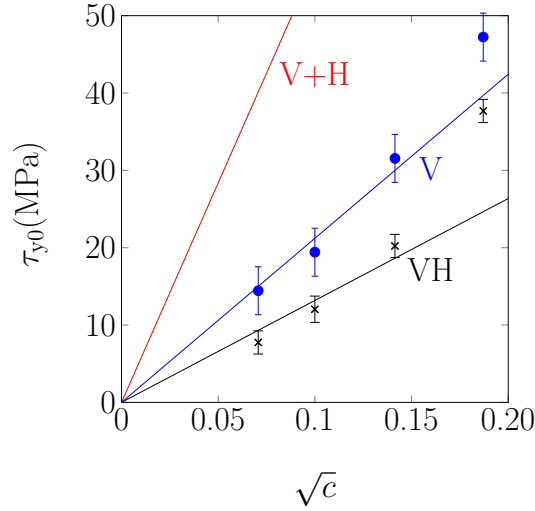


Figure 3.8 – Shear yield stress τ_{y0} as a function of the solute concentration.

other V clusters that modify the effective misfit volume of each solute, but even here the samples with H are consistently weaker than those without H.

Another interesting observation in Fig. 3.8 is the fact that based on the calculations given in previous section H atoms themselves can strengthen the material. We can envision that H atoms before binding to the vacancies are in the interstitial sites at bulk. Using Eq. (3.33), one can easily find the $\tau_{y0}-\sqrt{c}$ relation for the $V + H$ case in which both vacancies and H atoms are present in the material. This relation is shown by the red line in Fig. 3.8.

When H atoms and the vacancies bind together the strength decreases to the values that are given in that Figure. However, one needs to be careful about the initial state of the alloy. In the most physical cases the concentration of the lattice hydrogen atoms is far lower than the solutes in the alloys. Thus, they will bind to a fraction of solutes in the equilibrium state. Thus, there would not much hydrogen to strengthen the metal. But if the chemical potential of H atoms is kept constant, then there exist bulk H atoms, S–H complexes, and solutes in the material which are in thermodynamic equilibrium with the chemical potential. Now, if a defect like a crack or a dislocation is nucleated, the stress field of it would attract the bulk hydrogen atoms and increase the local concentration of them in close vicinity of the defect. Then these newly arrived H atoms can bind to the isolated solutes and softening happens. Quantification of this process needs further investigation.

Thus, in any case we can conclude that the softening effects of H atoms in alloys is significant.

Chapter 3. Softening and hardening of yield stress by hydrogen interstitials

The samples with H are approximately 40% weaker than the samples without H. This is comparable to the ratio of the root mean square interaction energies for the three VH types (37%), indicating that the interaction energy change is the dominant factor in the softening. The theory parameter w_c is, however, a function of the interaction energies as well and so, in principle, can vary between the V and VH systems, leading to some differences in strengthening. Prior results for solute strengthening suggest, however, that variations in w_c among different solutes in the same matrix are modest. For instance, in an Al matrix, $w_c = 15.7\text{\AA}$ for Mg (misfit volume $+5.7\text{\AA}^3$) while $w_c = 18.6\text{\AA}$ for Mn (misfit volume -13.3\AA^3) [89].

Our results here demonstrate, perhaps for the first time, a clear mechanism for the reduction of plastic flow stress due to the presence of hydrogen in an fcc metallic alloy. This softening is not necessarily unexpected, from the perspective of solute strengthening theory, but there has been no prior detailed analysis nor simulation study to firmly establish the phenomenon. The analysis here shows, however, that softening is expected only if the overall misfit strain tensor of the Solute-H complex is smaller than the Solute alone. H has a positive misfit volume, since it is interstitial, and hence solutes that also have positive misfit volumes are unlikely to be "relaxed" by the introduction of H. In general, the presence of H will likely introduce additional tetragonal distortions, which should also generally contribute to strengthening, since the theory shows that volumetric and deviatoric contributions are generally additive according to a geometric rule. Since, however, the full theory requires computation of the detailed interactions of the realistic dislocation structure with the Solute or Solute-H entities, out of which also emerges characteristic length scales ζ_c and w_c , it remains possible that softening may not occur even when the changes in misfit strain tensor suggest it. Nonetheless, a combination of solute strengthening theory [87, 88, 89] and first-principles calculations of Solute and Solute-H misfit strains can provide solid guidelines for anticipating H-induced softening in general and estimating the magnitude of the softening. Computation of Solute and Solute-H misfit strains can be accomplished using moderate-sized unit cells, and so is quite feasible with modern computational power; we discuss this in detail in the next Section.

3.4.4 Interaction of Carbon and Sulfur solutes with Hydrogen in Nickel

To demonstrate the general procedure for studying the energetic *and mechanical* interaction of hydrogen and solute atoms, we analyze the interaction of hydrogen atoms with the pre-existing solute/impurity atoms Sulfur and Carbon in fcc Nickel. First principles calculations are carried out using density functional theory (DFT) as implemented in the Vienna *Ab initio* Simulation Package (VASP) [122, 123]. Exchange and correlation are treated within the generalized gradient approximation (GGA) with the Perdew-Burke-Ernzerhof (PBE) parametrization [124]. Core electrons are replaced by the projector augmented wave (PAW) pseudopotentials [125]. The one-particle electronic

3.4. Hardening/softening effects of H atoms in nickel alloys

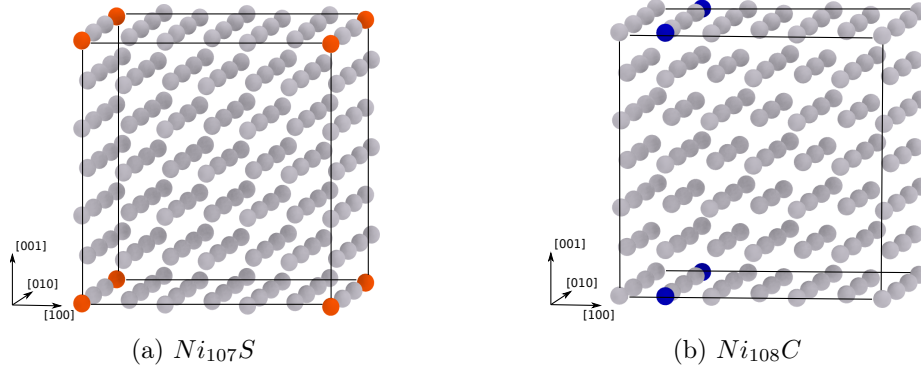


Figure 3.9 – Supercells containing (a) a substitutional S solute and (b) an interstitial C solute at the octahedral site. Gray, dark blue, and orange spheres denote the Ni, C, and S atoms, respectively.

eigenstates are calculated based on a spin-polarized plane-wave basis set with the cutoff energy of 500 eV and a second-order Methfessel-Paxton method [126] with 0.2 eV used to smear the partial occupancies. For the reciprocal space integrations, a Γ -centered Monkhorst-Pack [127] k -point sampling of $28 \times 28 \times 28$ is used for the 4-atom cubic unit cell and the density of this k -point mesh is kept consistent for supercells with larger dimensions. Based on the parameters mentioned above, Ni in stress-free bulk state is predicted to have lattice constant and elastic constants of $a = 3.524 \text{ \AA}$, $C_{11} = 273 \text{ GPa}$, $C_{12} = 157 \text{ GPa}$, and $C_{44} = 129 \text{ GPa}$, all close to the extrapolation of the experimental values to 0K ($C_{11} = 261.2 \text{ GPa}$, $C_{12} = 150.8 \text{ GPa}$, and $C_{44} = 131.7 \text{ GPa}$) [128]. We also obtain a magnetic moment of $0.64 \mu_B$ per atom close to the value of $0.62 \mu_B$ obtained by extrapolation of experimental values to 0K [129].

The typical geometry of the supercells containing S substitutional and C interstitial atoms are shown in Fig 3.9. The interaction energy of H with a solute X ($X=C$ or S) is calculated as

$$E_{X-H}^{\text{int}} = E_{X-H} - (E_H + E_X - E_{Ni}), \quad (3.34)$$

where E_{X-H} , E_X are E_H are the energies of supercells containing bulk Ni atoms with a $X-H$, X , and H solutes, respectively. E_{Ni} denotes the energy of the pure Ni supercell. The interaction energy E_{X-H}^{int} can be alternatively defined as $E_{X-H} - E^{\text{large}}$, where E^{large} is the energy of the system with isolated (non-interacting) solutes X and H located far from each other. We tested the values of E_{X-H}^{int} obtained from Eq. (3.34) against the results of the alternative formulation obtained from supercells of $3 \times 3 \times 3$ and $5 \times 3 \times 3$, in which the distance between X and H are $\approx 9 \text{ \AA}$ and $\approx 12 \text{ \AA}$, respectively, and good agreement is obtained between the two methods. To accurately obtain the misfit volume and misfit strain tensor, we performed calculations on various supercell sizes by duplicating the 4-atom unit cell to larger dimensions, $m_1 \times m_2 \times m_3$. After introducing the solute atom(s),

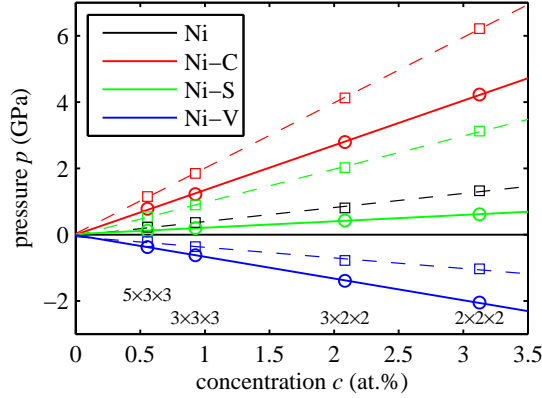


Figure 3.10 – Supercell pressure versus concentration for different solute complexes. Solid and dashed lines denote the cases without and with H atoms, respectively.

all the ions are fully relaxed until the maximum force is less than $1 \text{ meV}/\text{\AA}$ while holding the lattices of the supercell fixed at the pure Ni values ($m_i a$). For bulk Ni, although the supercells are constructed based on the stress-free unit cell, the stress tensors from the supercells of bulk Ni are quite small but not exactly zero. Therefore, in the following analysis, we eliminate effects of this stress by measuring only the stress tensor caused by the defect (i.e., $\sigma_X - \sigma_{Ni}$). In Fig. 3.10, good linear relationships are observed between the pressure (i.e., $-\frac{\sigma_{11} + \sigma_{22} + \sigma_{33}}{3}$) and the defect concentration. According to [89], the misfit volume of the defect can be obtained as

$$\frac{\delta V}{V} = \frac{1}{B} \frac{dp}{dc}, \quad (3.35)$$

where $B = 196 \text{ GPa}$ and $\frac{dp}{dc}$ are the bulk modulus of bulk Ni and the slope of the pressure–concentration curve, both obtained from our DFT calculations. For the misfit strain tensor, we choose one specific supercell, $3 \times 3 \times 3$, for all complexes and calculate the misfit strain associated with the measured stress state via Hooke’s Law, i.e., $\bar{\epsilon}^{(m)} = \mathbf{C}^{-1} \boldsymbol{\sigma}$. The stresses are measured in a large cell whereas the misfit strain tensor associated with the primitive unit cell. Thus, the measured misfit strain is converted to the true misfit strain via

$$\boldsymbol{\epsilon}^{(m)} = 4m_1 m_2 m_3 \bar{\boldsymbol{\epsilon}}^{(m)}.$$

The computed misfit strain tensors and H-Solute binding energies are summarized in Table 3.3. For S substitutional solutes, the misfit strain tensor is volumetric and positive. The interaction energy of an H atom at the octahedral site adjacent to this solute (see Fig. 3.11) is repulsive but relatively small (0.022 eV). However, the misfit volume of the S–H complex is 410% larger than that of a single S. The S–H misfit volume is also 62%

3.4. Hardening/softening effects of H atoms in nickel alloys

larger than the sum of the misfit volumes of isolated S and H interstitials, indicating significant mechanical distortions. The larger misfit volume with low repulsion suggests that, in the presence of the stress field of the dislocation, H atoms could diffuse to the S atoms on the tension side of the dislocation core, where both S and H are already favorable, and overcome the repulsive energy to form S–H complexes that have a larger misfit volume and thus are more favorable on the tensile side of the dislocation. The S–H complex also has a tetragonal distortion, indicating that it can interact with a screw dislocation whereas the individual H and S (away from the immediate screw core) would not interact with the screw dislocation. However, this tetragonal distortion is not significant.

For interstitial carbon, which occupies the octahedral site, the misfit strain tensor is also volumetric. The misfit volume of it is large. Adding a hydrogen interstitial on the tetrahedral site (see Fig. 3.11) increases the misfit volume 47%, which is only slightly larger (11.4%) than the sum of the misfit volumes of a single H and C interstitials. The misfit strain of this complex is also almost volumetric. However, the interaction energy of these two interstitials is repulsive and large ($\approx 0.73\text{eV}$). Since the change in misfit volume is small, formation of this complex is unlikely even in the vicinity of a dislocation.

Table 3.3 – Misfit strain tensor parameters for S and C atoms, and SH and CH complexes, in Ni.

solute	ξ	η	$\frac{\Delta V}{V}$	\mathbf{e}'_1	\mathbf{e}'_2	\mathbf{e}'_3	$E^{\text{int}}(\text{eV})$
H	1.0	1.0	0.2168	-	-	-	-
S	1.0	1.0	0.0985	-	-	-	-
S–H	0.877	0.877	0.5116	[100]	[010]	[001]	0.022
C	1.0	1.0	0.6882	-	-	-	-
C–H	0.796	0.796	1.0082	$[\bar{1}\bar{1}\bar{1}]$	$[\bar{1}\bar{1}0]$	[112]	0.734

S atoms are well-established embrittlers in Ni, being attracted to the grain boundaries. Co-segregation of S and H to the grain boundaries has been found to enhance embrittlement [130]. Thus the examination of S–H complexes at grain boundaries is a natural direction for future work. Here we simply conclude that S and H repel in the bulk lattice, and that any formation of an S–H complex would lead to an increased misfit strain and thus strengthening, rather than softening. For C, co-segregation of H and C is not expected. In contrast to VH case, the misfit distortion of S–H and C–H complexes are negligible. Thus misfit distortions of S–H and C–H do not play a significant role in hardening or softening of fcc–Ni.

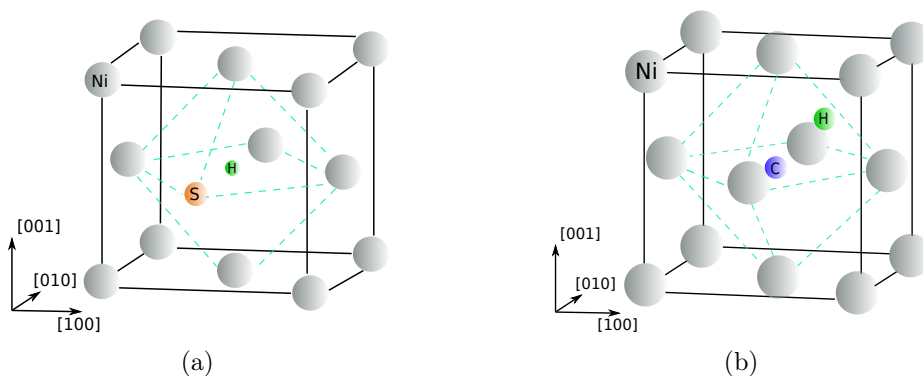


Figure 3.11 – Stable position of hydrogen interstitial in the vicinity of (a) a substitutional Sulfur atom and (b) an interstitial Carbon atom. Gray, dark blue, and orange spheres denote the Ni, C, and S atoms, respectively.

3.5 Summary

In summary, we first showed that H atoms can have strengthening effects on the flow properties of nickel. The results of the solute strengthening theory are in good agreement with the experimental results of the yield strength of polycrystalline nickel at low temperature. This observation implies that no hydrogen enhanced global plasticity (HEGP) process is anticipated in the low-temperature regimes.

Moreover, we have demonstrated that a softening effect (reduction in the stress required to move a dislocation) can be caused by the interaction of H atoms with solutes in fcc metal alloys. The softening arises when the Solute-H complex leads to a reduction in the misfit strain tensor, and we have used vacancies as a surrogate solute in a Ni matrix to demonstrate the effect. Interestingly, the softening effect is due to neutralization of the strengthening effects of H and vacancies. The simulation results are consistent with the predictions of solute strengthening theory, for both the scaling of the strength versus solute concentration and the magnitude of the softening. These results are perhaps the first atomistic simulations to support any mechanism for the proposed HELP theory in fcc metals, although connections to hydrogen embrittlement remain to be discovered. Solute-H strengthening is also possible and is indicated here by detailed DFT computations for S-H and C-H complexes in Ni. Thus, softening is not a generic effect and will only arise in specific alloy systems. Our DFT analyses for S and C shows the operational path for assessing any solute of interest in any fcc matrix material. There are also other possible effects of H on plastic softening or strengthening that are not considered here. For instance, “solute drag” strengthening by relatively mobile H should serve as a generic strengthening mechanism. H interactions that modify solute interactions in the very core of the dislocation may lead to either softening or strengthening; assessment of such possibilities would require extensive multiscale simulations [131]. H might influence dislocation/dislocation junction strengths, leading to strengthening or softening, similar to

3.5. Summary

Dynamic Strain Aging in Al alloys [132]. In most of these situations, H transport appears necessary and so assessment of mechanisms must also address the kinetic aspects of H transport. The field thus remains rich for exploration, and with important implications for industrial applications of high strength metal alloys.

4 Hydrogen–vacancy–dislocation interactions in α -Fe

This chapter is extracted from the following publication:

- (1) Hydrogen–vacancy–dislocation interactions in α -Fe, A. Tehranchi, X. Zhang, G. Lu, and W. A. Curtin, Modeling and simulations in material science and engineering, Volume 25 2017,025001.

4.1 Introduction

Here, using a quantum-mechanics/molecular-mechanics method (QM/MM), we find that the configuration of a single vacancy in the Fe edge dislocation core differs from that predicted by the Fe EAM potential. However, both QM/MM and EAM based simulations predict that a single vacancy located on the compressive glide plane of the dislocation can be transported with the dislocation as the dislocation glides. We then show, using Molecular dynamics (MD) simulations based on the EAM potential that, when a gliding dislocation interacts with various vacancy/hydrogen clusters in the glide plane of the dislocation, the dislocation will annihilate vacancies and form jogs, leaving behind smaller or zero vacancy clusters in its wake. Most importantly, this process is largely independent of the presence of hydrogen. These processes are driven by the very large energy reduction associated with annihilating energetically-costly vacancies in Fe. Therefore, we conclude that neither dislocations nor hydrogen play any clearly positive role in the formation of vacancy clusters and, thus, that nanovoid formation by the processes envisioned in recent work is not operative. We discuss other possible mechanisms for the vacancy accumulation/void creation process that might be assisted by the presence of hydrogen.

The remainder of this chapter is organized as follows. In Section 2, we described the simulation details. In Section 3, we present important benchmark energies for various configurations involving vacancies, hydrogen atoms, and/or dislocations, as computed

using molecular statics (MS) simulations with QM/MM and/or the Fe–H EAM potential. In Section 4, we present results on the reactions of vacancies or vacancy clusters with edge dislocations in Fe, with and without hydrogen. In Section 5, we discuss our results and their implications for hydrogen-assisted nanovoid formation.

4.2 Simulation Details

For MD simulations based on the Fe–H EAM potential, which constitute the majority of the studies in this chapter, we construct a rectangular simulation cell comprised of a bcc Fe crystal oriented with $X = [111]$, $Y = [1\bar{1}0]$ and $Z = [11\bar{2}]$, and of dimensions $L_x = 494 \text{ \AA}$, $L_y = 146 \text{ \AA}$ and $L_z = 280 \text{ \AA}$ as illustrated in Fig. 4.1. For problems involving a dislocation, we introduce a single edge dislocation of Burgers vector $1/2[111](1\bar{1}0)$ with line direction along Z and lying in the $Y=0$ plane. The edge dislocation is created by removing atoms from the perfect crystal in the narrow strip $-\sqrt{3}a_0/4 < X - X_0 < \sqrt{3}a_0/4$, $Y < 0$, where $a_0 = 2.86 \text{ \AA}$ is the lattice constant for α -Fe and X_0 is the X coordinate of the dislocation. All remaining atoms are then displaced according to the linear elastic displacement field for the edge dislocation [133], and the entire structure is relaxed using the conjugate gradient method [95]. The simulation cell is periodic along Z and along X , the latter introducing an artificial bending that does not, however, create any shear stress along the dislocation slip plane. Vacancies (V) are introduced at desired positions by removing the occupying Fe atom. H atoms are introduced by inserting them into the desired tetrahedral interstitial sites of the lattice or near-tetrahedral sites around vacancies. Various geometries are considered, as discussed below.

To drive dislocation motion, the system is loaded by applied forces on the Y surfaces corresponding to a desired resolved shear stress. MD simulations are performed in an NVT ensemble with a Langevin thermostat [97] using the velocity–Verlet algorithm [96] with the integration time step of 1 fs. The temperature of the system is fixed at $10^{-3}K$, so that MD is very nearly equivalent to a steepest-descent minimization. The molecular dynamics simulations are performed using the Large-scale Atomic/Molecular Massively Parallel Simulator (LAMMPS) [93] and atomic configurations are visualized using the Open Visualization Tool (OVITO) [94].

Interatomic interactions among atoms are described using an EAM potential introduced by Ramasubramaniam et al. [134] and modified by Song and Curtin [49] to prevent unphysical H aggregation in single-crystal Fe. The Peierls stress required to initiate dislocation glide is computed as 100 MPa, and all simulations involving dislocation glide reported below are thus executed at stresses slightly above 100 MPa. The potential used in the simulations is essentially identical to that used in the recent study of V–H–dislocation interactions [47]. To assess the validity of this potential for our studies involving Fe, H, and V, we have made comparisons of various energies as well as the structure of the core of the dislocation with and without a vacancy with the energies and structures obtained via the

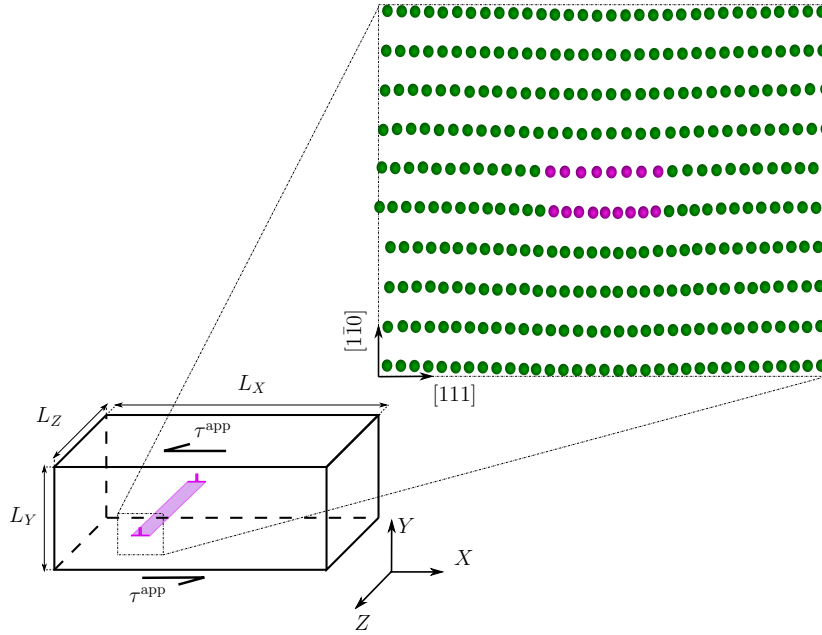


Figure 4.1 – Schematic of the simulation cell used to study edge dislocation/vacancy/hydrogen interactions. Color coding uses due to Common Neighbor Analysis with green indicating a bcc environment and purple indicating non-bcc environments.

QM/MM method. The QM/MM method is that developed by Lu et al. [65, 66, 67], which has previously been used to study interaction of hydrogen interstitials and dislocations in bcc Fe [135]. Stand-alone density functional theory (DFT) studies for point defects (V and H) were also performed in $4 \times 4 \times 4$ cubic unit cells with periodic boundary conditions. All DFT calculations are implemented in VASP [136, 122] with the projector augmented wave pseudopotentials (PAW) [124]. The energy cut off for the plane wave basis is set to be 300 eV and a $3 \times 3 \times 3$ Monkhorst–Pack [127] k-point mesh is used. The exchange and correlation function is approximated by the Perdew-Burke-Ernzerhof generalized gradient approximation (PBE-GGA) [124]. In QM/MM calculations, the EAM potential of Fe proposed by Shastry and Farkas [137] is employed in the MM region. This potential is rescaled to give the same lattice parameter and bulk modulus as those of the DFT calculations. The entire QM/MM system size is $202\text{\AA} \times 202\text{\AA} \times 6.25\text{\AA}$ in $[111]$, $[\bar{1}10]$ and $[\bar{1}\bar{1}2]$ directions. The dimensions of the QM region are $21\text{\AA} \times 10\text{\AA} \times 6.25\text{\AA}$. The k-point mesh of $1 \times 1 \times 5$ is used in the constrained DFT scheme.

4.3 Vacancy/Hydrogen/Dislocation interaction energies in Fe

A range of defect energies have been computed using molecular statics with DFT, the QM/MM method, or the Fe-H EAM potential. The results are summarized in Table 1.

Chapter 4. Hydrogen–vacancy–dislocation interactions in α -Fe

The vacancy formation energy in bulk bcc Fe is computed to be $E_V^f = 1.73\text{eV}$ for the EAM potential as compared to $E_V^f = 2.17\text{eV}$ as computed with QM/MM and also with standard periodic-cell DFT. The vacancy/hydrogen binding energy for VH_n clusters was reported previously [49] for $n=1-6$, with the EAM potential in generally good agreement with standard DFT studies. The difference between the binding energies calculated by DFT and EAM potential for all n except $n = 4$ were less than 0.05 eV. There is a large discrepancy in the results of DFT (-0.3 eV) and EAM (+0.08 eV) for $n = 4$, but this discrepancy has no significant effect on the analysis in this work. For the VH clusters, the EAM potential predicts $E_{VH}^b = 0.537$ eV as compared to the the DFT value of $E_{VH}^b = 0.62$ eV. The binding energy of a divacancy is computed to be 0.14 eV using the EAM potential and 0.16 eV in DFT. The structures of the Fe edge dislocation as predicted by the QM/MM method and the simulations based on the EAM potentials are shown in Figure 4.2. The two structures are in very good agreement.

Table 4.1 – Hydrogen-Vacancy-Dislocation interaction energies and barriers as calculated via DFT, QM/MM, and EAM interatomic potentials. E_V^f , E_{VH}^b , E_{VV}^b , E_{d-V}^{int} , E_{d-H}^b , E_{V-d}^m , E_{V-H}^b , E_{d-VH}^m , are the formation energy of a single vacancy, vacancy–H binding energy, vacancy–vacancy binding energy, dislocation–vacancy interaction energy, dislocation–H binding energy, migration barrier of a vacancy in the dislocation core, binding energy of a VH cluster in the dislocation core, and migration barrier of VH in the core of the dislocation, respectively.

	Stand alone DFT	QM/MM	EAM
E_V^f (eV)	2.17	-	1.73
E_{VH}^b (eV)	0.62	-	0.537
E_{VV}^b (eV)	0.16	-	0.14
E_{d-V}^{int} (eV)	-	-1.47	-1.08
Max E_{d-H}^b (eV)	-	0.47	0.37
E_{V-d}^m (eV)	-	0.14	0.1
E_{V-H}^b (eV)	-	1.617	1.677
E_{d-VH}^m (eV)	-	-	0.58

In the presence of the dislocation, a vacancy is placed in the center of the dislocation on the compressive side of the glide plane, where the vacancy should be most favorable due to its negative misfit volume. The interaction energy E_{d-V}^{int} between this V and the edge dislocation is computed as

$$E_{d-V}^{\text{int}} = E_{d-V} - (E_d + E_{\text{Fe}}^{\text{coh}} + E_V^f) \quad (4.1)$$

where E_d is the energy of the system with just the dislocation, $E_{\text{Fe}}^{\text{coh}}$ is the bulk Fe cohesive energy, E_V^f is the bulk vacancy formation energy, and E_{d-V} is the energy of the system with the vacancy in the dislocation core. The V/dislocation interaction energy is $E_{d-V}^{\text{int}} = -1.08$ eV for the EAM potential and -1.47 eV for the QM/MM method.

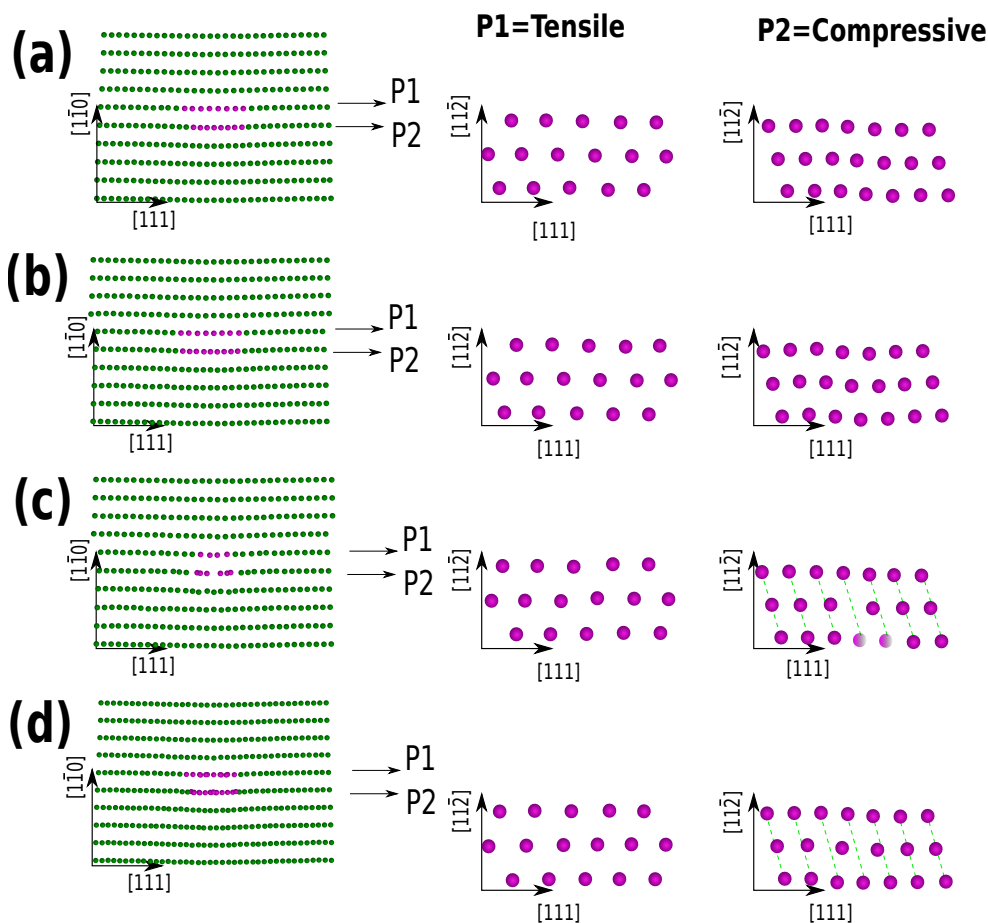


Figure 4.2 – The atomistic structure of an edge dislocation core in Fe as computed by molecular statics simulations using (a) the Fe-H EAM potential and (b) the QM/MM method. Blue symbols denote atoms in a local bcc environment and red symbols indicate all other atom environments. With a vacancy located on the first plane on the compressive side of the glide plane, and in the middle of the core, the computed structures are computed with (c) the QM/MM method and (d) the Fe-H EAM potential [134].

The difference between simulations based on EAM potentials and QM/MM for the vacancy in the core is thus nearly identical to the difference in formation energy. Thus, while the EAM predicts a rather weaker binding of the V to the dislocation core, the energy gain associated with vacancy annihilation in the core (see below) is nearly the same for EAM and QM/MM. In spite of the similar trends in energy, the configuration of the V/dislocation system obtained by QM/MM and EAM based calculations are quite different, as seen in Figure 4.2c. In the QM/MM model, the vacancy occupies a substitutional lattice position, with displacements of the surrounding Fe atoms toward the vacancy site. In contrast, in the EAM model the vacancy is shared by two atomic sites such that a single Fe atom sits in between two lattice sites.

Hydrogen/dislocation interactions have been previously studied using a related QM/MM method [135]. The largest interaction energy occurs for an H atom on the tensile side of the core, due to the positive misfit volume of H in the tetrahedral interstitial sites of the Fe lattice. The interaction energy at this site is -0.37 eV using the EAM potential as compared to -0.47 eV obtained from the QM/MM method. Thus, the EAM potential slightly underpredicts H binding to the core, but this difference will have limited effect on most results below. For an H atom on the compressive side of the core, the interaction is unfavorable with the EAM potential predicting an interaction energy of 0.118 eV.

4.4 Reactions of dislocations with Vacancy-Hydrogen clusters

We now address issues associated with moving dislocations interacting with a variety of vacancy/hydrogen clusters. For a single vacancy located ahead of the dislocation on the first plane on the compression side of the dislocation, the EAM potential predicts that the vacancy is indeed absorbed by the dislocation and transported along with it as reported in [47]. This behavior is unexpected, since the migration barrier for V in bulk Fe is 0.6 eV. However, the binding energy of a V in the core of the dislocation is quite large and the equilibrium position shows that the V is shared between two lattice sites, i.e. an Fe atom moves to a position in between two lattice sites (see Figure 4.2d). As a result of this local configuration, V migration in the glide direction can occur with a very low energy barrier. A Nudged Elastic Band (NEB) calculation using the EAM potential at zero stress shows that the migration barrier for V from the initial position to a neighboring position in the core is less than 0.1 eV, with the neighboring site have an energy only 0.08 eV larger. Thus, as the dislocation glides under the action of an applied stress, a V on the compressive side of the core can easily be dragged along with the dislocation. The QM/MM shows the same final result but with a different mechanism for transport of the single vacancy. When the vacancy is placed in the site neighboring the low energy site, the vacancy is mechanical unstable and moves back to the central low-energy position. Thus, as the dislocation glides, the vacancy follows relaxing into the (moving) low-energy site. When the dislocation glides by a single Burger's vector, the vacancy diffuses to the next atomic site to restore its original favorable position within the core. The nudged elastic band calculations show that the energy barrier for this diffusion process is 0.14 eV which is not significantly higher than that obtained from the molecular statics simulations based on the Fe-H EAM potential. For both EAM based simulations and QM/MM, a single vacancy can be transported along with a gliding edge dislocation. However, this conclusion holds only for a vacancy on the immediate compression plane below the glide plane. Both the EAM and QM/MM simulations show that a single vacancy in the second plane on the compression side of the dislocation, or on the first plane on the tension side, is not transported along with the dislocation. The binding energy and activation barrier away from the core, i.e. within a local bcc-like environment, does not allow for

4.4. Reactions of dislocations with Vacancy-Hydrogen clusters

near-barrierless transport of the vacancy. Therefore, the observation reported in [47] is limited to a single atomistic plane.

In the remainder of this section, we examine the interaction of vacancy and vacancy clusters with and without hydrogen by explicit molecular statics simulations using the Fe-H EAM potential.

The strong binding of V in the core (~ 1 eV for this potential, ~ 1.47 eV for DFT) provides a high driving force for the V to remain associated with the dislocation core as it glides. However, when a single vacancy being transported by the dislocation encounters an H atom in the lattice, the V and H bind together and are not transported with the dislocation, i.e. the dislocation moves forward leaving behind the VH cluster as reported in [47]. The energetics of this process is unfavorable: the strongest binding of the VH cluster in the dislocation core is 1.617 eV, which is much larger than the energy 0.537 eV of the VH cluster in the bulk. Thus, the lack of transport is presumably a kinetic issue. An NEB calculation shows that the energy barrier for diffusion of a VH complex from its minimum energy site within the core to the adjacent stable site is 0.68 eV, while the energy of VH in this stable site is 0.37 eV higher than its energy in the minimum energy site. Thus diffusion of VH within the core is not likely on MD time scales. Since the energy barrier for diffusion of individual H atoms and vacancies within the core of the dislocation are quite low, another possible mechanism is the separation of the VH followed by individual diffusion of the V and the H, and finally recombination to form VH. But the NEB calculations show that the separation of H and V requires an activation energy of 0.58 eV so that this separation is unlikely to occur within MD timescales. Dissociation of the VH cluster in the core is most favorable when the H is on the compression side of the glide plane, where it is unlikely to be found, and the H then migrates to the tensile side of the glide plane of the dislocation core.

With the VH cluster left behind a gliding dislocation, a second vacancy transported by a second dislocation to some positions near a previous VH cluster can bind to the VH to form a V_2H cluster. This cluster also remains behind as the second dislocation continues to glide. However, if this vacancy is in the atomic row adjacent to the VH cluster, the vacancies are annihilated and a double jog is formed, with the lone H atom left behind as the now-jogged dislocation continues to glide. Thus, the original VH cluster disappears entirely. This basic process establishes that stability of V-H clusters is easily defeated by vacancy annihilation and jog formation. Vacancy annihilation by dislocation climb, with associated formation of jogs, is a well-established phenomenon in metals.

We now examine increasingly complex $V - H$ clusters. If a di-vacancy on the compressive side of the glide plane is oriented along the glide direction, the dislocation passes by without absorbing the vacancies. However, as shown in Figure 4.3a, if the divacancy is oriented parallel to the dislocation line, the dislocation absorbs the two vacancies and forms a double jog. The same behavior is observed when a dislocation encounters a V_2H_2 cluster, as shown in Figure 4.3b. For increasing H concentration in the divacancy, i.e.

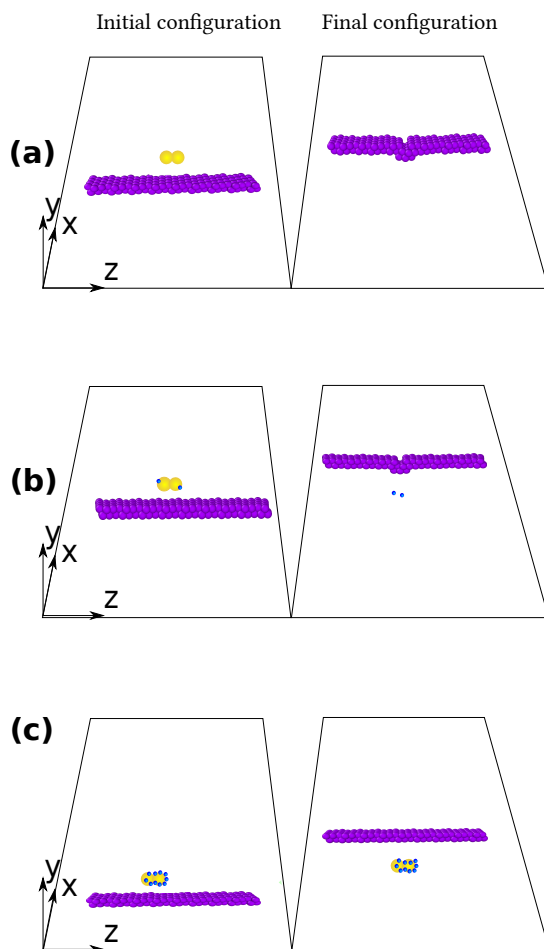


Figure 4.3 – Interaction of an edge dislocation with (a) V_2 (b) V_2H_2 (c) V_2H_{10} clusters.

V_2H_n $n > 2$, vacancy annihilation and jog formation occur up to $n = 8$. For $n = 10, 12$, the H atoms stabilize the divacancy cluster. Thus, H atoms only stabilize divacancies at when the H content is very high. For larger planar V_mH_n ($m > 2$) clusters lying in the compressive plane below the glide plane, annihilation and jog formation remain dominant. For a compact tri-vacancy cluster $m = 3, n = 0$, a double jog forms and only one vacancy remains. For V_3H_3 , the same process occurs but with a VH_3 cluster left behind. For a tri-vacancy cluster with vacancies aligned in a single atomic row parallel to the dislocation line, all three vacancies are annihilated by the dislocation in both hydrogen free ($n = 0$) and hydrogen ($n = 3$) cases. If the tri-vacancy cluster is aligned perpendicular to the dislocation line, then there is no annihilation and the dislocation simply passes by the cluster, with or without hydrogen. Table 2 summarizes the processes associated with the interaction of larger planar vacancy clusters on the compressive side of the glide plane and the edge dislocation. Results show that, with or without hydrogen, two or more of the vacancies are always absorbed to form a double jog separated by a short edge segment on the glide plane below the original glide plane. The dislocation with the

4.4. Reactions of dislocations with Vacancy-Hydrogen clusters

Table 4.2 – Reactions of an edge dislocation with various planar vacancy clusters, with and without hydrogen atoms. JD and D denote jogged and unjogged dislocations, respectively.

V_3	V_4	V_5
$V_3 + D \rightarrow JD + V$	$V_4 + D \rightarrow JD + V_2$	$V_5 + D \rightarrow JD + V$
$V_3H_1 + D \rightarrow JD + VH$	$V_4H + D \rightarrow JD + V_2H$	$V_5H_1 + D \rightarrow JD + V_2H$
$V_3H_2 + D \rightarrow JD + VH_2$	$V_4H_2 + D \rightarrow JD + V_2H_2$	$V_5H_2 + D \rightarrow JD + V_2H_2$
$V_3H_3 + D \rightarrow JD + VH_3$	$V_4H_3 + D \rightarrow JD + V_2H_3$	$V_5H_3 + D \rightarrow JD + V_2H_3$
-	$V_4H_4 + D \rightarrow JD + V_2H_4$	$V_5H_4 + D \rightarrow JD + V_2H_4$
-	-	$V_5H_5 + D \rightarrow JD + V_2H_5$

double-jog+climb defect continues to glide. The vacancy annihilation process is thus broadly favorable when there are at least two adjacent vacancies along the dislocation line direction, with or without hydrogen.

The processes observed above can be understood by examining the energetics of the reactions. Starting from a V_nH_m cluster and a straight dislocation denoted by D , the reaction that annihilates n' vacancies and nucleates a double-jogged dislocation denoted as JD can be written as $V_nH_m + D \rightarrow V_{n-n'}H_m + JD$. The change in total energy of the system for this reaction is $-n'E_V^f + E_{V_nH_m}^b - E_{V_{n-n'}H_m}^b + 2E_J$, where $E_{V_nH_m}^b$ is the formation energy of a V_nH_m cluster relative to n isolated V and m isolated H in the lattice and E_J is the formation energy of a single jog. Here we neglect the elastic jog-jog interaction energy. Since the vacancy formation energy is much larger, $\sim 1.7eV$, than the typical binding energies of V and H in clusters (at most ~ 0.6 eV), and the jog energy is not large, the process of double-jog formation is usually energetically favorable even in the presence of hydrogen atoms. For example, for a V_2H_2 cluster, the annihilation of the two vacancies lowers the energy by $\sim 3.4eV$ while the loss of two V-H interactions increases the energy by $\sim 1.24eV$ leading to a very large decrease of $\sim 2.16eV$ in the total energy. The only cases we have studied where a V_nH_m cluster is stable are the V_2H_m clusters with $m \geq 10$, where all H atoms reside in the bulk lattice after annihilation.

Growing voids by the accumulation of vacancies is thus generally expected to be defeated by annihilation to form double jogs. To study this further, we imagine that V_mH_n clusters can diffuse and join to form larger nanovoids consisting of near-spherical clusters of vacancies, and analyze dislocation interactions with such nanovoids. We form equiaxed clusters of sizes $n = 9, 17, 25, 33, 41, 49$ with the center located on the compressive glide plane of an approaching dislocation. For all cases, the dislocation is pinned by the nanovoid, as expected. With increasing applied stress the dislocation bows out and eventually

moves past the nanovoid. In all cases, the escape process is accompanied by double jog formation, as shown in Figure 4.4 for a V_{49} nanovoid. In the jog formation process, the void loses the outermost vacancies on the compressive glide plane of the dislocation, and so the size of the cluster is reduced by the jog formation process. The behavior is not altered by the presence of hydrogen. Specifically, for nanovoids of composition V_9H_{9n} , and $V_{25}H_{25n}$ with $n = 1, 2, \dots, 5$, the hydrogen atoms do not suppress annihilation and jog formation. For a much larger void of radius 17.5\AA , the dislocation is strongly pinned, escaping at $\tau = 650\text{MPa}$. With H atoms covering the void surface (H atoms at all near-tetrahedral sites on the void surface), the process is unchanged although the escape stress is reduced by 5%. While this suggests some possible hydrogen softening effect on the pinning strength of voids, that is not the focus here. The relevant conclusion from our analysis is that H does not stabilize voids or nanoclusters of vacancies against vacancy annihilation by the formation of double jogs.

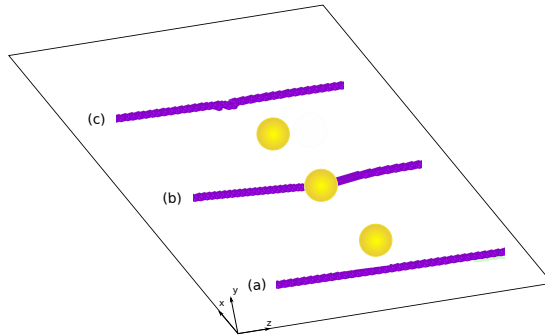


Figure 4.4 – Interaction of an edge dislocation with a V_{49} cluster. (a) Prior to dislocation intersection; (b) during dislocation bow out under increasing stress; (c) after the dislocation is unpinned, showing the formation of a double jog.

4.5 Discussion

The process of void growth presented in [47] is based on several assumptions. First, single vacancies are swept along with dislocations. Second, these vacancies are pinned when they interact with an H atom, or a prior VH cluster, so that the vacancy transport process leads to sustained growth of vacancies clusters and voids. Third, hydrogen atoms stabilize the various vacancy clusters/voids. Our results confirm that the single vacancy transport process can occur, although the details of the process differ between the QM/MM and EAM based simulations. However, both simulations confirm that this process is limited to vacancies only on the first plane on the compressive side of the glide plane. More importantly, our simulations show that vacancy clusters of two *or more* vacancies are most frequently reduced in size by vacancy annihilation and double-jog formation, with or without hydrogen. Only under conditions of very high hydrogen content in very small vacancy clusters can annihilation be prevented. Thus, the process proposed in [47] does not appear viable as an explanation for the observed nanovoids in Fe-based steel.

The annihilation process does contribute to the concentration of H into smaller vacancy clusters, but this process does not appear likely to allow growth of nanovoids. When an initial V_nH_m cluster is intersected by multiple dislocations, the vacancy annihilation process reduces the size to $V_{n-n'}H_m$ so that the ratio H/V increases, stabilizing the smaller cluster. However, if the cluster grows again due to transport of single vacancies by dislocations, the growth of the cluster at fixed H leads to reduced stabilization, if not continued annihilation and reduction in the cluster size. As a specific case, when a V_4H_{10} cluster is struck by a dislocation and loses 2Vs, the V_2H_{10} cluster becomes stable against further annihilation. However, the addition of another single V creates a V_3H_{10} cluster, which is less stable. The V_3H_{10} cluster can then lose 2V by annihilation and double-jog formation to form a very stable VH_{10} . The VH_{10} cluster can then add one additional vacancy, but this simply returns the system to its original V_2H_{10} structure. Such cycles of growth, annihilation, and regrowth can thus occur, but cannot create large stable V-H clusters. Stabilization of vacancy clusters thus requires the separate process of H diffusion. Even with extensive H diffusion, the stable clusters would be very small (a few vacancies with very high H content). As we have seen, nanovoids with surfaces fully saturated with H are not stable against annihilation when dislocations intersect them.

The mechanism in [47] also involved growth of larger V-H nanovoids by void migration and coalescence. The results here show that larger V-H clusters are almost always less stable against subsequent annihilation via dislocation interactions. Void migration is also a rather slow process, and becomes slower with increasing H content [138]. Results in [47] show the migration barrier for VH to be ~ 0.7 eV, larger than that of a single vacancy ~ 0.6 eV, and much larger than that for H (~ 0.05 eV). Thus, it can be anticipated that single vacancies formed by plasticity processes can be quickly stabilized by the addition of one or more mobile H atoms, but then such clusters become far less mobile. This is likely what leads to the increase in V concentration in the presence of H as shown in the simulations shown in [47]. However, those simulations do not study the size of V or V-H clusters, and it is likely that the V remain isolated, i.e. no clusters formed are VH_m . Addition of more vacancies to a cluster further reduces the cluster mobility, and makes such cluster susceptible to annihilation processes unless there is significant H diffusion. H embrittlement in Fe is also observed at extremely low H concentrations, on the order of 1-10 ppm or less. Stabilization of the high (surface) density of nanovoids as observed in steels would, if H plays any role, require diffusion of H over extremely large volumes/distances.

Nonetheless nanovoids are observed in the experiments in the presence of H. Thus, there must be other mechanism(s) in which H atoms contribute to stabilizing such voids. Here we speculate on a number of scenarios that remain as possible explanations for the observed nanovoids. Direct assessment of these scenarios need further research. First, it is possible that VH clusters form, migrate, and coalesce, but with the migration moving them away from active slip planes such that intersections with dislocations, and thus annihilation, is infrequent. Second, the nanovoids are observed along grain boundaries,

and it is possible that stabilization and diffusion of the VH cluster allows for VH diffusion to grain boundaries, leading to accumulation of V and H in the grain boundaries, with voids eventually being formed. The role of H in this process is unclear, however, since individual V could accomplish the same phenomenon, and with faster diffusion. In general, the high cost of forming vacancies in Fe (1.7 eV) implies that the equilibrium concentration is very low and that there is a strong driving force for almost any vacancy annihilation processes, suggesting that mechanisms relying on actual vacancy formation, stabilization, and migration are not likely. Third, H may (likely does) segregate rapidly to grain boundaries in Fe-based steels. The presence of H at the grain boundaries may inhibit dislocation transmission across grain boundaries, leading to accumulation of Burgers vector near the grain boundaries. This can, in turn, then lead to void nucleation at the grain boundaries, as observed in an entirely different system [139]. H could further stabilize such vacancies and limit their migration, leading to stabilization of small voids. We believe this last mechanism merits further investigation, and the weakening of grain boundaries by high densities of nanovoids can clearly favor cleavage-type failure processes along grain boundaries thus making a direct connection with embrittlement.

4.6 Summary

We have shown that QM/MM studies confirm that vacancies can be transported along with gliding edge dislocations in Fe, which is a surprising result. The transport of vacancies to pre-existing vacancy clusters, with or without hydrogen, is thus possible. However, we show that, across many different types of vacancy clusters V_nH_m with and without H, the annihilation of vacancies to form double-jogs on the dislocation is a dominating process. This is due to the large reduction of energy associated with vacancy annihilation. Therefore, the development of large V-H clusters by transport and trapping of vacancies is an unlikely phenomenon. The experimentally-observed presence of sustained vacancy clusters/voids on the fracture surfaces of H-charged specimens must thus occur by some other mechanism(s). Due to the results of our simulations, H atoms can not suppress these annihilation processes. The mechanism(s) associated with the observation of nanovoids at grain boundaries in Fe-based steels exposed to hydrogen thus remain open, with several possible processes discussed briefly here.

5 Effect of hydrogen atoms on precipitate hardening in α -Iron

The aim of this chapter is to examine the effect of the hydrogen atoms on the precipitate hardening in α -Iron. We chose Iron because the diffusion barrier of H atoms in bulk of this bcc metal is $\approx 0.05eV$ which enables us to simulate hydrogen diffusion and transport within conventional MD timescales. There is a popular belief in the field describing the H atoms as "defectants" that reduce the line tension of the dislocation [44, 43]. Thus, by increasing the hydrogen concentration to a critical value the line tension of the dislocations become low enough such that the nucleation of dislocations becomes spontaneous. This phenomenon can be considered as a HELP-like mechanism for hydrogen embrittlement. Hereby, we examine this hypothesis by performing direct simulations of bow-outing of an initially straight edge dislocation. The amplitude of the bow out of the dislocation can be considered as an indicator of the magnitude of line tension such that increase in line tension decreases the bow out amplitude and vice versa.

5.1 Theoretical framework

Consider an initially straight edge dislocation lied along the x_1 axis of the Cartesian coordinate system as shown in Figure 5.1. The dislocation is pinned at points $x_1 = 0$ and $x_1 = L_0$ and is subjected to shear stress $\tau_{32} = \tau$. Thus it starts to bow out. The energy of the bowed out dislocation can be written as:

$$\begin{aligned}
 E = & \underbrace{\Gamma \int_0^L \sqrt{1 + \left(\frac{dx_3}{dx_1}\right)^2} dx_1}_A - \underbrace{\int_0^L \lambda(x_1) (\Delta V p(x_1, x_3) + E_0) P(x_1) \sqrt{1 + \left(\frac{dx_3}{dx_1}\right)^2} dx_1}_B \\
 & - \tau b \underbrace{\int_0^L x_3 dx_1}_C.
 \end{aligned} \tag{5.1}$$

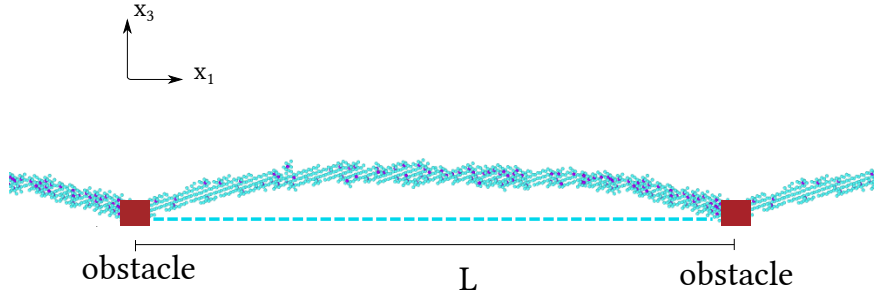


Figure 5.1 – Schematic diagram of an initially straight edge dislocation (dashed line) which is bowed out under application of shear. The light blue and purple spheres denote the Fe and H atoms, respectively. The initial length of the dislocation segment between two obstacles is L .

in which, Γ , $p(x_1)$, λ , ΔV , b , E_0 and $P(x_1)$ are the line tension, the pressure of the elastic field of the dislocation, density of the interstitial site per unit length of the dislocation, misfit volume of H interstitials, magnitude of the Burger's vector, the binding energy of H to screw dislocations and the probability of the occupation of a site with x_1 coordinate along the dislocation, respectively. It should be noted that during the bowing out process of the dislocation, the character angle of it changes along the dislocation line. Thus, the density of the binding sites of the hydrogen atoms along the dislocation becomes a function of character angle of it which itself is a function of x_1 . Moreover, here we approximated the interaction energy of the H atoms with the dislocation with the elastic $p\Delta V$ term. We assumed that the hydrogen atoms are bound to the core of the dislocation, thus the distance of H atoms and the core is the core radius of the dislocation. This approximation gives rise to a character angle-dependent variation of the interaction energies with maximum values at the edge segments and the minimum values at screw ones. This trend is in accordance with the results of the direct simulation of the interaction energies which are given in the next section.

For calculating the term B in Eq. (5.2) we need to find $P(x_1)$ via statistical mechanics calculations. The pressure field associated with the dislocation segment at r_c which is the core radius is :

$$p = \frac{-b_e G(\nu - 1) \sin \theta}{3\pi(1 - \nu)r_c} \quad (5.2)$$

$$b_e = b\sqrt{\left(1 - \frac{1}{b^2}|\mathbf{b} \cdot \mathbf{T}|^2\right)} \quad (5.3)$$

where b_e , G , ν , and \mathbf{T} are the edge component of the Burgers vector, shear modulus, Poisson's ratio of the material, and the unit tangent vector to the dislocation line, respectively. The probability of occupation of an atomic site located along the dislocation line can be found via equating the chemical potential of an H atom far from the dislocation

and one attached to the dislocation. After some standard calculations we come up with:

$$P(x_1) = \frac{c_0 \exp(p\Delta V/k_B T)}{1 + c_0 \exp(p\Delta V/k_B T)} \quad (5.4)$$

in which c_0 , ΔV , T and k_B are the background concentration, misfit volume of H interstitial, temperature and the Boltzmann constant, respectively. This calculation is valid in the case of fixed c_0 . In other words, the number of the H atoms bound to the dislocation can change during the bowing out process.

5.1.1 Bow out of the dislocation with a fixed remote concentration c_0

In order to solve the bow out problem we invoke calculus of variations to determine the governing differential equation. It should be noted that in this framework the number of the H atoms that can attach to the dislocation is free of any constraint, thus the governing differential equation can be obtained by plugging the energy functional Eq. (5.2) into the Euler–Lagrange differential equation:

$$\frac{dE}{dx_3} - \frac{d}{dx_1} \left(\frac{dE}{dx_3'} \right) = 0. \quad (5.5)$$

with the following boundary conditions

$$x_2(0) = x_2(L_0) = 0 \quad (5.6)$$

We call this theory as "unconstrained" theory.

5.1.2 Bow out of the dislocation with fixed number of absorbed hydrogen atoms

For the sake of relating the results of the theory to the MD simulations in which the number of hydrogen atoms does not change during the simulations. We imposed the constraint of constant number of H atoms. To this end, the following constraint is imposed:

$$N_0 = \lambda \int_0^L P(x_1) \sqrt{1 + \left(\frac{dx_3}{dx_1} \right)^2} dx_1 \quad (5.7)$$

this extra equation keeps the number of H atoms equal to a given value of N_0 . Then we need to modify the energy functional as:

$$\tilde{E} = E - \Lambda \lambda \int_0^L P(x_1) \sqrt{1 + \left(\frac{dx_3}{dx_1} \right)^2} dx_1 \quad (5.8)$$

in which Λ is the Lagrange multiplier. The Euler–Lagrange differential equation associated with the problem is

$$\frac{d\tilde{E}}{dx_3} - \frac{d}{dx_1} \left(\frac{d\tilde{E}}{dx'_3} \right) = 0. \quad (5.9)$$

The boundary conditions are

$$x_2(0) = x_2(L_0) = 0. \quad (5.10)$$

Eqs. (5.7) and (5.9) should be solved together within an iterative numerical scheme. To this end, we need to pay attention to the properties of the constraint (5.9) which can be included into term B in Eq. (5.2). The unknown parameter Λ can be included in E_0 which is the core–H interaction. In fact Λ describes the strength of the bond between H atoms and core of the dislocation. Thus, we can solve Eq. (5.5) for different values of Λ and find the minimum value of it that preserves the that preserves the number of atoms and choose its corresponding configuration as the minimum energy configuration. We call this theory as the "constrained theory".

5.2 Validation of the assumptions of the model

In this section, we describe the details of the simulations for finding the H–dislocation interactions and the diffusion barriers of dislocations. These simulations are necessary to validate the assumptions of the theory and recognition of its limitations.

5.2.1 Interaction of the H atoms and dislocations with different character angles

In the proposed theory we assumed that the interaction energy of H atoms and dislocations is a function of the dislocation character angle. This function which is the elastic interaction of the dislocation and the misfit volume of the H interstitial has its maximum at edge segment and then decreases by increasing the character angle and attains its minimum at screw segments. To validate this assumption we define the interaction energy E_i^{int} between an interstitial H atom located at the i th binding site at the core of the dislocation can be computed as

$$E_i^{\text{int}} = E_{d-H}^i - (E_d + E_H) \quad (5.11)$$

where E_d is the energy of the system with just the dislocation, and E_H is the solution energy of H in bulk bcc Iron. Since we are interested in simulation of the bowed dislocation which contains different character angles, here we find the binding sites and their corresponding interaction energies for the pure edge, 70°, 45°, and screw dislocations.

5.2. Validation of the assumptions of the model

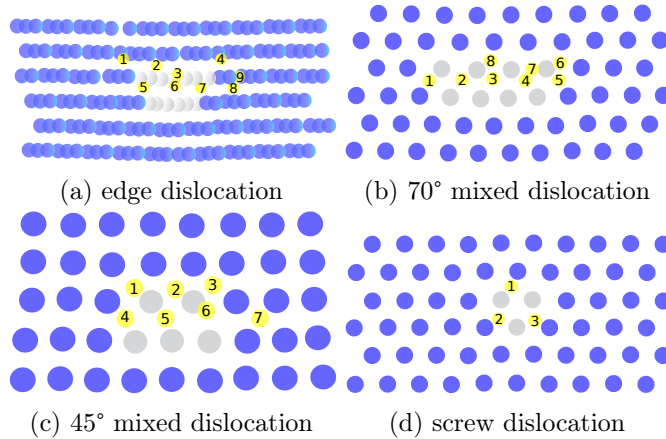


Figure 5.2 – Binding sites of the H atoms to different dislocations in α -Iron. The blue, white and yellow spheres denote the bcc Fe, dislocated Fe and H atoms, respectively.

For these simulations we construct rectangular simulation cells comprised of a bcc Fe crystal oriented with x_1 , x_2 and x_3 , and of dimensions L_1 , L_2 and L_3 as schematically illustrated in Figure 4.1. Table 5.1 contains the orientations and sizes of the simulation boxes corresponding to each dislocation.

Table 5.1 – The dimensions and orientation of the simulation boxes containing dislocations with different character angles in α -Iron.

θ	L_1 (Å)	L_2 (Å)	L_3 (Å)	\mathbf{e}_1	\mathbf{e}_2	\mathbf{e}_3
0°	138.5	118.95	24.7	$[\bar{1}\bar{1}2]$	$[1\bar{1}0]$	$[111]$
45°	120.3	118.9	14.3	$[\bar{1}\bar{1}0]$	$[1\bar{1}0]$	$[001]$
70°	140	118.9	24.7	$[112]$	$[1\bar{1}0]$	$[11\bar{1}]$
90°	147	144.8	23.4	$[111]$	$[1\bar{1}0]$	$[11\bar{2}]$

We introduce a single dislocation of Burgers vector $1/2[111](1\bar{1}0)$ with line direction along x_3 and lying in the $x_2 = 0$ plane. The dislocation is created by removing atoms from the perfect crystal in the narrow strip $-\sqrt{3}a_0/4 < X - X_0 < \sqrt{3}a_0/4$, $Y < 0$, where $a_0 = 2.86\text{Å}$ is the lattice constant for α -Fe and X_0 is the X coordinate of the dislocation. All remaining atoms are then displaced according to the linear elastic displacement field for the edge dislocation [133], and the entire structure is relaxed using the conjugate gradient method [95]. The simulation cell is periodic along Z and along X , the latter introducing an artificial bending that does not, however, create any shear stress along the dislocation slip plane. H atoms are introduced by inserting them into the different sites at the core of the dislocation. Various potential sites are investigated. Interatomic interactions among atoms are described using an EAM potential introduced by Ramasubramaniam et al. [134] and modified by Song and Curtin [49] to prevent unphysical H aggregation in single-crystal Fe. Figure 5.2 illustrates the stable sites for H atoms in each dislocation. The corresponding interaction energies are given in Table 5.2. It is evident that both

Chapter 5. Effect of hydrogen atoms on precipitate hardening in α -Iron

Table 5.2 – Binding energies (eV) of H atoms to different energy favorable sites in different dislocations in α -Iron.

# site	θ			
	90°	70°	45°	0°
1	-0.15	-0.19	-0.27	-0.19
2	-0.23	-0.31	-0.25	-0.15
3	-0.31	-0.25	-0.25	-0.19
4	-0.14	-0.30	-0.34	-
5	-0.37	-0.19	-0.33	-
6	-0.34	-0.19	-0.19	-
7	-0.37	-0.23	-0.21	-
8	-0.2	-0.06	-	-
9	-0.09	-	-	-

the number and the magnitude of the interaction energies of the sites are decreasing by decreasing the character angle of the dislocation from 90° (edge) to 0° (screw). Thus, the proposed interaction function that preserves this key feature is a good choice. Given the results of the aforementioned simulations, we can conclude that during the bowing out process in which an initially straight edge dislocation starts to bow out and develop mixed dislocation segments, the hydrogen atoms in the mixed dislocation segments should diffuse to the edge segments or resist against bowing out.

5.2.2 Barriers for diffusion of H atoms along and across the dislocation

It should be noted that the theoretical framework that is given in this chapter is a pure thermodynamic theory such that it only considers the energy difference between the different states. However, the kinetics of H diffusion plays a key role in the behavior of the dislocations as well. Thus, it is necessary to find the barrier for different types of H diffusion across and along the dislocation for rationalizing the simulations. It is well known that the barrier for the diffusion of H atoms in bulk of bcc Iron is low. However, since the number of the binding sites and the magnitude of the interaction energies for different segments of the dislocation are different the barrier for diffusion of H atoms along and across the dislocations should be investigated. To this end, we use a nudged elastic band (NEB) method to find the diffusion barriers between different stable sites of the H atoms along the dislocation. Table 5.3 shows the migration barriers for different diffusion paths along and across the dislocation.

Interestingly the barrier for the diffusion along the 70° dislocation is very low that makes diffusion very easy along that segment. This phenomenon is observed in the analysis of carbon diffusion along 70° dislocations in bcc Iron [140]. The diffusion barriers along the other paths are about $0.5eV$. These barriers are one order of magnitude larger than the

Table 5.3 – Maximum migration barriers (eV) of H atoms for diffusion between different energy favorable sites in different dislocations in α -Iron.

diffusion direction	θ			
	90°	70°	45°	0°
pipe	0.18	0.05	0.48	0.75
Transverse	0.6	0.66	0.32	0.35

diffusion barrier in the bulk of α -Iron.

Thus, we can conclude that the diffusion of H atoms during bowing out of the dislocation is not symmetric along the dislocation line.

5.3 Input of the model

In the view of the theoretical calculation given in the previous section, it is evident that the number of the H atoms that are used in the simulations is a very crucial parameter that should be carefully determined. Since in the MD simulations we cannot easily change the number of the hydrogen atoms, it is important to choose this number relevant to the real situations in the materials.

Based on the results of [141] the dislocation density of the heavily cold worked pure Iron is between $\rho = 1.6 \times 10^{14} \text{m}^{-2}$ and $\rho = 1.6 \times 10^{15} \text{m}^{-2}$ as an approximation we can assume that the spacing between the dislocations is $\sim \frac{1}{\sqrt{\rho}}$. Thus, the effective volume from which the hydrogen atoms migrate to the dislocation is between $\mathcal{V} = 1.5 \times 10^7 \text{\AA}^3$ and $\mathcal{V} = 4.94 \times 10^8 \text{\AA}^3$. Since the atomic volume of an Fe atom is $V_{\text{Fe}} = 11.69 \text{\AA}^3$, the effective number of Fe atoms which send their H interstitials to the dislocation is between $N_{\text{Fe}} = 7.94 \times 10^7$ and $N_{\text{Fe}} = 1.33 \times 10^6$. Thus, the number of H atoms which belong to the dislocation becomes $N_{\text{H}} = c_0 N_{\text{Fe}}$. For example the number of H atoms for specimen with $c_0 = 10^{-4}$ is between 133 and 422.

The other key parameter in the theory is the line tension of the dislocation. It should be noted that line tension itself depends on the character angle of the dislocation. However, here we used a constant value of $0.85 \times 10^{-9} \text{J/m}$ for Γ during the bow out. This value is chosen to produce the same bow out amplitude at $\tau = 200 \text{MPa}$ for the H-free dislocation. The density of the binding sites along the dislocation is 10^9site/m which is calculated by considering the average of the number of sites per unit length of different segments of dislocation. It should be noted that the in our simulations the number of the H atoms attached to the dislocation remains constant. The radius of the core of the dislocation is assumed to be 5.5\AA which is in accordance with the simulations. We used shear modulus $\mu = 82 \text{GPa}$ and the Poisson's ratio $\nu = 0.3$. The misfit volume of H interstitial is 3.8\AA^3 .

Figure 5.3a shows the amplitude of the bow out of the dislocation for different amounts of the attached hydrogen atoms under different applied shear stresses. The results of the both constrained and unconstrained theories are given. The results are normalized to the amplitude of bow out of the same dislocation without any attached hydrogen. It can be seen that the amplitude of the bow out decreases with the increasing the H atoms. It is also evident that bow out amplitude is considerably higher in the unconstrained cases in comparison to the constrained cases. This is a manifestation of hardening induced by the H atoms. The H atoms make the bow out of the dislocation harder. This phenomenon means that we need higher stresses to escape the dislocation from the obstacle.

In order to clarify the validity of the unconstrained theory versus the constrained theory we illustrated the percentage of change in the number of the total atoms which are attached to the dislocation during the bow out process calculated using the unconstrained theory in Fig. 5.3b. It can be seen that based on these calculations, if we start with 300 hydrogen atoms, by application of $\tau = 200MPa$, 8% of the hydrogen ($\Delta N = -24$) detach from the dislocation. Since we did not observe this phenomenon in the simulations, we conclude that the unconstrained theory is not good enough to explain the simulations and we need to use constrained theory in this case.

However, it can be seen that the magnitude of the change decreases by adding more hydrogen atoms to the initial state. The reason for this phenomenon is the significant decrease in the amplitude of bow out of the dislocation at which larger numbers of H atoms are attached. Thus, the dislocation remains straight and thus the screw segments do not develop. Thus, there is no need to the significant liberation of hydrogen. Thus, since in the simulations we did not see considerable amount of H liberation from the dislocation. We can conclude that the *constrained* theory is the relevant theory for justification of the simulations.

This constrained theory gives an approximation of the bow out process which can explain the trends in the simulations.

5.4 Simulation of the bow out of the dislocation

We start from the an initially straight edge dislocation lying along x_1 axis. The size of the simulation box is $l_1 \times l_2 \times l_3 = 236\text{\AA} \times 290\text{\AA} \times 280\text{\AA}$ which is chosen based on the results of the work of [142] to minimize the image forces in the dislocation. The simulation cell is periodic along the x_1 direction and the other directions are free. The edge dislocation is inserted along the x_1 direction by a same procedure that is explained the previous subsection. The atoms in the region $123\text{\AA} \leq x_1 \leq 131\text{\AA}$, $142\text{\AA} \leq x_2 \leq 150\text{\AA}$, $136\text{\AA} \leq x_3 \leq 143\text{\AA}$ are frozen to constitute a barrier against the glide of the dislocation.

The calculations are done at finite temperature. MD simulations are performed in an

5.4. Simulation of the bow out of the dislocation

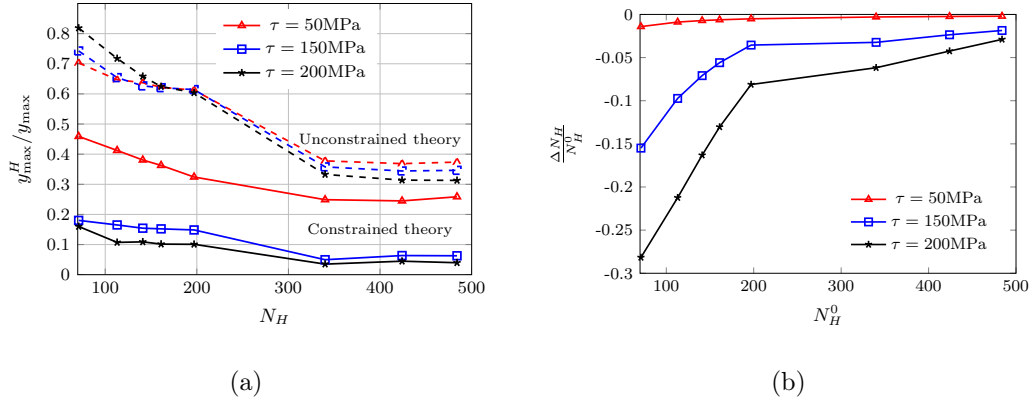


Figure 5.3 – (a) Normalized maximum bow out of the hydrogen charged dislocation subjected to different shear stresses. Dashed lines are the results of unconstrained theory and the solid lines are the results of constrained theory. (b) The relative decrease in the number of attached hydrogen atoms during bow out for various initial number of H atoms.

NVT ensemble with a Langevin thermostat [97] using the velocity–Verlet algorithm [96] with the integration time step of 0.4 and 1 fs for the hydrogen-charged and hydrogen-free cases, respectively. The temperature of the system is fixed at 300K. The molecular dynamics simulations are performed using the Large-scale Atomic/Molecular Massively Parallel Simulator (LAMMPS) [93] and atomic configurations are visualized using the Open Visualization Tool (OVITO) [94].

For the hydrogen-charged cases, the H atoms are added to the tetrahedral site in a cylinder of radius 10 Å around the dislocation line. Then the system is relaxed using conjugate gradient method to let the H atoms find their binding sites at the dislocation. The specimen is subjected to the incremental shearing stress of $\Delta\tau_{13} = 10\text{MPa}$ then we let the system run for 10 ps if the dislocation is bowed during that time interval we let the simulation run without increasing the applied shear stress. Otherwise, we increase the shear stress.

Figure 5.4 shows the configuration of the H-free specimen containing an initial edge dislocation subject to the different magnitude of applied shear. It can be seen that the configuration of the bowed dislocation is asymmetric. The bowed dislocation is mainly consisting of 70° and 45° segments that are connected via an intermediate edge segment. This configuration is observed and discussed in the literature [143]. By increasing the applied shear the dislocation attains its critical configuration at which a loop forms around the obstacle and dislocation escapes.

Figure 5.5 illustrates the configuration of the dislocation charged by 300 H atoms under different magnitudes of applied shear. It can be seen that the diffusion of the H atoms is asymmetric along the dislocation. The 70° segment can deliver its H atoms to the

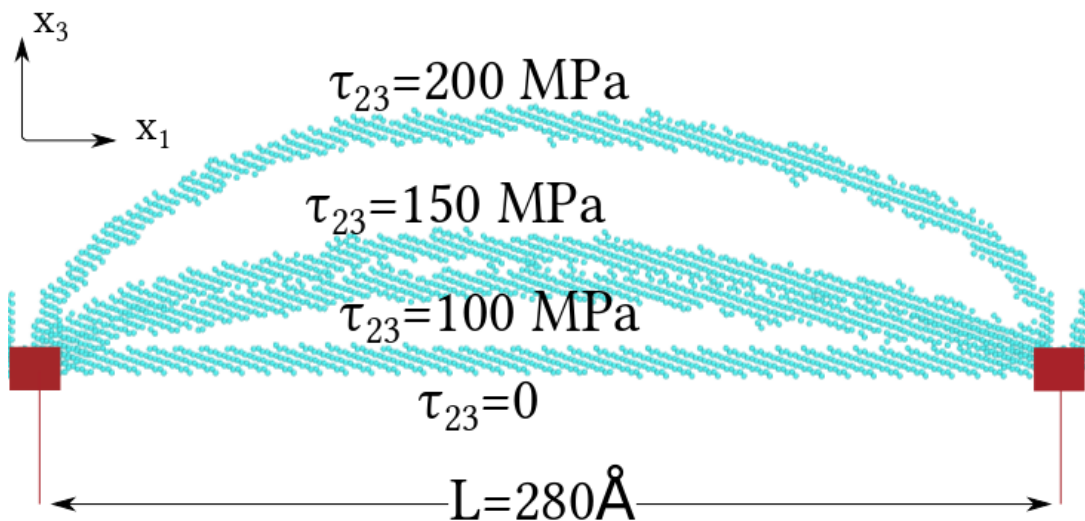


Figure 5.4 – Configuration of the bowed dislocation in the H-free specimen under different applied shear.

intermediate edge segment which can host more H atoms and the H atoms have lower energy there. However, the 45° segment fails to deliver its H atoms to the edge segment. Thus, the population of the H atoms at the 45° and edge segment constitutes barriers against the bowing out of the dislocation. Particularly the intermediate edge segment acts as secondary pinning point for the dislocation. Thus, the escape stress considerably increases in the presence of H atoms.

Now, we discuss the key features of the proposed theory and the results of the simulations. To this end, we need to determine the input of the model. Then we compare and discuss the predictions of the theory and results of the simulation. The maximum normalized amplitude of the hydrogen charged dislocation under $\tau_{23} = 150\text{MPa}$ and $\tau_{23} = 200\text{MPa}$ are 0.09 and 0.12, respectively. These values are in qualitative agreement with the predictions of the "constrained" theory which predicts values of 0.06 and 0.08 them, respectively. Thus, both theory and simulations confirm the reduction in the bow out of the dislocation in the presence of H atoms. This observation means increase in the line tension of the dislocation and hardening. Moreover, by increasing the load, due to the low diffusion barrier of pipe diffusion along the 70° segment, the H atoms migrate from that region to the edge segment in the middle of the dislocation and form a secondary pinning point, this phenomenon has further hardening effect.

5.5 Summary

In summary, since binding to the edge segment is more favorable for the H interstitial, they constitute resistance against developing screw and mixed dislocation segments. Moreover,

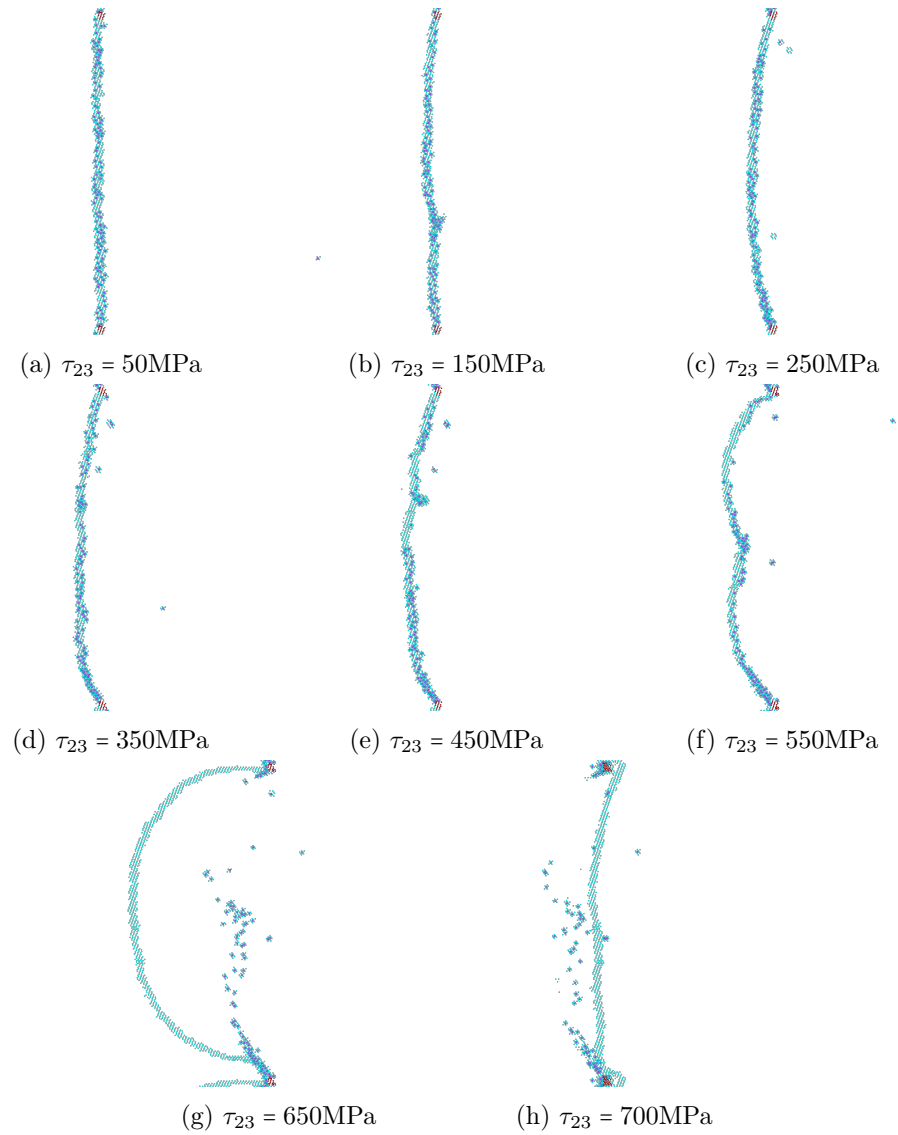


Figure 5.5 – Configuration of the bowed dislocation in the specimen charged with $N_H = 300$ under different applied shear strengths.

Chapter 5. Effect of hydrogen atoms on precipitate hardening in α -Iron

the diffusion of H atoms along the different segments of dislocations is not uniform. Thus, while the easy diffuse segment of 70° delivers its H atoms to the edge segments the hard-diffuse H atoms get stuck in the 45° segments. Thus, the formation of secondary pinning points and adding for hardening is envisioned. Thus, we can conclude that the H atoms cannot be considered as simple defactants that decrease the formation energy of the dislocations (i.e. line tension of it).

6 Effect of segregated hydrogen atoms on the dislocation–grain boundary interactions

There is experimental evidence of intergranular fracture in hydrogen-contaminated polycrystalline nickel at low temperatures, at which the hydrogen atoms are basically immobile. Thus, the hydride formation mechanism that needs long-range diffusion of hydrogen atoms cannot be responsible for this intergranular fracture. The aim of this chapter is to demonstrate the effect of the segregated hydrogen atoms on the interaction of the dislocations with the grain boundaries. To this end, we start from the grain boundaries that we examined in chapter two and investigate the stress developed in them due to the segregation of H atoms. Then we examine the effect of the H solutes on the strengthening of polycrystalline nickel.

6.1 Stress fields induced by the segregated hydrogen atoms at the grain boundaries

In this section, we start with the representative grain boundaries that we simulated in the second chapter to compare the stress field induced by the segregated H atoms. The geometric details of the simulations are the same as the simulations in chapter 2. The simulation box dimensions are $l_1 \times l_2 \times l_3 = 1080\text{\AA} \times 1000\text{\AA} \times 9.6\text{\AA}$. We chose large simulation samples to capture the stochastic effects of the segregated H atoms along GBs. We saturated the binding site of each grain boundary by using the simple solution method formulation which is given in Eq. (2.1). Then we relax the structure by using conjugate gradient method.

Fig. 6.1 illustrates the distribution of the resolved shear stress along the shown slip planes S_1 and S_2 of the GBs of interest. It should be noted that the hydrogen atoms have non-uniform distribution along x_3 axis, however, if we envision the case that a dislocation with line direction along x_3 -axis starts to approach to the boundary, it interacts with the average of the stress field along the x_3 direction. Thus, in these figures, we plotted the average of the stresses along the x_3 -axis. Another interesting finding is that the

Chapter 6. Effect of segregated hydrogen atoms on the dislocation–grain boundary interactions

magnitude of τ_{13} and τ_{23} are almost zero, thus the stress field cannot interact with the screw dislocations that have their Burgers vector along x_3 -axis.

By comparing the results of the simulations of grain boundaries with and without segregated hydrogen atoms, it can be seen that the excess resolved shear stress induced by H atoms on each slip plane have a certain distribution. In each region, if the resolved shear stress is positive in a grain, then that of the same slip plane in the opposite grain is negative and vice-versa. Moreover, if the resolved shear of slip plane S_1 is positive the resolved shear of the slip plane S_2 in the same grain is negative and vice-versa as shown in Figure 6.2.

Thus, we can recognize two different characteristic regions along the GBs as shown in this figure. Moreover, the dislocations that are moved toward the GB by the applied external loads are shown. It can be seen that if the external loading is a positive shear, in both region types at least one grain repels the originally attracted dislocations. Thus, the net Burgers vector becomes less on average. Moreover, the vertical component of the Burgers vector that was originally canceled in H-free case starts to accumulate. Thus it can be envisioned that in the case of positive shear, adding H atoms can help accumulation of slip in the boundary and enhance opening of it. In the tensile loading case, region type 1 attracts all the originally attracted dislocations and thus the net Burgers vector \mathbf{b}_{net} which is along \mathbf{e}_2 increases in that region. However, region type 2, repels all the previously attracted dislocations and thus, the net Burgers vector reduces. So we can expect that in the regions of type 1, the dislocations can induce steps and make the opening of the GB easier, but in the regions type 2 the GB does not get damaged. The details of the process are depicted in the Figure 6.2.

Now we turn our attention to the effect of the induced stresses on the process of slip transmit across the grain. In all cases, when the dislocation is attracted to the GB then its associated dislocation on the opposite grain and opposite slip plane is repelled from the boundary, thus transmission of the slip becomes easier in this cases. Moreover, the presence of the H atoms along the boundary makes the dissociation of the dislocations harder for the dislocations. Thus, we can envision that in some cases adding hydrogen can enhance slip transmit to the adjacent grain. However, the detail of the process largely depends on the atomistic structure of the GB and binding sites of hydrogen atoms.

6.2 Interaction of straight dislocations and the grain boundaries

In this section, we simulate the interaction of the screw and mixed dislocations with the representative boundaries in polycrystalline nickel. The effect of the stress field on the interaction of the dislocations and GBs and the atomistic details of the process will be examined. The simulation box is of dimensions $l_1 \times l_2 \times l_3 = 2170\text{\AA} \times 2000\text{\AA} \times 2.4\text{\AA}$. The

6.2. Interaction of straight dislocations and the grain boundaries

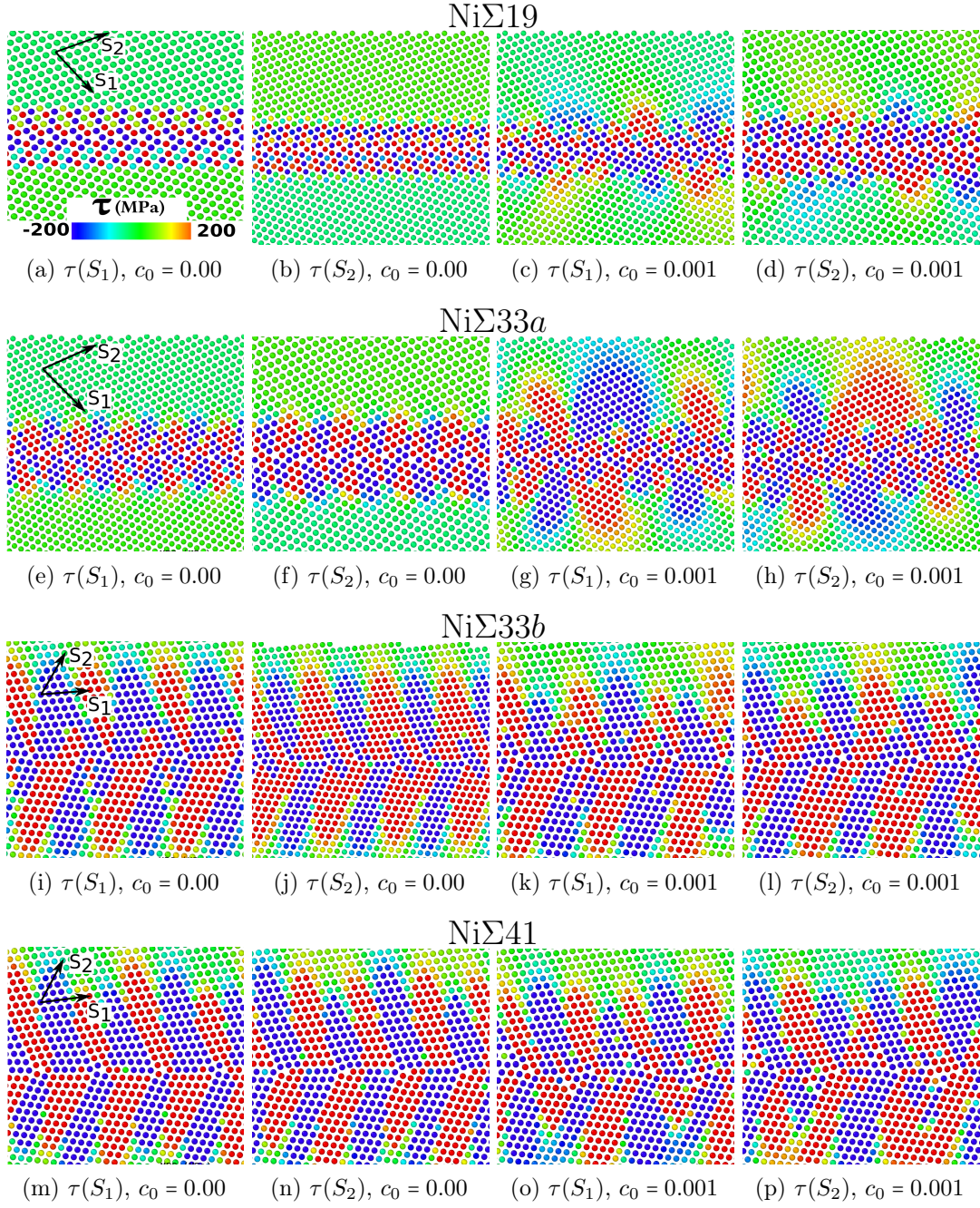


Figure 6.1 – Distribution of the resolved shear stress along the GBs of interest in both H-free and H-charged cases for two different slip planes. The hydrogen atoms are not shown for the sake of better illustration. c_0 is the remote concentration of the H atoms in the bulk of the material. $\tau(S_i)$ denotes the resolved shear along slip plane S_i .

Chapter 6. Effect of segregated hydrogen atoms on the dislocation–grain boundary interactions

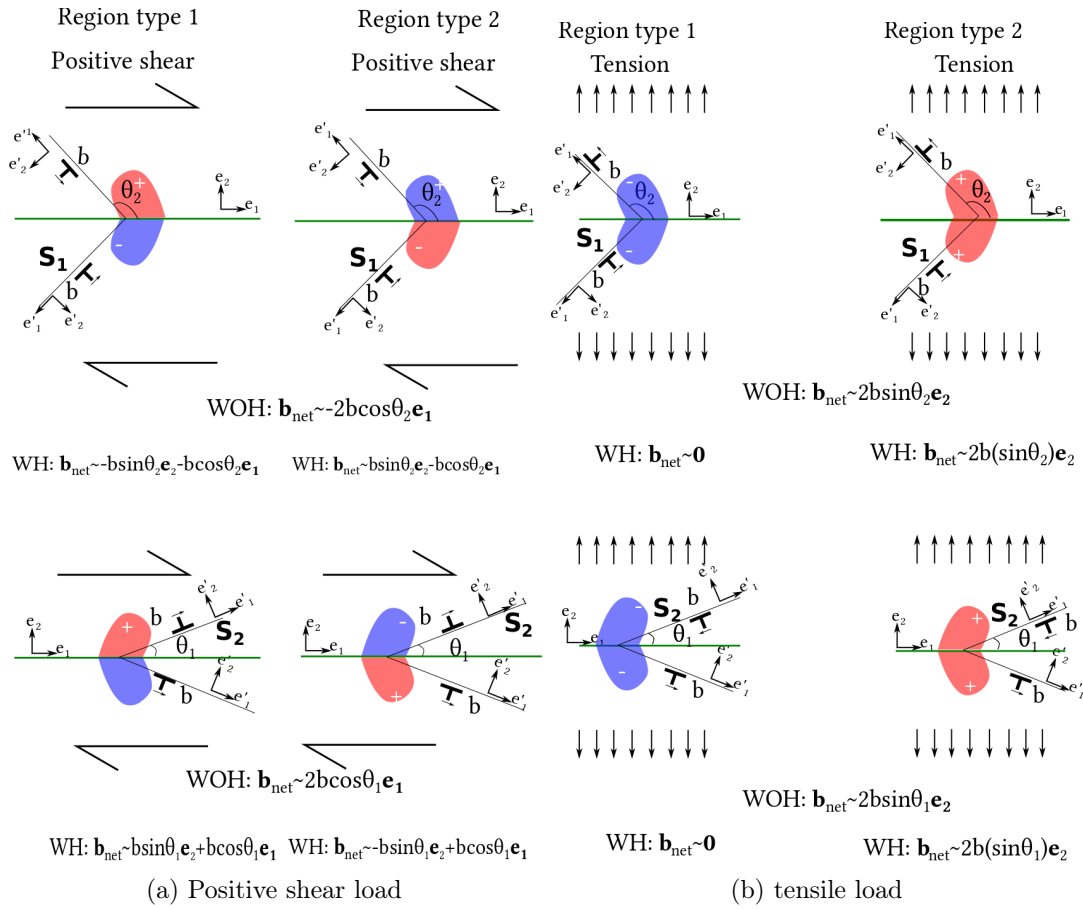


Figure 6.2 – The schematic diagram of the interaction of typical regions along the grain boundaries and the edge dislocations were driven to the GB by the external (a) shear and (b) tensile loading. The average net Burgers vector is shown in both H-free and H-charged cases. The blue and red regions illustrate the repulsive and attractive regions, respectively. WOH and WH stands for the H-free and H-charged cases, respectively. \mathbf{b}_{net} is the average Burgers vector in the grain boundary.

6.2. Interaction of straight dislocations and the grain boundaries

simulation box is periodic along z -axis and the dislocations are inserted by application of the displacement field of dislocation–GB system as is given in [144]. The MD simulations are performed in the NVT ensemble using a Langevin thermostat [97] and the velocity–Verlet algorithm [96] with integration time step of 1 fs. The temperature of the system is fixed to be $10^{-3}K$ since we are not probing thermally-activated processes here. The interatomic interactions among atoms are described using the Ni-H embedded atom method (EAM) potential introduced by Angelo et al. [90] and modified by Song and Curtin [48].

For the Mixed dislocation tests, we applied tensile stress σ_{22} to the specimen to drive the dislocation toward the boundary. Since the tensile stress does not induce any shear along the GB it does not facilitate/hinder the dissociation process of the mixed dislocation. For the screw dislocation cases, we applied the τ_{13} to the specimen. This component of shear does not facilitate/hinder the dissociation processes of the dislocations along the GBs. After sending the first dislocation we sent another dislocation on the exactly same glide plane of the previous one to see the possible hardening/softening effects of the H atoms.

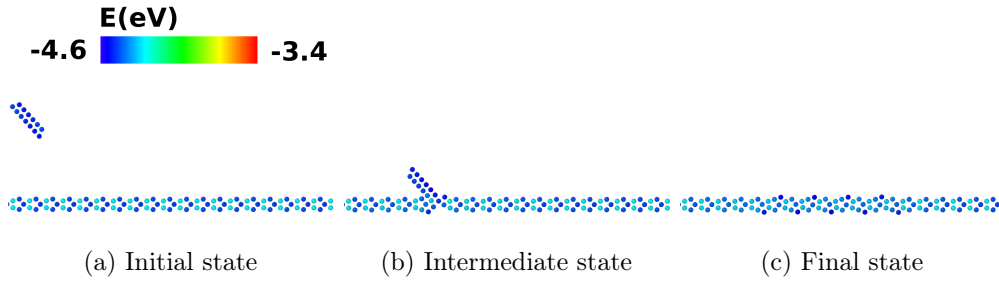
6.2.1 Screw dislocations

Figures 6.3–6.6 illustrates the key configurations of the screw dislocation–GB interactions for each grain boundary. Table 6.1 summarizes the results of the simulations.

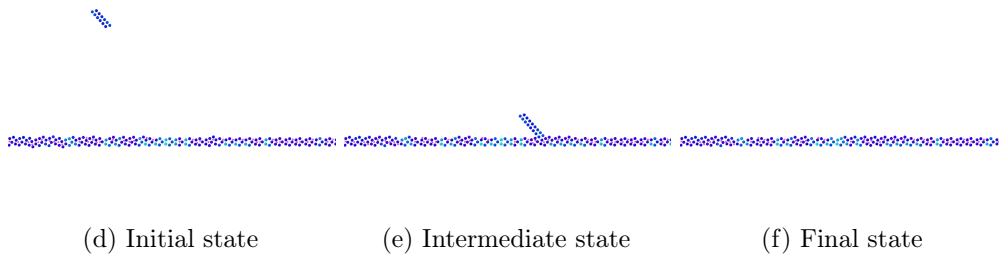
Table 6.1 – Reactions of the screw dislocations and grain boundaries of interest in different nickel bicrystals. The critical resolved shear stresses $\tau_c(MPa)$, at which the reactions happened are given. The following abbreviations are used. A: Dislocation Absorbed, D: Dislocation dissociated, T: Slip transmitted, P: partial dislocation emitted from the GB , J: the dislocation formed a junction with the stacking faults in GB.

		Screw dislocation							
		$c_0 = 0$				$c_0 = 0.001$			
		first		second		first		second	
θ		τ_c	Rxn	τ_c	Rxn	τ_c	Rxn	τ_c	Rxn
		(MPa)		(MPa)		(MPa)		(MPa)	
$\Sigma 19$	48	61	D	308	D	185	A	555	A
$\Sigma 27$	109	39	A	1334	P	39	A	1177	T
$\Sigma 33a$	45.3	30	D	412	D	30	A	766	P
$\Sigma 33b$	63.2	37	A	666	A	37	A	666	A
$\Sigma 41$	70.5	39	D	860	A	39	A	704	A

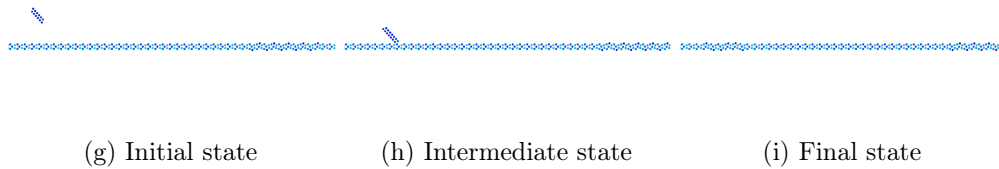
First dislocation, $c_0 = 0.0$, $\tau_c = 61MPa$



First dislocation, $c_0 = 0.001$, $\tau_c = 185MPa$



Second dislocation, $c_0 = 0.0$, $\tau_c = 308MPa$



Second dislocation, $c_0 = 0.001$, $\tau_c = 555MPa$

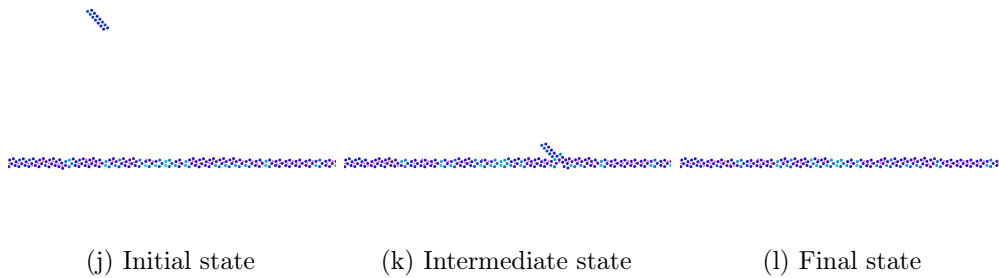


Figure 6.3 – Key atomistic configurations of the interaction of a screw dislocation with a $\Sigma 19(331)\langle 110 \rangle$ grain boundary. The purple spheres are the H atoms and the other spheres are the non-fcc nickel atoms which are colored due to their energy. (a)–(c), (d)–(f), (g)–(i), and (j)–(l) configurations denote the initial, intermediate and final configuration of first dislocation in H-free, second dislocation in H-free, first dislocation in H-charged, and the second dislocation in H-charged samples, respectively.

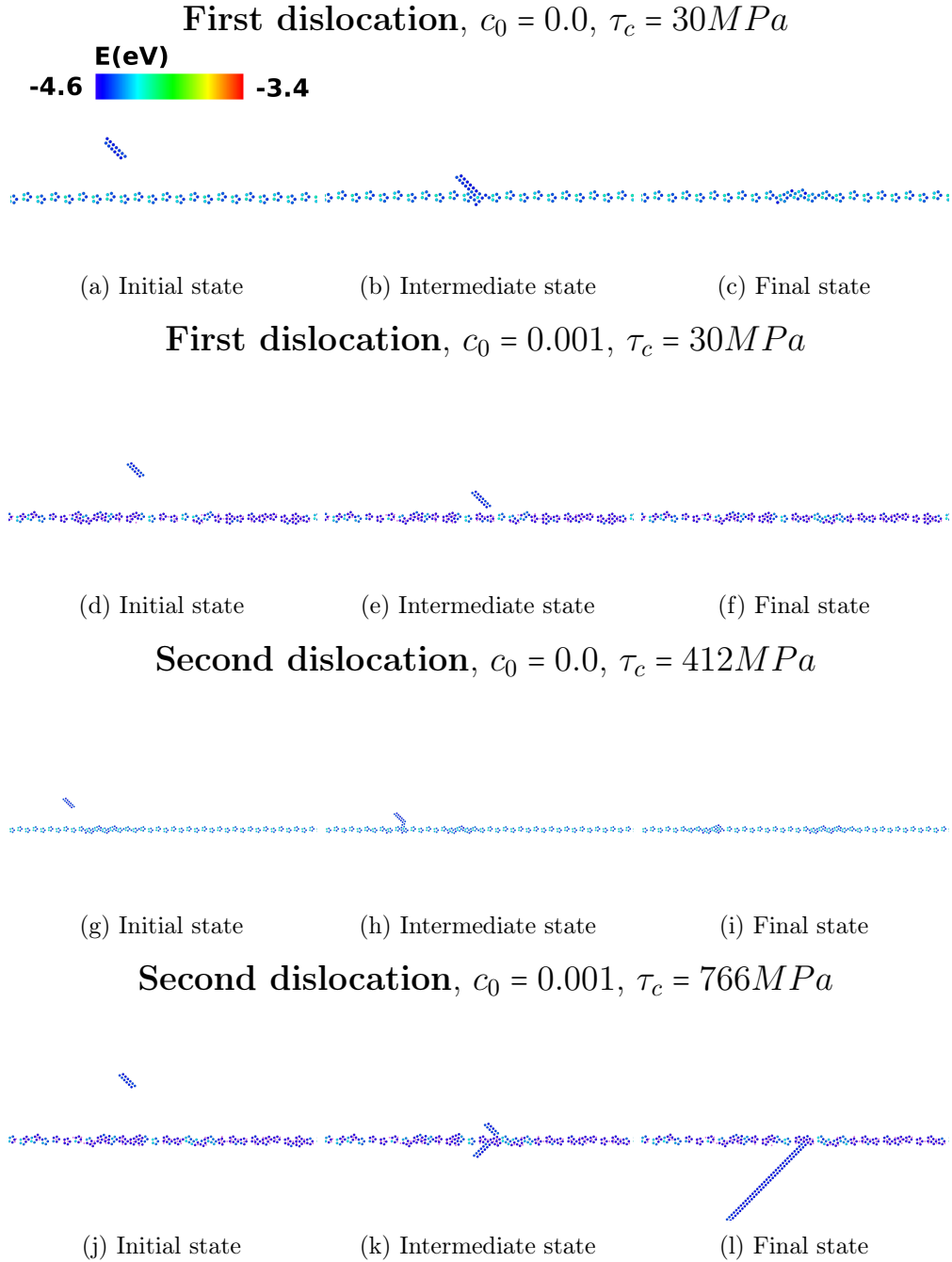


Figure 6.4 – Key atomistic configurations of the interaction of a screw dislocation with a $\Sigma 33a(441)\langle 110 \rangle$ grain boundary. The purple spheres are the H atoms and the other spheres are the non-fcc nickel atoms which are colored due to their energy. (a)–(c), (d)–(f), (g)–(i), and (j)–(l) configurations denote the initial, intermediate and final configuration of first dislocation in H-free, second dislocation in H-free, first dislocation in H-charged, and the second dislocation in H-charged samples, respectively.

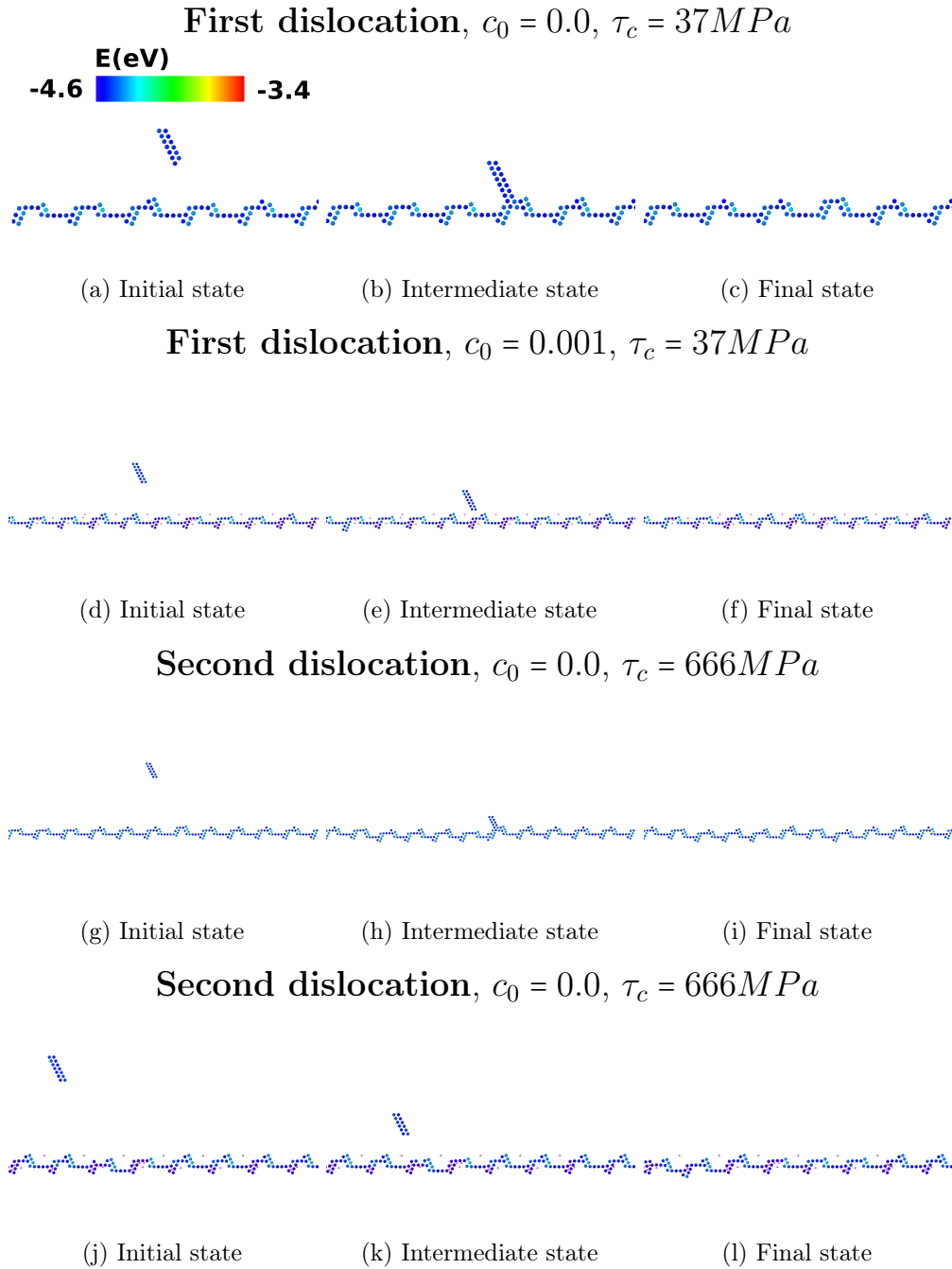


Figure 6.5 – Key atomistic configurations of the interaction of a screw dislocation with a $\Sigma 33b(554)\langle 110 \rangle$ grain boundary. The purple spheres are the H atoms and the other spheres are the non-fcc nickel atoms which are colored due to their energy. (a)–(c), (d)–(f), (g)–(i), and (j)–(l) configurations denote the initial, intermediate and final configuration of first dislocation in H-free, second dislocation in H-free, first dislocation in H-charged, and the second dislocation in H-charged samples, respectively.

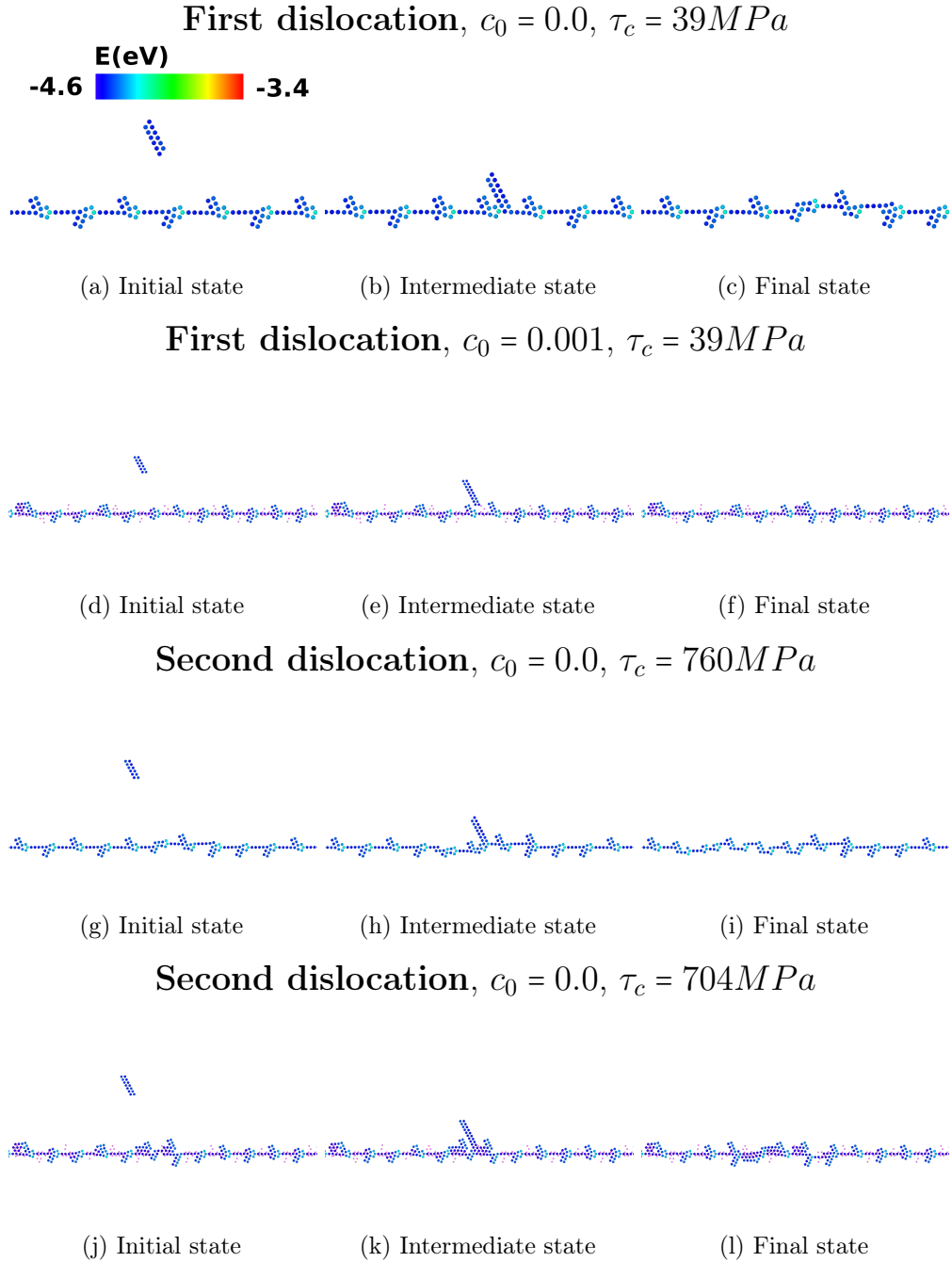


Figure 6.6 – Key atomistic configurations of the interaction of a screw dislocation with a $\Sigma 41(443)\langle 110 \rangle$ grain boundary. The purple spheres are the H atoms and the other spheres are the non-fcc nickel atoms which are colored due to their energy. (a)–(c), (d)–(f), (g)–(i), and (j)–(l) configurations denote the initial, intermediate and final configuration of first dislocation in H-free, second dislocation in H-free, first dislocation in H-charged, and the second dislocation in H-charged samples, respectively.

Chapter 6. Effect of segregated hydrogen atoms on the dislocation–grain boundary interactions

The screw dislocations in fcc metals dissociate to two Shockley partial dislocations.

$$\frac{a}{2}[1\bar{1}0]_{0^\circ} \rightarrow \frac{a}{6}[\bar{1}2\bar{1}]_{150^\circ}^T + \frac{a}{6}[2\bar{1}\bar{1}]_{30^\circ}^L \quad (6.1)$$

T and L denote trailing and leading partials, respectively. Both leading and trailing partials have mixed characters. Thus, they individually can interact with the stress field induced by the presence of H atoms along the GBs. However, apart from Ni Σ 19(331) \langle 110 \rangle case then it can be seen that the presence of the H atoms does not increase the resolved shear at which the first screw dislocation enters the GB. This observation is expected because the stress field induced by the presence of H atoms around the GB is not interacting with the screw dislocations. However, H atoms have both softening and hardening effects on the second screw dislocation. In Ni Σ 9(221) \langle 110 \rangle , and Ni Σ 33a(441) \langle 110 \rangle they hardened the material by increasing the magnitude of the load needed for entering the dislocation into the GB. While in the other cases they either did not have a significant effect or softened the material. This behavior is related to the atomistic interaction of the dislocation and GB.

In the H-free cases of Ni Σ 9(221) \langle 110 \rangle , Ni Σ 33a(441) \langle 110 \rangle and Ni Σ 41(443) \langle 110 \rangle the screw dislocation dissociates into grain boundary dislocations and in the other cases the dislocation is absorbed to the boundary. In the presence of H atoms, the dislocation is always absorbed and no dissociation happens. This behavior is due to the fact that dissociated process usually needs GB migration which does not associate with any diffusion or mass transport. By adding the hydrogen to the GB, migration of the GB needs diffusion of H atoms to the newly appearing stable sites. This phenomenon can hinder the dissociation process and enforce the dislocation to get absorbed to the boundary. So, the interaction of the GB and the dislocation depends on the character of the residual Burgers vector at the boundary.

In the cases of Ni Σ 19(331) \langle 110 \rangle and Ni Σ 33a(441) \langle 110 \rangle the first dislocation dissociates in H-free specimen but in the H-charged case, the first dislocation can not dissociate. Thus, a higher stress is necessary to drive the second dislocation to the H-charged GB in comparison to that of the H-free case. Thus, the material is hardened. In the Ni Σ 41(443) \langle 110 \rangle case in which the first dislocation dissociates but the GB dislocations can not glide along the GB the presence of the H atoms prevents the dissociation. However, the critical shear for the driving the second dislocation into the boundary decreases by the presence of H atoms. This phenomenon can be due to change in the character of the interaction between the dissociated/absorbed dislocation and the second dislocation. In Ni Σ 27(115) \langle 110 \rangle boundary the first screw dislocation can not dissociate along the boundary and arrival of the second screw makes the boundary to emit a partial dislocation. Addition of H atoms to this boundary enhances the transmission of slip when the second dislocation arrives. The stress needed for transmission of the slip is less than the stress necessary for emission of the partial.

6.2. Interaction of straight dislocations and the grain boundaries

6.2.2 Mixed dislocations

Figures 6.7–6.10 illustrates the key configurations of the mixed dislocation–GB interactions for each grain boundary. Table 6.2 summarizes the results of the simulations.

The mixed dislocations in fcc metals dissociate to a mixed 120° and an edge dislocation.

$$\frac{a}{2}[01\bar{1}]_{120^\circ} \rightarrow \frac{a}{6}[\bar{1}2\bar{1}]_{150^\circ}^T + \frac{a}{6}[11\bar{2}]_{90^\circ}^L \quad (6.2)$$

The leading and trailing partials has the edge and mixed character, respectively. Thus, they individually can interact with the stress field induced by the presence of H atoms along the GBs. It can be seen that in all cases the critical tensile stress by which the first dislocation enters the grain boundary is increased by the presence of H atoms. The behavior is expected because the stress fields that are induced by the presence of H atoms can interact with the mixed dislocation. It should be noted that we found both types of regions in which the stress field could repel/attract the dislocations. Here we did the simulations for the dislocations arriving to the repelling regions.

In all cases, except Ni Σ 33b(554) \langle 110 \rangle and Ni Σ 41(443) \langle 110 \rangle in which the dislocations form junctions with the pre-existing partial dislocations along the boundary before entering it, the mixed dislocations dissociate in H-free cases. Adding H atoms cannot prevent the dissociation in Ni Σ 9(221) \langle 110 \rangle and Ni Σ 19(331) \langle 110 \rangle cases. In these cases, the second dislocation in H charged specimens will enter the boundary in higher loads in comparison with the H free cases. In Ni Σ 33a(441) \langle 110 \rangle case, the presence of H atoms blocks the dissociation of the first dislocation and both the first and the second dislocation enters the grain boundary in higher loads. In Ni Σ 33b(554) \langle 110 \rangle and Ni Σ 41(443) \langle 110 \rangle cases, the first dislocation is hardened by the presence of H.

It can be seen that if the first mixed dislocation can reach to the boundary it always dissociates into grain boundary dislocations. In the cases of Ni Σ 9(221) \langle 110 \rangle and Ni Σ 19(331) \langle 110 \rangle the presence of H atoms along the boundary cannot change the reaction but postpones it to significantly higher stresses. In the case of Ni Σ 33a(441) \langle 110 \rangle the presence of H atoms prohibits the dissociation process at the grain boundary and the dislocation is just absorbed to the boundary. When the first dislocation dissociates the second dislocation also dissociates in the H free cases. However, in the H charged cases the second dislocation does not dissociate. Moreover, the reaction in all cases is hardened. Another behavior is observed for Ni Σ 33b(554) \langle 110 \rangle and Ni Σ 41(443) \langle 110 \rangle cases. These GBs are arrays of dislocations and thus they contain stacking faults. When the first dislocation is approaching them the stacking faults expand and the dislocations form junctions with them. Thus, the dislocations do not really reach to the GBs. The presence of the H atoms cannot change this process, but it can harden the material by increasing the stress at which the junctions are formed.

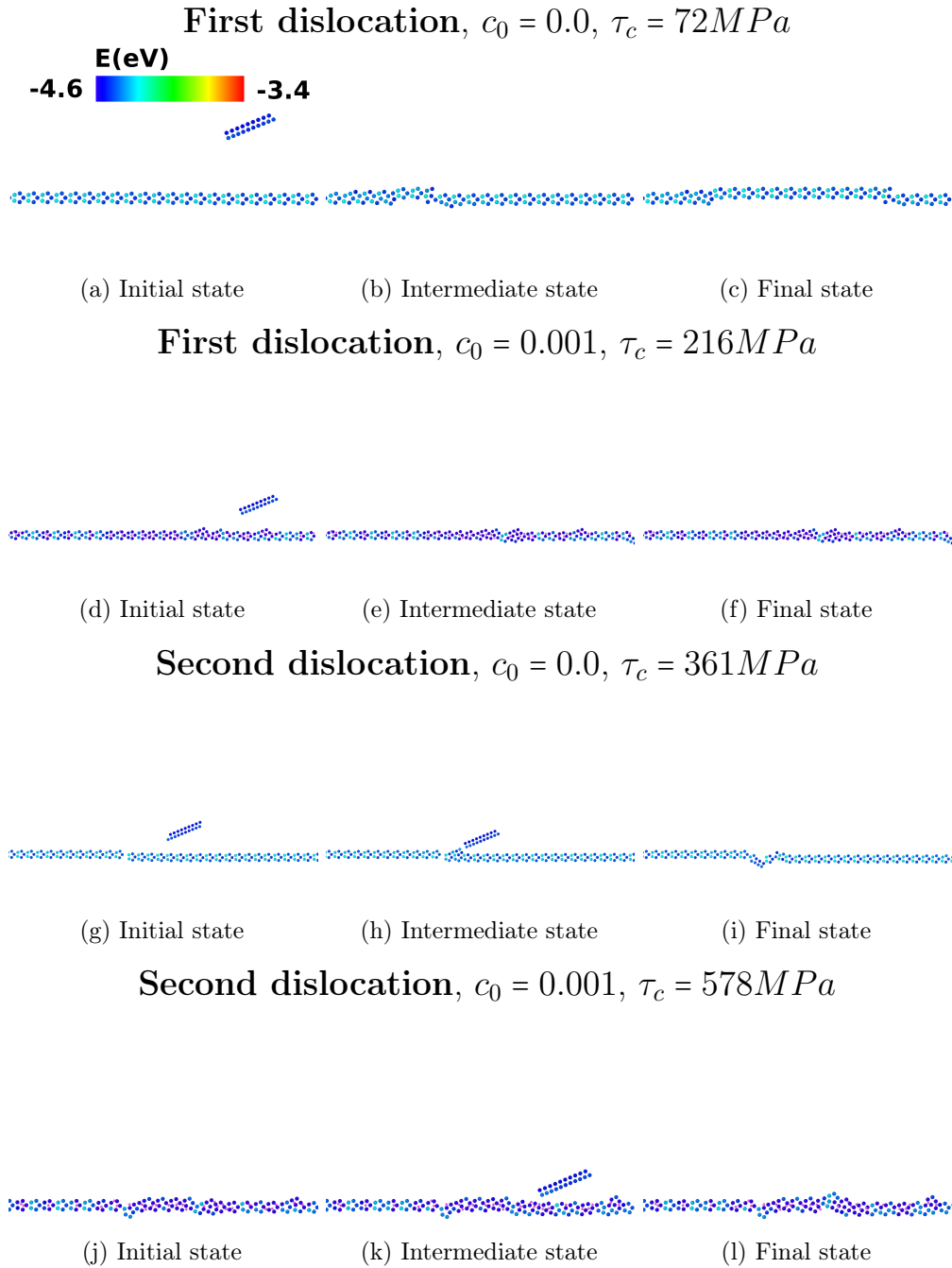


Figure 6.7 – Key atomistic configurations of the interaction of a mixed dislocation with a $\Sigma 19(331)\langle 110 \rangle$ grain boundary. The purple spheres are the H atoms and the other spheres are the non-fcc nickel atoms which are colored due to their energy. (a)–(c), (d)–(f), (g)–(i), and (j)–(l) configurations denote the initial, intermediate and final configuration of first dislocation in H-free, second dislocation in H-free, first dislocation in H-charged, and the second dislocation in H-charged samples, respectively.

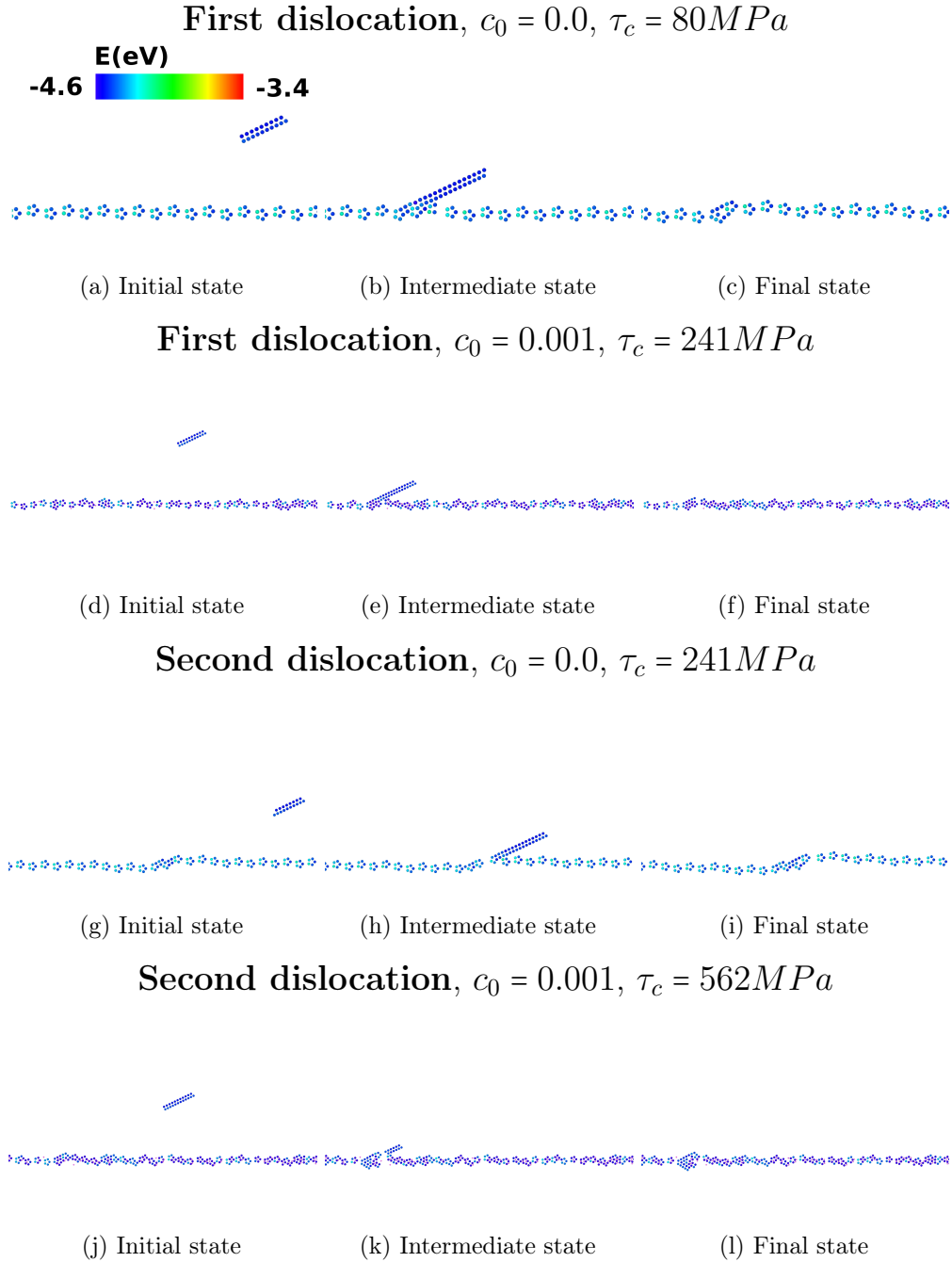


Figure 6.8 – Key atomistic configurations of the interaction of a mixed dislocation with a $\Sigma 33a(441)\langle 110 \rangle$ grain boundary. The purple spheres are the H atoms and the other spheres are the non-fcc nickel atoms which are colored due to their energy. (a)–(c), (d)–(f), (g)–(i), and (j)–(l) configurations denote the initial, intermediate and final configuration of first dislocation in H-free, second dislocation in H-free, first dislocation in H-charged, and the second dislocation in H-charged samples, respectively.

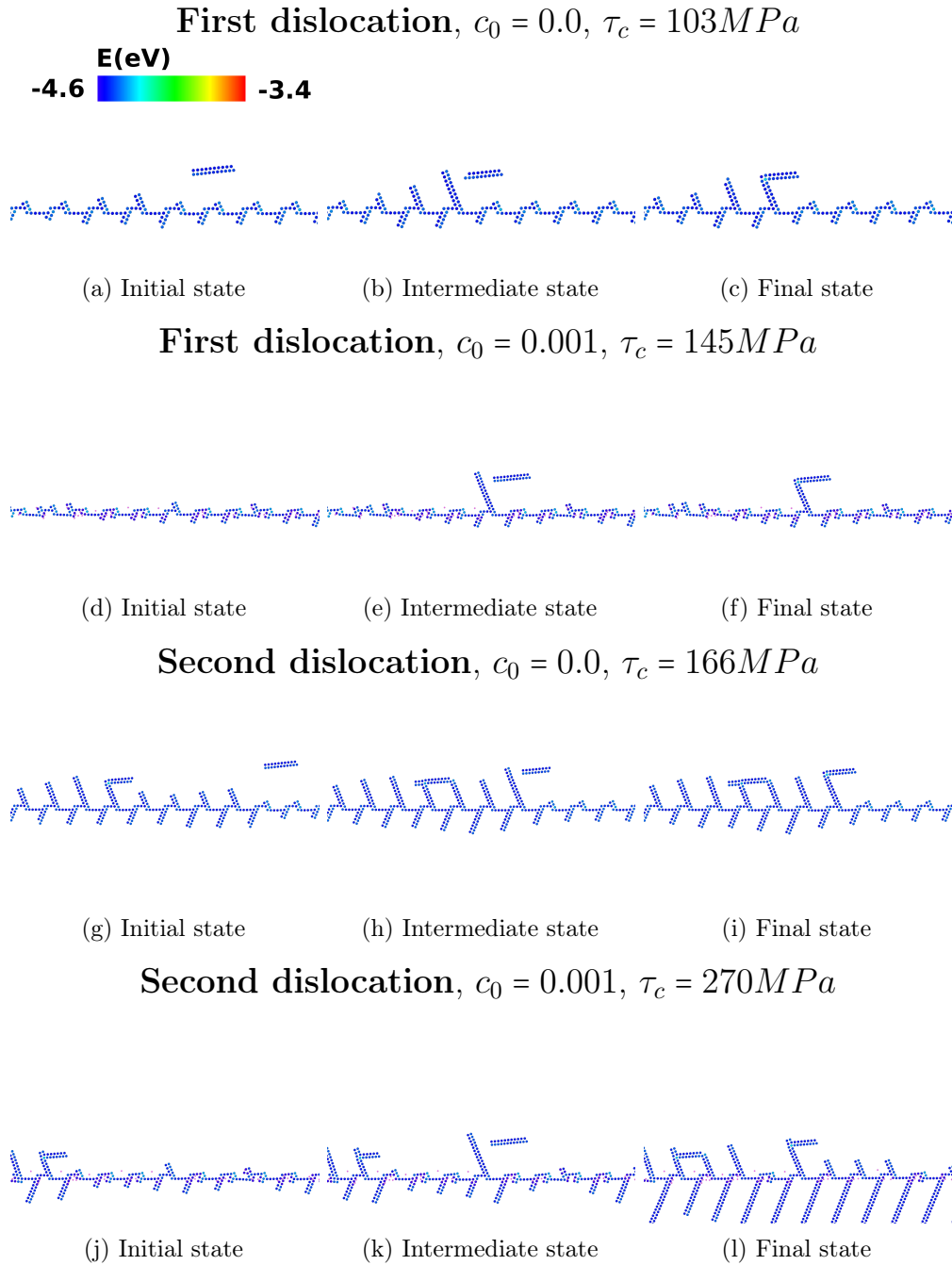


Figure 6.9 – Key atomistic configurations of the interaction of a mixed dislocation with a $\Sigma 33b(554)\langle 110 \rangle$ grain boundary. The purple spheres are the H atoms and the other spheres are the non-fcc nickel atoms which are colored due to their energy. (a)–(c), (d)–(f), (g)–(i), and (j)–(l) configurations denote the initial, intermediate and final configuration of first dislocation in H-free, second dislocation in H-free, first dislocation in H-charged, and the second dislocation in H-charged samples, respectively.

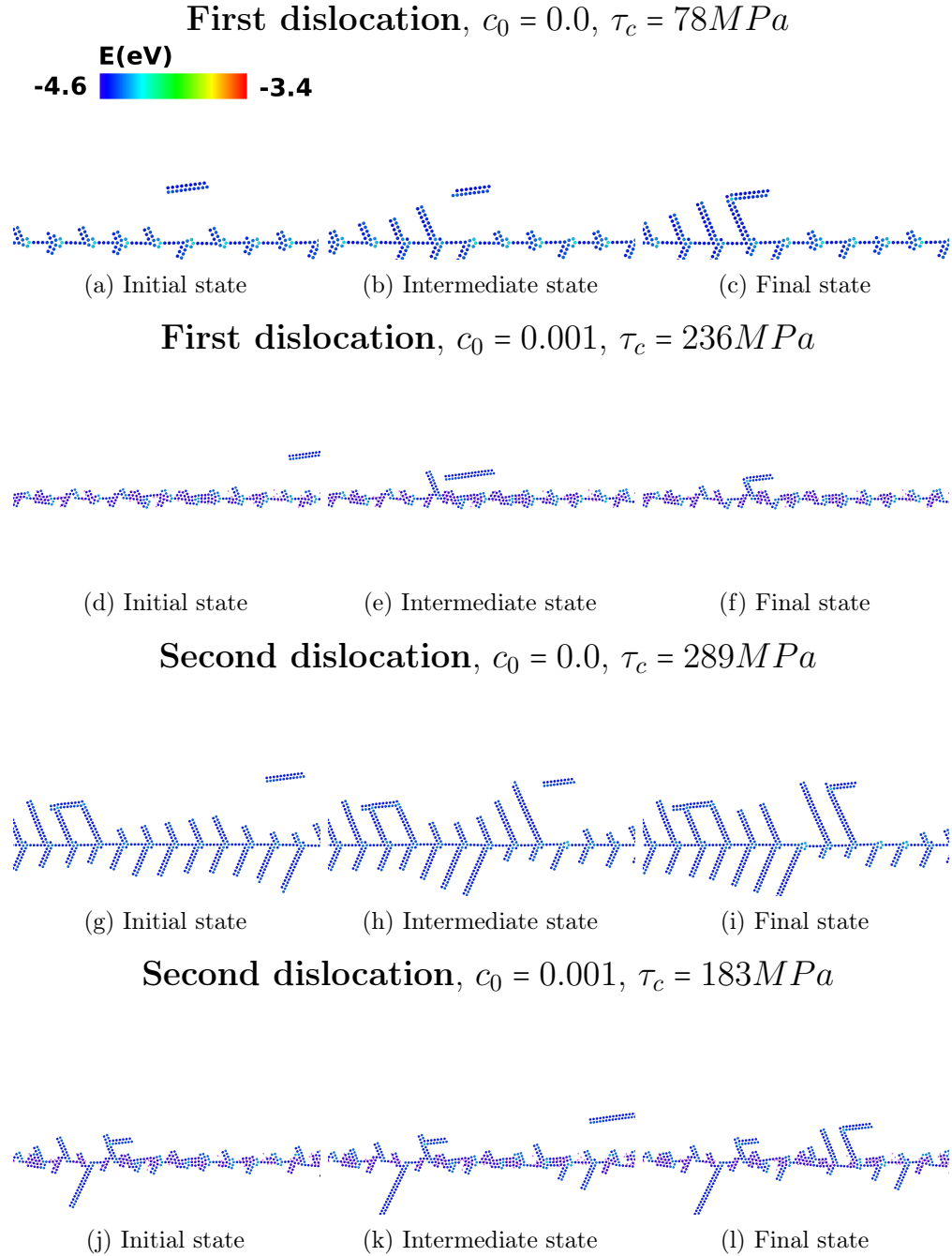


Figure 6.10 – Key atomistic configurations of the interaction of a mixed dislocation with a $\Sigma 41(443)\langle 110 \rangle$ grain boundary. The purple spheres are the H atoms and the other spheres are the non-fcc nickel atoms which are colored due to their energy. (a)–(c), (d)–(f), (g)–(i), and (j)–(l) configurations denote the initial, intermediate and final configuration of first dislocation in H-free, second dislocation in H-free, first dislocation in H-charged, and the second dislocation in H-charged samples, respectively.

Chapter 6. Effect of segregated hydrogen atoms on the dislocation–grain boundary interactions

Table 6.2 – Reactions of the screw dislocations and grain boundaries of interest in different nickel bicrystals. The critical resolved shear stresses τ_c (MPa), at which the reactions happened are given. The following abbreviations are used. A: Dislocation Absorbed, D: Dislocation dissociated, T: Slip transmitted, P: partial dislocation emitted from the GB, J: the dislocation formed a junction with the stacking faults in GB.

		Mixed dislocation							
		$c_0 = 0$				$c_0 = 0.001$			
		1st		2nd		1st		2nd	
θ		τ_c	Rxn	τ_c	Rxn	τ_c	Rxn	τ_c	Rxn
		(MPa)		(MPa)		(MPa)		(MPa)	
$\Sigma 9$	54.7	98	D	-	-	294	D	-	-
$\Sigma 19$	158	72	D	361	D	216	D	578	A
$\Sigma 33a$	154.7	80	D	241	A	241	A	562	A
$\Sigma 33b$	5.76	103	J	166	J	145	J	270	J
$\Sigma 41$	7.32	78	J	289	J	236	J	183	J

It can be seen that in the H-free cases of Ni $\Sigma 9$ (221)(110), Ni $\Sigma 33a$ (441)(110) and Ni $\Sigma 41$ (443)(110) the screw dislocation dissociates into grain boundary dislocations and in the other cases the dislocation is absorbed to the boundary. In the presence of H atoms, the dislocation is always absorbed and no dissociation happens. However, other than the case of Ni $\Sigma 9$ (221)(110) in which the presence of H atoms harden the materials in all other cases the critical stress for absorption/dissociation remains unchanged. The second dislocation in the H-free cases has different behaviors. For the Ni $\Sigma 9$ (221)(110) and Ni $\Sigma 33a$ (441)(110) cases at which the first dislocation is dissociated then the second one dissociates as well. However, in the case of Ni $\Sigma 41$ (443)(110), the second dislocation is absorbed. Interestingly, in the case of Ni $\Sigma 27$ (115)(110) partial dislocation is emitted after striking of the second dislocation to the boundary. The presence of hydrogen makes this boundary to emit a full dislocation at lower stress. The presence of hydrogen atoms hardens the GB against the second dislocation in the cases of Ni $\Sigma 9$ (221)(110), Ni $\Sigma 33a$ (441)(110) while it slightly softens/has no effect in the other cases.

From the comparison of the effect of H atoms on the behavior of the mixed and screw dislocations, one can conclude that the main parameter that plays a key role in hardening/softening of the first dislocation is the interaction of the stress field induced by the presence of the H atoms along the grain boundary. In the case of screw dislocations in which the stress field cannot interact with the dislocation, the critical stress by which the dislocation enters the GB remains the same in both H-free and H-charged cases.

However, in the mixed dislocation case, the presence of H atoms increases this stress. The hardening/softening of the second dislocation depends on the details of the interaction of the GB and dislocation.

6.3 Summary

In summary, the effect of the stress fields induced around grain boundaries on the hardening of the material is demonstrated by a set of simulations. The presence of H atoms along the GB can also change the interaction of the dislocations with the GB. Mainly it can inhibit the dissociation of lattice dislocations into grain boundary dislocations and enhance accumulation of the residual slip in the boundary. This effect can help decohesion of the H-charged grain boundaries.

7 Conclusion

In this thesis, we examined possible atomistic mechanisms of hydrogen embrittlement. The role of the segregated hydrogen atoms at the grain boundaries in enhancing both the nucleation and propagation of the intergranular cracks is examined by direct atomistic simulations. The simulations are performed for various grain boundaries relevant to the ductile behavior of polycrystalline nickel. The atomistic simulations which are based on a modified EAM potential which reproduces DFT segregation energies show little evidence of the enhancement of both fracture and decohesion in the presence of segregated H atoms. This result implies that the experimentally observed intergranular cracking of H-charged nickel is not a result of the presence of the equilibrium segregated H atoms along the grain boundary. Another possibility which is examined in this thesis is the effect of the presence of H atoms along the boundary on the dislocation–GB interactions. In general, the dislocations can enter the grain boundary and (i) dissociate in the sessile/mobile grain boundary dislocations, (ii) absorb to the boundary and induce residual slip (iii) transmit into the adjacent grain. The presence of H atoms modifies this behavior. Direct simulations of GB-dislocation interaction in the presence of H reveals that in most cases the presence of H atoms inhibits the dissociation of the dislocation. This means that the amount of residual slip is increased in the presence of H atoms and the material hardens and damage accumulates. Another interesting effect of the segregated H atoms is their induced stress field. The stress field around the GB changes due to the presence of H atoms, thus the interaction of the stress field with the coming dislocations can change the character of net residual Burgers vector along the grain boundary. The simulation of the interaction of the mixed dislocations with the H-free and H-charged grain boundaries in nickel showed that the repulsive stress fields can harden the material. Little evidence of such hardening is observed in the simulations the interaction of the same grain boundaries with screw dislocations. Thus, the hardening effect is due to the stress field. A simple analysis shows that the presence of stress fields can increase the component of Burgers vector perpendicular to the boundary and help decohesion.

Moreover, the role of H atoms on the strengthening of the material is investigated in

this thesis, first, we considered the H interstitials as solutes and invoked the solute strengthening theory to quantify this effect. The result of the solute strengthening theory is in very good agreement with the results of the tensile experiments at 77K for polycrystalline nickel. At room temperature, the solute strengthening theory gives slightly lower strengthening than experimental results. However, one can envision that solute drag process can strengthen the material further and fill the gap between the experimental and theoretical results. This observation implies that H atoms do not enhance global plasticity of the material. We also examined the interaction of H atoms with the pre-existing solutes in nickel. The results of the theory which is justified by direct simulations show that the presence of H atoms and forming solute–H complexes can have both hardening and softening effects. Thus, in the regions in the close vicinity of the crack tips or other defects in which the concentration of H atoms is comparable with the concentration of solutes, it can be envisioned that binding of H atoms to solute atoms can soften/harden the material.

Another proposed mechanism of H embrittlement is H enhanced nanovoid formation and growth (HENFG). We examined the hypothesis behind this theory which is the capability of H atoms to suppress the vacancy annihilation mechanism via direct simulations. The simulation of the interaction of edge dislocations in bcc iron with various vacancy–H complexes revealed that H atoms cannot significantly inhibit the jog formation process which is a known sink for the vacancies. Thus, finding the mechanism of the formation of the nano-voids in steel needs further investigation. One possible mechanism that can potentially explain the experimental observation is the concentration of damage during plastic deformation at certain parts of grain boundaries due to the presence of H atoms along the grain boundaries. The damaged zones that have high residual Burgers vectors can be nuclei of the nano-voids.

The other theory that is proposed in the literature for justification of HE is the defactant theory. This thermodynamics based theory suggests that H atoms can reduce the formation energies of defects such as dislocations. Thus, at a critical value of H concentration in metal the formation of dislocation becomes spontaneous and a HELP mechanism occurs. We examined this theory by direct simulation of bowing out of an edge dislocation in bcc-Iron. The results of the simulations showed that the kinetics of H diffusion along and across the dislocation plays a key role in the behavior of the dislocation. The presence of H atoms significantly increased the scape shear stress of the dislocation. This means that the material is hardened. Moreover, the magnitude of the bow out in H-charged specimens is lower than those of the H-free specimens implying the increase in the line tension due to the presence of H atoms. This result is in contrast to the defactant theory. Furthermore, the pipe diffusion of H atoms along the dislocation formed new pinning points along the dislocation. This phenomenon can harden the material further.

In summary, the results of the various atomistic simulations of mechanisms of H embrittlement in metals showed that the HELP, HEDE, and HENFG processes cannot explain

all the basic mechanisms of H embrittlement. Considering H atoms as solutes, and taking their effect on the behavior of the other defects such as pre-existing solutes, dislocations, and grain boundaries into account and also pay more attention to the kinetics and H diffusion in the metals can widen the knowledge of HE process.

Bibliography

- [1] W. H. Johnson. On some remarkable changes produced in iron and steels by the action of hydrogen acids. *Proceedings of Royal Society of London*, 23:168–175, 1875.
- [2] R. L. S. Thomas, J. R. Scully, and R. P. Gangloff. Internal hydrogen embrittlement of ultrahigh-strength aermet 100 steel. *Metallurgical and Materials Transactions A: Physical Metallurgy and Materials Science*, 34(2):327–344, 2003.
- [3] Sabine Bechtle, Mukul Kumar, Brian P Somerday, Maximilien E Launey, and Robert O Ritchie. Grain-boundary engineering markedly reduces susceptibility to intergranular hydrogen embrittlement in metallic materials. *Acta Materialia*, 57(14):4148–4157, 2009.
- [4] DH Lassila and HK Birnbaum. The effect of diffusive hydrogen segregation on fracture of polycrystalline nickel. *Acta Metallurgica*, 34(7):1237–1243, 1986.
- [5] Y. Lee and R. P. Gangloff. Measurement and modeling of hydrogen environment-assisted cracking of ultra-high-strength steel. *Metallurgical and Materials Transactions A: Physical Metallurgy and Materials Science*, 38 A(13):2174–2190, 2007.
- [6] R. P. Gangloff. Hydrogen-assisted cracking. *Comprehensive Structural Integrity*, 6:31–101, 2007.
- [7] C.S. Marchi and B.P. Somerday. Technical reference on hydrogen compatibility of materials. pages Tech. Rep. SAND2008–1163.
- [8] H Matsui, H Kimura, and S Moriya. The effect of hydrogen on the mechanical properties of high purity iron i. softening and hardening of high purity iron by hydrogen charging during tensile deformation. *Materials Science and Engineering*, 40(2):207–216, 1979.
- [9] SMHKH Moriya, H Matsui, and H Kimura. The effect of hydrogen on the mechanical properties of high purity iron ii. effect of quenched-in hydrogen below room temperature. *Materials Science and Engineering*, 40(2):217–225, 1979.

Bibliography

- [10] H Matsui, H Kimura, and Akihiro Kimura. The effect of hydrogen on the mechanical properties of high purity iron iii. the dependence of softening in specimen size and charging current density. *Materials Science and Engineering*, 40(2):227–234, 1979.
- [11] Akihiko Kimura and H Kimura. Hydrogen embrittlement in high purity iron single crystals. *Materials Science and Engineering*, 77:75–83, 1986.
- [12] SX Xie and JP Hirth. The effect of hydrogen on reversible and irreversible softening of spheroidized steel. *Materials Science and Engineering*, 60(3):207–212, 1983.
- [13] A Kimura and HK Birnbaum. Plastic softening by hydrogen plasma charging in pure iron. *Scripta metallurgica*, 21(1):53–57, 1987.
- [14] F Iacoviello, M Habashi, and M Cavallini. Hydrogen embrittlement in the duplex stainless steel z2cnd2205 hydrogen-charged at 200 c. *Materials Science and Engineering: A*, 224(1-2):116–124, 1997.
- [15] J Eastman, F Heubaum, T Matsumoto, and HK Birnbaum. The effect of hydrogen on the solid solution strengthening and softening of nickel. *Acta Metallurgica*, 30(8):1579–1586, 1982.
- [16] Richard P Gangloff. Hydrogen assisted cracking of high strength alloys. Technical report, DTIC Document, 2003.
- [17] R.P. Gangloff and R. P. Wei. Gaseous Hydrogen Embrittlement of High Strength Steels. *metallurgical transactions A*, 8(July):1043–1053, 1977.
- [18] John R Scully, Hakan Dogan, Richard P Gangloff, and Daoming Li. Controlling Hydrogen Embrittlement in Ultra-High Strength Steels. *Corrosion 2004*, 2004.
- [19] ZD Harris, AK Lawrence, G Guetard, JT Burns, and BP Somerday. The influence of deformation temperature on the initiation of hydrogen-induced intergranular cracking in nickel. In *Proceedings of 2016 international hydrogen conference*, pages 358–366, 2016.
- [20] Samantha K Lawrence, Yuriy Yagodzinsky, Hannu Hänninen, Esa Korhonen, Filip Tuomisto, Zachary D Harris, and Brian P Somerday. Effects of grain size and deformation temperature on hydrogen-enhanced vacancy formation in ni alloys. *Acta Materialia*, 128:218–226, 2017.
- [21] Daniel P Abraham and Carl J Altstetter. Hydrogen-enhanced localization of plasticity in an austenitic stainless steel. *Metallurgical and Materials transactions A*, 26(11):2859–2871, 1995.
- [22] P Sofronis and IM Robertson. Transmission electron microscopy observations and micromechanical/continuum models for the effect of hydrogen on the mechanical behaviour of metals. *Philosophical Magazine A*, 82(17-18):3405–3413, 2002.

-
- [23] PJ Ferreira, IM Robertson, and HK Birnbaum. Hydrogen effects on the interaction between dislocations. *Acta materialia*, 46(5):1749–1757, 1998.
- [24] Yukitaka Murakami. The effect of hydrogen on fatigue properties of metals used for fuel cell system. In *Advances in Fracture Research*, pages 167–195. Springer, 2006.
- [25] T Matsumoto, J Eastman, and HK Birnbaum. Direct observations of enhanced dislocation mobility due to hydrogen. *Scripta Metallurgica*, 15(9):1033–1037, 1981.
- [26] Afroz Barnoush and Horst Vehoff. In situ electrochemical nanoindentation: A technique for local examination of hydrogen embrittlement. *Corrosion Science*, 50(1):259–267, 2008.
- [27] V Gaspard, Guillaume Kermouche, David Delafosse, and Afroz Barnoush. Hydrogen effect on dislocation nucleation in a ferritic alloy fe–15cr as observed per nanoindentation. *Materials Science and Engineering: A*, 604:86–91, 2014.
- [28] BA Wilcox and GC Smith. Intercrystalline fracture in hydrogen-charged nickel. *Acta Metallurgica*, 13(3):331–343, 1965.
- [29] T Boniszewski and GC Smith. The influence of hydrogen on the plastic deformation ductility, and fracture of nickel in tension. *Acta metallurgica*, 11(3):165–178, 1963.
- [30] DH Lassila and HK Birnbaum. Intergranular fracture of nickel: the effect of hydrogen-sulfur co-segregation. *Acta Metallurgica*, 35(7):1815–1822, 1987.
- [31] T Neeraj, R Srinivasan, and Ju Li. Hydrogen embrittlement of ferritic steels: observations on deformation microstructure, nanoscale dimples and failure by nanovoiding. *Acta Materialia*, 60(13):5160–5171, 2012.
- [32] Alexander R Troiano. The role of hydrogen and other interstitials in the mechanical behavior of metals. *trans. ASM*, 52(1):54–80, 1960.
- [33] WW Gerberich, P Marsh, J Hoehn, S Venkataraman, and H Huang. Hydrogen/plasticity interactions in stress corrosion cracking. *Corrosion–Deformation Interactions (CDI’92), Les Editions de Physique, Les Ulis*, pages 325–353, 1993.
- [34] RA Oriani and PH Josephic. Equilibrium aspects of hydrogen-induced cracking of steels. *Acta Metallurgica*, 22(9):1065–1074, 1974.
- [35] W.W. Gerberich and T. J. Foecke. Hydrogen enhanced decohesion in fe-si single crystals: implications to modeling of thresholds hydrogen effects on materials behavior. In *editors: Moody, N. R. and Thompson, A. W. (Warrendale, PA: TMS)*, pages 687–701, 1990.
- [36] RA Oriani. A mechanistic theory of hydrogen embrittlement of steels. *Berichte der Bunsengesellschaft für physikalische Chemie*, 76(8):848–857, 1972.

Bibliography

- [37] W. W. Gerberich, P. G. Marsh, and J. W. Hoehn. Hydrogen induced cracking mechanisms - are there critical experiments? In *Hydrogen Effects in Materials*, pages 539–551, 1996.
- [38] J Song, M Soare, and WA Curtin. Testing continuum concepts for hydrogen embrittlement in metals using atomistics. *Modelling and Simulation in Materials Science and Engineering*, 18(4):045003, 2010.
- [39] C. D. Beachem. New model for hydrogen- assisted cracking (hydrogen embrittlement). *Met Trans*, 3(2):437–451, 1972.
- [40] Howard K Birnbaum and Petros Sofronis. Hydrogen-enhanced localized plasticity—a mechanism for hydrogen-related fracture. *Materials Science and Engineering: A*, 176(1):191–202, 1994.
- [41] IM Robertson. The effect of hydrogen on dislocation dynamics. *Engineering Fracture Mechanics*, 68(6):671–692, 2001.
- [42] DF Teter, IM Robertson, and HK Birnbaum. The effects of hydrogen on the deformation and fracture of β -titanium. *Acta materialia*, 49(20):4313–4323, 2001.
- [43] Reiner Kirchheim. Solid solution softening and hardening by mobile solute atoms with special focus on hydrogen. *Scripta Materialia*, 67(9):767–770, 2012.
- [44] Reiner Kirchheim. Revisiting hydrogen embrittlement models and hydrogen-induced homogeneous nucleation of dislocations. *Scripta materialia*, 62(2):67–70, 2010.
- [45] Reiner Kirchheim, Brian Somerday, and Petros Sofronis. Chemomechanical effects on the separation of interfaces occurring during fracture with emphasis on the hydrogen-iron and hydrogen-nickel system. *Acta Materialia*, 99:87–98, 2015.
- [46] Afrooz Barnoush and Horst Vehoff. In situ electrochemical nanoindentation: a nanomechanical approach to rank hydrogen embrittlement in extremely small volumes, effects of hydrogen on materials. In *Proceedings of the 2008 International Hydrogen Conference (ASM International)*, Published: Jul, pages 187–194, 2009.
- [47] Suzhi Li, Yonggang Li, Yu-Chieh Lo, Thirumalai Neeraj, Rajagopalan Srinivasan, Xiangdong Ding, Jun Sun, Liang Qi, Peter Gumbsch, and Ju Li. The interaction of dislocations and hydrogen-vacancy complexes and its importance for deformation-induced proto nano-voids formation in α -fe. *International Journal of Plasticity*, 74:175–191, 2015.
- [48] Jun Song and W. A. Curtin. A nanoscale mechanism of hydrogen embrittlement in metals. *Acta Materialia*, 59(4):1557–1569, 2011.
- [49] Jun Song and WA Curtin. Atomic mechanism and prediction of hydrogen embrittlement in iron. *Nature materials*, 12(2):145–151, 2013.

-
- [50] P Sofronis and RM McMeeking. Numerical analysis of hydrogen transport near a blunting crack tip. *Journal of the Mechanics and Physics of Solids*, 37(3):317–350, 1989.
- [51] J. Lufrano, P. Sofronis, and D. Symons. Hydrogen transport and large strain elastoplasticity near a notch in alloy x-750. *Engineering Fracture Mechanics*, 59(6):827–845, 1998.
- [52] J. Lufrano, P. Sofronis, and H.K. Birnbaum. Elastoplastically accommodated hydride formation and embrittlement. *Journal of the Mechanics and Physics of Solids*, 46(9):1497–1520, 1998.
- [53] J. Lufrano and P. Sofronis. Enhanced hydrogen concentrations ahead of rounded notches and cracks-competition between plastic strain and hydrostatic stress. *Acta Materialia*, 46(5):1519–1526, 1998.
- [54] J. Lufrano and P. Sofronis. Numerical analysis of the interaction of solute hydrogen atoms with the stress field of a crack. *International Journal of Solids and Structures*, 33(12):1709–1723, 1996.
- [55] Mohsen Dadfarnia, Philip E Schembri, Petros Sofronis, James W Foulk, Kevin A Nibur, Dorian K Balch, et al. On modeling hydrogen-induced crack propagation under sustained load. *JOM*, 66(8):1390–1398, 2014.
- [56] Mohsen Dadfarnia, May L Martin, Akihide Nagao, Petros Sofronis, and Ian M Robertson. Modeling hydrogen transport by dislocations. *Journal of the Mechanics and Physics of Solids*, 78:511–525, 2015.
- [57] Emilio Martínez-Pañeda, Christian F Niordson, and Richard P Gangloff. Strain gradient plasticity-based modeling of hydrogen environment assisted cracking. *Acta Materialia*, 117:321–332, 2016.
- [58] Emilio Martínez-Pañeda, S del Busto, Christian Frithiof Niordson, and C Betegón. Strain gradient plasticity modeling of hydrogen diffusion to the crack tip. *international journal of hydrogen energy*, 41(24):10265–10274, 2016.
- [59] A Alvaro, I Thue Jensen, N Kheradmand, OM Løvvik, and V Olden. Hydrogen embrittlement in nickel, visited by first principles modeling, cohesive zone simulation and nanomechanical testing. *international journal of hydrogen energy*, 40(47):16892–16900, 2015.
- [60] Davide Di Stefano, Matous Mrovec, and Christian Elsässer. First-principles investigation of hydrogen trapping and diffusion at grain boundaries in nickel. *Acta Materialia*, 98:306–312, 2015.
- [61] WT Geng, AJ Freeman, R Wu, CB Geller, and JE Reynolds. Embrittling and strengthening effects of hydrogen, boron, and phosphorus on a σ 5 nickel grain boundary. *Physical Review B*, 60(10):7149, 1999.

Bibliography

- [62] AM Tahir, R Janisch, and A Hartmaier. Hydrogen embrittlement of a carbon segregated σ_5 (310)[001] symmetrical tilt grain boundary in α -Fe. *Materials Science and Engineering: A*, 612:462–467, 2014.
- [63] Xiao Zhou, Daniel Marchand, David L McDowell, Ting Zhu, and Jun Song. Chemo-mechanical origin of hydrogen trapping at grain boundaries in fcc metals. *Physical review letters*, 116(7):075502, 2016.
- [64] Xiao Zhou and Jun Song. Effect of local stress on hydrogen segregation at grain boundaries in metals. *Materials Letters*, 196:123–127, 2017.
- [65] Xu Zhang and Gang Lu. Quantum mechanics/molecular mechanics methodology for metals based on orbital-free density functional theory. *Physical Review B*, 76(24):245111, 2007.
- [66] Xu Zhang, Chong-Yu Wang, and Gang Lu. Electronic structure analysis of self-consistent embedding theory for quantum/molecular mechanics simulations. *Physical Review B*, 78(23):235119, 2008.
- [67] Yi Zhao, Chongyu Wang, Qing Peng, and Gang Lu. Error analysis and applications of a general qm/mm approach. *Computational Materials Science*, 50(2):714–719, 2010.
- [68] Mao Wen, Zhiyuan Li, and Afrooz Barnoush. Atomistic study of hydrogen effect on dislocation nucleation at crack tip. *Advanced Engineering Materials*, 15(11):1146–1151, 2013.
- [69] Shinya Taketomi, Ryosuke Matsumoto, and Noriyuki Miyazaki. Atomistic study of the effect of hydrogen on dislocation emission from a mode ii crack tip in alpha iron. *International Journal of Mechanical Sciences*, 52(2):334–338, 2010.
- [70] Ryosuke Matsumoto, Shinya Taketomi, Sohei Matsumoto, and Noriyuki Miyazaki. Atomistic simulations of hydrogen embrittlement. *international journal of hydrogen energy*, 34(23):9576–9584, 2009.
- [71] Zhong Hu, Seiji Fukuyama, Kiyoshi Yokogawa, and Shingo Okamoto. Hydrogen embrittlement of a single crystal of iron on a nanometre scale at a crack tip by molecular dynamics. *Modelling and Simulation in Materials Science and Engineering*, 7(4):541, 1999.
- [72] Xuejun Xu, Mao Wen, Zhong Hu, Seiji Fukuyama, and Kiyoshi Yokogawa. Atomistic process on hydrogen embrittlement of a single crystal of nickel by the embedded atom method. *Computational materials science*, 23(1):131–138, 2002.
- [73] Johann von Pezold, Liverios Lymperakis, and Jörg Neugebauer. Hydrogen-enhanced local plasticity at dilute bulk h concentrations: The role of h-h interactions and the formation of local hydrides. *Acta Materialia*, 59(8):2969–2980, 2011.

-
- [74] Mei Q Chandler, MF Horstemeyer, MI Baskes, PM Gullett, GJ Wagner, and B Jelinek. Hydrogen effects on nanovoid nucleation in face-centered cubic single-crystals. *Acta Materialia*, 56(1):95–104, 2008.
- [75] B. Kuhr, D. Farkas, and I.M. Robertson. Atomistic studies of hydrogen effects on grain boundary structure and deformation response in fcc ni. *Computational Materials Science*, 122:92–101, 2016.
- [76] Jun Xiong, Yaxin Zhu, Zhenhuan Li, and Minsheng Huang. Hydrogen-enhanced interfacial damage in ni-based single crystal superalloy. *Scripta Materialia*, 143:30–34, 2018.
- [77] X. Zhou, B. Ouyang, W.A. Curtin, and J. Song. Atomistic investigation of the influence of hydrogen on dislocation nucleation during nanoindentation in ni and pd. *Acta Materialia*, 116:364–369, 2016.
- [78] X.W. Zhou, F. El Gabaly, V. Stavila, and M.D. Allendorf. Molecular dynamics simulations of hydrogen diffusion in aluminum. *Journal of Physical Chemistry C*, 120(14):7500–7509, 2016.
- [79] R.J. Zamora, K.L. Baker, and D.H. Warner. Illuminating the chemo-mechanics of hydrogen enhanced fatigue crack growth in aluminum alloys. *Acta Materialia*, 100:232–239, 2015.
- [80] G.P.M. Leyson, B. Grabowski, and J. Neugebauer. Multiscale description of dislocation induced nano-hydrides. *Acta Materialia*, 89:50–59, 2015.
- [81] Ryosuke Matsumoto, Shoichi Seki, Shinya Taketomi, and Noriyuki Miyazaki. Hydrogen-related phenomena due to decreases in lattice defect energies—molecular dynamics simulations using the embedded atom method potential with pseudo-hydrogen effects. *Computational Materials Science*, 92:362–371, 2014.
- [82] Ali Tehrani and William A. Curtin. Atomistic study of hydrogen embrittlement of grain boundaries in nickel: I. fracture. *Journal of the mechanics and physics of solids*, 2017.
- [83] A Tehrani, X Zhang, G Lu, and W. A. Curtin. Hydrogen–vacancy–dislocation interactions in α -fe. *Modelling and Simulation in Materials Science and Engineering*, 25(2):025001, 2016.
- [84] A Tehrani, B Yin, and WA Curtin. Softening and hardening of yield stress by hydrogen–solute interactions. *Philosophical Magazine*, 97(6):400–418, 2017.
- [85] J Song and W. A. Curtin. Mechanisms of hydrogen-enhanced localized plasticity: An atomistic study using α -fe as a model system. *Acta Materialia*, 68:61–69, 2014.

Bibliography

- [86] Petros Sofronis and Howard K Birnbaum. Mechanics of the hydrogen-dislocation-impurity interactions—i. increasing shear modulus. *Journal of the Mechanics and Physics of Solids*, 43(1):49–90, 1995.
- [87] G. P. M. Leyson, W. A. Curtin, L. G. Hector, and C. F. Woodward. Quantitative prediction of solute strengthening in aluminium alloys. *Nature Materials*, 9(9):750–755, 2010.
- [88] G. P. M. Leyson, L. G. Hector Jr., and W. A. Curtin. First-principles prediction of yield stress for basal slip in mg-al alloys. *Acta Materialia*, 60(13-14):5197–5203, 2012.
- [89] G. P. M. Leyson, L. G. Hector Jr., and W. A. Curtin. Solute strengthening from first principles and application to aluminum alloys. *Acta Materialia*, 60(9):3873–3884, 2012.
- [90] James E Angelo, Neville R Moody, and Michael I Baskes. Trapping of hydrogen to lattice defects in nickel. *Modelling and Simulation in Materials Science and Engineering*, 3(3):289, 1995.
- [91] MI Baskes, Xianwei Sha, JE Angelo, and NR Moody. Trapping of hydrogen to lattice defects in nickel. *Modelling and Simulation in Materials Science and Engineering*, 5(6):651, 1997.
- [92] DE Jiang and Emily A Carter. First principles assessment of ideal fracture energies of materials with mobile impurities: implications for hydrogen embrittlement of metals. *Acta materialia*, 52(16):4801–4807, 2004.
- [93] Steve Plimpton. Fast parallel algorithms for short-range molecular dynamics. *Journal of computational physics*, 117(1):1–19, 1995.
- [94] Alexander Stukowski. Visualization and analysis of atomistic simulation data with ovito—the open visualization tool. *Modelling and Simulation in Materials Science and Engineering*, 18(1):015012, 2009.
- [95] M.R. Hestenes and E. Stiefel. Methods of conjugate gradients for solving linear systems. *Journal of Research of the National Bureau of Standards*, 49(6):409, 1952.
- [96] William C Swope, Hans C Andersen, Peter H Berens, and Kent R Wilson. A computer simulation method for the calculation of equilibrium constants for the formation of physical clusters of molecules: Application to small water clusters. *The Journal of Chemical Physics*, 76(1):637–649, 1982.
- [97] T. Schneider and E. Stoll. Molecular-dynamics study of a three-dimensional one-component model for distortive phase transitions. *Physical Review B*, 17(3):1302–1322, 1978.

-
- [98] VP Rajan and W. A. Curtin. Crack tip blunting and cleavage under dynamic conditions. *Journal of the Mechanics and Physics of Solids*, 90:18–28, 2016.
- [99] James R Rice. Dislocation nucleation from a crack tip: an analysis based on the peierls concept. *Journal of the Mechanics and Physics of Solids*, 40(2):239–271, 1992.
- [100] Viggo Tvergaard and John W Hutchinson. The relation between crack growth resistance and fracture process parameters in elastic-plastic solids. *Journal of the Mechanics and Physics of Solids*, 40(6):1377–1397, 1992.
- [101] Yueguang Wei and John W Hutchinson. Steady-state crack growth and work of fracture for solids characterized by strain gradient plasticity. *Journal of the Mechanics and Physics of Solids*, 45(8):1253–1273, 1997.
- [102] Matthew R Begley and John W Hutchinson. The mechanics of size-dependent indentation. *Journal of the Mechanics and Physics of Solids*, 46(10):2049–2068, 1998.
- [103] Srinath S Chakravarthy and W. A. Curtin. Stress-gradient plasticity. *Proceedings of the National Academy of Sciences*, 108(38):15716–15720, 2011.
- [104] S Olarnrithinun, SS Chakravarthy, and W. A. Curtin. Discrete dislocation modeling of fracture in plastically anisotropic metals. *Journal of the Mechanics and Physics of Solids*, 61(6):1391–1406, 2013.
- [105] LB Freund, JW Hutchinson, and PS Lam. Analysis of high-strain-rate elastic-plastic crack growth. *Engineering Fracture Mechanics*, 23(1):119–129, 1986.
- [106] LB Freund and JW Hutchinson. High strain-rate crack growth in rate-dependent plastic solids. *Journal of the Mechanics and Physics of Solids*, 33(2):169–191, 1985.
- [107] T Siegmund, NA Fleck, and A Needleman. Dynamic crack growth across an interface. *International Journal of Fracture*, 85(4):381–402, 1997.
- [108] Z Wu and W. A. Curtin. Brittle and ductile crack-tip behavior in magnesium. *Acta Materialia*, 88:1–12, 2015.
- [109] Jian-Sheng Wang and PM Anderson. Fracture behavior of embrittled fcc metal bicrystals. *Acta metallurgica et materialia*, 39(5):779–792, 1991.
- [110] Jian-Sheng Wang and Sinisa Dj Mesarovic. Directional dependence of corrosion fatigue of iron-silicon bicrystals. *Acta metallurgica et materialia*, 43(10):3837–3849, 1995.
- [111] Y Cheng, Z-H Jin, YW Zhang, and H Gao. On intrinsic brittleness and ductility of intergranular fracture along symmetrical tilt grain boundaries in copper. *Acta Materialia*, 58(7):2293–2299, 2010.

Bibliography

- [112] Tanushree Sinha and Yashashree Kulkarni. Alternating brittle and ductile response of coherent twin boundaries in nanotwinned metals. *Journal of Applied Physics*, 116(18):183505, 2014.
- [113] Johannes J Möller and Erik Bitzek. Fracture toughness and bond trapping of grain boundary cracks. *Acta Materialia*, 73:1–11, 2014.
- [114] James R Rice. Hydrogen and interfacial cohesion. *Metallurgical Society of AIME*, pages 455–466, 1976.
- [115] SP Lynch. A fractographic study of hydrogen-assisted cracking and liquid-metal embrittlement in nickel. *Journal of Materials science*, 21(2):692–704, 1986.
- [116] VI Yamakov, DH Warner, RJ Zamora, E Saether, WA Curtin, and EH Glaessgen. Investigation of crack tip dislocation emission in aluminum using multiscale molecular dynamics simulation and continuum modeling. *Journal of the Mechanics and Physics of Solids*, 65:35–53, 2014.
- [117] DH Warner, WA Curtin, and S Qu. Rate dependence of crack-tip processes predicts twinning trends in fcc metals. *Nature materials*, 6(11):876–881, 2007.
- [118] Céline Varvenne, Aitor Luque, and William A Curtin. Theory of strengthening in fcc high entropy alloys. *Acta Materialia*, 118:164–176, 2016.
- [119] GPM Leyson and WA Curtin. Solute strengthening at high temperatures. *Modelling and Simulation in Materials Science and Engineering*, 24(6):065005, 2016.
- [120] F Zhang and WA Curtin. Atomistically informed solute drag in al–mg. *Modelling and Simulation in Materials Science and Engineering*, 16(5):055006, 2008.
- [121] Yu N Osetsky and D J Bacon. An atomic-level model for studying the dynamics of edge dislocations in metals. *Modelling and Simulation in Materials Science and Engineering*, 11(4):427–446, 2003.
- [122] Georg Kresse and Jürgen Furthmüller. Efficient iterative schemes for ab initio total-energy calculations using a plane-wave basis set. *Physical Review B*, 54(16):11169, 1996.
- [123] G. Kresse. From ultrasoft pseudopotentials to the projector augmented-wave method. *Physical Review B*, 59(3):1758–1775, 1999.
- [124] John P Perdew, Kieron Burke, and Matthias Ernzerhof. Generalized gradient approximation made simple. *Physical review letters*, 77(18):3865, 1996.
- [125] Peter E Blöchl. Projector augmented-wave method. *Physical Review B*, 50(24):17953, 1994.

-
- [126] M. Methfessel and A. T. Paxton. High-precision sampling for brillouin-zone integration in metals. *Physical Review B*, 40(6):3616–3621, 1989.
- [127] Hendrik J Monkhorst and James D Pack. Special points for brillouin-zone integrations. *Physical Review B*, 13(12):5188, 1976.
- [128] GA Alers, JR Neighbours, and H Sato. Temperature dependent magnetic contributions to the high field elastic constants of nickel and an fe-ni alloy. *Journal of Physics and Chemistry of Solids*, 13(1):40–55, 1960.
- [129] M. B. Stearns. *Numerical Data and Functional Relationships in Science and Technology, Magnetic Properties of Metals, Subvolume a 3d, 4d and 5d Elements, Alloys and Compounds*, volume 19. 1986.
- [130] D. H. Lassila and H. K. Birnbaum. Intergranular fracture of hydrogen-sulfur of nickel : the effect of hydrogen-sulfur co-segregation. *Acta Metallurgica*, 35(7), 1987.
- [131] Lisa Ventelon, B Lüthi, E Clouet, L Proville, B Legrand, D Rodney, and F Willaime. Dislocation core reconstruction induced by carbon segregation in bcc iron. *Physical Review B*, 91(22):220102, 2015.
- [132] MA Soare and WA Curtin. Solute strengthening of both mobile and forest dislocations: The origin of dynamic strain aging in fcc metals. *Acta Materialia*, 56(15):4046–4061, 2008.
- [133] Hull D. and D. J. Bacon. *Theory of dislocations*. Oxford Oxfordshire ; New York: Pergamon Press, 1984.
- [134] Ashwin Ramasubramaniam, Mitsuhiro Itakura, and Emily A Carter. Interatomic potentials for hydrogen in α -iron based on density functional theory. *Physical Review B*, 79(17):174101, 2009.
- [135] Yi Zhao and Gang Lu. Qm/mm study of dislocation—hydrogen/helium interactions in α -fe. *Modelling and Simulation in Materials Science and Engineering*, 19(6):065004, 2011.
- [136] Georg Kresse and Jürgen Hafner. Ab initio molecular dynamics for liquid metals. *Physical Review B*, 47(1):558, 1993.
- [137] Vijay Shastry and Diana Farkas. Molecular statics simulation of fracture in-iron. *Modelling and Simulation in Materials Science and Engineering*, 4(5):473, 1996.
- [138] Yu Wang, Damien Connétable, and Dôme Tanguy. Hydrogen influence on diffusion in nickel from first-principles calculations. *Physical Review B*, 91(9):094106, 2015.
- [139] MP Dewald and WA Curtin. Multiscale modelling of dislocation/grain-boundary interactions: I. edge dislocations impinging on σ_{11} (1 1 3) tilt boundary in al. *Modelling and Simulation in Materials Science and Engineering*, 15(1):S193, 2006.

Bibliography

- [140] Akio Ishii, Ju Li, and Shigenobu Ogata. “conjugate channeling” effect in dislocation core diffusion: Carbon transport in dislocated bcc iron. *PloS one*, 8(4):e60586, 2013.
- [141] G. K. Williamson and R. E. Smallman. Iii. dislocation densities in some annealed and cold-worked metals from measurements on the x-ray debye-scherrer spectrum. *Philosophical Magazine*, 1(1):34–46, 1956.
- [142] BA Szajewski and WA Curtin. Analysis of spurious image forces in atomistic simulations of dislocations. *Modelling and Simulation in Materials Science and Engineering*, 23(2):025008, 2015.
- [143] Dmitry Terentyev, DJ Bacon, and Yu N Osetsky. Interaction of an edge dislocation with voids in α -iron modelled with different interatomic potentials. *Journal of Physics: Condensed Matter*, 20(44):445007, 2008.
- [144] RH Wagoner. Calculating dislocation spacings in pile-ups at grain boundaries. *Metallurgical and Materials Transactions A*, 12(12):2015–2023, 1981.

Ali Tehranchi

CONTACT INFORMATION

Laboratory for Multiscale Mechanics Modeling
École polytechnique fédérale de Lausanne
MED 3 1126 (Batiment MED) Station 9, 1015,
Lausanne, Switzerland
Cell-phone: +41-78-7488923
Telephone: +41 21 69 31958
E-mail: ali.tehranchi@epfl.ch
E-mail: ali.tehranchi@gmail.com



RESEARCH INTERESTS EDUCATION

Mechanical behavior of materials, DFT calculations, MD simulations, Hydrogen embrittlement

École polytechnique fédérale de Lausanne, Lausanne, Switzerland

Ph.D. student, Mechanical Engineering , November 2013–Now

- Research Topic: *Predictive mechanisms of hydrogen embrittlement*
- Adviser: Professor William A. Curtin
- Honor: *Full financial support from Mechanical Swiss National Science Foundation (SNSF)*

Sharif University of Technology, Tehran, Iran

M.Sc., Structural Engineering , Jan 2009

- Thesis Topic: *Calculation of characteristic lengths associated with the first strain gradient theory by using inter-atomic potentials.*
- Adviser: Professor Hossein M. Shodja
- Area of Study: Structural Engineering
- Honor: *Rank 1st between student entered in 2006, GPA: 18.67/20*

B.S., Civil Engineering, August 2006

- Honor: *Rank 2nd between student entered in 2001*

B.S., Petroleum Engineering, August 2006

- Area of study: Reservoir Engineering

REFEREED JOURNAL PUBLICATIONS

Tehranchi, A., Yin, B. and Curtin, W.A., 2017, Softening and hardening of yield stress by hydrogen–Solute interactions, *Philosophical Magazine*, Vol. 97, issue 6, pp. 400–418. doi:10.1080/14786435.2016.1263402.

Tehranchi, A., Zhang, X., Lu, G and Curtin, W.A., 2017, Hydrogen–Vacancy–Dislocation Interactions in α -Fe, *Modelling and Simulation in Materials Science*, Vol. 25, Issue 2, article id. 025001. doi:10.1088/1361-651X/aa52cb

Tehranchi, A., and Curtin, W.A., 2017, Atomistic study of Hydrogen embrittlement of grain boundaries in Nickel: I. Fracture, *Journal of the mechanics and physics of solids*, Vol. 101, pp. 150–165. doi:10.1016/j.jmps.2017.01.020

Tehranchi, A., and Curtin, W.A., 2017, Atomistic study of Hydrogen embrittlement of grain boundaries in Nickel: II. Decohesion, *Modelling and Simulation in Materials Science*, Vol. 25, Issue 7, article id. 075013. doi:10.1088/1361-651X/aa87a6

Shodja, H.M. and Tehranchi, A., 2010, A formulation for the characteristic lengths of fcc materials in first strain gradient elasticity via Sutton–Chen potential, *Philosophical Magazine*, Vol. 90 , pp. 1893–1913. doi:10.1080/14786430903571453

	<p>Mofid, M., Tehranchi, A., A. Ostadhossein, 2010, On the viscoelastic beam subjected to moving mass. <i>Advances in engineering software</i>, Vol. 41, pp. 240–247. doi:10.1016/j.advengsoft.2009.08.001</p> <p>Shodja, H.M., Ahmadpoor, F, and Tehranchi, A, 2012, Calculation of the Additional Constants for fcc Materials in Second Strain Gradient Elasticity: Behavior of a Nano-size Bernoulli–Euler Beam with Surface Effects, <i>Transactions of ASME journal of applied mechanics</i> Vol. 79, pp.021008-1–8. doi:10.1115/1.4005535</p> <p>Shodja, H.M., Zaheri, A., Tehranchi, A., 2013, Ab initio calculations of characteristic lengths of crystalline materials in first strain gradient elasticity, <i>Mechanics of Materials</i> Vol. 61, pp.73-78. doi:10.1016/j.mechmat.2013.03.006</p>
CONFERENCE PRESENTATION	<p>Tehranchi, A., Curtin, W. A. Atomistic study of Hydrogen embrittlement of grain boundaries in Nickel In: <i>DPG 2017, Dresden, Germany</i>, March 20–25, 2017.</p> <p>Shodja, H.M., Tehranchi, A., Ghassemi, M. An atomistic study of interacting crack and inhomogeneity in fcc metals under polynomial loading In: <i>Proceedings of 12th international conference on fracture ICF</i>, July 12-17, 2009.</p> <p>Shodja, H.M., Tehranchi, A., Ghassemi, M. An atomistic study of interacting crack and inhomogeneity in fcc metals In: <i>Proceedings of Recent advances in non-linear mechanics</i>, August 24–27, 2009.</p> <p>Shodja, H.M., Tehranchi, A. A nanoscopic study of Kelvin problem in fcc metals. In: <i>37th international conference on solid mechanics (SOLMECH)</i>, September 6–10, 2010.</p>
REFeree SERVICE	<ul style="list-style-type: none"> • Reviewed some manuscripts for <i>Journal of the mechanics and physics of solids</i>, <i>Acta Materialia</i> and <i>Philosophical Magazine</i> • Reviewed a book proposal about theory of elasticity for Wiley.
TEACHING EXPERIENCE	<p>École Polytechnique Fédérale de Lausanne, Lausanne, Switzerland</p> <p><i>Teaching Assistant</i></p> <ul style="list-style-type: none"> • Solid mechanics, Spring 2017. • Solid mechanics, Spring 2016. • Introduction to mechanics of structures, Spring 2015. • Introduction to mechanics of structures, Spring 2014. <p>Sharif University of Tech., Tehran, Iran</p> <p><i>Teaching Assistant</i></p> <ul style="list-style-type: none"> • Mechanics of materials II, Fall 2004–Spring 2009. • Advanced Engineering Mathematics, Fall 2006. • Theory of elasticity I, Spring 2006–Spring 2009. • Micromechanics of defects in solids, Spring 2010.
HARDWARE AND SOFTWARE SKILLS	<ul style="list-style-type: none"> • Programming: MATLAB, C++, Fortran, Mathematica • scientific publishing softwares: LaTeX • Simulation softwares: LAMMPS, Quantum Espresso
EXPERTISE	<p>Mathematics:</p> <ul style="list-style-type: none"> • Real and Complex Analysis, familiar with differential geometry and manifolds <p>Mechanics:</p> <ul style="list-style-type: none"> • Augmented continuum theories, fracture mechanics, atomistic simulations including classical molecular dynamics and density functional theory, statistical mechanics

REFERENCES
AVAILABLE TO
CONTACT

Prof. William A. Curtin (e-mail: william.curtin@epfl.ch; phone: +41216937366)
• Professor, Mechanical Engineering, École polytechnique fédérale de Lausanne

